Bioavailability of Engineered Nanoparticles

Maryam Al-Ejji

October 2019

A thesis submitted to Imperial College London in fulfilment of the requirements for the degree of Doctor of Philosophy (PhD)

Department of Materials

Imperial College London

Declaration

I declare that this is my own work and any external collaboration or any references to other work are appropriately acknowledged or referenced.

Copyright Declaration

Abstract

Engineered nanomaterials (ENMs) are finding increasing applications because of their unique physicochemical properties. The increasing usage of these nanomaterials, however, raises concerns about their potential toxicity and of lack of control or even understanding over the life cycle from production, to use, and finally disposal. ENMs used in consumer products are highly likely to reach the environment during use and disposal, so it is critical to investigate their potential impact. Detailed mechanistic information about the particles and their state at the point of exposure to organisms must be developed to understand this risk. In this thesis, the possible transformation of ENMs in synthetic and realistic environments is explored, and the impact on marine organisms investigated. The work encompasses comparisons of transformations under inorganic versus organic sulfides and anaerobic digestion and correlative experiments on the effect of these particles on marine algae.

Natural organic matter (NOM) is the main content of the natural system, and in particular, humic acid (HA) is an organic matter that is known to influence the transformation of silver nanoparticles (AgNPs). An *in situ* sulfidation process was used to follow the transformation of citrate-capped silver nanoparticles (Cit-AgNPs) in environments containing organic versus inorganic sulfide. In both cases, sulfidation was observed, with a core-shell structure being more stabilised in organic components, and humic acid capped silver sulfide nanoparticles (HA-Ag_2SNPs) displayed evidence of a hollow sphere structure.

Anaerobic digestion is a wastewater treatment plant process, so ENMs polluting consumer waste streams will likely be exposed to this process. Its impact on particle transformation is essential to understand, as well as any impact that the particle may have on the digestion processes. Thus, ENMs were tested within a lab-scale anaerobic digester: 10 mg/l of AgNPs, titanium oxide nanoparticles (TiO_2NPs), cerium oxide nanoparticles (CeO_2NPs) and silver sulfide nanoparticles (Ag_2SNPs) were shown to have no significant effect on biogas production, indicating that at low concentrations, the ENMs do not interfere with the reactors. Also, there was no differences between the impacts of AgNPs and Ag_2SNPs on the performance of the reactor, and both structures aggregated and became fully sulfided). The speciation of zinc oxide nanoparticles (ZnONPs) and zinc sulfide

nanoparticles (ZnSNPs) were observed after 35 days: 54% of ZnONPs had absorbed iron oxyhydroxides (Zn-Fe-Ox), and the rest had a different ratio of zinc oxide (ZnO), zinc phosphate Zn_3PO_4, and ZnS. ZnSNPs had mostly transformed into zinc phosphate (Zn_3PO_4). Both ZnONPs and ZnSNPs had a ratio of ZnO, which was not less than 15%.

Finally, to achieve the objective of mimicking the environmental conditions, AgNPs were aged in Economic Co-operation and Development-((3-(N-morpholino) propanesulfonic acid) medium (OECD-MOPs). The medium was prepared according to organisation guidance 201 before AgNPs incubation. An algal growth inhibition test with MOPS buffer was carried out by spiking the freshwater green algae *Raphidocelis subcapitata* (*R. subcapitata*) with the particle-containing medium. The morphology of algal cells after treatment showed extensive deformation and disorganised cell walls. Some cells had evident changes on the cell wall from a rigid structure to a 'hairy' exterior and, in more extreme cases, had released extracellular polymeric substances (EPS). This EPS trapped the particles outside the algae and resulted in nanoparticle aggregation. Cytotoxicity was observed when Algae were exposed to AgNPs as well as some sulfidation, which correlated with intracellular uptake, dissolution, and precipitation of secondary Ag_2SNPs. For the AgNPs, the release of ions was directly linked to toxicity, and this changed in the presence of light, oxygen, and EPS.

Acknowledgements

I am appreciated the whole support and everything that had been offered by my supervisors Prof. Mary Ryan and Prof. Alexandra Porter for their inspiration as leaders of their field. I grateful for their patient and encouragement also their guidance during the experiments and writing up. I would like to thank Dr Marian Yallop from University of Bristol (UB) for sharing her experience and time regarding green algae cells. Thanks to Dr Tom Scott for helping me to work in Dr Ian Thomson's lab and the good care and help from his postdoc Dr Fariza Amma from Oxford University, I would like to thank her for every moment I spend working with her. I want to thank all the postdoc who helped and left ICL or BU. Dr Angela Goode, Dr Kelly Atkins, Dr Hew, and Dr Miguel Gonzales for working under the same project team and his help before he left. I would like to thank Dr Mohamed for his support when he was student until now as a postdoc for helping me during the last months. Two postdoc ladies who inspired me and answered my questions, tried to help and shared tips, since my start Dr Rosalia and Dr Elenora.

I want to thank Qatar University for its confidence and the opportunity for sponsored my PhD. I special thanks and gratefulness to Professor Mariam Al-Ali, Dr Noora Al-Thani, Dr Abubaker, Dr Mohammed and all the QU's staff for their continued encouragement. The most appreciation is to my parents and my family. I would like to thank my friend and sister Noora Al-Qahtani for her accompany during our study and everything.

I am extending all the appreciations to everyone who helped and supported me. My best time I spend was in EM suit, I am glad that I was trained by Dr Mohamoud, Cathey, Catriona and Mikal. I would like to thank all environmental engineering staff and student who allow me to use their labs and helped to use the equipment. I must thank all the student who was around and shared their experience in ICL, like Nouf, Corinne, Tenisha, Aigrm, Mila, Mille, Emma, Liya, Juhani, and Fatemeh, Tim, Chris, and Mustafa.

Publications and Conferences

Multimetallic Microparticles Increase the Potency of Rifampicin against Intracellular Mycobacterium tuberculosis Timothy Ellis, Michele Chiappi, Andrés García-Trenco, Maryam Al-Ejji, Srijata Sarkar, Theoni K. Georgiou, Milo S. P. Shaffer, Teresa D. Tetley, Stephan Schwander, Mary P. Ryan, and Alexandra E. Porter. ACSNano2018, 12, 5228−5240.

Spatially Resolved Dissolution and Speciation Changes of ZnO Nanorods during Short-Term in Situ Incubation in a Simulated Wastewater Environment. Miguel A.Gomez-Gonzalez, Mohamed A. Koronfel, Angela Erin Goode, Maryam Al-Ejji, Nikolaos Voulvoulis, Julia E. Parker, Paul D. Quinn, Thomas Bligh Scott, Fang Xie, Marian L. Yallop, Alexandra E. Porter, and Mary P. Ryan, *ACS Nano* 2019, 13, 10, 11049–11061.

Materials Science & Engineering, 3rd World Congress on August 24-26, 2017, Barcelona, Spain, Understanding Engineered Nanomaterials in the Environment: Silver Nanoparticles (AgNPs), Maryam Al-Ejji, Alexandra Porter, and Mary Ryan.

Contents

Figures

List of Tables

List of Abbreviations

AgNPs	Silver Nanoparticles
Cit-AgNPs	Citrate capped Silver Nanoparticles
Tween-AgNPs	Tween capped Silver Nanoparticles
PVP-AgNPs	Polyvinylpyrrolidone capped Silver Sulfide Nanoparticles
Ag_2SNPs	Silver Sulfide Nanoparticles
Cit-Ag_2SNPS	Citrate capped Silver Sulfide Nanoparticles
PVP-Ag_2SNPS	Polyvinylpyrrolidone capped Silver Sulfide Nanoparticles
Ag ion	Silver ion
HA	Humic Acid
IHSS	International Humic Substances Society
NOM	Natural Organic Matter
DOM	Dissolved Organic Matter
SRFA	Suwannee River fulvic acid
WWTPs	Wastewater Treatment Plants
ZnSNPs	Zinc sulfide nanoparticles
$Zn_3(PO_4)_2$	Zinc Phosphate
Zn-Fe oxy/hydroxides	Zinc absorbed in Iron oxyhydroxides
ZnONPs	Zinc Oxide Nanoparticles
SEM	Scanning Electron Microscopy
STEM	Scanning Transmission Electron Microscopy

TEM	Transmission Electron Microscopy
BF-TEM	Bright Field Transmission Electron Microscopy
DF-TEM	Dark Field Transmission Electron Microscopy
SAED	Selected Area Electron Diffraction
DLS	Dynamic Light Scattering
EDX	Energy Dispersive X-Ray Spectroscopy
ENM	Engineered Nanomaterial
HAADF	High Angle Annular Dark Field
HRTEM	High Resolution Transmission Electron Microscopy
EELS	Electron Energy Loss Spectrum
ADF	Angular Direct field
ICP-MS	Inductively Coupled Plasma Mass Spectrometry
ICP-OES	Inductively Coupled Plasma Optical Emission Spectroscopy
TOC	Total Organic chromatography
XAS	X-ray Absorption Spectroscopy
XANES	X-ray absorption near edge structure
EPS	Extracellular Polymeric Substances
ENMs	Engineered Nanomaterials
NPs	Nanoparticles
PVP	Polyvinylpyrrolidone
ROS	Reactive Oxygen Species

UA	Uranyl Acetate
UV-Vis	Ultraviolet Visible Spectroscopy
ZnONWs	Zinc Oxide Nanowires
OECD	Organisation for Economic Co-operation and Development
MOPs	3-(N-morpholino)propanesulfonic acid buffer)
R. subcapitata	*Raphidocelis Subcapitata*
XG	Xanthan Gum

Chapter 1: Introduction

1. Introduction

Nanomaterials have one dimension ranging from 1 nm to 100 nm and have unique properties [1]. These materials have distinct properties compared to their bulk counterparts: their high surface to volume ratio and diverse chemical, magnetic, optical, electronic, and mechanical properties are examples of their differentiating characteristics [2–4]. Applications of nanotechnology expand into consumer products through the use of manufactured engineering nanomaterials (ENMs). Silver nanomaterials (AgNMs) and zinc oxide nanomaterials (ZnONMs) are considered a very important class of material due to their unique physicochemical properties. AgNMs are well-known antibacterial agents utilised in many consumer products and industrial applications. The high demand for these products has increased AgNMs production to approximately 55 tons/year worldwide[5]. ZnONMs are wide bandgap semiconductors, implemented as sensors, catalysts, and others. The production of ZnONMs is estimated at 550 tons/year [5].

The increased use of nanomaterials in many applications intensifies the risk of environmental exposure to these materials at different stages during their life cycle, including disposal of raw materials and products. Therefore, the environmental impacts of these nanomaterials need to be understood by investigating their transformation and fate at these different stages of their life cycle. The surface of nanomaterials plays an essential role in their transformation. Nanomaterials have surface-area-to-volume ratios higher than bulk materials that can result in increased chemical and bio-reactivity.

Environmental exposure of nanomaterials can occur intentionally and unintentionally. During the release of ENMs into environmental systems, many exposure conditions can affect their physicochemical properties. For instance, sulfidation of silver nanoparticles (AgNPs) was suggested during their transformation in both soils and wastewater treatment plants (WWTPs) [6,7]. Sulfidation is the process of introducing sulfide ions into materials or molecules [8]. Sulfide sources are created naturally from ore minerals, such as copper and iron sulfides, as well as from the decomposition of natural organic matter [9,10]. At the same time, during their transformation zinc oxide nanoparticles (ZnONPs) undergo sulfidation and transformed into Zn phosphate nanoparticles ($Zn_3(PO_4)_2$) [7,11]. When nanoparticles have reached sewage systems and entered WWTPs, they tend to accumulate in sludge solids [12].

Most of these sludges are applied to soils in agriculture [13] which introduce nanoparticles through a primary pathway into the food chain [14].

Natural organic matter (NOM) can be identified as a combination of organic compounds that could contain negatively charged organic compounds and includes a wide range of molecular sizes and chemical compositions [15,16]. Dissolved organic matter (DOM) refers to the portion of dissolved organic carbon with a diameter < 0.45 micrometres. Most of the dissolved organic carbon found at the molecular level are in the form of polymeric organic acids, defined as humic substances. These substances are described as yellow organic acids with a molecular mass ranging between 1000 and 2000 Dalton (Da). The majority of dissolved organic carbon is classed as the organic compound in natural water [15,17]. This organic matter can change the physicochemical properties of engineered nanomaterials. DOMs affect dissolution of AgNPs and the rate of ZnONPs dissolution [18,19]. Therefore, investigating the behaviour of nanoparticles after discharge into the environmental system, which includes an interaction with NOM, can more accurately predict the risk of nanoparticles to living species. For example, ageing of nanoparticles in simulated water containing humic acid (HA) can be tested to characterise the impact of aged nanoparticles after transformation in HA [20] .

The release of ionic species *via* dissolution of nanoparticles is one of the main factors that contributes to measured toxicity. However, the nanotoxicity of these materials to microorganisms is more complicated than this; many parameters can affect the toxicity of nanoparticles, such as the particular properties of nanoparticles, e.g. their surface chemistry, the microorganism species type, and environmental conditions [21]. Some nanoparticles tend to aggregate, which means decreasing the nanoparticles' effective surface area and reducing their toxicity. For example, while titanium dioxide (TiO_2) NPs are insoluble, these NPs settle as aggregated particles after being spiked in wastewater and anaerobic digestion [22]. They can still exhibit a toxicity effect because of the physical contact between the microorganisms and nanoparticles [23]. Moreover, nanoparticle absorption by organic matter and biomass changes the NP's surface charge that may also affect their toxicity [24].

The chemistry, shape, aggregation state, surface charge, and solubility all affect the environmental toxicity of nanoparticles. This thesis presents research on the transformation

of AgNPs and ZnONPs exposed to different environmental conditions. The transformation of AgNPs, and effects on the toxicity on freshwater algae, as a first step in the aquatic food chain, were assessed within simulated water (humic acid) and the effect of these particles on the performance of a model WWTP were tested and related to their chemical transformations.

The scope of this thesis is to study the bioavailability of ENMs and their transformations in freshwater and sewage systems to understand and predict how they affect microorganisms at the point of exposure to them. A central goal was to characterise and visualise how these materials interact with, and are uptaken by algae and their effects on algal response [25]. The transformation of the ENMs can influence their bioavailability and are particularly linked to the environmental conditions surrounding the transformed nanoparticles. The primary objective was to investigate the transformation of ENMs within different surroundings and conditions, such as a simulated *in situ* sulfidation environment and the interaction of ENMs under different conditions and within anaerobic conditions, by putting the ENMs into a model anaerobic digestion system. The transformation of ENMs was targeted to illustrate the most suitable technique(s) to characterise the transformed nanoparticles.

Chapter 2: Literature Review

2. Literature Review

2.1. Physicochemical properties of Engineering Nanomaterials

Physicochemical properties are critical to the behaviour of ENMs in different environmental media. These properties differ considerably according to the particular type of nanoparticle, the synthesis methods, and the applications. The critical determinants of ENMs behaviour in the environment and bioreactivity are their chemical composition, size distribution, surface charge, concentration, specific surface area, solubility, zeta potential, stability and shell structure [26].

The specific surface area of nanoparticles is greater than that of bulk materials. The distribution of atoms and molecules on their surfaces are numerous, which leads to a dramatic increase in free surface energy. As a result, their reactivity can rise significantly, which may affect the bioreactivity of nanoparticles towards microorganisms [13,14]. Smaller-sized nanomaterials have a higher surface area-to-volume ratio that can increase chemical reactivity [27]. When cuboctahedral nanoparticles become larger (Figure 2-1), their surface area-to-volume ratio decreases, which means that the % of atomic surface fraction reduces. Therefore, we can conclude that the biological reactivity is drastically enhanced [28].

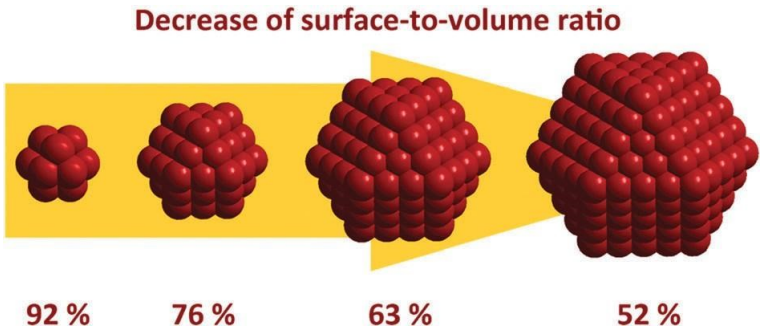

Figure 2-1: Schematic of the relationship between the reduction of surface area-to-volume ratio (atomic surface fraction in percentage) and particle size. The diagram is reprinted (adopted) with permission from The Royal Society of Chemistry [28].

Metallic nanoparticles typically maintain their stable suspension when coated with surfactants, whether organic or inorganic compounds [29]. In an unstable colloidal solution,

nanoparticles aggregate with neighbouring particles to form larger particles and then lose their surface reactivity and catalytic behaviour [30]. The surface charge of the nanoparticles is affected by immersing them in an aqueous solution to be charged by protonation/deprotonation on the particle surfaces [31]. The formation of surface charges will interact with the dissolved ions in the solution, resulting in an electrical double layer surrounding the charged particles [32]. In the electrical double layer, the more accumulated counter-ions are the Stern layer while the depleted co-ions are the diffuse layer (Figure 2-2). The surface charge of nanoparticles is positively affected by their transport. Therefore, the surface charge density influences the translocation process of nanoparticles through a nanopore [33]. The curvature and surface charge depend on the size of the particles [34,35].

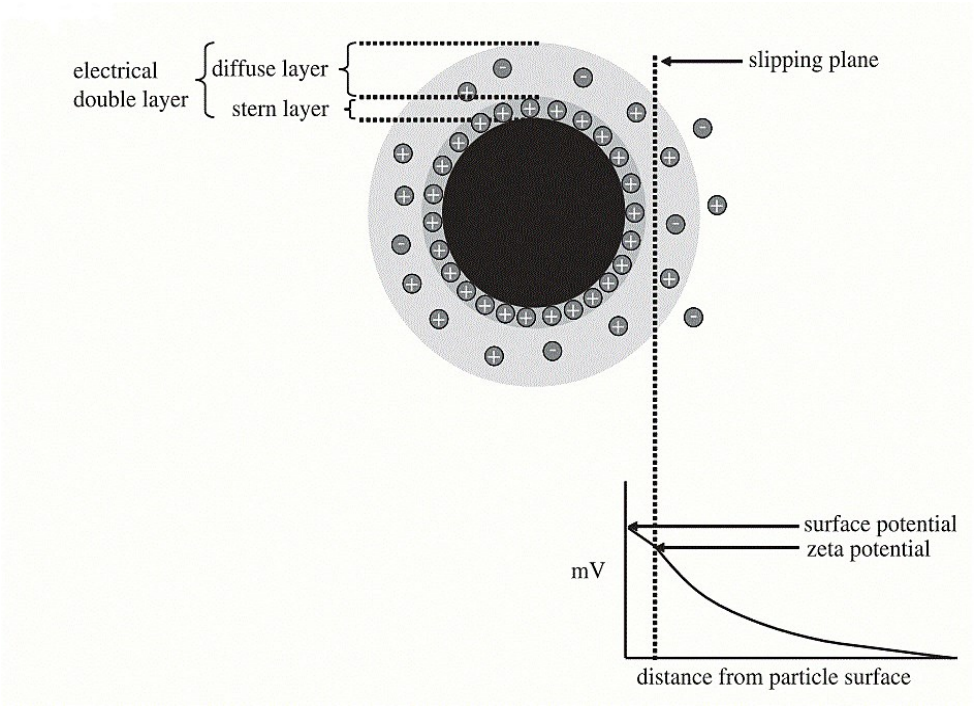

Figure 2-2: Schematic of the electrical double layer located around the nanoparticles' surrounding in the colloidal solution or medium. The electric potential can explain the theory of zeta potential of nanoparticles in a solution in a slipping plane. The diagram is reprinted (adopted) with permission from [36].

Important factors involving solution chemistry, that impact the physicochemical properties of nanoparticles, include ionic strength of the electrolyte composition, pH and the

concentration of natural organic matter (NOM) [36]. Similarly, in colloidal solutions, NOM compounds with high molecular weight can induce the aggregation of nanoparticles, whereas NOMs with low molecular weight increases their mobility [37]. For instance, in an aquatic environment, the stability and mobility of a silver nanoparticle (AgNP) suspension depend on effective processes like agglomeration, surface dissolution of Ag and sedimentation [38,39]

2.2. Nanoparticle synthesis and stability induced by a capping agent.

In general, there are two categories of nanomaterial synthesis: top-down and bottom-up approaches. Top-down approaches are chemical, physical, and mechanical processes that can break bulk materials into NPs. In contrast, bottom-up approaches build nanomaterials from molecules or atoms, much like how bricks are used to build a wall [40,41]. The bottom-up is preferable because it is cleaner and produces NPs with a more homogenous composition. Moreover, the chemical composition of synthesised nanomaterials is adopted to produce monodisperse NPs more thermodynamically in equilibrium. Nanomaterial formation involves two main processes, namely nucleation and growth [42]. Before these processes are explained, a summary of synthesis techniques is provided.

The typical synthesis method of NPs is chemical bath deposition, which is simple and uses mild conditions [43]. The chemical reduction method was first published in 1857 by Faraday and then improved in the 1950s by Turkovich and his colleagues to synthesise gold NPs [44]. This method involves heating a chloroauric acid ($HAuCl_4$) solution to boiling point followed by the reduction of sodium citrate ($Na_3C_6H_5O_7$) (2.1). The NPs produced had a diameter of 20 nm and a uniform shape. This synthesis method was developed with different reaction conditions and achieved controlled NP diameters [45].

$$2HAuCl_4 + 4Na_3C_6H_5O_7 \rightarrow H_2 + 2Au^0 + 4CO_2 + 4\,NaC_5H_5O_5 + 8NaCl \quad (2.1)$$

Similarly, AgNPs can be obtained with the stability of capping agents. These agents can be molecules, polymers or biological molecules that work through a charge or stabilisation mechanism. NPs have also been synthesised by using a potent reducing agent, namely sodium borohydride ($NaBH_4$), represented by Equation (2.2) [46]:

$$AgNO_3 + NaBH_4 \rightarrow Ag + \frac{1}{2} H_2 + \frac{1}{2} B_2H_6 + NaNO_3 \quad (2.2)$$

When the reduction of the metal salt is taking place, many atoms are formed, and as a consequence, the resultant NPs are less than 10 nm in size [47]. In general, for AgNPs, a silver nitrate salt ($AgNO_3$) is reduced by $NaBH_4$ with $Na_3C_6H_5O_7$ as a capping agent. This agent is employed to improve the stability of particles and prevent their interaction. Therefore, the surface energy increases and the aggregation further decreases [40]. Polyvinylpyrrolidone (PVP; $(C_6H_9NO)_n$ is a soluble polymer agent that has been utilised to work against the agglomeration of metal colloids, thus stabilising nanoparticles [48]. A further explanation of coating agent is provided below.

2.2.1. Nanoparticle Nucleation and Growth

Two separate processes, nucleation, and growth can influence the size and shape distribution of synthesised NPs. Nucleation is defined as a process of discrete particle formation with a new phase in a primary single-phase system representing a homogenous solution. Meanwhile, the growth can be explained as an increase in size when additional material is deposited on the particles [44]. Through the nucleation of AgNPs with citrate, Ag seeds are created by reducing the metal ion precursors. [49] During the agglomeration of these seeds, small clusters are formed and grow to become larger clusters. This growth is induced by the presence of a complexing agent or stabiliser [50]. If organic molecules are present at the initial stage of cluster growth, surface capping or covalent linkage is likely to yield smaller NPs. This reaction produces massive NP clusters with varied shapes and sizes [49].

In the initial stage of citrate reduction, a few seeds of AgNPs with citrate anions form into an enormous citrate complex. When the citrate complex grows slowly by aggregation, it outspreads to an optimal size. In this case, any further accumulation is prevented by the citrate complex's robust repelling surface layer. Further nanocrystal growth is observed through growth, in which Ag^+ ions are reduced at the AgNPs crystalline surface.

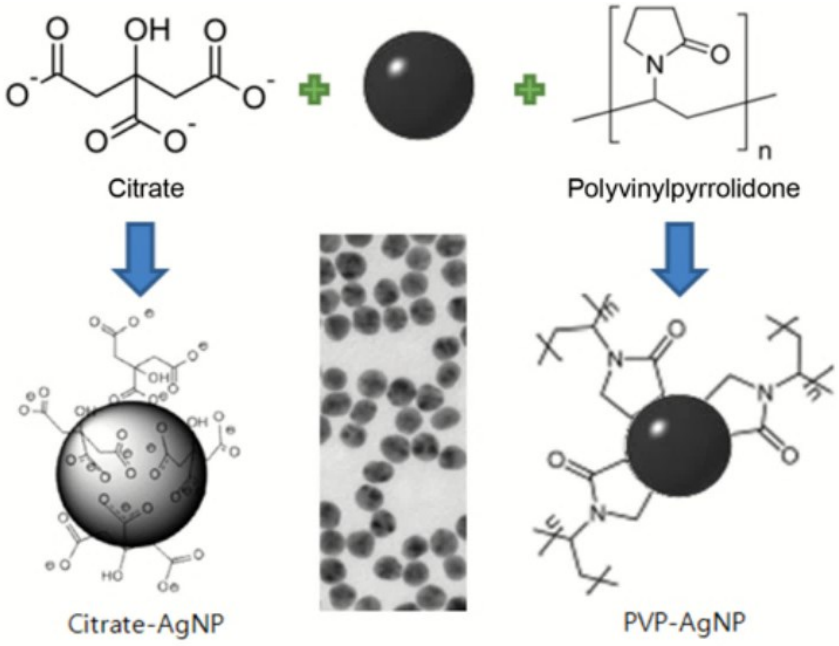

Figure 2-3: The chemical structure of citrate and PVP stabiliser agents that cap AgNPs showing their adsorption on the particle surface (particles size = 40-50 nm). The figure is provided by Springer Nature and Copyright Clearance Centre and reprinted (adopted) with permission from [51].

2.2.2. Capping Agent

Several capping agents are utilised to stabilise the colloidal NP solution. The agents most recommended by the Organisation for Economic Co-operation and Development Working Party on Manufactured Nanomaterials (OECD WPMN) to test cytotoxicity [52] are citrate and PVP, which differ in the ways in which they to prevent aggregation (Figure 2-3). These capping agents can be employed as AgNP stabilising agents because of their low toxicity. The stability mechanisms of citrate and PVP are electrostatic and steric repulsion, respectively [51]. The AgNPs must be made stable before adding them to an environmental medium that subsequently alters their physicochemical properties. Therefore, the chemical stability of the AgNP colloidal solution in different media and under several conditions is often examined to emphasise the effects of surface modification [52]. The surface chemistry of citrate capped AgNPs has a negative charge in water at pH 7. This is provided by the attachment of three carboxyl groups (COO−) onto the surface of AgNPs that cause an electrostatic repulsion between the Cit–AgNPs in solution.

In comparison, PVP consists of a pyrrolidone ring with a highly polar amide group as well as polar methylene and methine groups in the rings and the backbone [53]. The pyrrolidone ring immobilised on the surface of AgNPs induces steric repulsion, while groups on the pyrrolidone ring can induce electrostatic repulsion. Thus, a PVP capping agent stabilises *via* a combination of mechanisms. PVP is considered a shape-controlled agent that promotes the growth of crystal facets such as Ag nanowires, whereby PVP can strongly bind to the {100} facets of Ag and then, when it disperses in polyols, enables growth in the <111> direction [54]. Moreover, PVP is a remarkably stable polymer that, importantly, has carbonyl oxygens where the hydrogen bond is a solvent molecule [55,56].

2.2.3. The Stability of Engineered Nanomaterials (ENMs)

Colloidal stability is critical determinant of the toxicological outcomes of ENMs and their transformation in different conditions. The strength of a nanoparticle in a colloidal solution can be interpreted according to various explanations. The first is related to the solubility of the particles, and the second is the net electrostatic surface interaction of the particles. These interactions can be explained according to the classic theory of Derjaguin–Landau–Verwey–Overbeek (DLVO).

The solubility of small particles is different from that of bigger particles for several reasons. The first reason is that smaller particles dissolve more rapidly than larger particles because of their larger surface area-to-volume ratio. Given the Noyes–Whitney equation, the solubility of particles and the saturation concentration at the particles surface are shown in the equation below [38]:

$$\frac{\mathrm{dM}}{\mathrm{dt}} = \frac{\mathrm{DA}}{\mathrm{H}} (\mathrm{C_s} - \mathrm{C}) \quad (2.3)$$

where ($\frac{dM}{dt}$) is the rate of dissolution, D is the factor of diffusion, A is the surface area, H is the thickness of diffusion layers, C_s is the saturation concentration and C is the bulk concentration.

The second justification is the increase in a factor called the Kelvin effect of nanoparticles, which is also represented as the curvature of nanoparticles and is a thermodynamically enlarged solubility driving force. Mihranyan et al. [39] and Kwon and Messing [57] studied the

influence of the particle radius (r) on its solubility (S) by using the Ostwald–Freundlich equation:

$$S = S_{\circ} \exp \exp \left(\frac{2\gamma_{sl} V}{RTr} \right) \left[\frac{mol}{l} \right] \quad (2.4)$$

where $S_{\circ}$ is the equilibrium solubility for the flat plate, γ_{sl} is the solid–liquid interfacial energy, V is the molecular weight of the solid phase, R is the gas constant and T is the temperature. The equation shows that when the particle size gets smaller, the solubility is substantially increased, while the rest of the factors remain constant [57]. Mihranyan *et al.* [39] also specified the magnitude of the dissolution factor of hypothetical particles of molecular weight, surface tension, surface change and dielectric constant.

The other explanation for the stability of nanoparticles is found in DLVO theory. This is applied in colloidal science and explains the total interaction energy between particles. It provides a realistic explanation for the aggregation of nanoparticles in a solution[58]. Initially, DLVO theory was applied in colloidal science to obtain information about the interaction between particles, which is represented by the van der Waals force and the electrical double layer. This reaction is described in terms of the potential energy curve that is the sum of repulsive and attractive forces between each nanoparticle. The attractive force is the Van der Waals force (V_A) and the repulsive is the electrical double layer force (V_R) surrounding the nanoparticles. The interaction of these forces can be described as the stability and aggregation of nanoparticles in a solution [59]. The net attraction of particles can be at a primary or secondary minimum, as illustrated (Figure 2-4).

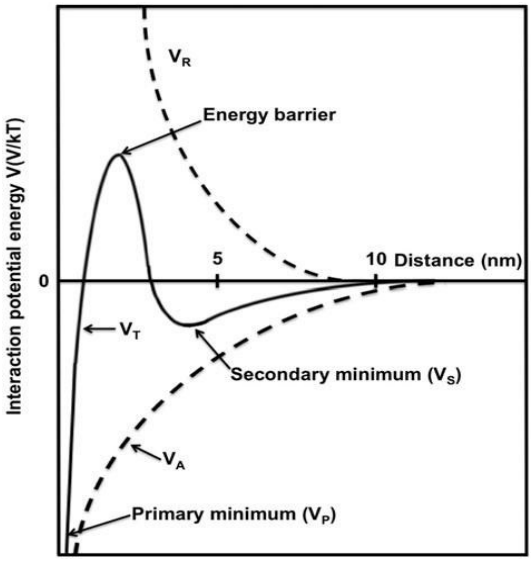

Figure 2-4: Diagram of the DLVO model for colloidal stability, reprinted (adopted) with permission from [60] Taylor & Francis.

When the particles are located in the primary minimum, they tend to aggregate irreversibility, whereas when the particles are in the secondary minimum, reversible aggregation occurs. The particles can be separated when a shear force is applied, such as stirring and sonication. The DLVO forces cannot predict aggregation of engineering nanoparticles. As ENMs have surface coatings such as PVP, polyelectrolyte coatings or NOM that introduce strict repulsion forces, they will present in the net attraction of the secondary minimum. Thus, DLVO theory developed and proposed additional short-range forces, such as osmotic, bridging between hydrophobic acid-bases interaction and magnetic forces [61,62]. The factors controlling the aggregation of colloids are reported to be the same as those controlling the aggregation of nanoparticles. These factors are pH, particle size, surface chemistry, ionic strength and solution composition [63].

2.3. Transformations of Engineering Nanomaterials

The transformation of nanomaterials can be explained in different perspectives depending on the type of transformation, such as chemical, physical, biological or interaction with macromolecules. Chemical modification can be identified as the reaction where the conversion of compounds changes to a different one with variation in the structure, composition or valency. Chemical transformation can involve several types that include changes occurring in the material surface and oxidation state of different surface structures

such as a core–shell structure, which is a surface reaction [64]. Physical transformation can be explained as the physical changes of nanomaterials that have been exposed to different conditions that caused some of their physiochemical properties to change when they are subjected to aggregation/disaggregation, agglomeration or adsorption mechanisms. Biological interaction with macromolecules is an interaction of nanomaterials with biological systems like cells. Classification of the nanomaterial's transformation depends on the variation of physiochemical properties observed before (as pristine) and after reaction. Therefore, the transformation types are controlled by the conditions, which, in reality, cannot be explained as one simultaneous transformation.

2.3.1 Silver Nanoparticles

AgNPs are one of the most interesting metallic nanoparticles owing to their distinctive chemical, physical and antimicrobial properties [65]. They exist in many types of consumer products, such as paints, fabrics, clothes, detergents, sports goods, personal care products, medical applications, cosmetics and food storage [66]. AgNPs released from these products are discharged and transported from municipal sewer systems to WWTPs, eventually reaching sewage sludge. Half if the sewage sludge is used for agricultural applications, especially soil [67]. When AgNPs enter the environment, they can cause toxicity to plants and other organisms [68].

The absolute concentration of AgNPs in the environment is not easy to measure, but some researchers have offered predictions. A study on predicted environmental concentrations (PECs) was conducted for AgNPs in the sludge of WWPT. The highest estimated quantities for the US and Europe were 5.86 and 4.44 mg/kg, respectively. A probabilistic material flow analysis was applied that targeted a framework to derive probability distributions of PEC values for AgNPs. Its purpose was to calculate a whole lifecycle concentration of AgNPs in complex systems [69,70]. The United States Environmental Protection Agency (USEPA) reported that the Ag concentration in sewage sludge is between 1.94 and 856 mg/kg as dry mass. Experts collected 84 samples of sewage sludge from different facilities to measure the concentration of Ag, and illustrated the minimum and maximum concentrations [71]. Another study focused on biosolid samples produced in the UK, Australia and the US from 1950 to 2009. The outcome showed that the highest concentration was

found in the oldest samples, and the concentration range was between 4.3 and 332 mg/kg [72].

The sulfidation of AgNPs is key to understanding the bioavailability of Ag because it tends to convert to silver sulfide (Ag_2S) through WWTPs [6]. Kaegi *et al.* conducted a transformation of AgNPs *via* pilot-scale WWTP [69] and concluded that the diameter is strongly dependent on the sulfidation kinetics [70]. The solubility of Ag_2S is extremely low ($K_{sp} = 5.92 \times 10^{-51} M^3$) [73], so the sequestration of Ag in this manner may be responsible for reducing toxicity and its effects [74].

2.3.2. Dissolution of Silver Nanoparticles

Dissolution and release of Ag^+ ions contributes to the antibiotic properties of the AgNPs, their fate in the environment and toxicity to organisms [75]. Dissolution can be explained as the changes to the physiochemical properties of AgNPs where the release of Ag ions is described as a thermodynamic favourable reaction at room temperature (ΔG 298º = −11.25 kJ/mol). The mechanism of this process is oxidative dissolution *via* the reaction of metallic Ag with dissolved oxygen (DO) and protons, which was shown by Liu and Hart *et al.* [76]:

$$4\,Ag_{(s)} + O_2 = 2\,Ag_2\,O_{(s)} \qquad \Delta G\ (298^{o}K) = -11.25\ kJ/mol \qquad (2.5)$$

$$\frac{1}{2}Ag_2\,O_{(s)} + \frac{1}{2}H^+ \leftrightarrow Ag^+ + OH^- \qquad logKs\ (298\ ^{o}\ K) = -7.71 \pm 0.03 \qquad (2.6)$$

$$\frac{1}{2}Ag_2\,O_{(s)} + \frac{1}{2}\,H_2O \leftrightarrow Ag^+ + AgOH \qquad logKs\ (298\ ^{o}\ K) = -5.75 \pm 0.25 \qquad (2.7)$$

$$\frac{1}{2}Ag_2\,O_{(s)} + \frac{1}{2}\,H_2O \leftrightarrow Ag^+ + Ag(OH)_2^- \qquad logKs\ (298K) = -3.72 \pm 0.03 \qquad (2.8)$$

The dissolution process is mediated by the formation of Ag–O when Ag oxidation is taking place on the surface of AgNPs to produce silver oxide (Ag_2O). This layer is dissolved in the solution and releases Ag ions until it is completely dissolved [77]. The kinetic model was developed by Zhang *et al.,* who described the Ag ion release by relying on hard-sphere theory, which used the Arrhenius equation [78]. The extent of oxidation can be affected by the proportion of atoms on the nanoparticles' surface, which is directly linked to their size and shape. Moreover, the additional ionisation of Ag is influenced by the experimental conditions. The dissolution mechanism is a complex and dynamic process[79].

Figure 2-5 shows the scaled ions released from the AgNPs to approach the theoretical dissolution process.

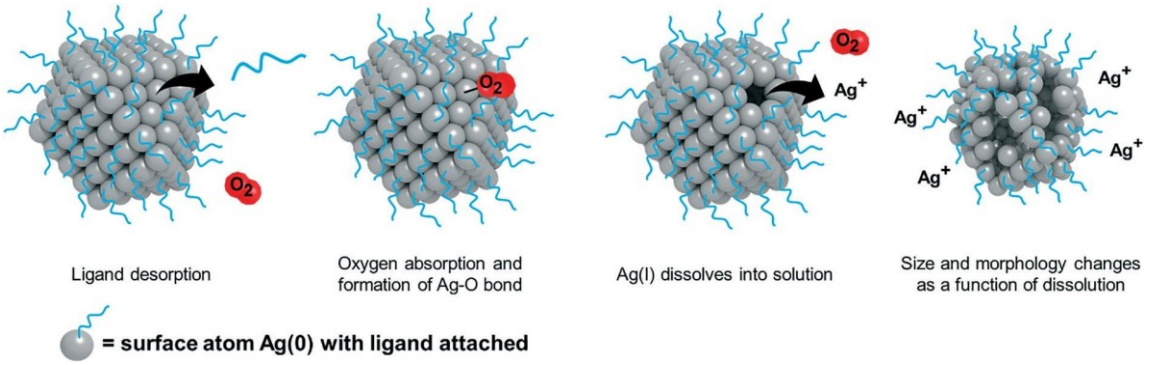

Figure 2-5: Schematic of the theoretical dissolution mechanism shown from left to right atom by atom from the Ag particle. The dissolution process is as follows: (i) ligand desorption, (ii) formation of the Ag–O layer in the particle surface formed by the oxidation from Ag (0) to Ag ions, (iii) continuous dissolution of Ag ions and (iv) changes in the particle's size and morphology. The diagram was reproduced (adopted) from [79] with permission from The Royal Society of Chemistry.

The kinetic model was developed by Zhang *et al.*, who described the Ag ion release by using hard-sphere theory, which used the Arrhenius equation [78]. The kinetics of this process can be influenced by different factors, including pH, temperature, inorganic and organic molecules in the solution and particle coating [80]. Sulfidation can take place after oxidation because of the extremely low solubility of Ag_2S, and this reaction is shown in the equations below:

$$2Ag^{+} + H_2S \rightarrow Ag_2S + 2H^{+} \quad (2.9)$$

$$2Ag^{+} + HS^{-} \rightarrow Ag_2S + H^{+} \quad (2.10)$$

$$2Ag^{+} + S^{2-} \rightarrow Ag_2S \quad (2.11)$$

The pathway of Ag_2SNP formation can be explained in two mechanisms: oxysulfidation and exchange and complexation reaction. Firstly, the oxysulfidation reaction can be explained by the AgNPs' interactions with hydrosulfide ion (HS) to form Ag_2S NPs under environmental conditions. When these interactions take place in the presence of DO, then the rate of sulfidation depends on the direct oxysulfidation and oxidative dissolution [76]. In the second mechanism, two cases exist. In the first one, when sulfide concentration is high, the formation of Ag_2S NPs is carried out by a direct particle–fluid reaction with Ag ions attached by sulfide, which is explained by direct oxysulfidation. In the second one, when sulfide concentration is low, oxidative dissolution and precipitation have to exhibit when Ag ions are released as an intermediate in this reaction [76].

On the other hand, Ag ions released from the oxidised surface of AgNPs can form an oxidised Ag-protective layer around the particles because of the formation of Ag_3OH. thereby avoiding any further oxidation [81]. Several studies have investigated the formation or sulfidation of Ag_2S NPs by presenting different structures of Ag_2S NPs and depending on the molar ratio between Ag and S to form particular Ag_2S NPs structures [82].

2.3.2.1 Speciation and transformation of AgNPs

AgNPs react differently to organic and inorganic species in the environment, which noticeably change their bioreactivity. With Ag, these species can form a complex that influences the solubility product, toxicity, and bioavailability of AgNPs. In the case of sewage sludge products, insoluble Ag_2S is the most favourable complex in the sulfur-rich phase due to low solubility detected by transmission electron microscopy (TEM) [5]. The transformation of AgNPs can be explained *via* redox and non-redox reactions. For non-redox reactions, the formation of Ag_2SNPs is through the exchange reaction when Ag ions are released and then *via* the cation exchange reactions that had occurred. When Ag ions and Ag_2S interact in the presence of Fe, the cations exchange formation is FeS [83]. The redox reaction can be understood by the low solubility of Ag_2S, where the strong oxidation agent can exchange reactions such as Cl and O_3 [84].

The physical transformation of ENMs is related to their stability. As explained previously (section 2.2), aggregation and agglomeration can influence the stability of ENMs. Aggregation and agglomeration of NPs are related to the high surface energy that reduces the surface area at constant volume, which minimises the free enthalpy of the system [3,68]. The meaning of aggregation and agglomeration concepts in particle science is building, that is, the loose bond can easily disperse the particles and a rigid bond is created by fusion, respectively [85]. The impact of both features on the nanoparticles' stability has a substantial influence on the reactivity, mobility, fate, and bioavailability. However, most available studies focus on the aggregation, disaggregation and dispersion of nanoparticles to indicate the nanoparticles' future or performance resulting in biological activities [3].

The transformation of nanoparticles can be noticed when NPs interact with different sizes of particles or macromolecules surrounding them, such as NOM and its several forms. The impact of NOM on the sulfidation of AgNPs depends on two parameters: firstly, the stabilisation of AgNPs and reactivity with respect to prevention aggregation and dissolution; and secondly, the absorption of HS on the AgNPs' surface. The stability of AgNPs within NOM can be explained according to the type, concentration and higher molecular weight [24]. In general, when sulfur binds to a thiol group, it will strongly bind to metallic Ag while the reduced sulfur and reduced nitrogen can bind with the ionic Ag. Therefore, once the NOM has a high content of reduced sulfur and nitrogen, then the sulfur–thiol group is expected to bind strongly to the AgNPs, thus reducing the dissolution rate of AgNPs more than the lower concentration in NOM [24]. The phenomenon of HS absorption on the AgNPs' surface depends on several factors, such as pH, change and type and molecular weight of NOM. High molecular weights of moieties in NOM inhibit the absorption of HS on the AgNPs' surface compared to lower molecular weights [86].

Humic acids (HAs) have several functional groups that are shown in (Figure 2-6). HAs are considered as one of the major fractions of dissolved organic matter (DOM) that are present in the environment, such as in soils, sediments and the aquatic ecosystem [87]. The composition of HA consists of quinone, phenolic, enolic, carboxylic acid, peptides, sugars and other functional groups [88]. The main molecular structure comprises hydrophilic and hydrophobic portions. The hydrophilic portions contain OH^- groups while the hydrophobic portions contain aromatic and aliphatic chain rings [89].

The structure of HA is assumed and generated by a classical and standard system of calculation that depends on previous research [90]. Quinone moieties in DOM are hypothesised to be the main redox-active functional group; they are ubiquitous in DOM [38,91]. Quinones are organic compounds that contain at least two carbonyl groups [C=O]. They have a reversible transfer of electrons that causes the interaction of abiotic and biotic redox [39,57]. Moreover, quinones are considered to cause the production of the reactive oxygen species (ROS). The reduction of quinones leads to more stabilised semiquinones by aromatic rings and then a further reduction to a more stable hydroquinone [92]. For instance, DOM can mediate reductions of organic pollutants or behave like an electron shuttle between mineral phases and bacteria [93]. DOM can likewise act as an indirect electron acceptor when behaving as a re-oxidant for inorganic electron acceptors such as sulfur and iron[38,39,58], or it can act as a direct electron acceptor for microbial respiration [94]. Researchers have reported the formation of thiosulfate ($S_2O_3^{2-}$) and sulfur (S_s) (sourced from soil, water and ocean) in DOM when the oxidation of sulfide takes place for several hours at pH 6 [95]. By contrast, the reaction of Sigma-Aldrich's HA with sulfide leads to the formation of elemental sulfur. This formation is possible and could be influenced by the redox-active contents of transition metals such as iron, but it explains only a small fraction of sulfide transformations [96]. It has been confirmed that Sigma-Aldrich's HA is reactive to sulfide when it is reduced by electrochemical treatment but is lower than oxidised HA[97]. The use of the commercial HA instead of a product from the International Humic Substance Society (IHSS) from the Suwannee River in south-eastern Georgia, USA, is due to the shortage of supply and the high demand.

The transformation of AgNPs to Ag_2S under the influence of organic matter, in this case, HA, could use a different mechanism to change the surface properties [99]. The presence of HA in the environment can impact the transformation of AgNPs by altering the physical and chemical properties of AgNPs. The attachment of HA onto the surface of AgNPs increases their colloidal stability. In addition, the toxicity of AgNPs can be reduced due to the absorption of HA onto the AgNPs' surface.

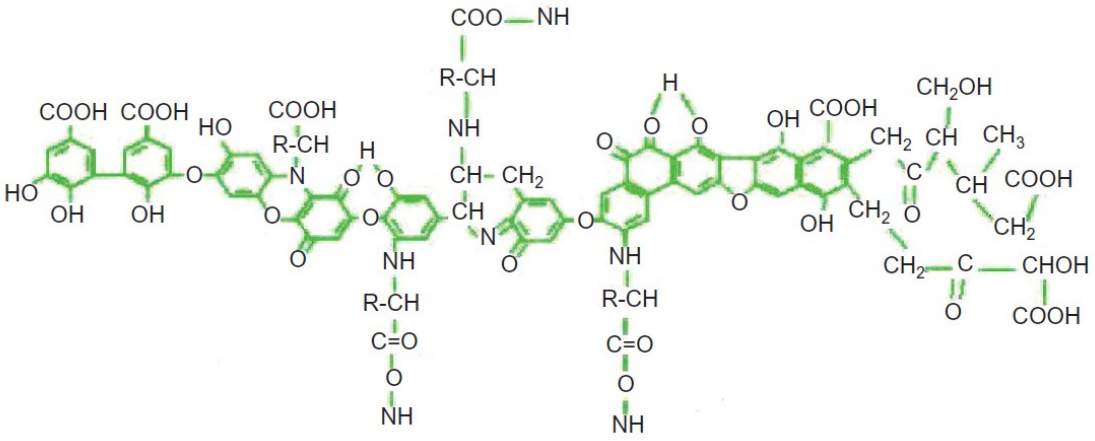

Figure 2-6: Structure of Humic acid, reprinted (adopted and reproduced) with permission from [90] Copyright (2011) Taylor & Francis Ltd.

The attachment of HA has been explained by Sánchez-Cortés *et al.* [100]. They used infrared spectroscopy and Raman spectroscopy to analyse AgNPs capped with citrate and showed that both fulvic and humic absorbed to different extents depending on their size and pH. Furthermore, they observed that sorption occurs in the carboxyl group when it has an acidic pH, whereas the phenol group and aliphatic moieties are preferable at an alkaline pH. They also showed that humic substances with higher molecular weights are adsorbed by the hydrogen ion bond while the lower ones are adsorbed *via* the hydrophobic and electrostatic forces.

In a recent study [100], standard humic acid (SRHA) from IHSS was prepared as NOM to study the transformation of Ag ions with NOM that mediates the AgNPs' formation in the dark. The binding of metal to HA depends mainly on the distribution of -OH/-COOH groups [89]. In the first hours of interaction between SRHA and Ag ions, the Ag-OOC- species is formed by binding between Ag ions and carboxylic groups in SRHA (Reaction 1). Owing to the instability of the Ag-OOC species, its transformation could extend further to other Ag species. The Ag ions bound to SRHA confirm the formation of metallic Ag after 20 days and a partial transformation of Ag-OOC- ligands, which indicate that SRHA(ox) had oxidised to SRHA(ox^{n+1}) in Reactions 2 and 3, respectively. Next, the same ligand is observed to release Ag ions that gradually convert to the Ag-S- species,

particularly in the stage where SRHA is nearly exhausted (Reaction 4). Likewise, the Ag-S- species could be formed when the slow transformation of AgNPs by the thiol in SRHA has occurred (Reaction 5) [69,74,101,102].

$$Ag^{+} + SRHA(-COOH) \overset{-H^{+}}{\longleftrightarrow} Ag^{1}(-OOC-)\,SRHA\ (fast) \qquad \text{(Reaction 1)}$$

$$Ag^{1}(-COOC-)SRHA \rightarrow Ag^{0} - SRHA(ox)(slow) \qquad \text{(Reaction 2)}$$

$$Ag_{n}^{0} - SRHA(ox^{n}) + Ag^{+} \overset{+e^{-}}{\longrightarrow} Ag_{n+1}^{0} - SRHA(ox^{n+1})(slow) \qquad \text{(Reaction 3)}$$

$$Ag^{1}(-OOC-)SRHA \rightarrow Ag^{1}(-S-)SRHA(slow) \qquad \text{(Reaction 4)}$$

$$Ag_{n}^{0} - SRHA(ox^{n}) \rightarrow Ag_{n-1}^{0}Ag^{1}(-S-)SRHA(ox^{n-1})(slow) \qquad \text{(Reaction 5)}$$

The formation of nanosized Ag_2SNPs (39 ± 9 nm) was observed to increase along with the increase in the ratio of Na_2S to AgNPs coated with PVP. The Ag_2SNPs aggregate and build a chain-like structure between NPs (Figure 2-7). To assess the sulfiding of AgNPs with different surface coatings, citrate and Tween functionalised NPs have been studied at low and high concentrations of sulfide ions, with and without Suwannee River fulvic acid (SRFA), which is considered a part of NOM. This research showed that sulfidation takes place as a direct interaction between AgNPs and sulfide species. At a high concentration of sulfide, the Tween–AgNPs tend to form sulfided particles that retain unreacted metallic sub-grains at the edge and are less extended for lower concentrations. No variations were seen in the Cit–AgNPs, which exhibited partial direct sulfiding. Dissolution followed by a dilution of AgNPs is affected by the surface coatings, resulting in a higher dissolution of Tween–AgNPs dissolution than of Cit–AgNPs. The effect of SRFA appears to slow the dissolution of Tween–AgNPs at low sulfide concentration ratio and decrease the aggregation of Cit–AgNPs [103]. Comparing AgNP coatings is very informative because of their influence on the dissolution rate and potential mechanism of sulfidation, which has been observed in different structures [103]. The sulfiding of Cit–AgNPs with various particle sizes was investigated on the basis of their morphology with access to HA. The conclusion was drawn that Ag_2S is reactively formed in an HA-free system, leading to the formation of the core (Ag^0)-shell Ag_2S transformed to a hollow Ag_2S structure; the suggested mechanism was similar to the Kirkendall effect in oxygenated water [104]. In Figure 2-8, the

morphology of sulfided Cit–AgNPs with a size of 20 nm was studied in the presence and absence of HA; this shows partially sulfided nanoparticles after 5 min. Furthermore, the core-shell structure was found with 250 mg/l HA. According to energy dispersive x-ray spectroscopy, the grey area is Ag_2S while the white area is the metallic Ag. With an extended sulfidation time, the core-shell structure shows a light grey area, which confirms the presence of Ag_2S [104].

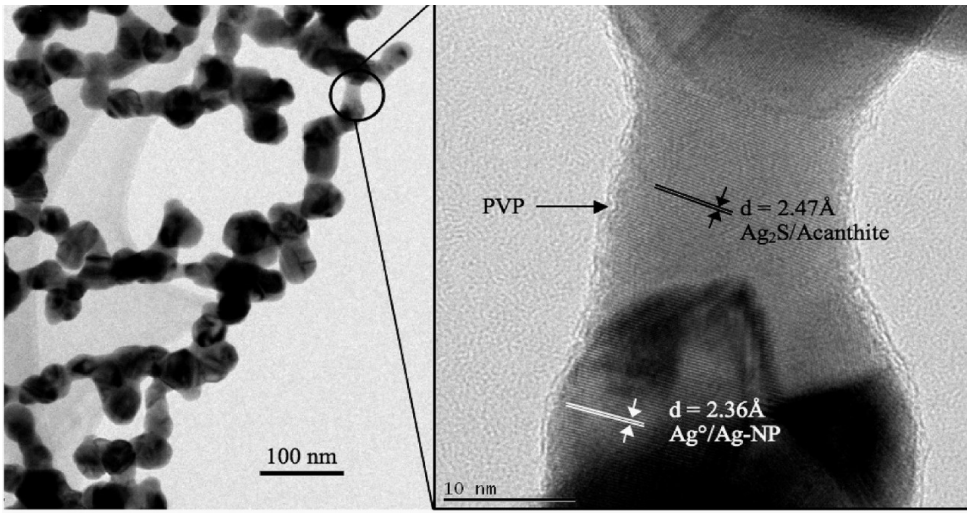

Figure 2-7: Sulfidation of PVP–AgNPs within Na_2S. Low magnification TEM image shows nanobridges (left image), and the high magnification micrograph shows Ag_2S. Reprinted (adapted) with permission from [105] Copyright (2011) American Chemical Society.

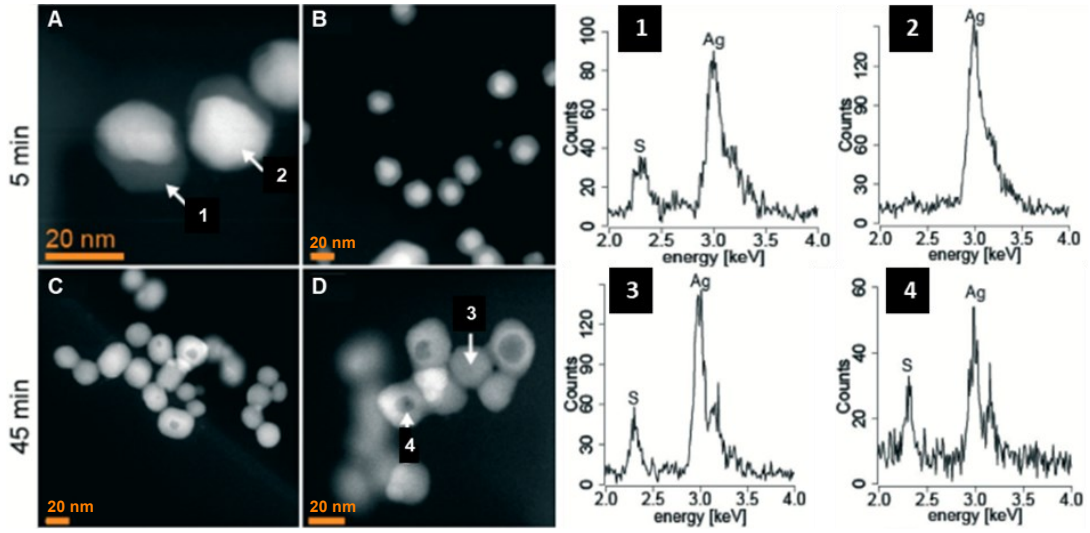

Figure 2-8: High-angle annular dark-field micrograph showing the sulfidation of Cit–AgNPs in the absence (A, B) and presence (C, D) of 250 mg/l HA. (1)–(4) show the EDX spectra region indicated by the arrows. Reprinted (adapted and reproduced) with permission from [104] Copyright (2011) American Chemical Society.

The stability of Ag_2SNPs in the aquatic environment was evaluated in natural water. Li *et al*. [106] studied the dissolution rate of Ag_2SNPs within and without DOM in light and dark conditions. Depending on the dissolution figures of Ag_2SNPs, the percentage of Ag ions increased first and then rapidly dropped, which indicates that Ag_2SNPs has reconstitution after dissolution. More NP dissolution occurred in an acidic condition under both light and dark conditions. The dissolution of Ag_2SNPs in the light was remarkably high but was reduced within DOM concentrations due to the Ag ions trapped by NOM. This result obtained the same effect with ZnONPs [107]. The release of Ag ions in the dark are negligible within, and without DOM, and so the reduction of Ag ions from Ag_2SNPs is assigned by the complexation of DOM. The presence of Fe^{+3} in natural water also showed that release of Ag ions from Ag_2SNPs in light increased remarkably compared to the dark condition, which indicated the transformation and complexation. This outcome is possible evidence that Ag_2S NPs can be photoinduced in a natural aquatic environment.

2.3.2.2. Potential for the ecotoxicity of AgNPs in the environment

AgNPs comprise a wide range of commercial nanoparticles and work as broad-spectrum antimicrobial agents to control bacterial growth in aquatic organisms [85,108]. 10 nm diameter

AgNPs can damage the cell membrane of *Escherichia coli*. The pattern of antibacterial activity of AgNPs can inhibit bacterial growth at a low concentration in different microorganisms, such as yeast, *E. coli* and *Staphylococcus aureus*. The antimicrobial effect of AgNPs may have a relationship with certain bacteria species. For instance, there are two types of bacteria, gram-positive and gram-negative, that differ in the structure of their membranes, particularly in the thickness of the peptidoglycan layer [109]. The mechanism of antimicrobial behaviour of glutathione (GSH)-coated AgNPs was reported for its effect on the gram-negative bacteria *E. coli*, which were damaged because the colloid penetrated into the cytoplasm and, consequently, the Ag interacted with the cell compartments. By contrast, the microbial effect was constrained in the gram-positive bacteria, *S. aureus*, where the thickness of the peptidoglycan layer of the cell resisted penetration [108].

The common mechanism of bacteria cell death occurs when a reactive oxygen species (ROS) produces a hydroxyl radical (OH•). This radical targets and disrupts multiple cellular processes, including disulfide bond formation, iron homeostasis and central metabolism. These processes are linked to the increasing production of ROS and the increasing permeability of bacteria membranes [110].

The main causes of the high toxicity of microorganisms are Ag ions and Ag-based compounds, but there is a limitation to this antimicrobial effect because it has no continuous release. This limitation can be overcome by AgNPs, which can reach the bacteria and, because of their high surface-to-mass ratio, produce a high concentration around the cell that in turn leads to a greater microbicidal effect for a longer time [111,112]. The release of Ag ions under standardised conditions can be explained. When the compounds have free thiols along with $Na_3C_6H_5O_7$, they inhibit the ions' release probably through surface binding and oxygen exclusion from active sites. The strongest binding of Ag ions was observed in compounds that have free thiols, such as GSH and cysteine [113]. A study revealed that the toxicity of nanosilver depends on the concentration of Ag ions inside the bacterium; this includes two main factors: extracellular dissolution and dissolution of AgNPs on the particle–cell interface [112]. Figure 2-9 shows the possible interaction of AgNPs and transformation with dissolution on the external and internal environments, which are the medium and bacteria cell compartments, respectively.

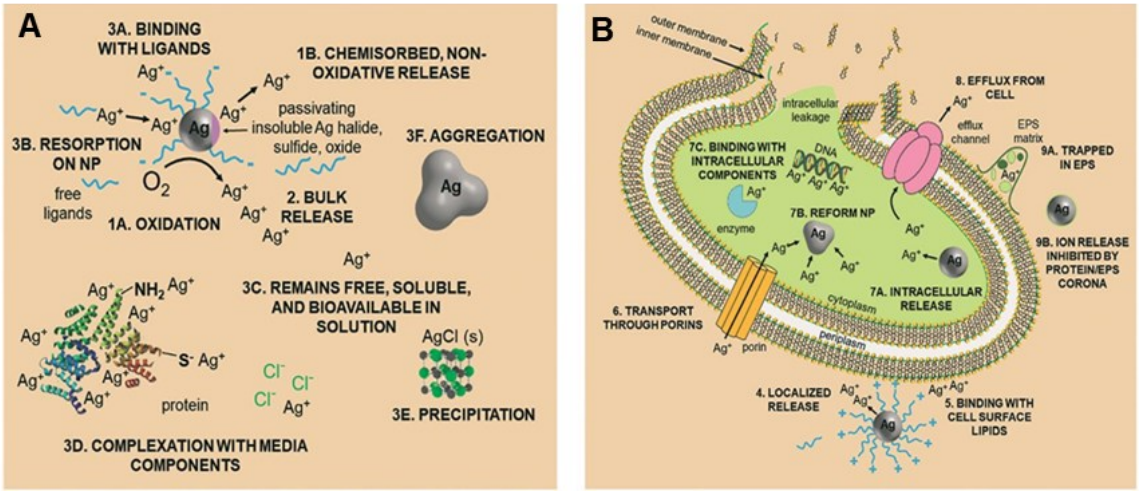

Figure 2-9: Different mechanisms of AgNPs exposure that potentially release Ag ions: (A) Ag in media and external to the bacteria cell, and (B) Ag interaction within the cell and inside the cell. Reprinted (adopted) with permission from [79] by permission of The Royal Society of Chemistry.

The toxicity of AgNPs with various coatings and sizes was detected by examining the dose–response pattern of *E. coli* after exposure to Ag ions. *E. coli* was stimulated by a low concentration of all AgNPs and $AgNO_3$. Antibacterial activity was controlled by several factors, such as modulating the release of Ag ions, particle size and shape or type of coating as well as the availability of oxygen [114]. Ecotoxicity was investigated by a suite of *in vitro* and *in vivo* tests. The impact of HA on the toxicity of AgNPs at exposure to pH 6–9 was studied, and HA was found to mitigate the toxicity of AgNPs to bacteria at pH 9. Toxicological response was explained in terms of the doses of dissolved Ag [115]. The concentration of AgNPs or the release of Ag ions can influence the toxicological effect and significantly inhibit bacteria production when the AgNPs' concentration is more than 1 mg/l. The bacteria were exposed to a low concentration of AgNPs (10 and 20 µg Ag/l) for 24 hours. The production of a bacterial community was reported to have been altered when alkaline phosphatase was reduced[116].

The effect of AgNPs on plants was investigated with various sizes (5, 10 and 25 nm) and coatings (PEG and carbon). The plants were poplars (*Populus deltoides nigra*) and *Arabidopsis thaliana* and were exposed to different concentrations of AgNPs (0.01–

100 mg/l). The results of this investigation revealed that, above a specific concentration, all AgNPs formed were phytotoxic to these plants. Moreover, a substantial effect was detected on the elongation of roots, the fresh weight and the evapotranspiration of both plants [117].

Another study showed that AgNPs reduce the growth and metabolism of wheat and the sand matrix; they reduced the length of shoots and roots. The transmission electron microscopy (TEM) images also confirmed the presence of AgNPs in both the shoots and roots of the wheat, illustrating that the AgNPs had been taken up and transported from the sand [118]. This outcome could trigger an alteration in gene expression, as shown when *A. thaliana* was exposed to 5 mg/l of PVP-coated AgNPs (20 nm). This alteration yielded the up-regulation of 286 genes and down-regulation of 81 genes [119].

The ecotoxicological effect was studied for multicellular aquatic and terrestrial organisms. Two aquatic organism models were used: Medaka and Zebrafish. Gum arabic-coated AgNPs were found to have the highest toxicity to *Japanese medaka*, whereas AgNPs that have PVP and citrate coatings have lower toxicity [120]. The release of Ag ions was also significantly toxic to zebrafish embryos [121], and AgNPs could modify the embryos' development [122].

2.3.1.4. Transformation of AgNPs in WWTP, sludge and soil

The AgNPs undergo a series of transformations, because in the thermodynamic state, the oxidation of Ag is favoured at room temperature and tends to form Ag_2S due to low solubility. Ag_2S is formed in aquatic systems, such as wastewater sewerage systems, and terrestrial systems, such as WWTPs, sludge and soil. The transportation and destination of AgNPs have been reported in wastewater sewers by introducing spiked Tween–AgNPs into a 45-km-long main trunk sewer [70]. Samples were collected at different distances after the expected times of AgNPs travel were calculated. The results showed that the raw wastewater samples included 15% PVP–AgNPs that had sulfided to Ag_2S after a 5-hour reaction time. Therefore, this finding confirmed that AgNPs had partially sulfided in the sewer system and reached WWTPs [70]. It was found that polyoxyethylene fatty acid ester–AgNPs could be adsorbed into wastewater biosolids in sludge. Their transformation from wastewater to sludge was enhanced by an effluent [69]. Both these results suggested that AgNPs transferred into sludge as the Ag_2S species. In anaerobic-activated sludge, the Cit–AgNPs incubated have different sizes (10–100 nm), which are shown to depend

significantly on the sulfidation kinetics [123]. Similarly, research revealed that the sulfidation of PVP–AgNPs is more favourable in anaerobic than aerobic conditions [124].

In soil systems, AgNPs can be applied intentionally and released unintentionally from various pathways; for example, they can be freed from sludge during incineration and from sewer sludge in WWTPs [125,126]. In anaerobic soils, AgNPs of 15 and 50 nm with PVP coating transformed into Ag_2S, Ag_2O, $AgNO_3$ and HA complexes while uncoated AgNPs of 50 nm were transformed into HA complexes. The present study highlights how different coating agents of AgNPs may affect their transformation and, therefore, the bioreactivity within the environment [127]. The Ag speciation of spiked PVP–AgNPs was determined in terrestrial soil. After 18 months, approximately 47% of the Ag remained as Ag^0, and the rest was oxidised and consequently sulfided to Ag_2S (measured using X-ray absorption spectroscopy [XAS]). In sediment, approximately 27% of the Ag was transformed into Ag-sulfhydryl, and 55% was sulfided to Ag_2S [128].

2.4. Wastewater treatment sewage sludge

2.4.1 Sludge Treatment and Disposal

Sewage sludge consists of raw primary sludge and secondary activated sludge, which are produced during wastewater treatment [129]. In the United Kingdom, wastewater sludge production in 2009 was approximately 1.2 Mt of dry solids, of which 77% was applied to agricultural land. By comparison, in the EU, there were 6.5 Mt of dry solids produced per year. Sludge production has increased considerably by 50% since 2005 [130]. Therefore, in the next decade, sludge disposal may become more difficult. The challenges of sludge treatment include maintaining a cost-effective and secure sludge disposal technique and building confidence in the recycling and disposal options [129].

2.4.2. Anaerobic Digestion

Sewage sludge has organic matter that is biologically converted to a gas that usually contains 70% methane and 30% carbon dioxide. This process is undertaken in an oxygen-free system, which is equipped with a collector for the gas produced during the process. The sludge is added and then the digester is operated using a ‘draw and fill’ process. This process reduces the volatile by-products by 50% from the original sludge. It is also very sensitive to low concentrations of toxic pollutants [129].

2.4.3. Zinc Oxide Nanoparticles

ZnONPs are naturally found as zincite with manganese impurities. They are involved in a broad range of consumer products and other applications [131]. ZnONPs are semiconductors [132] and are described as unique nanomaterials due to their electrical conductivity, semiconducting, optical and piezo electrical properties [133]. Given their wide-range band gap (3.3 eV) in the near UV spectrum with higher excitation binding energy at room temperature, ZnONPs are considered a natural n-type of electric conductive material [133–138]. This type of nanomaterial has been involved in very remarkable applications [93]. The most important properties of ZnONPs are their antibiotic and antifungal properties that have contributed on photochemical activities and catalytic nanomaterials. At the UVA 315–400 nm range and UVB 280–315 nm range, ZnONPs are processed at high optical absorption. Therefore, they can be used as antibacterial and UV protectors in consumer products [139].

The toxicity caused by the antibacterial mechanism of ZnONPs depends on different suggested causes; the first is the dissolution of ZnONPs to ionic zinc [140]. Some previous research also found that the partial dissolution of ZnONPs can affect toxicity. The interaction of Zn nanomaterials on the aquatic system is summarised in Figure 2-10. The figure shows several transformation pathways that could influence the fate of metal oxide and metal nanomaterials and their physicochemical properties.

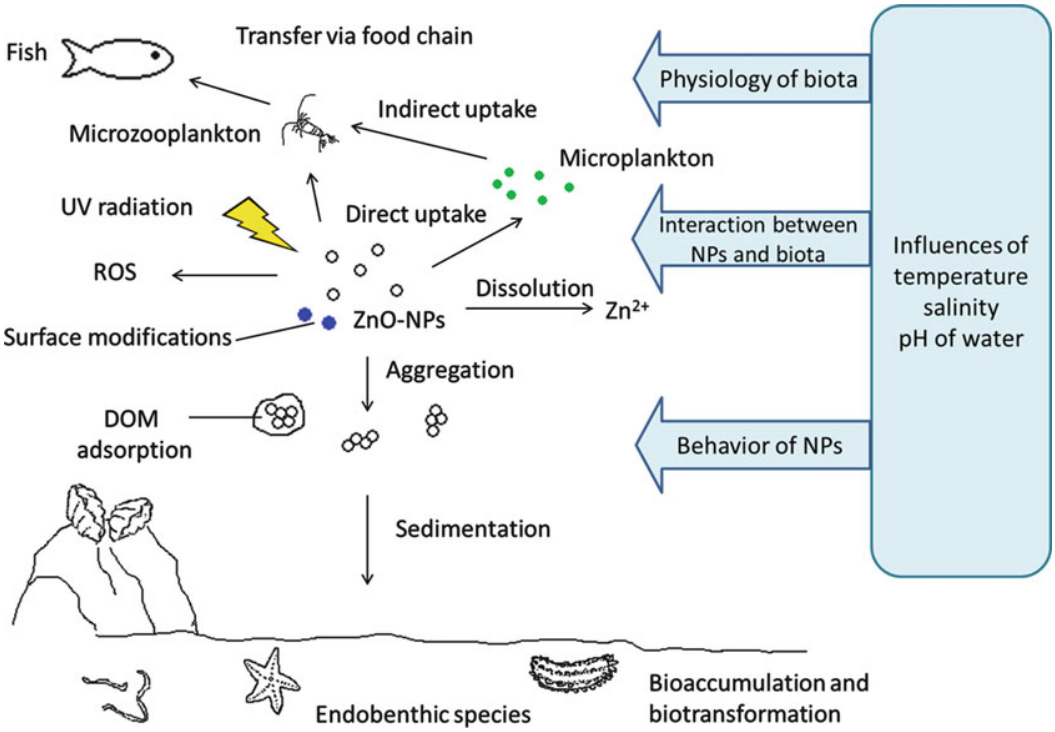

Figure 2-10: Transformation of ZnONPs within an aquatic system. Different interactions of ZnONPs are introduced with several conditions. Diagram provided by Springer Nature and Copyright Clearance Centre and reprinted (adopted) with permission from [141].

The toxicity of ZnONPs to algae was studied within a different condition. For example, the photoreactivity of ZnONPs and TiO_2NPs has been studied on *Raphidocelis subcapitata* (*Pseudokirchneriella subcapitata*) algae, which inhibited algae growth under visible light, UVA (315–400 nm) and UVB (280–315 nm) irradiation conditions. The cell membrane was destabilised by adding 0.3 mg of ZnONPs, which caused localised fraying and destructions of the outer cell wall [142] (Figure 2-11). Moreover, the growth inhibition and toxicity of *R. subcapitata* algae were investigated with different sizes and shapes of ZnONPs. The smaller spherical and rod shapes of ZnONPs were more toxic than the larger sizes, while the smaller spherical ZnONPs were more destructive to algae [143]. Increasing the concentration of ZnONPs to 0.1 mg /l raised the growth inhibition rate of *R. subcapitata*, to over 90% [144]. Another investigation took place on several types of algae species, including *R. subcapitata*, which was tested in different concentrations, and three modified ZnONPs. This resulted in the formation of large aggregations of modified coated ZnONPs at pH 7 and 8 [145]. The effect of ZnONPs in other algae species was studied. *Dunaliella*

tertiolecta was tested within ZnONPs, and bulk forms and showed that ZnONPs were more toxic and to inhibited growth to the algae. The no observed effect concentration (NOEC) after testing for 96 hours test was found in the concentrations of 0.1 and 1.0 mg/l, and the median effective concentration (EC50) was in 0.50 and 3.00 mg/l, respectively, for ZnONPs with sizes of 100 and 200 nm [146]. For ZnONPs with a size of 20 nm, the NOEC and EC30 values found for the Chlorella species were 5 and 20 mg/L, respectively [147].

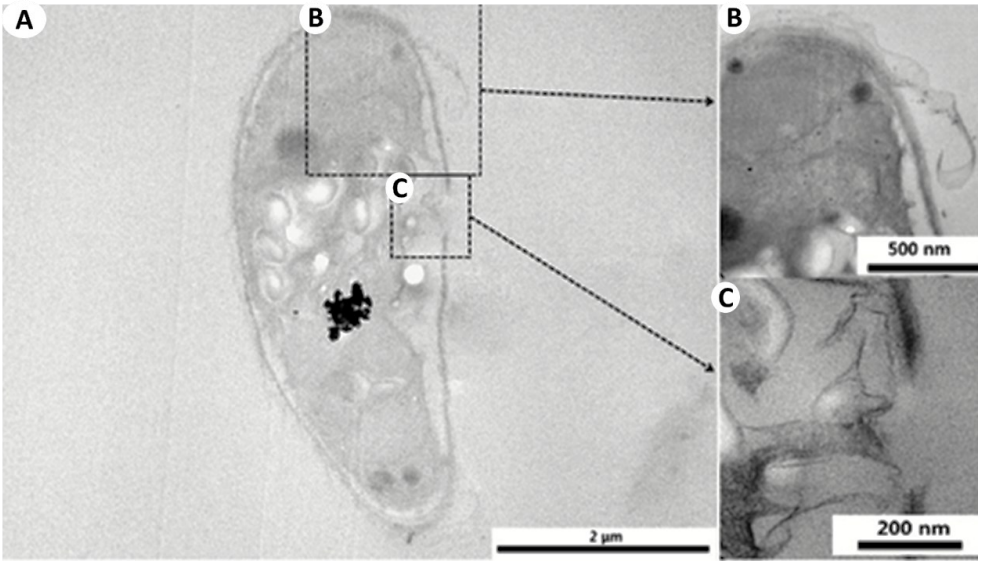

Figure 2-11: (A) Bright-field TEM micrograph for the *Pseudokirchneriella subcapitata* algae after incubation of 0.3 mg/1 ZnONPs for 48 hours. (B) A magnified micrograph of the algae cell wall with localised fraying. (C) Distortion of the outer cell membrane. Images provided by Elsevier Ltd. and reprinted (adopted) with permission from[142].

The ZnONPs' transformation within the WWTP has been widely studied by analysing the Zn-K edge X-ray absorption near edge structure (XANES) spectra, which illustrated the different ratios of three compounds, namely ZnS, $Zn_3(PO_4)_2$ and Zn-Fe oxy/hydroxides. The ZnONPs were altered within the anaerobic digestion of active sludge, and the major species observed was ZnS after biosolids were incubated in reduced sludge within a week [7]. The transformation of ZnONPs was likewise studied within the raw organic waste and the digested organic waste [148].

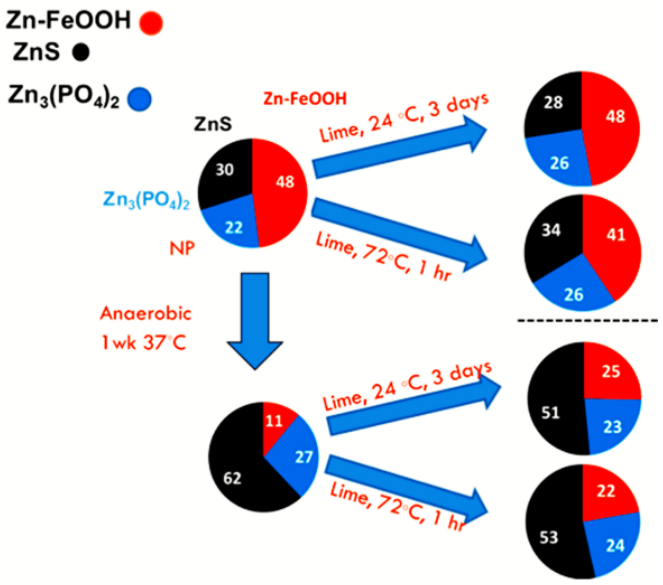

Figure 2-12: Pie charts for Zn speciation of biosolids formed from the addition of lime, heated treatment of oxic and reduced ZnONPs and AgNPs amended sludges. The ratio of the speciation was identified from the linear combination fitting for the Zn K-edge of XANES spectra. Reprinted (adopted) with permission from [7] Copyright (2041) American Chemical Society.

Figure 2-12 shows the speciation of ZnONPs, where the biosolids are investigated after stimulation by the addition of lime and heat treatment (24 °C, 3 days and 72 °C, 1 hour) of the sludge. The heated and oxic nanoparticles showed amended sludges to detect the changes of Zn speciation. Overall, the speciation did not change much after the treatment within the above condition of lime addition and heat treatment. After one week of the same treatment, sludges had anaerobically digested at 37 °C, and the resulting speciation portion was mostly ZnS mineral, reduced Zn−Fe oxy/hydroxide and unaffected $Zn_3(PO_4)_2$. Then all the portions changed slightly after the same condition of lime addition and heat treatment was applied. Therefore, Zn speciation ratios depend on the conditions and contents, of the sludge such as their redox and moisture conditions [7].

2.5. Fate of Engineering Nanomaterials

Several reports have focused on the chemical transformation and aggregation of AgNPs in order to investigate their fate in the environment; however, this fate is required to be determined in term of long term with the aquatic environment [75]. The fate of AgNPs in the environment can be determined through describing and modelling their parameters using descriptors, such as surface affinity, sorption, solvent exchange, aggregation, sedimentation and dissolution kinetics [122]. However, these descriptions may be considered to be gaps in the surface water and WWTP effluents, biosolids, sediments, soils and air. The model by Gottschalk for predicting the environmental concentration of AgNPs is reported above. The transformation of ENMs can occur *via* WWTP sludge to effluent solid and biosolid runoff to water surface [149]. Studying the fate of AgNPs and their transformation in the environment is vital when investigating their impact on soil, plants and human health [150]. The behaviour and transformation of AgNPs have been explained according to the type of system, such as aquatic or terrestrial. Before the fate of AgNPs in both systems can be illustrated, features should be explained first to determine their potential impact. In the section above, the ENMs' physicochemical properties are considered as factors or features because of their potential to influence the fate of ENMs.

The ionic strength of the medium can influence the stability of the diffuse layer for the electrical double layer. When ionic strength increases, the thickness of the electrical layer decreases and then takes the lead in increasing the agglomerated particles that favour a reaction [151]. This behaviour of ionic strength and the agglomeration of uncoated, citrate- and $NaBH_4$-coated AgNPs were observed in a suspension with high pH (pH > 7). It was reported that ionic strength did not influence the agglomeration of AgNPs with a PVP coating. Therefore, this result reflects that particles are stabilised as a result of steric repulsions caused by uncharged coating materials [152].

Partitioning of the solid solution is a key feature that helps determine the potential mobility and bioavailability of nanoparticles in soils. The high surface area and surface charge of ENMs may suggest a strong adhesion to the reactive surface of soils, such as soil minerals and organic matter[32]. A method for determining the retention of nanoparticles in soils has been developed. Advanced filtration technology makes it possible and achievable to separate individual nanoparticles and small aggregated particles from their dissolved

species by using 0.45 μm filters. This method can be used to recognise the retention of nanoparticles and the solute ions that result from their dissolution [153].

Mobility is one of the main factors in soil that is affected by nanoparticle availability to soil biota, the distribution through the soil and its efficient persistence [154,155]. The mobility of nanoparticles in a porous medium can be mainly controlled by aggregation and deposition mechanisms [154]. These processes are affected by physiochemical properties and the characterisation of the soil, such as clay content and type, pH, soil organic matter type and amount, flow velocity, composition of soil solution etc. [156].

A characteristic of bacteria is their capability to form biofilms. Biofilms are effectively a community of bacteria that adheres to surfaces *via* the production of extracellular polymeric substances (EPS) or as a multilayer coating of bacteria cells. The structure of biofilms significantly resists antimicrobial impacts of NPs due to the physical protection provided by several layers of bacteria cells [157]. Biofilms are commonly found in the solid and water-sediment interface and affect the fate and transportation of AgNPs that have different coatings. The existence of biofilm, bovine serum albumin (BSA) and alginate in the porous media influences the affinity of Cit–AgNPs, which is demonstrated by attachment efficiency (α). This increases the affinity gram-negative *Pseudomonas aeruginosa* and gram-positive *Bacillus cereus* biofilms. Meanwhile, the PVP–AgNPs attach to glass beads and increase the biofilm [158]. They significantly reduce retention at low ionic strength in biofilm-coated sand in contrast to clean sand. The reason for this reduction is the repulsive electrosteric force between the PVP coating and the EPS of the biofilm. Moreover, a mature biofilm coating is an earlier breakthrough of PVP-n Ag when compared to a younger biofilm coating or to clean sand. These outcomes may indicate the impact of the repulsive surface force combined with the selection of pore size and a more developed biofilm [159].

2.6. Objectives and layout of the thesis

The purpose of this thesis is to study the bioavailability, stability and transformations of AgNPs and ZnONPs in sludge and freshwater environments. The sulfidation behaviour of AgNPs under anaerobic conditions with simulated water is characterised to observe the transformation process and alterations of the crystal structure, which are related to the stability of the sulfided AgNPs. The behaviour of a matrix of engineered nanoparticles

(ENPs) was compared to AgNPs and ZnONPs under anaerobic digestion processes in simulated sludge. In the same processes, the impact of ZnONMs and AgNMs on the production of biogas was studied. In addition, the speciation's of ZnONMs were compared within the time of digestion. Both AgNPs and ZnONPs were aged in the OECD-MOP medium within different conditions to understand their stability and dissolution in simulated freshwater conditions. These aged nanoparticles were incubated within green freshwater algae cells to predict their impacts on algal health.

The structure of the thesis first starts with a literature review (Chapter 2) on the physiochemical properties of ENPs and focuses on the stability, transformation, fate, and dissolution mechanism of AgNPs and ZnONPs. The chapter includes an overview of the ecotoxicity of AgNPs and ZnONPs towards different microorganisms and a summary of the latest literature on ZnONPs speciation, to compare them with the present study.

Chapter 3 describes several of the techniques applied in the thesis to assist the objective of the project. These techniques are including the characterisation of ENMs to identify their physiochemical properties, morphology, and chemical and structural information.

In Chapter 4, the sulfidation of AgNPs was investigated within an anaerobic system of hydrogen sulfide gas and within HAs. The physiochemical properties of sulfided particles were compared, and Ag_2NPs with different particle sizes and coating agents were prepared to test these particles performance and impact under anaerobic digestion.

In Chapter 5, two sets of anaerobic digestion experiments were carried out. The first one tested a group of commercial ENPs and synthetic AgNPs and Ag_2SNPs. The anaerobic digestion behaviour of sludge within organic waste was tested in terms of pH changes and biogas production. The second set of experiments focused on commercial ZnONPs, ZnSNPs, PVP–AgNPs and synthesis Ag_2SNPs in the matter of biogas production. Moreover, the speciation of commercial ZnONPs and ZnSNPs under the same condition of anaerobic digestion was studied using XAS. There is a gap in literature which investigate the transformation Zn- and Ag-containing NMs to AD performance using real-world AD sludge.

Chapter 6 reports on the stability of AgNPs and ZnONPs within an algal culture medium and aged under different light and dark conditions. The dissolution of both nanoparticles

was determined by inductively coupled plasma-mass spectrometry (ICP-MS) and inductively coupled plasma-optical emission spectroscopy (ICP-OES). The aged AgNPs and ZnONPs were incubated to understand the interaction of aged nanoparticles with algal cells by using TEM and scanning transmission electron microscopy–electron energy loss spectroscopy (STEM–EELS).

Finally, Chapter 7 summarises the outcomes and conclusions of the thesis and gives suggestions for future work.

Chapter 3: Characterization techniques

3. Characterisation techniques

Several techniques were used to characterise ENMs in different environments to help investigate their transformation and impact on their surroundings. The characterisation of ENMs was carried out according to the type of sample (treated or untreated) and their properties.

3.1. Dynamic light scattering and zeta potential.

Dynamic light scattering (DLS) is used to identify a particle's size and involves the application of laser light to the particle solution. The light then scatters back with a different intensity. This variation depends on the diffusion coefficient (the hydrodynamic radius) of the particles. DLS can determine the size dispersions and aggregation of nanoparticles. This technique works when a sample of solution or suspension are loaded in a polystyrene cuvette and a laser beam is applied. The beam then scatters back with a different intensity, depending on the Brownian motion of the particles in the solution. The scattered light is detected by two detectors set at either 90° or 173° from the light source. Its intensity has to be in a certain range to allow detection. This diffusion process of particles is called the diffusion coefficient and can be utilised to obtain the size of particles in a suspension *via* the Stokes–Einstein relationship. The size of particles is referred to as the hydrodynamic radius or Stokes's radius. The Stokes–Einstein equation is as follows:

$$D = \frac{k_B T}{6\pi\eta r} \tag{3.1}$$

where D is related to the diffusion coefficient of suspension, r is the radius, k_B = $1.38X10^{-23}$J is Boltzmann's constant, T is the temperature of the suspension and η is the dynamic viscosity. The diffusion coefficient (D) is affected by the core size of particles and their surface structure. The concentration of the ions in suspension can affect the speed of a particle's diffusive motion. This effect relates to the change in thickness of the electrical double layer of ions. This layer is produced around the nanoparticles by the low conductivity of suspension, which slows down the speed of diffusion [160].

The zeta potential (ζ) is a physical property that is a measure of the colloidal stability and surface charge of nanoparticles. The measurement of zeta potential relies on the nature of

the particles and the suspension or colloidal solution. In this solution, a net charge affects the distribution of ions surrounding the particles in the solution, resulting in an increase in the concentration of counter-ions. This influence extends into a region called the electrical double layer. Conventionally, this layer is predicted to exist as two separate inner regions. The area with strongly bonded ions is called the Stern layer, and the outer layer of loosely bonded ions is called the diffuse layer.

The particles move through the colloidal solution because of gravity or an applied voltage, and the ions also move. There is a distance around the particles that exists as a boundary where ions do not move with the particles, known as the surface of hydrodynamic shear or the slip plane. This is located in the diffusion layer, and it is represented as the zeta potential. When the zeta potential is very positive or very negative, the particles will repel one another so the suspension will be stable. We have to consider an important parameter during the discussion of zeta potential, that is, the pH of the solution. The technique for measuring zeta potential is to apply an electric field across the sample that induces charged particles to move. The velocity and direction of the movement of the particles (electrophoretic mobility) depend on the applied field. The velocity of the particles in the applied field will depend on the strength of the electric field, the dielectric constant of the liquid, the viscosity of the liquid and the zeta potential. The electrophoretic mobility of a particle can be determined using the Henry equation:

$$U_E = \frac{2\epsilon\zeta f(Ka)}{3\eta} \tag{3.2}$$

where UE is the electrophoretic mobility, ε is the dielectric constant, ζ is the zeta potential, f(Ka) is Henry's function and η is the viscosity. Henry's function has a value of either 1.5 or 1.0, and the value 1.5 is used for the zeta potential of an aqueous solution that has electrolyte concentrations, referred to as the Smoluchowski approximation [161].

3.2. UV-visible spectroscopy / surface plasmon resonance

The physicochemical properties of nanoparticles can be identified by UV-visible spectroscopy. The absorption spectrum describes the variations in size and shape of nanoparticles as reflected on the surface plasmon resonance (SPR) band [162,163]. For

spherical AgNPs, an SPR band was reported to be located between 390 and 400 nm and characterised by the yellow/organic colour of AgNPs suspension [164].

The SPR is defined as the oscillations that occurred because of the interaction between the electron loss of metallic nanoparticles and the incident light (an electromagnetic field). The frequency of an electromagnetic field with a specific wavelength can cause a resonance, when it has the same frequency of the materials, result in a strong scattering of light. This phenomenon has captured the attention of scholars due to its wide range of applications, such as in sensors, biomedicine and others [165].

The working principle of the machine is tested on the liquid form of the specimen, which is placed with a reference sample to allow the UV beam from a projector to pass through both samples. After the beam passes through the liquid samples (reference and specimen), the energy of the UV beam will excite the orbital electron to a higher energy state. The excited electron will pair with an electron in its ground state and then the excited electron will deexcite and go back to a lower energy level, causing an emitted photon to be detected [166].

UV-visible spectroscopy is used to confirm the presence of spherical AgNPs in suspension. Moreover, it can confirm the shape and size of synthetic AgNPs before and after an experiment, such as the introduction of a medium to AgNPs or a sulfidation process. If the location of the SPR peak has changed, then that means the size or shape has variations. UV-visible spectroscopy has also been used to confirm the sulfidation of AgNPs, which have shown a wider peak or disappeared. Therefore, the shape of the peak and its width can indicate that the polydispersity of the nanoparticles' size is related to the aggregation state [163].

3.3. Inductively coupled plasma-optical emission spectroscopy (ICP-OES)

ICP-OES is a powerful and sensitive analytical technique that can trace most of the elements in a sample. This technique detects the elements in samples by using a plasma, which is the fourth state of matter. This spectroscopy device consists of detector, spectrometer, source and unit for processing the data. In general, when a sample contains elements that have been exposed to plasma energy (photons), the component elements are

excited. The excited components, which are electrons, will get back to the lower energy position, resulting in the emission rays of photons. These photons correspond with wavelengths that can be detected and then determined by a spectrometer. The intensity of the emissions from the element's components and the position of the photon's wavelengths are used to determine and measure the type of elements and their concentration. The instrument used to run the analysis is Thermo Scientific iCAP 6000 series Optical Spectrometer with an attached CETAC ASX-520 AutoSampler. To confirm the calibration accuracy, the calibration curves were checked prior to each analysis and plotted with more than seven concentration points using standards [167,168].

3.4. Inductively coupled plasma-mass spectrometry (ICP-MS)

Elemental concentration is measured by a quadrupole-based ICP-MS. The range of the concentration this technique measures is in parts per billion (ppb), unlike ICP-OES, which provides the measurement in parts per million (ppm). The spectrometer of ICP-MS is characterised by DC voltage application and a high-frequency field between four sequential mounted rods. The liquid samples are nebulised through the plasma to generate ions and then directed to the mass spectrometer by a supersonic beam that generates collisions and adiabatic expansions. These ions are transferred to the quadrupole of the MS, which generates species with a mass-to-change ratio (m/z) according to the variation of the electric field. Not all species will be deflected at trajectories; the specific m/z ratio will reach the detector thanks to the spectrometer, which works as a filter to exclude higher or lower m/z charged fragments. When the ions are sticking in the detector, a range of electrical signals are generated due to the ion-electron multipliers. When the positive ions hit the negative ones on the detector surface, a number of electrons are generated, thus intensifying the signal. The electrons, as a current, are translated into the unit of counts per second, which is correlated to the number of atoms that generate the signals within the sample through the use of the calibration curve. This curve is previously prepared according to calibration standards.

The use of ICP-OES and ICP-MS is dependent on the medium tested and its sample preparation. ICP-OES is used to find the concentration of synthesised nanoparticles in-house and measure high concentrations (due to limitations of very low concentrations). However, sample preparation for an ICP-OES is less complicated than for ICP-MS. ICP-

MS can be applied to study the dissolution of 1 mg/l Cit–AgNPs in a culture medium, which is considered a complex medium.

3.5. Transmission Electron microscopy

Transmission electron microscopy (TEM) can be utilised to study the size of AgNPs along with their dispersion or aggregation. It can be combined with energy dispersive X-ray spectroscopy (EDX) and electron energy loss spectroscopy (EELS) to determine the metal composition of the nanoparticles. TEM can provide remarkable information about the surface morphology and crystallinity/phase of a sample. The crystallographic information can be provided by using selected area electron diffraction pattern. The TEM setup involves a gun that generates an electron beam that subsequently passes through different electromagnetic lenses. The electron source is generated by a thermionic source, such as a tungsten or LaB_6 filament. When a signal is detected, a camera can be magnified and projected onto the screen. The more projector electromagnetic lenses increase the magnification. The specimen size has to be no more 3 mm in diameter with a thickness of under 100 nm [169]. The TEM resolution is higher than SEM in terms of magnitude. the resolution of TEM with aberration corrected system has about 0.5 Å while TEM with non-aberration corrected system has around 1-2 Å [170]. The microscopy scheme in (Figure *3-1*) shows scanning electron microscopy (SEM), TEM and scanning transmission electron microscopy (STEM) set ups.

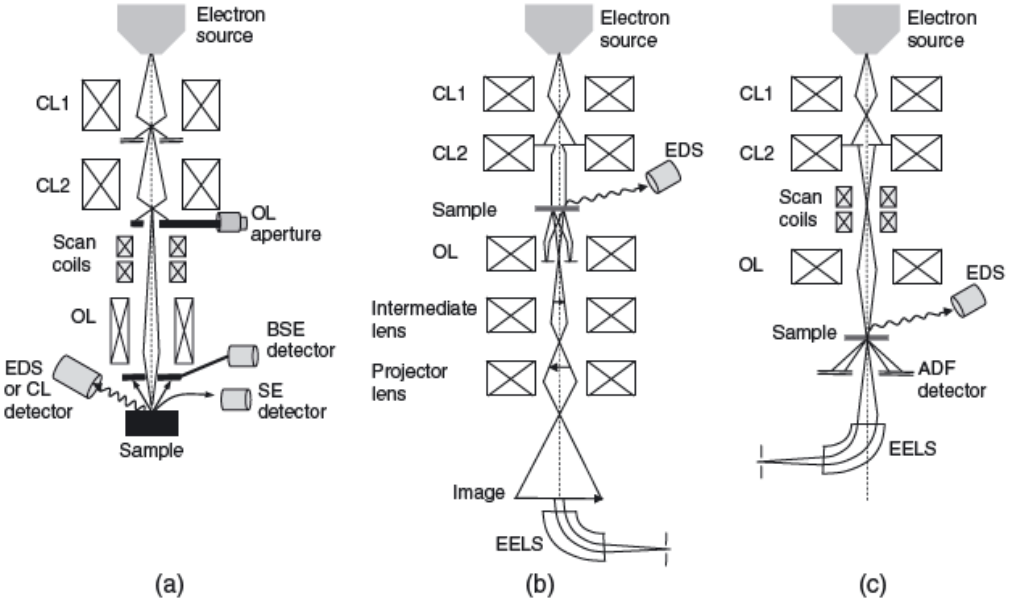

Figure 3-1: Schematic for different set-ups of electron microscopes, where (a) shows scanning electron microscopy (SEM) and (b) and (c) are transmission electron microscopy (TEM) and scanning transmission electron microscopy (STEM), respectively. Illustrated are the following: CL: condenser lens, OL: objective lens, BSE: backscattering electron, SE: secondary electron, EDS: electron dispersive x-ray spectroscopy, Cl: cathodoluminescence, EELS: electron energy loss spectroscopy and ADF: annual dark field. Reprinted (adopted) with permission from [171] Copyright (2013) John Wiley & Sons, Ltd.

The interaction of a primary electron incident in the specimen will result in different signals. The signals generated depend on the specimen thickness. For sufficiently thin samples, the electron beam can be transmitted through the sample or will generate several signals, such as Auger electrons, secondary electrons, backscattered electrons, photons and characteristic X-rays [172].The detection of each signal depends on which type of detector amplifies the signal to allow electron microscopes to obtain the required information about information such as the morphology, chemical composition and crystallinity of the specimen. Figure 3-2 shows the different interactions from the incident of an electron beam with the samples. The electron beam passes through the sample and interacts with electrons or nuclei in the sample. For example, diffracted electrons can form dark and bright regions

within the images. Diffraction limits the spatial resolution of the image and can be defined using the Rayleigh criterion:

$$R = \frac{0.61\lambda}{NA} \tag{3.3}$$

where λ is the wavelength of electron radiation, and NA is the numerical aperture of lenses. The resolution is related to the wavelength and energy of the electrons. Hence, based on Planck's constant (h):

$$\lambda = ph \tag{3.4}$$

where p is the particle momentum. The potential energy of the electrons eE is transferred into kinetic energy:

$$eE = \frac{1}{2}mv^2 \tag{3.5}$$

where e is the electron charge, m is the electron mass and v is the speed of the electron. The momentum equation can be applied to the previous equation to find the relationship between acceleration voltage and electron's wavelength, as follows:

$$\lambda = \frac{h}{\sqrt{2meE}} \tag{3.6}$$

Taking relativistic considerations into account, version of Equation (3.6) can be changed to:

$$\lambda = \frac{hc}{\sqrt{2EE_0 + E^2}} \tag{3.7}$$

Most of the work in this thesis was carried out at an operating voltage 200 keV. Several complications occurred during the imaging of the samples in the TEM; notably, the resin was not stable. The resin sample was more stable under the beam in STEM and so the instrument was operated in this mode in this thesis.

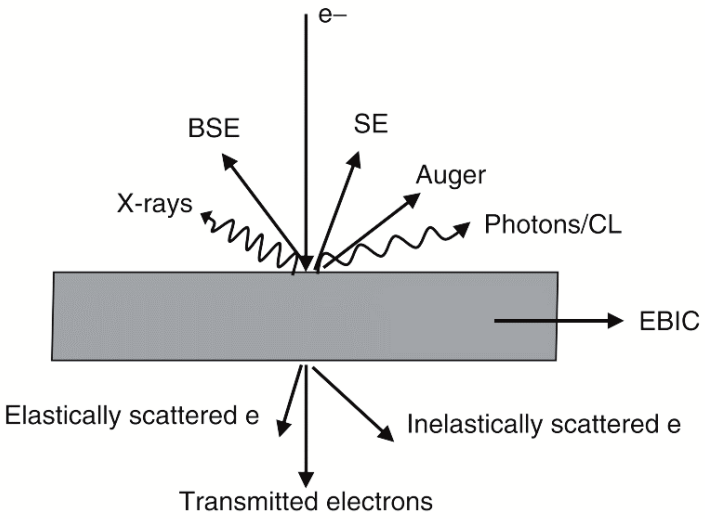

Figure 3-2: Summary of the interaction of electron-specimen and the possible signals that resulted. BSE: backscattering electrons, SE: secondary electrons, CL: cathodoluminescence and EBIC: electron beam induced current. Reprinted (adopted) with permission from [171] Copyright 2013 John Wiley & Sons Ltd.

3.5.1. Energy Dispersive X-ray Spectroscopy

EDX uses x-rays to characterise the chemical composition and concentration of an element in a sample. When high-energy electrons interact with sample's atoms, they cause an emission of characteristic x-rays from the sample. An electron from the high energy electron beam strikes an atom, prompting the ejection of one electron from the inner shell of the atom (e.g., a K shell). This phenomenon will leave a vacancy of ejected electrons. Thus, the atom will return to a lower energy state by filling the vacancy with an electron from a higher energy state. The release of energy takes the form of an x-ray and is expressed in electron volts (eV). This energy of the x-ray is equal to the energy differences between two levels. A solid state detector is used to collect the x-ray spectrum that specifies lines from each detected element [173].

3.5.2. Selected Area Electron Diffraction

Selected area electron diffraction (SAED) can be applied to determine the crystal structure of a specimen in electron microscopy [174]. The selected area aperture limits the electron beam to select out a circular region of the specimen that is usually larger than 100 nm in

diameter. Most electron beams will pass through the specimen to create a bright central point. The wavelength of the electrons is short which for example at 200 keV is equal 0.00251 nm [175]. Due to the interaction between the electron's waves and the crystal lattices, some of the electrons are scattered with different angles which causes the formation of the electron diffraction. This diffraction can assist imaging of the specimen with a main function of providing the structural information about the specimen. The electron diffraction patterns can be generated when a parallel beam passes through suitable samples' thickness then electrons inelastically scattered (halo background) are consequently elastically scattered. The Bragg diffraction maxima (spots) have produced by the Elastic scattering [175]. When the spots appeared that means the specimen mostly is partially crystalline. These diffracting electrons arise from a set of planes of spacing which are occupied within different atoms. The advantage of TEM is the ability to identified crystallographic orientations [176]. The SAED can thus be used to crystallographic phase of the material, to differentiate between metallic Ag and Ag_2S.

3.5.3. High-resolution Transmission Electron Microscopy

This mode of imaging can obtain information about the properties of the material and the atomic scale of the sample [174]. The formation of the high-resolution transmission electron microscopy (HRTEM) micrograph depends on phase contrast obtained using a large objective aperture. This permits the contribution of the whole beam during the imaging of both transmitted and diffracted beams. The interference pattern that results from the differences of the optical path is changed by microscopic parameters such as spherical aberrations, focusing, coherence and energy spread.

3.5.4. Scanning Transmission Electron Microscopy

A scanning transmission electron microscope is provided with a gun of emitted electron beams focused to probe a selected region on the specimen. The size of the probe emphasises the resolution of STEM and relies on the gun source and lens system of the microscope. The detection of a signal count on the angular distribution of scattered electrons depends on the scattered angle and type. The high-angle annular dark field (HAADF) has elastic scatter through a high angle which is >50 mrad of (HAADF detector), whereas inelastic scatter is through small angles which are <10 mrad of bright field (BF) detector and 10-50 mrad and annular dark field (ADF) detector. The intensity of signals collected using the HAADF detector is related to the atomic number (Z^2). EDS and electron energy loss

spectroscopy (EELS) can be performed in STEM mode to provide further information regarding the transformation, structure, and elemental composition of the specimen under investigation.

3.5.5. Electron Energy Loss Spectroscopy

This spectroscopy involves measuring the energy loss dispersion of the inelastic scattered high-energy electrons that have been transmitted through the thin specimen. When the interaction between the electron (from the gun) and the specimen's electrons occurs, an inelastic scattering process results when an electron is ejected from an atom in the specimen. During this event, a certain quantised amount of energy of the incoming electron is lost as momentum is transferred from the incoming electron to the electron within the sample [177,178], this loss is characteristic of the electronic structure of the material. Inelastic scattering may occur due to different processes occurring within the material, including an ionisation even, photon excitation and intra and inter band transitions [178]. When an electron beam hits a specimen's electron, the inelastically scattered electron will be collected by a detector, and its energies (the energy loss) is recorded. The electrons that have not lost any energy contribute to the zero-loss energy peak. The interaction between electrons, particularly electrons of inner shell atoms, can cause changes in the electrons' energy detected as a loss spectra, which relate to the electronic properties (including its band structure) of the material and can be used to characterise the elemental composition of the sample [178].

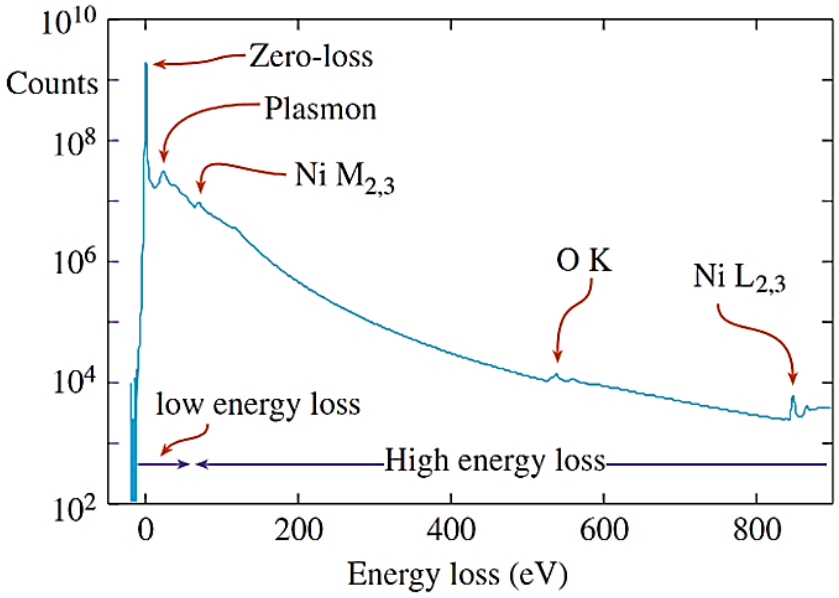

Figure 3-3: EELS spectrum with a characteristic logarithmic background intensity is showing the zero-loss peak, which is more intense, the low energy loss region, including a bulk plasmon peak, and then the low- and high-energy loss regions including ionisation peaks and fine structure reprinted (adopted) with permission from [179].

The EEL spectrum is divided into three excitation regions: low loss (transitions from and within the valence band), high loss (core loss region, including ionisation events) and zero-loss peak (Figure 3-3). Most of the electrons that pass through the specimen will elastically scatter and may lose some initial energy. The first dominant feature in the EEL spectrum is the zero-loss peak (the highest peak). The vibration of atoms in crystal structures is related to phonons and can be a source of the inelastic scattering (*i.e.*, energy loss). The valence band – low loss region - in EELS also involves excitations. These excitations occur in the loosely bonded electrons of the outer shells, which generate energy losses of less than 50 eV n. In the same region, the plasmon oscillations are equivalent to the UV-Vis modes of the optical absorption spectrum.

The core loss region is located above 100 eV, which provides information regarding the excitation of electrons from the inner shells of the atoms. When an inner shell electron has enough energy from an incident electron, it becomes excited and moves into an unoccupied level above the band gap. This process of excitation or ionisation provides useful

information about the composition, oxidation state, co-ordination, or bonding environment within the sample; the fine structure in the spectrum is related to the density of states (DOS) of the material. When the excited electrons return to the ground state, a characteristic X-ray must be produced to identify the elemental composition of the specimen. The binding energies of the inner core electrons are in the range of hundreds to several thousands of eV. The intensity of the spectrum decreases as the energy loss increases.

3.6. X-ray absorption spectroscopy

The XAS technique is employed to identify the geometry of matter and/or its electronic structure. X-ray radiation has adequate energy to eject a core electron from the atomic shells, where each one has the characteristic binding energy necessary to eject an electron from its shell. As a result, sufficient electrical and structural information can be delivered. An x-ray beam emitted from monochromatic sources has to pass through a homogenous specimen that will absorb and excite electrons. X-ray energy equal to the binding energy of electrons will be absorbed as a promoted core electron in an unoccupied or continuum state. If the x-ray energy is high enough for the binding energy of the electron, it will eject the electrons emitted as photoelectrons with kinetic energy. The total energy of both will depend on the variation between the binding energy of core electrons and the incident x-rays. Energy will decrease as a result of the x-rays being transmitted through the solid specimen. This can be quantified by the intensity transmitted by the x-ray (I_t) related to the initial intensity of the incident x-ray (I_0). The degree of x-rays absorbed by the material can be identified as the absorption coefficient $\mu(E)$ and can be derived from the transmitted x-ray as shown in the below equation:

$$\mu(E) = \log (I_0/I_t) \tag{3.8}$$

Moreover, the absorption coefficient can be derived from the fluorescence of the x-ray and the core-hole generation when electron excitation occurs. The electron hole will then be filled by another electron in the atom, which will decay from the excited state by emitting an x-ray characterised by the initial excitation of the core electron. Therefore, the relationship of x-ray fluorescence to $\mu(E)$ is described by the following equation that is used to determine $\mu(E)$:

$$\mu(E)\ \alpha\ (I_f/I_0) \tag{3.9}$$

I_f represents the fluorescence intensity that results from the absorbed x-ray at specific energy. All atoms have an intrinsic absorption coefficient ($\mu_0(E)$) that relies on several x-rays [180]. When absorption and energy are plotted, the resulting function shows a steep increase as a sharp peak of a specific energy. This rise in energy is often represented as an absorption edge matching the binding energy of the excited core electron. The binding energy of each element is the same as the absorption edge of the element. Thus, XAS is a technique that distinguishes between elements in which an x-ray can be turned into the different energies required to promote core electrons within several elements. XAS is also unique in its ability to identify the metal-ligand system of metal nanoparticles. Most studies are applied to identify the K and L3 edges of core electron transitions (referred to as 1s valence electron in p-orbitals and 2p to valence d-orbitals, respectively).

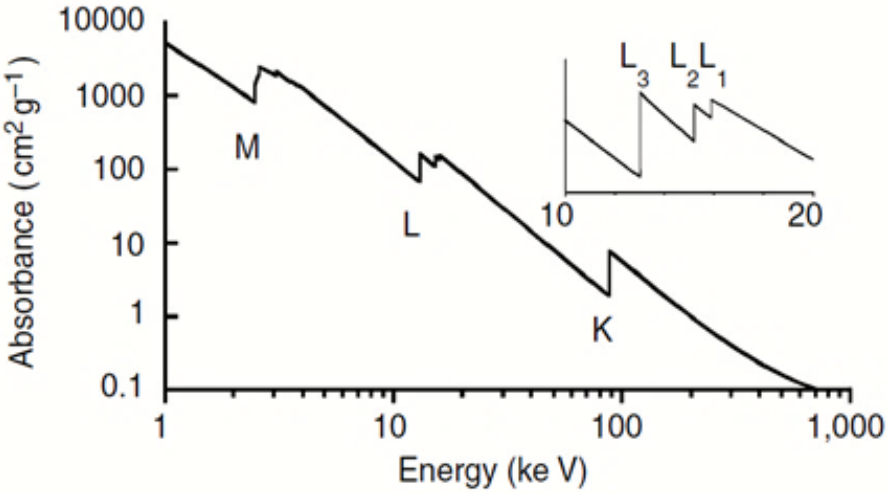

Figure 3-4: Low-resolution x-ray absorption spectrum of Pb shows the main transitions of the M, L and K edges. Reprinted (adopted) with permission from [181].

The general objective of XAS is to measure the effective absorption coefficient μ(E) of an element, obtained as a function of x-ray energy. When the element interacts with the local environment, changes are observed to the value of μ(E). This can measure the absorption near and above the edge of the element and results as a spectrum of the K-edge XAS spectrum (Figure 3-4). This spectrum consists of two regions: XANES and x-ray absorption

fine-edge structure (EXAFS). Each region displays valuable specific information. This thesis focuses on the K-edge (XANES) region in the XAS spectrum (Figure 3-5).

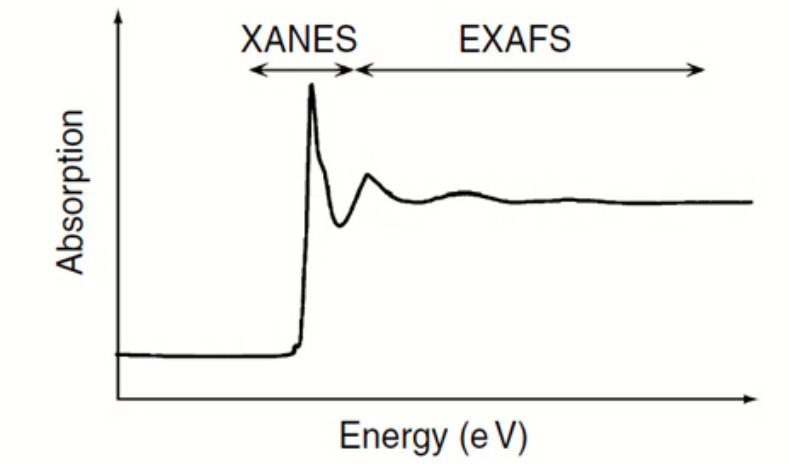

Figure 3-5: Schematic of XAS illustrating the regions of XANES and EXAFS. Reprinted (adopted) with permission from [181].

3.6.1. XAS Analysis

The data analysis of XAS for the XANES spectrum is summarised by a few steps, starting with the subtraction of background absorption, which acts as a pre-edge region. The application of the normalisation step allows a comparison between each spectrum. When the spectrum of the interest element consists of two or more oxidation states, it can be fitted to a linear combination using the absorption spectra. This reference standard of the same element helps measure the composition ratio of the speciation.

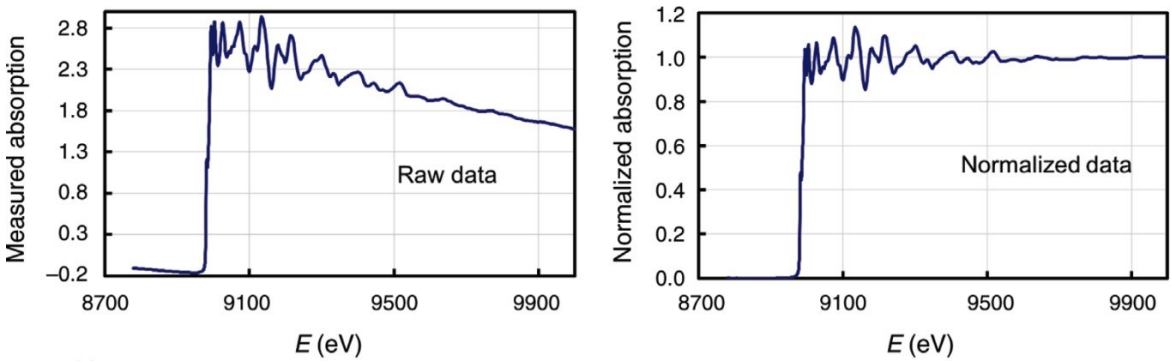

Figure 3-6: X-ray absorption spectrum of raw data presenting the pre-edge and post-edge before normalisation. The left spectrum starting at 0 shows the aftermath of the normalisation of data. Reprinted (adopted) with permission from [182].

3.6.2. Normalisation

The normalisation XANES spectrum eliminates differences (e.g., thickness, detector effects and concentration effects) between specimens. Thus, the only variation to the normalised spectra is assigned by the chemical speciation of the element and its interaction with the local environment. The normalised spectra of several elements can then be plotted quantitatively in comparison with the standard spectra. The methodology of normalisation of the XAS spectrum involves removing the background and fitting a linear or quadratic function of the pre-edge and post-edge regions, depending on the regions. The spectra will then be divided by the edge step to obtain the normalised spectra. Therefore, the pre-edge region starts at 0 while the edge step is equal to 1 (Figure 3-6). Linear combination fitting (LCF) is a quantitative analysis method applied to measure the fraction of species composition in a specimen. This model can obtain the speciation of unknown samples through the linear combination of the standard spectra which are the known composition and structure of the species of the interest element in the sample.

Chapter 4: Mechanisms of sulfidation of silver nanoparticles (AgNPs)

4. Mechanisms of sulfidation of silver nanoparticles (AgNPs)

4.1. Introduction

Silver nanoparticles and silver ions react with sulfide in aqueous solutions under both aerobic and anaerobic conditions, forming extremely insoluble silver sulfide species [74]. Two sulfidation mechanisms depend on concentrations of sulfide. The first can be explained as a partial sulfidation dominated by a low S/Ag ratio in which, at lower concentrations, silver predominantly undergoes oxidative dissolution and precipitation [76]. For example, (PVP)-AgNPs sulfidation was investigated with HS^- and resulted in a chain-like fractal structure forming a nanobridge between AgNPs and Ag_2S NPs. The explanation for this structure is that the surface of silver first oxidised and then partially dissolved before rapid precipitation to build the nanobridge between both Ag_2S and AgNPs. Using PVP as a capping agent prevents aggregation; however, it does not inhibit sulfidation [105]. The second mechanism occurs at a high concentration of sulfide and can directly transform the AgNPs to Ag_2SNPs under a solid-fluid reaction. The sulfiding of Cit-AgNPs with a size of 5 nm in dissolved H_2S and HS^- species, indicated the transformation pathways of AgNPs in the environment differs depending on the specific media its immersed in, which reveals the direct oxsulfidation and oxidative dissolution rates [76].

The aim of this chapter is to explain the mechanisms of syntheses of AgNPs and Ag_2SNPs stabilised by two different capping agents and sulfided AgNPs in the presence and absence of low molecular weight and highly concentrated humic acid to obtain stabilised, partially sulfided particles. This will help to elucidate the transformation mechanisms of AgNPs in a model system and will provide a panel of NPs at various stages of silver transformation for testing of aquatic toxicity (Chapter 6). The results of this chapter are arranged into two parts: the first is the sulfidation of AgNPs after synthesis by hydrogen gas and humic acid; the second is the synthesis of different coatings of Ag_2SNPs to investigate their behaviour during anaerobic digestion (chapter 5).

4.2. Experiment methodology

4.2.1. Synthesis of a Silver Nanoparticle suspension

Synthesis of citrate-capped AgNPs (Cit-AgNPs): silver nanoparticles were synthesised *via* chemical reduction using sodium borohydride ($NaBH_4$) as the reductant and sodium citrate ($Na_3C_6H_5O_7$) as the stabilising ion; the protocol was based on a modified Brust–Schiffrin method previously optimised by our research group [183]. A solution of $AgNO_3$ (1 mM) and $Na_3C_6H_5O_7$ (1 mM) were added to 250 ml of boiling water. Then, a solution of $NaBH_4$ (1 mM) was added within ten seconds, making the colour of the solution yellow, which indicates AgNPs formation. The solution was maintained at a temperature of 100 ºC for 30 minutes and was then left to cool at room temperature. The suspensions of AgNPs were washed three times with DI water to remove any impurities and residual unbound citrate. During the washing steps, the suspensions were centrifuged at a relative centrifugal force with a maximum value (RCF_{max} = 13,000 g). The concentration of the final silver particles after removing all unbound citrate was 25 ppm, and the purified suspension was sealed and stored in the dark in a refrigerator. The particles were regularly checked using UV-Vis spectroscopy measurements, TEM, and EDX to confirm their purity of colloidal solution and stability.

4.2.2. Sample preparation for sulfidation experiment using H_2S gas.

After synthesis of Cit-AgNPs, the concentration of the batch was determined by ICP-OES, and the size distribution and zeta potential diluted in deionised water are checked before further experiments were carried out. A stock solution of humic acid (HA) from Sigma Aldrich was prepared by adding 250 mg of 500 ml Milli-Q water and then stirring for 12 h in the dark, followed by separation with a filtered Amicon centrifuge with a size of 10 kDa at a speed of 4500 g for 30 min. HA filtration was targeted to obtain homogeneity of a smaller molecular size of HA to remove any particulate or insoluble materials. After ultrafiltration, the solution was adjusted to a pH of 7 by a 25 mM NaOH solution, and it was then injected into the H_2S generation system under stirring conditions. The resulting HA-HS^- was transferred by syringe to a small head bottle, sealed with parafilm, and placed in the refrigerator before beginning the reaction. The total organic carbon concentration and the pH were measured by the total organic chromatography (TOC) machine and a pH meter.

4.2.3. Sulfidation experiment with H_2S gas production system

The system setup contains an *in situ* hydrogen sulfide gas that is generated by reacting a known weight of sodium sulfide Na_2S 200 mg (Fisher Scientific) with dilute nitric acid HNO_3 (1:20) with a flow of nitrogen gas, as shown in (Figure 4-1). It consists of three flasks, which are connected by hose tubing with stopcocks. First, the system must be evacuated and flushed with nitrogen gas for 30 minutes in each flask to control its flow by a gas flow meter and the stopcocks. When H_2S was generated in the first flask, by starting drops of acid, it was then carried with the N_2 flow to the 2nd flask, where AgNPs suspension or humic acid had already been injected. The gas continued to purge throughout the system, and a zinc chloride $ZnCl_2$ scrubber (Fisher Scientific) was used to remove unreacted gas. For safety reasons, a sensor for H_2S gas was placed near the system for any leakage (none was observed). The experiment was conducted at room temperature and atmospheric pressure with a gas flow rate of 15 min/ml under stirring. The amount of hydrogen sulfide in the system was identified by placing an H_2S detection tube (GASTEC, Japan) in the hose tube connected between the first and second flasks to identify a calibration curve for the system. Based on the reactions in each flask, the following equations are demonstrated:

$$Na_2S\,(aq) + 2HNO_3\,(aq) \rightarrow H_2S\,(g) + 2NaNO_3\,(aq) \quad (4.1)$$

$$H_2S\,(g) + 2Ag \rightarrow Ag_2S\,(aq) + 2H_2\,(g) \quad (4.2)$$

$$H_2S\,(g) + ZnCl_2\,(aq) \rightarrow ZnS\,(aq) + 2HCl\,(aq) \quad (4.3)$$

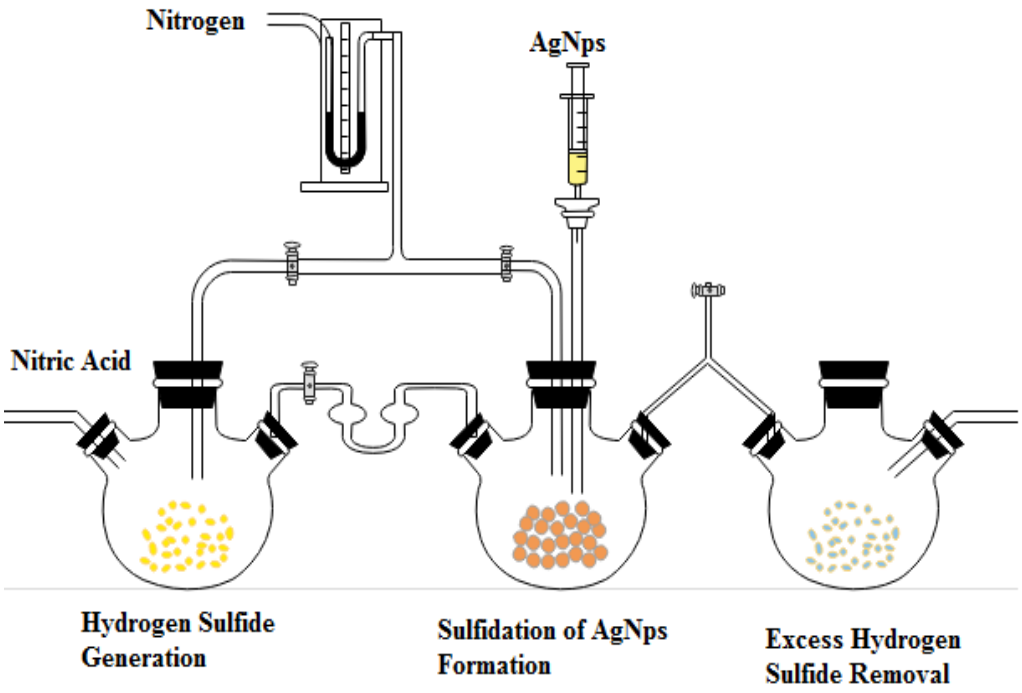

Figure 4-1:Schematic showing the experiment setup used to make sulfided Ag nanoparticles. This consists of three flasks, where the first has added Na2S and a syringe with diluted HNO_3 connected with a pump adjusted to a speed of 0.2 ml/min. The second flask was placed on a hotplate for stirring at room temperature and connected with a syringe of a colloidal AgNPs suspension. The third flask contains a $ZnCl_2$ substrate to eliminate H_2S gas.

The detection tube was placed to identify a calibration curve once all parameters were fixed for all experiments. This methodology for hydrogen sulfide detection was developed by the electrochemistry group at Imperial College and published in the literature [184]. The mechanism of the detection tube is to observe changes in the colour of lead acetate filled in a sealed glass tube where the amount of change represents the concentration of H_2S gas. The flow rate of gas is fixed to determine the volume of passed gas with time to plot a relationship between the gas concentration in a unit of volume (ppm) and time (Figure 4-2). The calibration plot determined the concentration of gas when it was generated by the reaction of different acids with sodium sulfide in the system [184]. It shown that the system was saturated with hydrogen sulfide gas 15 minutes after starting the experiment. The experimental setup was adjusted based on all parameters for sulfidation of AgNPs-citrate,

HA-AgNPs, and purged filtered HA. The volume of each sample was 20 ml injected by a needle to ensure there was no air in the system.

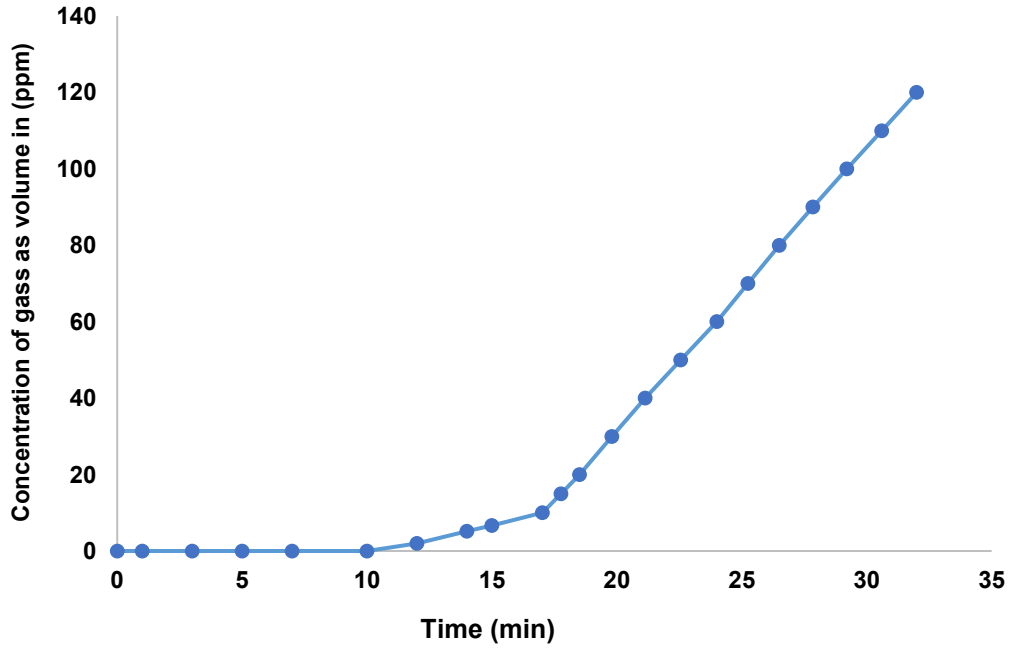

Figure 4-2: Calibration plot for H_2S ppm in a 100 ml flask size with a medium gas rate of 15 min/ml with an HNO_3 20:1 concentration considered a measurement of the H_2S concentration with controllable parameters.

The sulfiding of Cit-AgNPs was performed in the presence and absence of HA by H_2S exposure as described above. The transformation of AgNPs was investigated in a hydrogen sulfide environment as this gas has been found dissolved in rivers, seas, and wastewater, so this experiment tends to mimic potential transformation conditions in the environment. For all sulfidation of Cit-AgNPs, 25 mg/l with a total volume of 20 ml was sulfided to obtain a partial sulfided particle. UV-vis absorption spectra were conducted before and after exposure to the H_2S environment to confirm the sulfiding of Cit-AgNPs. Also, sulfiding of Cit-AgNPs in HA was investigated by adding Cit-AgNPs to HA to obtain a concentration of 25 mg/l and a volume of 20 ml. Before the AgNPs-HA injection, the suspension was sonicated for three minutes to ensure a good dispersion of the nanoparticles within the HA and was exposed to H_2S gas for 17 minutes, corresponding to 10 ppm of the gas concentration. Then, HA-Ag_2SNPs were centrifuged and washed twice with deionized

water. The interaction of HA-HS^- with Cit-AgNPs was examined based on the reaction of 25 mg/l of Cit-AgNPs in a total volume of 1.5 ml HA-HS^- in an Eppendorf tube for 15 minutes sealed by parafilm. Then, the colloidal suspension was separated from the unbonded HA-HS^- by centrifugation (13000 g, 30 min) and was washed twice by deionised water. The chemical analysis of HA was characterised by inductively coupled plasma mass spectroscopy (ICP-MS). The concentrations of Fe and P were measured within the same HA of 10 mg C /l concentration which contains 102 ± 1 µg/l and 93 ± 10 µg/l, respectively were illustrated as mean ± standard error [185]. In comparison, the sulfur is 0.28 mg/l that was determined in a dissolved concentration of HA of 25 mg C/l by x-ray fluorescence spectroscopy (XRF) [98].

A diagram summary of the H_2S experiment flow is given below (Figure 4-3.i) sulfiding of AgNPs by direct interaction of H_2S gas with AgNPs; ii) direct interaction of AgNPs spiked with HA; iii) indirect sulfiding HA-H_2S before adding AgNPs (Figure 4-3.iv). For all direct experiments, the parameters were fixed (the gas flow meter, the acid dropper, volume, stirring speed, and the mass of Na_2S) while for indirect experiments, the volume of HA-HS^- with AgNPs was 1.5 ml. The indirect sulfiding process used the same HA-HS^- from the direct methodology.

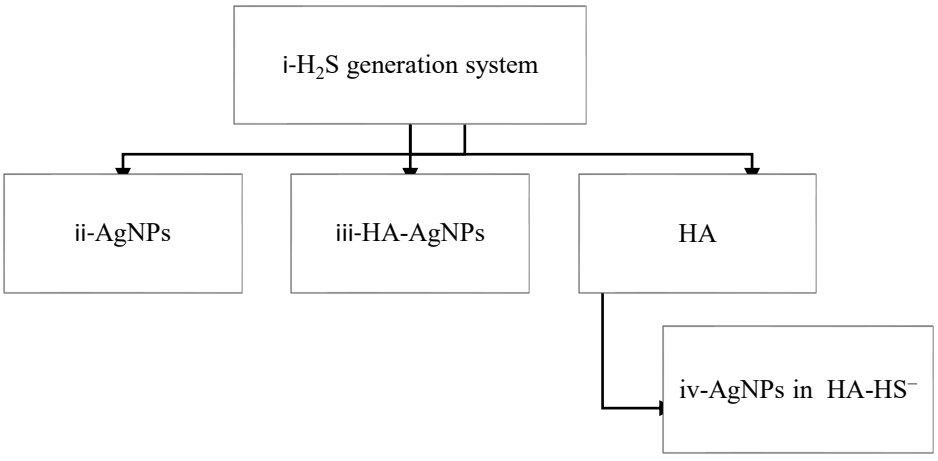

Figure 4-3:Schematic flow diagram for the H_2S exposure experiments.

4.2.4. Synthesis small (<30 nm) silver sulfide nanoparticles suspension with citrate and PVP stabilisers

The synthesis of silver sulfide nanoparticles Ag_2SNPs is dependent on the synthesis of Cit-AgNPs. In this experiment, Milli-Q water was purged using N_2 gas for 30 minutes before beginning the same steps for Cit-AgNPs, and during the formation of Ag_2SNPs N_2 passed through one flask head. Before the end of the experiment, sulfidation of 0.1M Polyvinylpyrrolidone PVP (55000 MW) and sodium sulfide Na_2S nonahydrate (0.5 mM) were freshly prepared. Then, two batches were prepared: one for Cit-Ag_2SNPs and one for PVP and Na_2S. The role of both citrate and PVP is to function as complexing and stabilising agents (with the citrate and PVP acting as electrostatic and steric stabilizers, respectively). In the literature, citrate has been used for the same roles in the chemical deposition of the Ag_2S/Ag heterostructures due to its involvement in photochemical reactions[186]. After the addition of the stabiliser, the Na_2S solution was slowly added until the colour of the solution turned dark red, at which point the solution was maintained at the same boiling temperature (95º) for one hour with vigorous stirring. It was then left to cool in the dark and washed by centrifugation using the same steps for Cit-AgNPs for purification. The same storage protocols were also used (dark and refrigerated).

4.2.5. Synthesis of large PVP-silver sulfide nanoparticles

The synthesis protocol for PVP-Ag_2SNPs was adopted from the synthetic method used in a previous study [187]. In brief, silver nitrate ($AgNO_3$) was reacted with elemental sulfur in the presence of the stabilizer PVP. In the paper, the authors stated that the molar ratio was Ag:S ~ 1: 2.6. 500 ml of a dissolved 1mM $AgNO_3$ solution was added to an Erlenmeyer flask, placed on a hotplate covered with aluminium foil, and stirred to dissolve 625 mg of PVP (with molar mass = 50,000 Da). This solution was heated to 60°C after it dissolved, and the elemental sulfur (42.0 mg) was dissolved in 50 ml ethanol at 60°C, so could be added at a rate of 2–3 drops per second and stirred for five hours. The solution was heated to 80°C for 15 minutes to ensure that ethanol completely evaporated. It was then left to cool to room temperature, centrifuged at a speed of 3400 g for 1.5 h, washed with deionised water for purification, suspended in deionised water, and kept in a refrigerator under dark conditions, as previously described.

4.2.6. Dynamic light scattering, zeta potential measurements, and UV-Vis spectroscopy

The average hydrodynamic diameter and Zeta potential (ζ) of AgNPs and Ag_2SNPs with and without the presence of HA were both measured using a Malvern Zetasizer Nano Series dynamic light scattering (DLS) instrument. The instrument setup had a 663 nm light wavelength and a backscattering angle at 173° with a pH function at 20°C. The samples were sonicated before testing, and the measurements were repeated at least three times. For UV-vis absorbance, spectra were collected within a range of wavelengths from 300–800 nm (as per literature data for Ag and Ag_2S) [103,188].

4.2.7. Transmission electron microscopy (TEM), selected area electron diffraction (SAED), and energy-dispersive X-ray spectroscopy (EDX).

The size and morphology of the particles were identified using transmission electron microscopy (TEM; JEM-2100F, Jeol, Tokyo, Japan, operated at 200 kV). The sample preparation method for TEM might cause drying-induced aggregation of the particles; to minimise this effect, the carbon grid was baked in an oven at 120 ºC for two hours under vacuum overnight or washed the grid with ethanol and placed in fitter paper to dry them out. To prepare the sample, a small drop of solution was placed on a 300-mesh copper carbon grid and directly dried under a vacuum in the dark. The size distribution was determined by counting and measuring at least 200 particles using ImageJ software. TEM was combined with the selected area electron diffraction (SAED), which was used to identify the crystallinity phases of the particles. The d-spacing distance of the lattice was calculated and compared with standard reference structures. Energy-dispersive X-ray spectroscopy (EDX) was used to determine the elemental analysis for AgNPs and Ag_2SNPs, respectively, and to confirm their purity.

4.3. Results and discussion

4.3.1. Silver nanoparticle characterisation

The morphology of synthesised nanoparticles was investigated by bright-field transmission electron microscopy (BF-TEM) and HR-TEM. Quasi-spherical particles with an FCC structure with a lattice spacing of 0.235 nm were observed in (Figure *4-4***Error! Reference source not found.**, A,B), consistent with literature reports. Different contrast of AgNPs is shown in the BF-TEM image due to different crystal orientations. Also, the average size

distribution of the nanoparticles was measured by the ImageJ software to be approximately 15 ± 3 nm, after measuring 200 particles, as shown in (Figure 4-4,C). A selected area electron diffraction (SAED) pattern revealed the lattice spacings of synthesised particles (Figure 4-4,D). The lattice planes closely match those of metallic silver planes [(111), (200), (220), and (311), representing the corresponding d-spacings of 0.239 nm, 0.207 nm, 0.145 nm, and 0.125 nm (ICSD ref. 01-087-0597)]. The EDX spectrum showed no sulfur signal, and the washing steps successfully removed any potential impurities (e.g., Cl^-, Na^+) shown in (Figure 4-4, E). The average hydrodynamic diameter and zeta potential (ξ) of Cit-AgNPs were 23±5 nm with a polydispersity index (PDI) of 0.181, and -33.2 ± 4.7 mV at pH 6.8 ± 0.08. The negative charge of the zeta potential confirmed electrostatic stabilisation by citrate. Therefore, the particles in the colloidal solution tended to repel each other, avoiding aggregation.

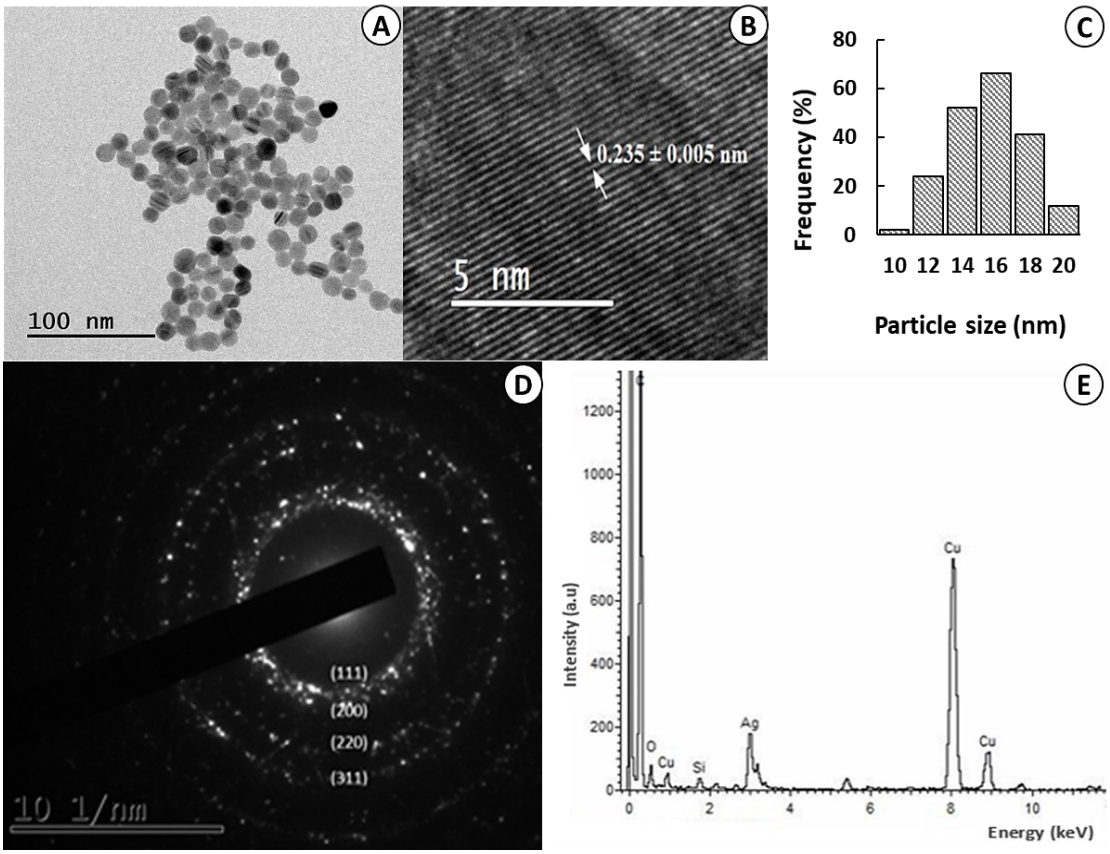

Figure 4-4: (A) Bright-field TEM micrograph for AgNPs (magnification 80 kx) (B) High-resolution TEM (magnification = 600 kx) showing the size of lattice spacings at 0.235 nm. (C) The size distribution of AgNPs calculated for n = 200 particles using ImageJ software.

(D) EDX spectrum for AgNPs stabilised by sodium citrate. (E) Selected electron diffraction pattern (SADP) revealed the corresponding planes (camera length 30 cm).

4.3.2. Part 1: Sulfiding AgNPs by Hydrogen sulfide gas and the presence of humic acid during the process

4.3.2.1. Characterisation of silver sulfide nanoparticles

The direct sulfiding Cit-AgNPs shown in the micrograph of bright-field TEM and HRTEM images elucidate the transformation to a silver sulfide structure, which illustrates a slightly large average size distribution that was 19 ± 2 nm (Figure 4-5, A-C). The crystal phase of Ag_2SNPs was identified by the measurement of d-spacing of 0.502 ± 0.02 nm, which matches the plane (011) that confines the monoclinic Ag_2S (ICSD ref. 01-075-1061). In (Figure 4-5, D and E), EDX spectra were acquired by dark-field scanning transmission electron microscopy (DF-STEM) images in two positions of the same particle to identify the distribution of both elements Ag and S to confirm the diffusion of sulfur atoms in the metallic Ag. Both spectra were acquired to try to characterise potential core-shell structures, which might have a short lifetime because AgNPs are rapidly transformed to Ag_2SNPs in H_2S environment [103,189,190]. For each of the different batches, sulfiding experiments were repeated to determine whether a methodology to 'detect' a core-shell structure could be identified. However, the process was too rapid, and all the particles showed fully sulfided nanoparticles with a different distribution of both element Ag and S. In addition to the EDS spectra, elemental mapping was applied for whole particles in the STEM image in (Figure 4-5, F and J) which confirmed full sulfidation. Figure 4-5,H was acquired for the UV-vis absorption of Cit-AgNPs after the reaction in the H_2S atmosphere. The surface plasmon resonance peak, which was the maximum absorption peak of Cit-AgNPs located at 393 nm, is indicated as a rapid loss of UV-vis absorbance. This was explained as spontaneous sulfiding, which is dominated by direct sulfidation [103]. When the nanoparticles began to sulfide, their colour is changed to dark red and then to pale yellow after about six hours. The average hydrodynamic diameter was measured for both colours without exposing the particles to air during the colour changes, which indicated the same particle size of 39.06 ± 10 nm, with a PDI of 0.46 and zeta potential (ξ) = -34.7 mV with a pH value of 6.62. The colour changes of sulfided AgNPs can explain the changes in the structure of Ag to Ag_2S, and according to the interplanar distances, the monoclinic system

is larger than the face centre cubic (FCC) system. The hydrodynamic size was checked after this interaction at 48 h and indicated that the Ag_2NPs had become larger. This can be explained by the fact that this particle was sulfided and suspended in the colloidal solution by the oxysulfidation process in a high concentration of sulfide. The un-reacted sulfide in the solution might encourage the aggregation of Ag_2SNPs followed by precipitation.

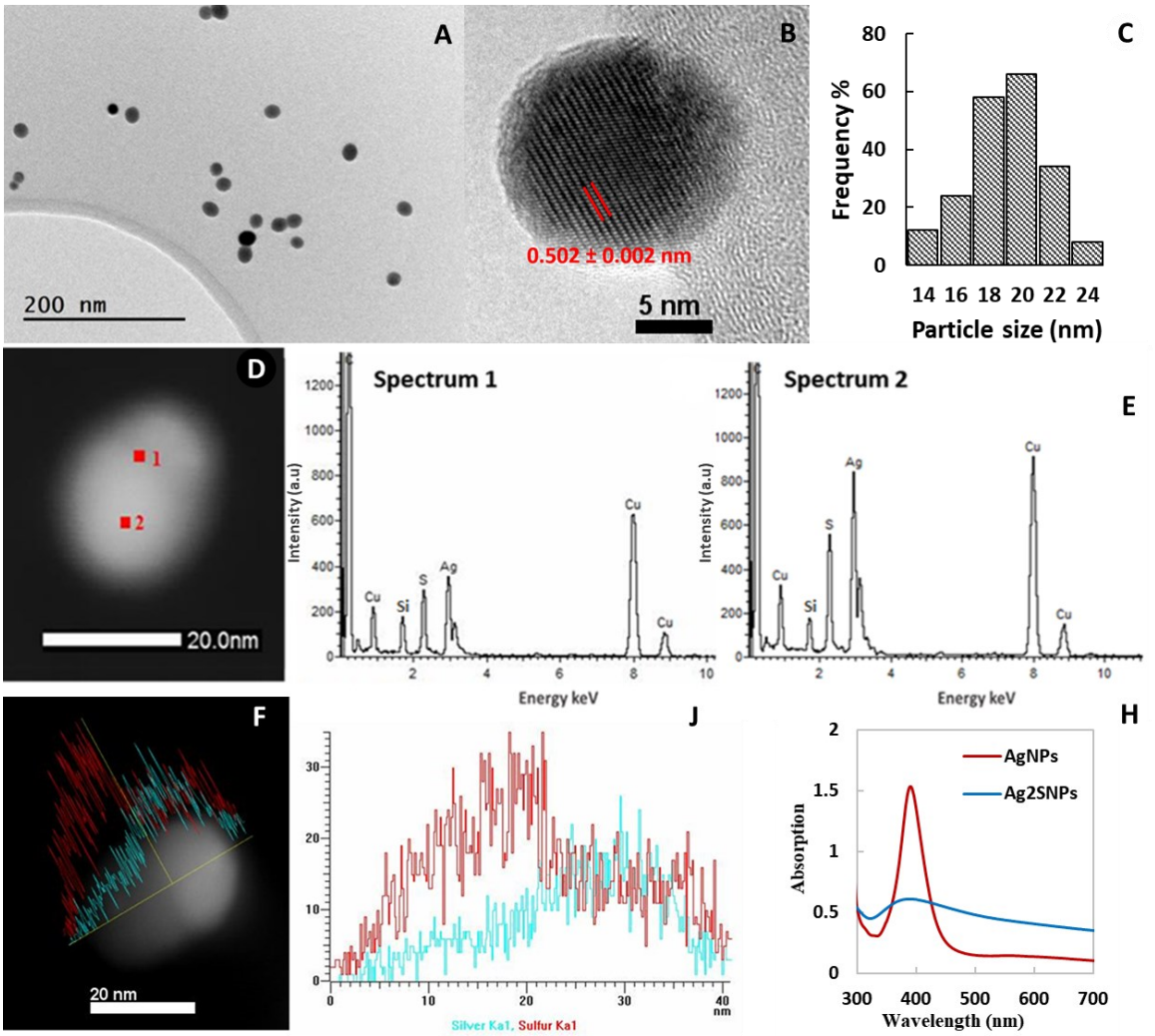

Figure 4-5: (A) TEM of AgNPs after sulfidation by H_2S gas (magnification = 100 kx); (B) HRTEM of A_2SNPs showed a lattice fringe in the plane corresponding to (011) and equivalent to Ag_2S (ICSD ref. 01-075-1061, and the magnification = 300 kx; (C) the size distribution of Ag_2SNPs measured from different TEM images, n = 210 particles and the darkfield TEM image for a particle; (D) The variations in Ag and S distribution in two regions shown by the EDX spectra (E); (F, J) STEM and line mapping for Ag and S; (H) UV-Vis absorption spectra confirming the sulfidation of Cit-AgNPs.

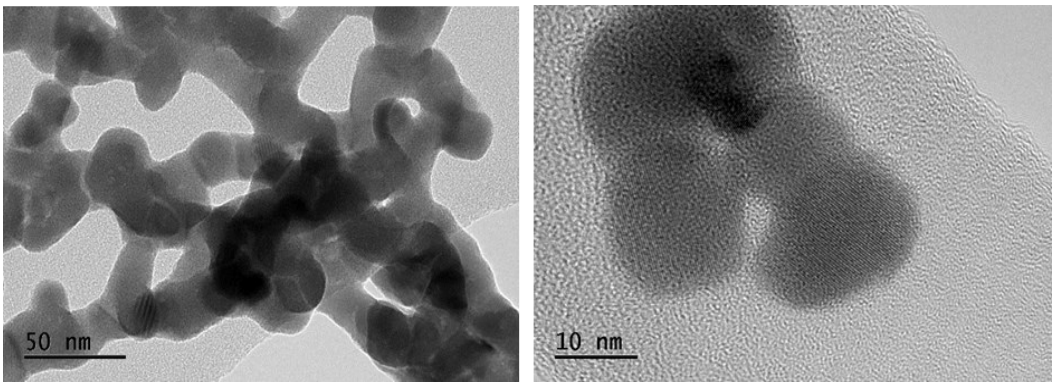

Figure 4-6: TEM micrographs showing the morphology of washed Ag_2SNPs that had been obtained by H_2S gas. In the left the low magnified micrograph are fused and agglomerated particles; the right image shows some of these particles at high magnification.

After this experiment, one batch of Ag_2SNPs was washed twice with DIW and ultrafiltration to remove excess sulfur and obtain purified sulfided nanoparticles for further experiments. However, applying this step affected the morphology of Ag_2SNPs dramatically, causing an aggregated, semi-sintered, and coarsened Ag_2SNPs structure to form (Figure 4-6). This suggests that the washing/ultracentrifugation destabilised the functionalised surface, enabling close contact and particle reactions to occur. This step was avoided for the direct sulfiding of AgNPs by H_2S gas, particularly after the sulfided experiment and before the colour completely changed. At the same time, the particles (Figure 4-8) had been washed and were more stable under the electron beam than their non-washed counterparts. The reason is that some NPs had not entirely transformed, and at the same time, once the NPs were washed by ultracentrifugation that can remove unreacted sulfide in the solution which could cause further precipitation and aggregation with no washing. In different batches of direct sulfidation, changes in the particles' s optical properties were investigated with time as the sulfide particles were exposed to air for 1 min, three, six, and ten hours. After each exposure time, UV-vis absorption spectra were collected (Figure 4-7). The kinetics of particle aggregation can be determined by measuring the rate of absorption loss at the surface plasmon resonance (SPR) peak of AgNPs in an aqueous solution [74]. It was noticed that in the spectrum of ten minutes, the sulfided particles

shifted upwards to a higher wavelength and broadened, different from the absorption spectra shown in (Figure 4-5). The broad and redshift peaks were related to losing the SPR and increasing the particle size, indicating partially observable sulfidation and aggregation. The peak that related to the total loss of SPR became straighter (smoothed) after three hours, which means all free electrons turned to bonded electrons. Notably, a broad peak between 600-650 nm indicates that aggregation continued, which may be due to the fully sulfided Ag_2SNPs reaching an equilibrium and then precipitating, as shown after six and ten hours. During the collection of spectra, the suspension colours shifted from purple to grey with black precipitation. These changes were unnoticeable in the first sulfidation process because the suspensions were kept sealed in a dark fridge.

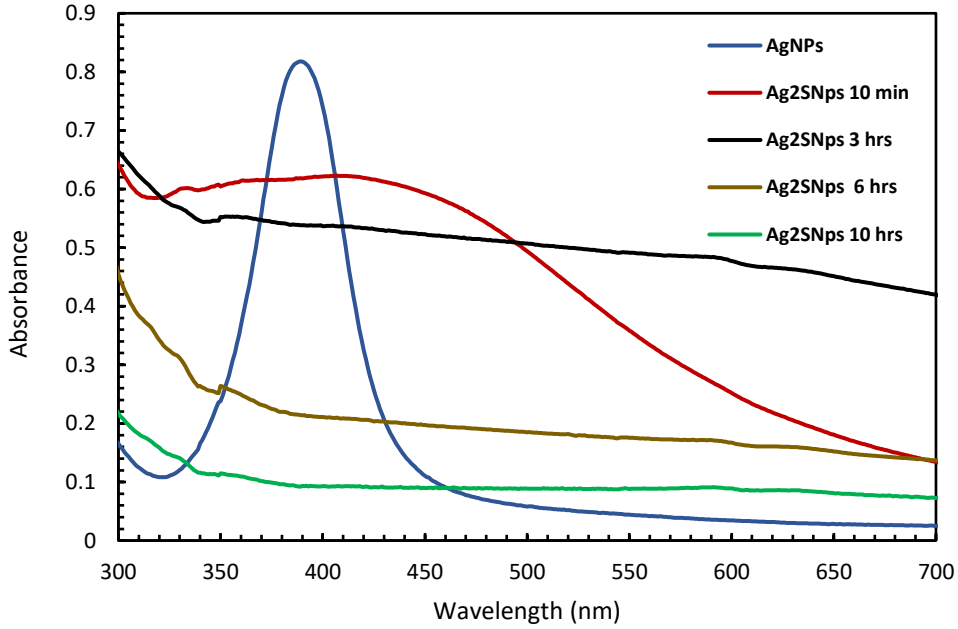

Figure 4-7:UV-vis absorption spectra of Cit-AgNPs after sulfidation. The concentration used in this batch was 10 mg/l.

4.3.2.2. Sulfidation of AgNPs in the presence of HA

To investigate the kinetics of sulfidation of Cit-AgNPs with HS^-, a filtered HA with a concentration of 500 mg/l was prepared and measured to have a TOC of 650 mg/l after filtration by 10-kDa. In the literature, an ultrafiltration process was applied to obtain the low molecular weight of humic acid and reported that Aldrich humic acid has a

hydrophobic nature [76]. From previous work, the low molecular weight of natural organic matter was observed more with carboxyl groups, while the higher molecular weight had more aromatic structures [105]. High molecular weight natural organic matter can increase the colloidal stability of Cit-AgNPs, adsorbing and binding on the surface more than the displaced citrate, which significantly enhances the electrostatic repulsion force by having more negative charges on the surface [103].

As described above, two methodologies were carried out for the sulfidation of AgNPs in the presence of HA: direct and indirect interactions between AgNPs and H_2S. For direct sulfidation, the same HA solution was mixed with Cit-AgNPs and sonicated to disperse the AgNPs in HA, before taking the same conditions into account as in the previous experiment, such as the volume and concentration of AgNPs. The characterisation of HA-AgNPs was investigated before and after sulfidation. In (Figure 4-8, A-C), the morphology of HA-AgNPs showed the same quasi-spherical shape of Cit-AgNPs and the same crystal structure due to the matching SAED patterns and interplanar distance in the HRTEM image. The morphology of the HA-Ag_2SNPs was still spherical, but dark surface spots were observable on some of the particles (Figure 4-8, D). Analysis of the HRTEM of some observed particles in the dark region found the interplanar distance for the monoclinic structure of the Ag_2S (Ref-00-014-0072) and the metallic Ag (Figure 4-8, E). The Ag_2S lattice spacing of 0.392 ± 0.004 nm corresponded with (-101) and the metallic Ag was 0.234 ± 0.002 nm for (111) plane, which identified to be the same for the Cit-AgNPs.

The same particles were shown in a brighter area in the STEM image and darker in the BF-TEM (Figure 4-8, F and H). The brighter area composition in STEM mod can indicate a lower average Z (atomic number) or a more significant number of atoms and molecules [104]. In our case, the brighter area had more Ag than the grey one, which was rich in S as the same shown in EDS spectra in (Figure 4-5 E). These observations were similar to previous observations showing the sulfidation of Cit-AgNPs and Tween-AgNPs sulfided by Na_2S in the presence of fulvic acid [183]. In this report they showed a brighter area and a grey area as being high-and low-intensity sub-grains. The STEM-EDX spectrum shown in (Figure 4-8, J) confirmed the existence of Ag and S. This batch was imaged before and after being washed twice in deionized water, resulting in a more stabilised structure during imaging. All the images for HA-Ag_2SNPs were taken using the washed particles. These sulfided

nanoparticles had a core-shell structure (Figure 4-8, D-F and H). The structure of core-shell in terms of thickness distributed around the surface Ag_2SNPs was not homogeneous in size.

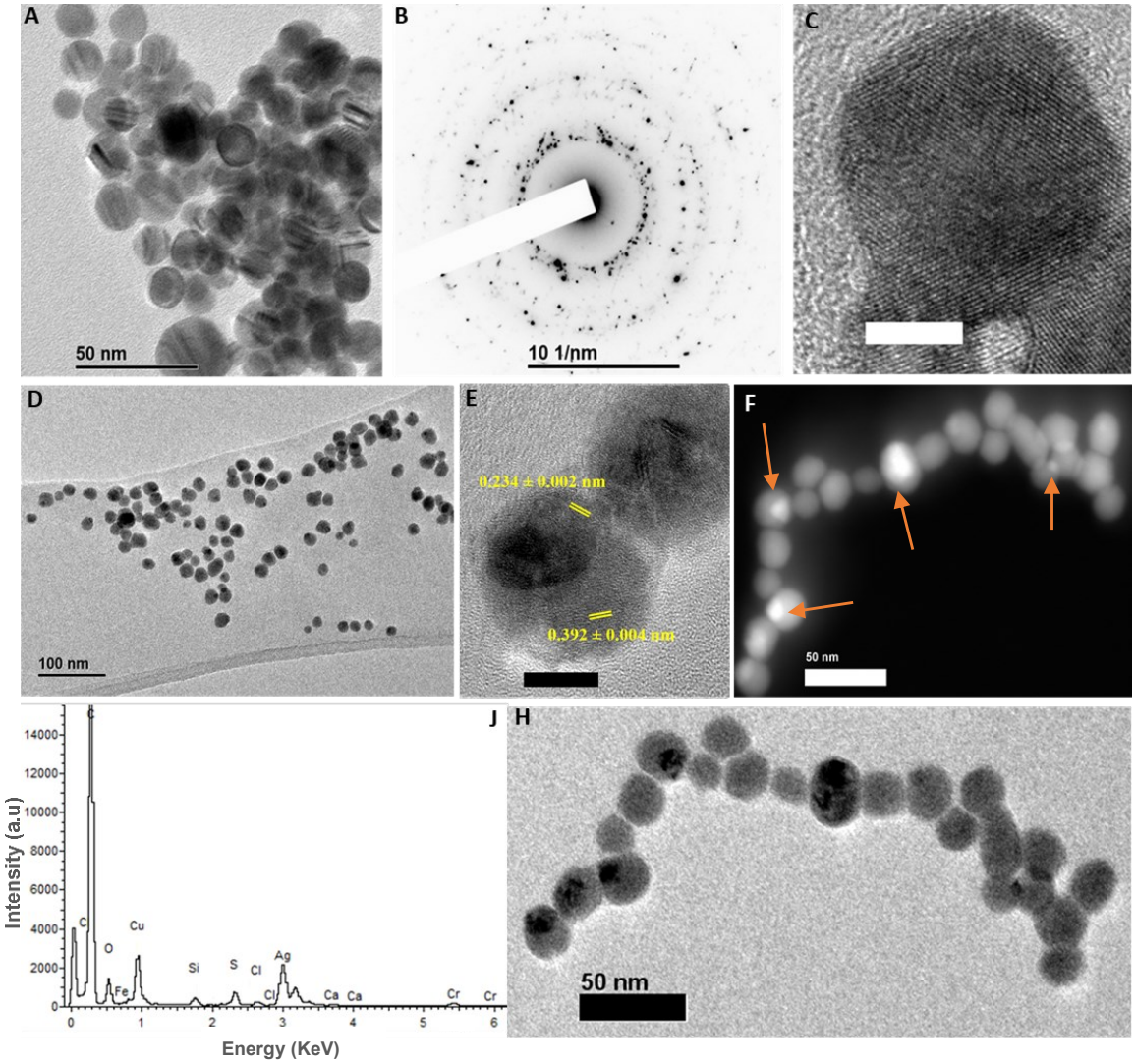

Figure 4-8:(A) BF-TEM of AgNPs after being spiked into HA (magnification = 120 kx), (B) SAED for the collected HA-AgNPs, (C) HR-TEM of HA-AgNPs with a matching interplanar distance of 0.235 nm of Cit-AgNPs (magnification = 600 kx and scale bar = 5 nm), (D) Morphology for HA-AgNPs sulfided by H_2S (magnification = 50 kx), (E) HRTEM for a particle showing metallic Ag and HA-Ag_2SNPs with lattice spacing of 0.234±0.002 nm and 0.392±0.004 nm, respectively (scale bar = 10 nm and magnification = 300 kx), (F) DF-STEM of HA-Ag_2SNPs (magnification = 100 kx), (J) STEM-EDX spectrum, (H) BF-TEM for the particles in image F.

For indirect sulfiding, an HA solution was exposed to H_2S gas, using the same conditions as direct sulfiding. The resulting solution was HA- HS^- and was mixed with Cit-AgNPs in an Eppendorf tube for 15 minutes before being washed twice by deionised water. The resulting Ag_2SNPs-HA had lighter and darker subgrains, which indicates partially and fully sulfided particles attached to a series of nanoparticles (Figure *4-9*, B). HRTEM and FFT analyses showed a monoclinic Ag_2SNP (ref-01-07501061), which was close to the d-spacing 0.504 ± 0.005 nm, 0.326 ± 0.002 nm, and 0.2521 ± 0.001 nm corresponded to the planes (-120), (100), and (220), respectively (Figure *4-9*, C and D). The shell thickness of the HA-coated nanoparticles was determined by measuring an average intensity line profile across the surface structure seen on several nanoparticles, which was 1.45 ± 0.5 nm in thickness (Figure *4-9*, E and F). The FFT profile was analysed to confirm the AgNPs had sulfided and the monoclinic structure. However, the hollow structure in the literature is explained as a cavity, but in these particles, it was noticed that there is a shell structure with the same planes of Ag_2SNPs. This shell is sulfided Ag with HA absorbed on the surface around the whole particles within the subgrains. The sulfidation of AgNPs was confirmed by EDX spectroscopy (Figure *4-9*, H) for the BF-TEM image shown in (Figure *4-9*, J). The sub-grain formation structure was observed by the sulfiding Cit-AgNPs in the presence of HA in oxygenated water. For the same size of Cit-AgNPs (20 nm), the presence of HA accelerated sulfiding and resulted in the formation of the Ag core-shell (Ag_2S), which transformed into a hollow structure [186].

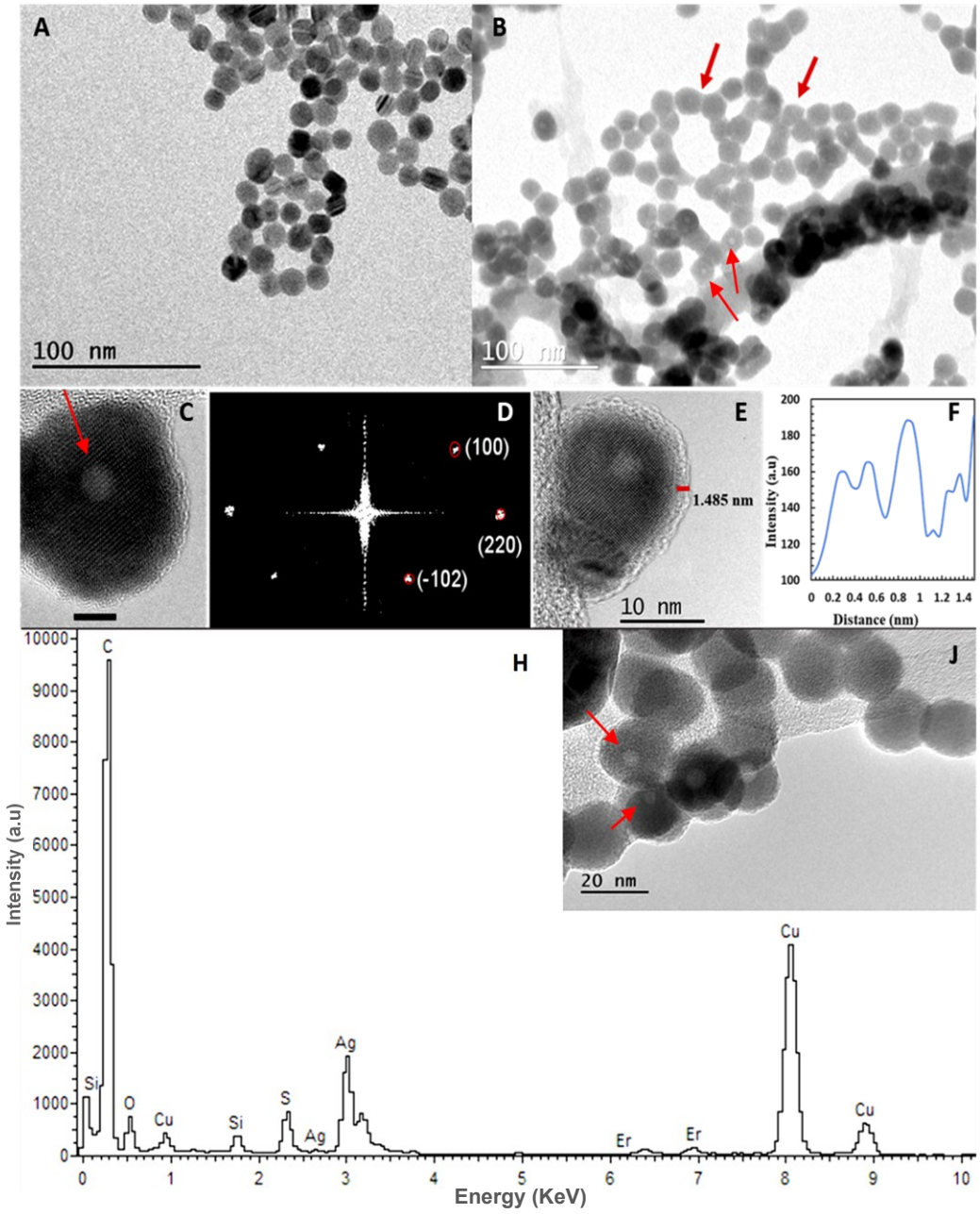

Figure 4-9:(A) Cit-AgNPs capped by citrate; (B) DF-TEM of Cit-AgNPs that had sulfided in the presence of HA-HS for 15 min; (C) HRTEM for the same particles (magnification = 500 kx and scale-bar = 5 nm); and (D) FFT showing that these particles were possibly hollow. (E) A layer of HA adsorbed onto the surface of NPs (magnification = 500 kx); (F) an intensity line profile collected across the red line marked in (E) to show the thickness and roughness of the adsorbed HA; and (H) the EDX spectrum for Ag_2SNPs-HA in the BF-TEM image in the frame (J) taken with a magnification of 200 kx.

Physiochemical characterisation was performed to investigate the properties of the transformed AgNPs. The absorption of the UV-vis spectrum indicated the establishment of AgNPs sulfiding in the presence of HA (Figure *4-10*), average hydrodynamic size, and zeta potential in (Table 4.1). The surface plasmon resonance band of AgNPs was observed at 400 nm (Figure *4-10*), confirming their spherical shape. The peak had a redshift from 400 nm to 410 nm and a slightly increased intensity, which confirmed the influence of HA on the stability of AgNPs and indicated the growth of particle size and aggregation [187].

Table 4.1 summarises the physiochemical properties of Cit-AgNPs before and after sulfidation. This information was compared to demonstrate the alteration of the average hydrodynamic size, polydispersity index, zeta potential, and the measured pH. This indicated the changing of chemistry and stability of the transformed AgNPs and illustrated the possible alteration that takes place during the sulfidation of AgNPs within the environmental conditions. The hydrodynamic size and zeta potential of AgNPs increased in magnitude from 24 ± 0.34 nm and -31.01 ± 2 mV to 35.02 ± 5.5 nm and -33.26 ± 2.4 mV, respectively. Compared with the HA-AgNPs, the sulfided AgNPs, in the presence of HA-HS^- , had a reduced absorption intensity and a small blue shift with a broader peak related to the formation of Ag_2SNPs-HA[191,192]. The same behaviour appeared in Ag_2SNPs-HA and HA-Ag_2SNPs, showing an increase in hydrodynamic size and stability after sulfidation. The indirect sulfiding particles had a larger size than the direct HA-Ag_2SNPs. The sulfided concentration of the same solvent volume was almost constant in all H_2S experiments because of the fixed parameter which are ambient temperature and system parameters. On the other hand, for the indirect sulfiding particles, the concentration of AgNPs in the volume 1.5 ml was higher than in 20 ml, so the ratio between Ag and S was different from indirect sulfiding, which explains the greater stability and higher negative value of zeta potential. Moreover, the distribution of Ag_2SNPs in (Figure *4-8*, D) and (**Error! Reference source not found.**, B) are different, illustrating the variation in the p article size where direct sulfiding particles are smaller than hollow-Ag_2SNPs particles.

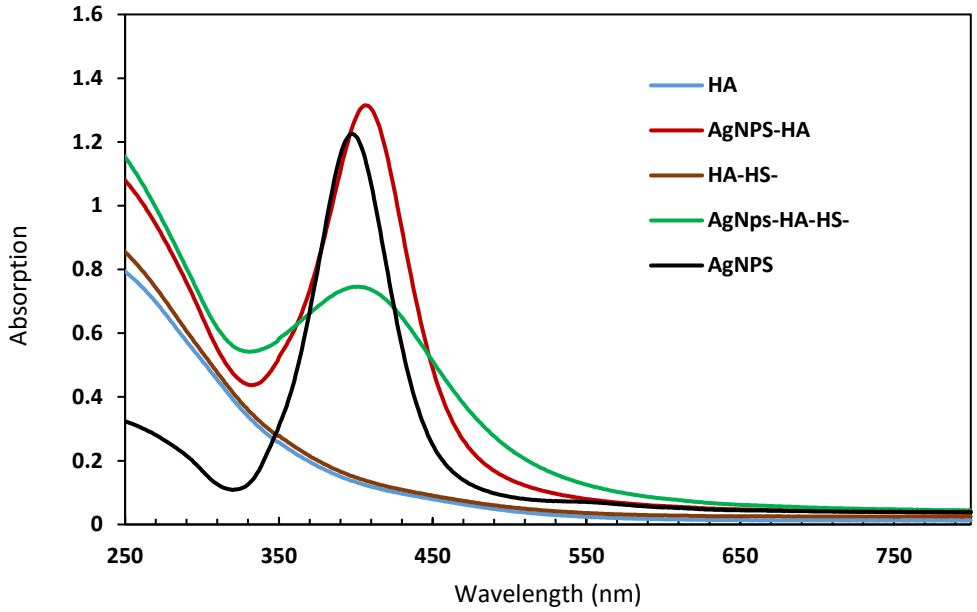

Figure 4-10:UV-vis spectra for the AgNPs and HA-AgNPs, before and after sulfidation, in presence HA-HS− (HA, and HA-HS− spectra shown for comparison)

Table 4-1:Hydrodynamic diameter and zeta potential of AgNPs in the presence of HA and HS-.

Materials	Average Hydrodynamic Diameter (nm)	PDI	ζ-Potential (mV)	pH
Cit-AgNPs	24 ± 0.34	0.47	-31.01 ± 2	6.7 ± 0.08
HA-AgNPs	35.02 ± 5.5	0.518	-33.26 ± 2.4	7.01 ± 0.05
HA-Ag_2SNPs (iv)	106.3 ± 10	------	-37.7 ± 1.8	6.6 ± 0.03
HA-Ag_2SNPs (ii)	42.7 ± 13	0.5	-40.7 ± 3.1	6.6 ± 0.5

*(iv) HA-HS^- indirect sulfiding was prepared, then AgNPs were added with a total volume 1.5 ml (ii) HA-AgNPs direct sulfiding was mixed before being introduced to H_2S, and the total volume was 20 ml.

Introducing the sulfiding mechanism is significant to understand the transformation of engineering nanoparticles in the natural environment and wastewater plant. Sulfidation of inorganic Ag_2NPs, as well as organic HA-Ag_2SNPs and Ag_2SNPs-HA, was accomplished through a reaction with H_2S gas in an oxygen-free system. The reaction of gas-solid between H_2S gas and bulk Ag is processed using the following equation:

$$2Ag + H_2S \rightarrow Ag_2S + H_2 \quad (4.4)$$

This reaction can take place when Ag is exposed to pure or dry H_2S which passed through by an inert gas, such as nitrogen or argon [188]. For our reaction, the water was present as a colloidal solution, which provided a suitable medium for the gas to be dissolved and then react with the silver. Thus, the sulfidation process followed the following equation[103,193]:

$$2Ag + H_2S + 1/2\, O_2 \rightarrow Ag_2S + H_2O \quad (4.5)$$

From the result of the Ag_2SNPs formation, Cit-AgNPs transferred directly to Ag_2SNPs *via* the diffusion of sulfide ions towards the core particle [103] which was checked after introducing a different concentration of H_2S gas by varying the exposure time within the same concentration and volume of Cit-AgNPs. The morphology of Ag_2SNPs had a monoclinic structure and spherical shape in DF-TEM micrograph, matching the AgNPs, and the citrate layer was notably adsorbed into the surface. The aggregation and dissolution of Ag_2NPs could be induced over time at room temperature.

The observation of HA-Ag_2SNPs was demonstrated by the influence of a lower molecular weight and a high concentration of humic acid. The sulfidation of HA-AgNPs showed bright and dark subgrains on the surface, which was considered a core-shell structure in the HRTEM analysis (Figure *4-9*, E). Also, the hollow sphere structure was found in both types of Ag_2SNPs, which usually formed after the core-shell structure, and before the totally sulfided particles. In contrast, the sulfidation of Ag_2SNPS as an inorganic nanoparticle was achieved as fully sulfided nanoparticles, notably faster than HA-Ag_2SNPs which act as organic coated nanoparticles. The slow rate of reaction can be explained by surface adsorption and ligand exchange of HA on the surface of the nanoparticles. It has been suggested that the binding of Ag ions and HA is stronger than that of fulvic acid [194]. It has also been shown that when citrate exchanges with HA and reacts with HS^- that forms high oxidised sulfur, it can facilitate sulfidation [104]. However, the peak of Cit-AgNPs before and

after introduced HA and HS^- observed differently comparing to the peak of AgNPs-HA which showed a slight red shift (10 nm) (red peak in Figure 4-10). The explanation for this shift might not provide strong evidence to support the citrate exchange hypothesis, especially given a high concentration of low molecular HA. It can bind to the absorbed citrate, which would significantly increase colloidal stability [103].

This can be confirmed by observing an acidic pH change after sulfidation, which could confirm the surface structure changes caused by the aggregation of particles. Also, an Aldrich humic acid stock solution contains Fe and S elements that are approved by ICP-MS, as mentioned in the above section. Therefore, when adding AgNPs to HA, some portion of AgNPs will be sulfided by the S ratio content in HA; then, Fe can cause releases of nanosilver. The formation of nanosilver from Ag_2SNPs was noticed within different waters, such as wastewater treatment plant effluent, landscape water, and river water. The investigation of this formation was investigated by TEM and EDS, which had found the presence of nanosilver that indicated their photoinduced from Ag_2SNPs in the existence of Fe (III) that may take place commonly in aquatic environments [195].

The transformation of Ag_2SNPs pathways within the presence of Fe in water can be summarised into two pathways in light and dark conditions when the reduction of Fe (III) to Fe (II) takes place, the release of hydroxyl radicals results, which significantly contributes to the dissolution of Ag_2SNPs by Ag ions, which are reduced to nanosilver by Fe(II) [195–197]. These proposed two steps of reactions are combined under the light condition and summarized in the following equations:

$$Fe^{3+} + H_2O \xrightarrow{hv} Fe^{2+} + \cdot OH + H^+ \quad (4.6)$$

$$2Ag_2S + 4 \cdot OH + 3O_2 \xrightarrow{hv} 4Ag^+ + 2H_2O + 2SO_4^{2-} \quad (4.7)$$

$$Ag^+ + Fe^{2+} \xrightarrow{hv} Ag^0 + Fe^{3+} \quad (4.8)$$

where equation (4.6) [195,196,198,199] indicates the photoreduction of Fe (III) that produces the hydroxyl radical in the light, which allows to dissolve Ag_2SNPs and generates sulfate in equation (4.7) [195,200,201]. The reduction of dissolved oxygen is remarkably noticeable than

in the presence of Fe (II), which would reduce the Ag ions to nanosilver in equation (4.8) [195].

While in the dark, the transformation Ag_2SNPs within the presence of Fe was postulated by the cation exchange reactions [202] rather than the oxidation pathway. The cation exchange reactions can occur between the metallic ions and metal sulfides because of the differences of the metal sulfides solubilities [203]. Li et al. proposed that the reaction between Ag_2SNPs and Fe (III) in the dark could remobilise the silver through cation exchange reaction. The reaction may result in the formation of Fe_2S_3, which is not stable; therefore, it will decompose to FeS [200] and follow a second reaction between silver ions and FeS to recombined Ag_2SNPs [106]. Since these reactions have to reach equilibrium in a short time, the silver ion concentration tends to remain constant [195].

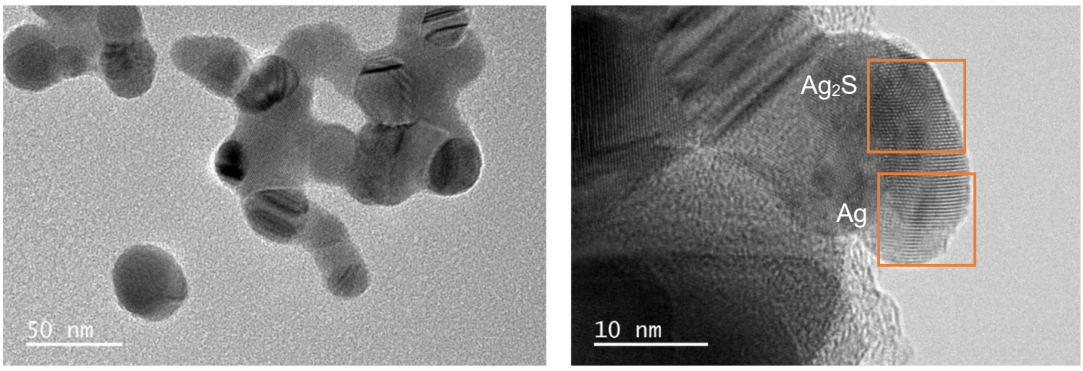

Figure 4-11: BF-TEM micrograph showing the sulfidation of Cit-AgNPs by *in situ* H_2S gas resulted in Ag/Ag_2SNPs heterostructure. The d-spacing for Ag and Ag_2S are 0.3091 ± 0.002 nm and 0.2864 ± 0.004 nm, respectively. The magnification of both micrographs in left 100 kx and right 600 kx.

The sulfidation of AgNPs is a kinetic process where the interaction of Ag and S will continue until it reaches equilibrium with no further reaction that can happen in controlled environments and parameters. In this work, Cit-AgNPs were *in situ* sulfided by H_2S gas, showing a different interaction from when AgNPs were exposed to H_2S gas, when AgNPs had previously been incubated in HA before sulfided, and when sulfided the AgNPs incubation them in HA-HS^-. For the inorganic Ag_2SNPs, which in this case no humic acid had involved, the formation of Ag_2SNPs can be explained by initiating redox cycling

reactions (Ag_2S-Ag, ion-Ag and metallic-Ag_2S). This reaction has been illustrated as *in situ* sulfidation in sulfur-rich environments in which Ag ions *in situ* form Ag metallic and then reformation Ag_2S. Therefore, the formation of Ag_2SNPs is a redox transformation that should be a nano-heterostructure of Ag/ Ag_2SNPs (Figure *4-11*). This can be explained by the fact that the core-shell structure of this interaction was not easy to stabilise for a long time in most of the repeated experiments with fully sulfided nanoparticles.

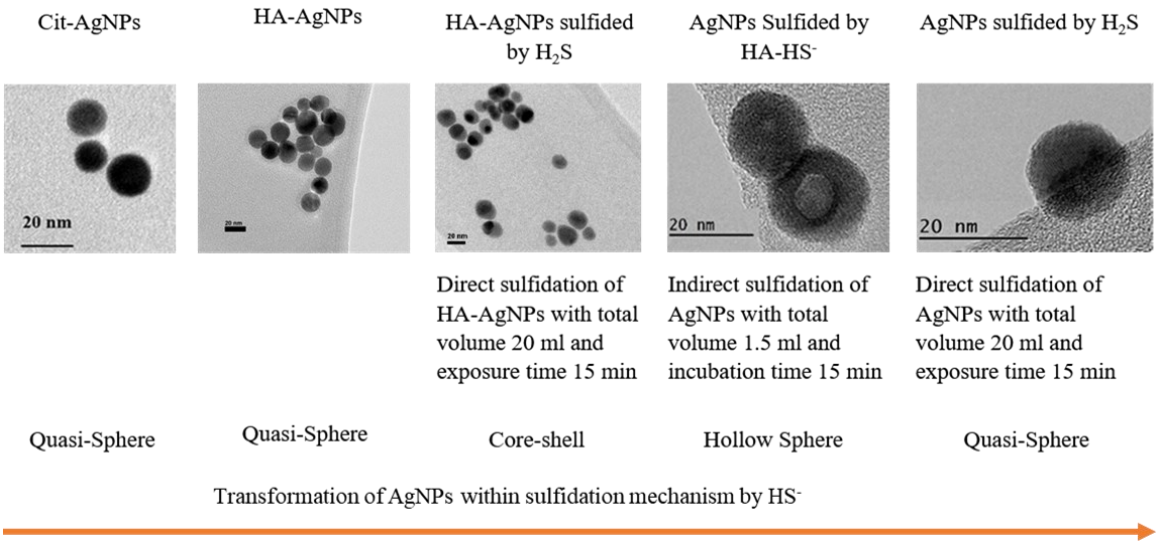

Figure 4-12: BF-TEM micrographs demonstrate the sulfidation of Cit-AgNPs to HA-Ag_2SNPs, which has emphasised the variation of nanoparticle shapes within the sulfidation mechanism by HS^-.

The sulfide AgNPs by HA^- can produce the whole structure illustrated in (Figure *4-12*). In this experiment, the lower molecular weight (MW) and high concentration (HC) of HA were used to identify both effects on the AgNPs structure (MW and HC) to describe the sulfidation process. As mentioned above, all the parameters maintained the same concentration of H_2S gas. Then, we changed how the AgNPs interact with HA-HS^-. The conclusion is that HS- absorption on the surface of AgNPs can stabilise and sulfide them at the same time. The mechanism is that reduced sulfur will bind to ionic silver, while the binding sulfur to the thiol group in HA will strongly bond to metallic silver. Then, by changing the sulfidation time or the concertation of AgNPs and HA-HS^-, the structure will change because it depends on the Ag/S molar ratio.

4.3.3. Part 2: Characterisation of synthesised Ag_2SNPs

4.3.3.1. Silver sulfide nanoparticle characterisation

The preparation of the Ag_2SNPs protocol was extended from the synthesized Cit-AgNPs to obtain a colloidal solution of Ag_2SNPs with a narrow size with two different ligands citrates and PVP. Also, a PVP-Ag_2SNPs colloidal suspension with a larger size than the above synthesis method was prepared. Figure *4-13* shows the morphology, SAED, and HRTEM acquired for PVP-Ag_2SNPs-20 nm, Cit-Ag_2SNPS and PVP-Ag_2SNP > 50 nm. In (Figure *4-13*, A-C), the PVP-Ag_2SNPs- 20 nm show an irregular quasi-sphere structure. For the electron diffraction pattern, all batches showed the same monoclinic structure of Ag_2S reported in (ICSD ref. 00-014-0072), as illustrated in (Table 4.2). Therefore, the HRTEM image of the interplanar distance 0.342 ± 0.001 nm represents the planar spacing for the (-111) orientation from the same reported structure of Ag_2S. Figure *4-13*, D-F for the Cit-Ag_2SNPs showed a more uniform quasi-sphere structure and indexing of the HRTEM images give a 0.281 ± 0.002 nm d-spacing for the plane (-112). The larger PVP-Ag_2SNPs was quite irregular compared to the smaller particles, as expected, for the growth of larger particles by chemical reduction methods, and the interplanar distance in HRTEM was measured to be 0.251 ± 0.007 nm, corresponding to the (022) plane in (Figure *4-13*, J-I).

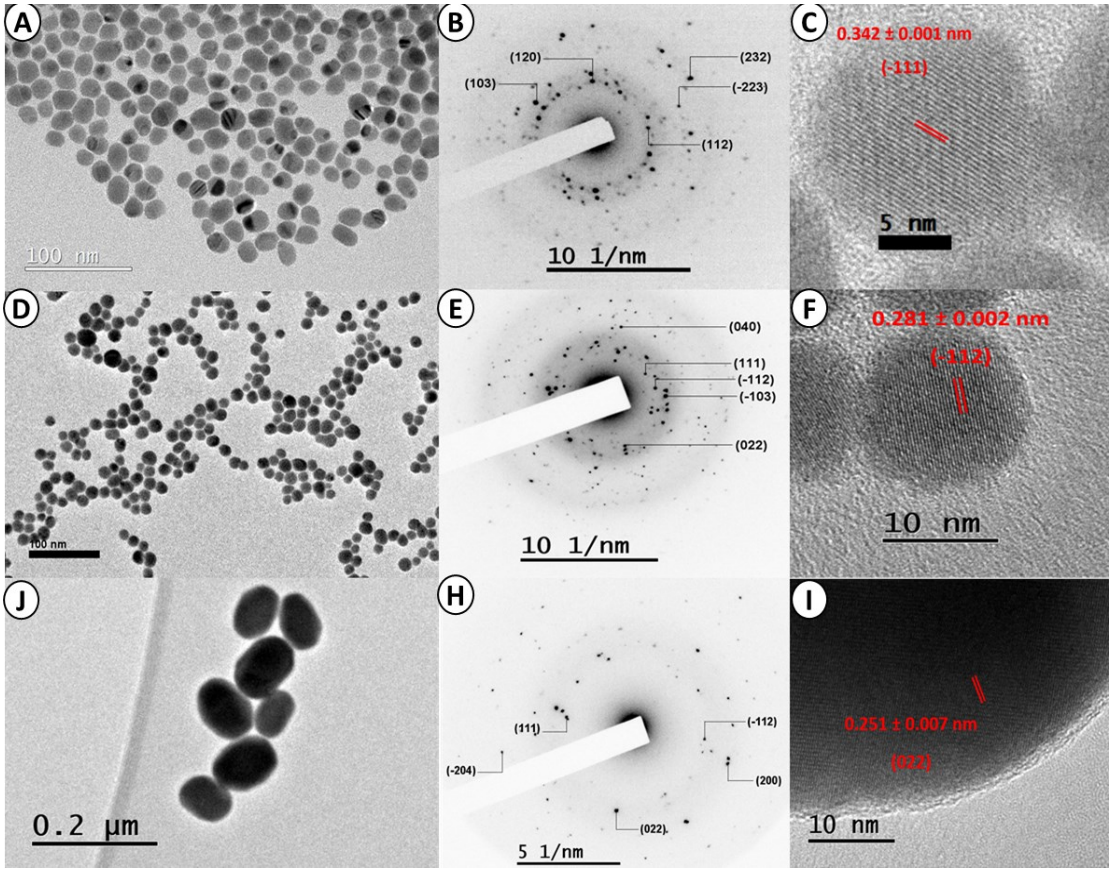

Figure 4-13: (A-C) the morphology acquired from TEM and the analysis of SAED and HRTEM images to identify the interplanar spacing of each synthesised PVP-Ag_2SNPs, (D-E) for the CitAg_2SNPs and (J-I) for PVP-Ag_2SNP > 50 nm with different protocols.

Table 4-2: : Interplanar distance of Ag_2S (acanthite) reported and measured from the selected area electron diffraction pattern of the synthesised Ag_2SNPs.

PVP-Ag_2SNPs			Cit-Ag_2SNPs			PVP-Ag_2SNPs > 50 nm		
hkl	Reported	Measured	hkl	Reported	Measured	hkl	Reported	Measured
	(Å)	(Å)		(Å)	(Å)		(Å)	(Å)
(120)	2.664	2.653	(111)	3.080	3.009	(111)	3.080	3.037
(112)	2.456	2.454	(-112)	2.836	2.812	(-112)	2.836	2.805
(103)	2.047	2.043	(-103)	2.383	2.356	(022)	2.583	2.597
(-223)	1.579	1.579	(022)	2.583	2.510	(200)	2.083	2.017
(232)	1.379	1.349	(040)	1.733	1.771	(-204)	1.554	1.553

Figure *4-14* shows the average size distribution found by measuring the size of 200 particles using ImageJ, which determined the average size of the length and the width of each particle for accuracy. PVP-Ag_2SNPs, Cit-Ag_2SNPs and PVP-Ag_2SNPs > 50 nm were 19.2 ± 3.4 nm, 16.45 ± 3.6 nm, and 85.44 ± 16. 45 nm, while the average hydrodynamic diameter was measured to be 29.16 ± 0.3 nm, 25.43 ± 1.2 nm, and 119.56 ± 3.1 nm. The average hydrodynamic diameter was identified by DLS, which confirmed a slightly larger diameter of the particles in colloidal solutions. The zeta potential (ξ) of the batches was -27.8 ± 8.1 mV, -33. 75 ± 2.6 mV and -18.53 ± 0.96 mV. According to these values, Cit-Ag_2SNPs are expected to be more stable. EDX spectra of the synthesised Ag_2SNPs colloidal solutions were analysed to show the content of silver Ag and sulfur S, which is close to the stoichiometric sulfide Ag_2S (but an excess of Ag is evident for smaller particles). The molar ratios of Ag to S in the EDX spectra, as represented in (Figure *4-15*) are ~ 2.4:1, 2.3:1, and 2.1:1.

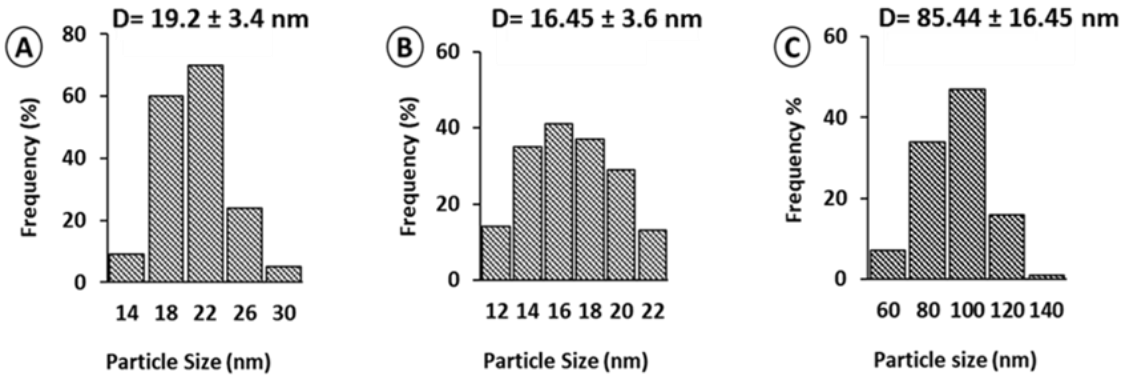

Figure 4-14: The average size distribution of nanoparticles diameter (D) with resulting values calculated by ImageJ software from TEM images (A)PVP-Ag_2SNPs, (B) CitAg_2SNPs, (C) for PVP-Ag_2SNP > 50 nm.

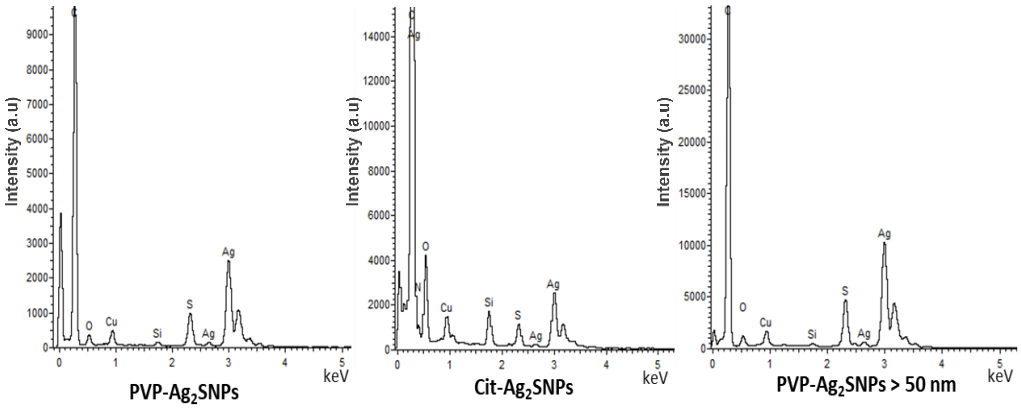

Figure 4-15: EDS spectra for the synthesised Ag_2SNPs.

The synthesis of Ag_2SNPs in a colloidal solution with different capping agents and sizes was achieved for further investigation. According to the SAED and HRTEM analyses, all batch structures confirmed the formation of monoclinic acanthite α-Ag_2S at low temperatures [184]. The target was to synthesise Cit-AgNPs and Cit-Ag_2SNPs with approximately similar sizes and stabiliser agents. Citrate has a small molecular weight and is used as a chelating agent containing three carboxylic acid functional groups that increase the negative charge on the surface of nanoparticles via electrostatic repulsion [204]. The stabilisation mechanism was formed through the binding of one or more oxygen atoms from the carboxylic acid functional group to the Ag ion. It was used as a complexing and stabilising agent to prevent agglomeration, due to the Ag surface adsorbing it during the

synthesis of Ag_2SNPs in colloidal solutions and nano-powder [74,205–207]. By contrast, PVP contains a polar group and a strong hydrophilic component (pyrrolidone rings), which work as a capping agent for dissolved metals *via* steric and electrostatic stabilisation [208]. The complex structure of PVP and Ag is introduced through the higher binding energy of PVP to Ag (100) facets and direct binding through oxygen atoms [209]. Because of the strong binding, PVP is considered a more efficient stabiliser for AgNPs than a citrate capping agent [204]. Therefore, a ligand exchange mechanism was carried out to obtain a small size of PVP-Ag_2SNPs. As noted in previous work, gold nanoparticles (AuNPs) with citrate stabilisation could be exchanged with PVP by immersing citrate nanoparticles in a PVP solution with a different concentration. However, they found that the process did not totally remove citrate due to the strong negative charge of zeta potential [210]. The same methodology was applied after the synthesis of Ag-AuNPs to eliminate reduction agents (citrate and tannic acids) before following up with washing steps that confirmed the stability and purity of the nanoparticles [207]. The stability of the Ag_2SNPs batches was significant; thus, a regular check was performed to observe the morphology changes during the storage conditions. It was noticed that higher stability was indicated for PVP- Ag_2SNPs, which have longer standing over time in the storage condition was PVP- Ag_2SNPs with the most significant size.

4.4. Summary

The synthesis of Ag_2SNPs with two different capping agents was achieved using a chemical bath method in the presence of nitrogen gas. The most stable species of silver sulfide nanoparticles over time was PVP-Ag_2SNPs (>50 nm) > PVP-Ag_2SNPs > Cit Ag_2SNPs, while the stability in solution was the opposite. The sulfiding of Cit-AgNPs by H_2S gas in an oxygen-free system with controllable parameters can help specify the gas concentration. Inorganic and organic Ag_2SNPs were sulfided through direct and indirect reactions with H_2S gas. The sulfiding mechanism was a direct sulfiding for both types of Ag_2SNPs. The morphology and crystal structure of Ag_2SNPs varied based on the rate of sulfiding and the adsorbed HA, which is considered a natural organic matter. The observation of transformed AgNPs is key for the bioavailability and toxicity of AgNPs when released to different environmental systems.

Chapter 5: The effect of engineered nanoparticles on the performance of an anaerobic digester focusing on the chemical transformation of zinc nanomaterials (ZnNMs)

5. The effect of engineered nanoparticles on the performance of an anaerobic digester focusing on the chemical transformation of zinc nanomaterials (ZnNMs)

5.1. Introduction

The field of ENMs has attracted the attention of the scientific community because of their rapid growth and their extensive applications, particularly in personal care and cosmetics. However, concerns have been raised about the impact of these particles on human health and the environment [211]. Depending on their application, ENMs enter the environment by different pathways, such as freshwater, WWTPs, sludge, and soil. This project investigates titanium dioxide (TiO_2), ceric dioxide (CeO_2), zinc oxide (ZnO), and silver nanoparticles (AgNPs). Due to their significant production volume and high risk of environmental exposure, ZnONPs and AgNPs were selected and investigated in a model anaerobic digester. ZnONPs have a vast range of applications, partly because of their unique antimicrobial properties; therefore, they are common toxic pollutants found in WWTPs [212,213].

Sewage sludge is the main products of wastewater treatment processes that had increased their production in 2009 and reached 1.2Mt of dry solids which mostly applied in agricultural land [130].Therefore, further treatment can be applied to sludge before disposal. Anaerobic digestion (AD) process is one of the various stages of WWTPs that can be applied to treat the sewage sludge and several kinds of organic wastes. This is a complex technology that widely involves microorganisms in converting organic matter into biogas such as methane which can be used as energy sources [214]. The AD process's performance depends on various parameters, including the temperature, pH, using organics waste as substrate, etc. The conditions of microorganisms have to be suitable to preserve a balance AD system [215]. These parameters are enhancing biogas production, which is the critical product of AD. The biogas production is mainly considered an indicator for enhanced AD system; therefore, the impact of ENMs on the AD system can be identified by the variation of biogas volume. Furthermore, the investigation of ENMs transformations as they are

discharged through a WWTP and accumulated in sewage sludge will allow us to understand their lifetime, fate and impacts in soils and freshwaters [11] as waste water sludge is a major pathway by which ENMs are released into these environments.

Anaerobic digestion is the common treatment process for sewage sludge, so the transformation of selected ENMs was studied within this system to identify their transformations and effects on its performance [7,11]. Several studies have investigated the transformation of ZnONPs in sludges. Lombi et al., studied the transformation of ZnONPs after anaerobic digestion and found that, after one hour, ZnONPs had fully transformed to ZnS. The same ZnS in wet sludge had transformed entirely to $Zn_3(PO_4)_2$ and Zn associated with Fe oxy/hydroxides after drying biosolids for 60 days under 37 ºC [11]. In another report, the fate of ZnONPs and AgNPs were studied during a pilot WWTPs. The speciation of both was determined in biosolids by XAS, which owed that Zn had transformed into $Zn_3(PO_4)_2$, ZnS, and Zn associated Fe oxy/hydroxides. The Zn species in the form of $Zn_3(PO_4)_2$ persisted in sludge and biosolids while ZnS and Zn associated Fe oxy/hydroxides had different ratios redox state and water content in the biosolids. The speciation of Ag and Ag_2S persisted in all treatment of the sludge [7]. In separate work, Zn speciation was examined within freshly produced and stockpiled biosolids. The speciation showed differences in the average ratio of Zn in both biosolid types by using linear combination fitting (LCF) of K-edge XANES. The ZnS was not found in the aged biosolids because of the presence of Cu sulfides, which has a higher kinetic stability [216]. However, XANES suggested a portion of Zn might be complexed by P, which is emphasised as hopetite $Zn_3(PO_4)_2$. Also, Zn can transform into Zn-substituted ferrihydrite and can be complexed by cysteine in aged biosolids [217]. In the present work, the impact of ZnNMs and AgNMs on the biogas production in anaerobic sludge were measured and compared and the speciation of ZnNMs after anaerobically digestion was characterised.

In this chapter, biochemical methane potential (BMP) assays were used to study the impact of ENMs on biogas production. This process uses a small amount of substrate with an inoculum of anaerobic microorganisms under mesophilic conditions [218]. The first part of the protocol compares the influence of a group of engineered ENMs on biogas production. A concentration of 10 mg/l of CeO_2NPs, TiO_2NPs, Cit-AgNPs, Ag_2SNPs (25 nm) and Ag_2NPs (100 nm) were added to the anaerobic digesters, except the ZnONPs concentration

that was 50 mg/l. The higher concentration of ZnONPs was used to investigate how their morphology and speciation changed after incubation in the sludge. Some difficulties were encountered because a phosphate buffer was initially used in the fixation step, but this buffer was avoided in later experiments. The experiment was designed to take samples after three hours of anaerobic digestion and at the end of the exposure (35 days). Therefore, the first part of the experiment compares the behaviour of the anaerobic digestion system following incubation with ENMs by measuring biogas generation over time. The same procedure was applied in the second part of the experiment by characterising the speciation of ZnONPs and ZnSNPs over the same time. The bulk transformation of ENMs were checked by ICP-Ms.

Scanning transmission electron microscopy (STEM) and elemental analysis via electron dispersive x-ray (EDX) were employed to investigate the transformation of ZnONPs and ZnSNPs – a transformation product of ZnO NPs - in anaerobic digester (AD) sludge. Low and high concentrations were applied to the sludges in this experiment; the lowest was about 5 mg/l, and the highest was greater than 50 mg/l. The high concentration was used to identify the speciation of these NPs by x-ray fluorescence (XRF) microscopy and to collect x-ray absorption near edge structure (XANES) spectra using a synchrotron beam. The high concentration can be considered to be the worst-case scenario. AgNPs and Ag_2SNPs – a transformation product of AgNPs - were also incubated with anaerobic digester sludge to understand their impact on the performance of the AD. These spatially resolved chemical mapping technique made it possible to study transformations of individual ENMs and variations between individual particles in the highly complex media of the sludges. This study the first study which links the transformations of Zn- and Ag-containing NMs to AD performance using real-world AD sludge.

5.2. Materials and Methods

5.2.1. Experimental design and the ENPs

Mesophilic anaerobic digested sludge (primary sludge or inoculum sludge) was collected from Agrivert, a local sewage WWTP in Oxford, UK. A diagram of the experimental setup found in (Figure 5-1), shows the mixing was done in anaerobic chamber with a flash of 95% N_2 and 5% H_2 gases. Before feeding the inoculum into the substrate (dried alfalfa [C3]), the inoculum's pH was adjusted to 7.4 using hydrochloric acid. The mixture of the

inoculum and the substrate depends on the calculation of volatile solids (VS), and the basic information for both is shown in (Table 5-1).

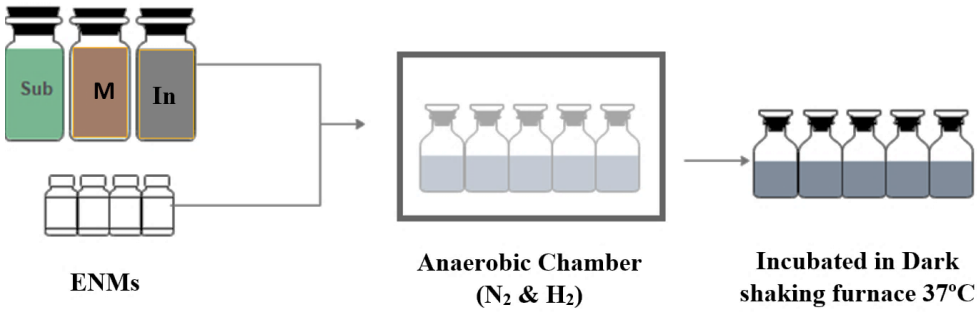

Figure 5-1: A sketch of the experimental setup for anaerobic digestion for sludge mixed with ENPs, where the first mixed stage includes the substrate (Sub), medium (M), inoculum (In), and colloidal solution of the ENPs.

Table 5-1: Characterisation of the primary sludge (inoculum) and the chemical composition of dried alfalfa leaf's plant as a dried organic waste or substrate.

Parameters	**Inoculum**	**Dried Alfalfa**
pH	6.5 (2nd experiment)	
Total solids (TS)%	0.0451	90.15
Volatile solids (VS)%	0.6722	90.66
VS (g/ml)	0.0291	—
VS (g)	—	0.145
TS (g)	—	0.16
S (amount of substrate in each vial) (g)	—	0.18
Solid/inoculum (S/I)	0.5	—
Inoculum/solid (I/S)	2	—

The inoculum and substrate were mixed first, followed by a mineral medium and the ENPs, all of which took place in glass serum bottles. A mineral medium can be considered as an artificial wastewater medium and was used to feed the bacteria in the inoculum for the assay of anaerobic digestion. This assay was prepared with deionised water (DIW), NH_4Cl, NaCl, $MgCl_2.2H_2O$, $CaCl_2.2H_2O$, Na_2HPO_4, $NaHCO_3$, cysteine, trace metals, selenite solution, and a vitamin mixture. Each of the ENMs and the control sample were prepared

in three repetitions in bottles sealed by butyl rubber stoppers with aluminium crimp caps and placed in a shaker-incubator that had been set at the mesophilic temperature of 37 ºC. Gas chromatography (GC) was used to detect biogas production.

Commercial ENPs and in-house NPs are used for the anaerobic digestion experiments; CeO_2NPs (< 10 nm), TiO_2NPs (< 20 nm), ZnONPs (10–30 nm), ZnONPs (80–200 nm) and AgNPs-PVP (20 nm) were purchased from United State (US) Research Nanomaterial, Inc.; ZnSNPs (> 100 nm) were purchased from Nanoshel, LLC, United Kingdom (UK); and Cit-AgNPs (20 nm), Cit-Ag_2SNPs (25 nm) and PVP-Ag_2SNP (< 100 nm) were prepared in-house. The stock of commercial NPs was 2000 mg/L, were prepared and sonicated one hour before the experiment and used within one to two hours. The stock suspension of some of the in-house NPs was concentrated to reach 250–300 mg/l, and the commercial NPs were diluted, and both the in-house and commercial NPs were sonicated before spiking them to the inoculum–medium mixture in the digester vial.

In the first set of experiments, CeO_2NPs (< 10 nm), TiO_2NPs (< 20 nm), ZnONPs (10–30 nm), Cit-AgNPs (20 nm), Cit-Ag_2SNPs (25 nm) and PVP-Ag_2SNPs (> 100 nm) were spiked into the AD sludge with the same concentration of 10 mg/l, except 57 mg/l was used with ZnONPs to investigate their transformation and compare their impact on biogas production. In this part of the work, the behaviour of the anaerobic digestion with ENMS samples was compared in the presence of the substrate. In the first experiment, it was challenging to find particles in the STEM images after digestion due to adsorption of NPs into the inoculum sludge and the embedding and staining sample preparation steps. Moreover, because phosphate buffer and uranyl acetate were used during the sample preparation for imaging after sampling, conclusions about the transformation of ZnONPs in sludge could not be draw from this experiment as artefactual Zn phosphate could have precipitated.

In the second trial, the goal was to study the effects of both low and high concentrations of ZnO NPs. The effects of the NPs on biogas production might not be as apparent for low concentrations in comparison to high concentrations so the higher concentrations were used as a worst-case scenario for the impact of the nanomaterials on the performance of an anaerobic digester. In this experiment, the anaerobic digestion samples were divided into two groups: with and without a substrate. The same sludge source, substrate, and mineral

medium was used with concentrations of 5, 50, 500, and 1000 mg/l for ZnONPs (80–200 nm) and PVP-AgNPs (20 nm). For PVP-Ag_2SNPs (> 100 nm), the concentrations were 50, 100, and 500 mg/l. Different concentrations to the volume of the anaerobic digitiser of Ag_2SNPs were used due to the lack of samples. Samples of ZnSNPs and ZnONPs (10–30 nm) with a high concentration of 500 mg/l were also digested in one serum bottle without adding the substrate separately to investigate their morphology and transformation within the anaerobic digestion period of 35 days.

5.2.2. Powder X-ray diffraction (XRD)

To identify the structural characteristics of the ENPs, powder samples were investigated using the Panalytical (X'Pert PRO) XRD machine. A sufficient amount of ENM dry powder was used without any further preparation; it was placed in the zero-diffraction reference substrate (SiO) and covered with Mylar film (approximately 3 μm). Mylar was used to avoid contamination and to ensure the safety of handling nanoparticles in the machine.

5.2.3. Fixation and staining of sludge anaerobic digestion.

After incubation and digestion, a mixture of sludge was obtained via a sterilised needle and centrifuged at 3,000 rpm for five minutes. Three washing steps took place for the pellets with a 0.1-M phosphate buffer (pH 7.4), then fixed in the same buffer and 2.5% glutaraldehyde for four hours at 4°C. The samples were washed three times with a 0.1-M HEPES buffer. After that, the pellets were stained using a mixture of 0.2-M HEPES, 1% osmium tetroxide (OsO_4) and 0.1% uranyl acetate (UA) for 48 hours before washing. After being washed three times with DIW, the samples were dehydrated with a series of graded ethanol (50%, 70%, 95%, and 100%) and washed with acetonitrile (Sigma Aldrich, UK). The samples were infiltrated with a resin-based on a Quetol, which was prepared by mixing 6 g of Quetol, 7.75 g of nonenyl succinic anhydride (NSA), 3.3 g of methyl acid anhydride (MNA), and 0.3 g of benzyl dimethylamine (BDMA) (Agar Scientific, UK). The samples were infiltrated with 50%, 75%, and 100% acetonitrile resin solutions freshly prepared each day. The embedded samples were set in pure resin under vacuum conditions before being cured at 60°C for 48 hours.

Fixation of the second batch of sludge was done using methods described in the literature [22]. In brief, 1 ml of digested sludge was centrifuged at 10,400 g for two minutes. Then, the

pellets were fixed with 3% glutaraldehyde for four hours, washed with a sodium cacodylate buffer (pH 7.4), and stained with the same buffer and 1% osmium tetroxide for one hour. After that, the pellets were washed with the same buffer. The dehydration of the samples was done with a series of graded ethanol. The same infiltrated steps (embedding and staining), as mentioned above, were applied to this batch. In this part of the experiment, the phosphate buffer and buffers containing phosphate were avoided in sample preparations for imaging to distinguish the phosphorus source within the sample from the inoculum sludge or medium. Furthermore, uranyl acetate emitted from the preparation protocol to avoid precipitation of Uranyl acetate in the presence of phosphorus [219]. This precipitation of phosphorus can affect the ratio of different zinc species since phosphorus can react with Zn^{2+} during transformation.

5.2.4. Morphology and elemental analysis of the anaerobically digested samples

Using an ultramicrotome, resin blocks of NPs in sludges were cut into 200-nm thick sections with a diamond knife in a water bath and collected onto 300 mesh copper grids, except for the Zn-based NPs. Gold grids were used for all the ZnNMs (ZnONPs and ZnSNPs) to avoid an overlap of 0.93 keV and 8.04 keV x-ray emission peaks with copper grids. The morphology and composition of features of interest within the samples was determined using a Jeol 2100F TEM operated at 200 keV connected to an Energy dispersive X-ray detector (Oxford).

5.2.5. Sample preparation for X-ray absorption spectroscopy (XAS)

The experiment was carried out using the Core XAS B18 Core XAS, which is a microfocus beam with a high flux versatile mullite-pole wiggler. The design of this beamline is based on three optical elements. First, a collimating Si mirror is placed 20 m from the beam source, which ranges from 2 keV to 35 keV. Second, a double crystal monochromator is used for fast scanning; it consists of two sets of crystals, Si (111) and Si (311). Then, a double toroidal mirror is placed 25 m from the beam source to focus the beam in both the horizontal axis and the vertical axis of the samples; the position of the mirror is fixed in both directions. In this experiment, the energy scan was selected to range between 6550 eV and 6850 eV. Each sample was measured in triplicate to determine the average and reduce the noise. For speciation studies on the transformation of ZnNMs within anaerobic digestion systems, samples were collected at three hours, 72 hours, and at the end of the digestion process at 35 days. Once collected and processed, the samples were prepared

using the protocol described above, and cut into 500-nm thick sections, then they were placed in triplicate onto (that uses a sodium cacodylate buffer) a low-stress silicon nitride (SiN) window with 200 µm, 5x5 mm frame and a 1000 nm, 2x2 mm window. All the windows with samples were placed in a holder to be aligned in the middle of the bath X-ray beam and were secured using Kapton polyimide foils (width about 80 µm). The normalisation of the XAS spectra was determined using Athena software.

Both anaerobic digestion experiments were conducted at Begbroke Science Park at the University of Oxford with the help of Dr Fariza Amman. Dr Fariza prepared most of the first part of the experiment at Oxford, and the samples were processed (embedding, staining, and imaging) in Imperial College of London ICL by the author. The second part of the experiment was prepared by both the author and Dr Fariza; all samples were processed (fixing and embedding) for imaging analysis by the author. For the beamtime experiment, samples were prepared by the author. Dr Mohamed Koronfel and the author visited the beamtime for the rest of the samples to investigate the speciation of the ZnONPs and ZnSNPs. Dr Mohamed Koronfel helped the author with the analysis.

5.3. Results and Discussion

5.3.1. Part 1: The anaerobic digestion of several ENPs

5.3.1.1. Characterisation of the ENPs

Both commercial and synthesised ENPs were characterised to identify their morphology, size and elemental composition before spiking them in anaerobic digestion vials. The characterisation of the morphology of the commercial CeO_2NPs, TiO_2NPs, ZnONPs (both sizes), ZnSNPs, and PVP-AgNPs was determined *via* bright-field TEM (BF-TEM). Some of the ENPs used in anaerobic digestion experiments required further syntheses, including the Cit-AgNPs, PVP-Ag_2SNPs (100 nm), and Cit-Ag_2SNPs (25 nm). This is mentioned in Chapter 4, while the commercial PVP-AgNPs characterisation is shown in the Appendix. Their characterisation was periodically checked before each experiment, and the physiochemical properties were the same as those mentioned in the results section of Chapter 4.

The commercial ENPs including TiO_2NPs and Ce_2ONPs, were characterised (Figure 5-2). The morphology and crystal structure were characterised by BF-TEM, which showed an spherical-cubic morphology with a tetragonal crystal structure (Figure 5-2, A) confirmed by selected area electron diffraction (SAED) (Figure 5-2, B). The average diameter of the TiO_2NPs was 25.1 ± 9.2 nm, measured from bright-field TEM images (n= 200 particles) (Figure 5-2, C). The XRD pattern in (Figure 5-2, D) confirmed a crystal structure of (Ref-00-021-1272), which is the same as that in the SAED. The EDS spectrum of TiO_2NPs is shown in (Figure 5-2, E) was performed to confirm their purity. Figure 5-2, F-J shows the characterisation of the CeO_2NPs, which confirms the cubic crystal structure in the SAED (Figure 5-2, G). The average diameter distribution of the CeO_2NPs was 19.3 ± 10.02 nm (Figure 5-2, H). The XRD pattern (Figure 5-2, I) had the same crystalline structure characterised by SAED (Ref-01-081-0792). The EDS spectrum result confirmed the presence of Ce and O only in the CeO_2NPs (Figure 5-2, J).

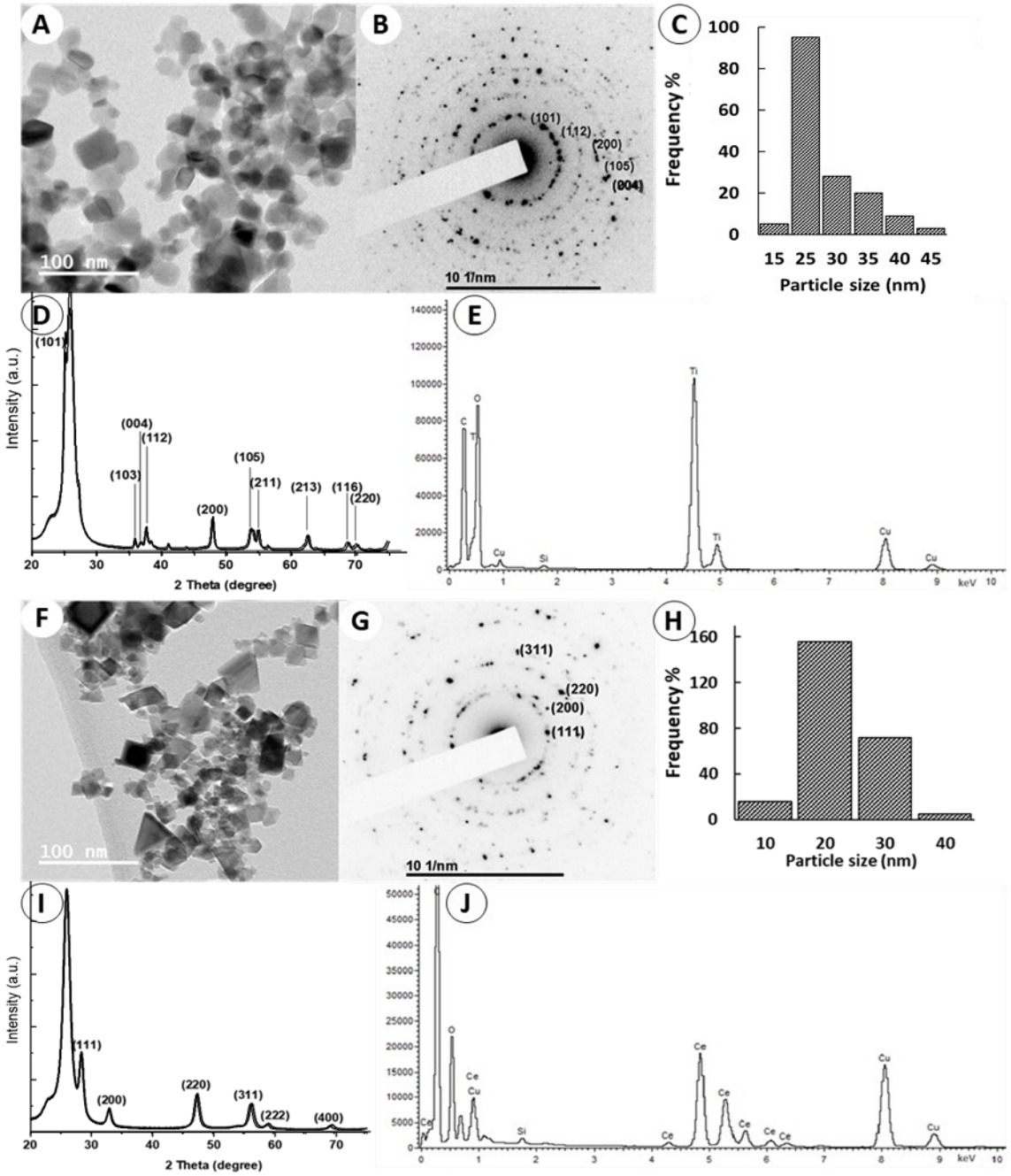

Figure 5-2: The physiochemical characterisation of pristine commercial TiO_2NPs (A-E) and Ce_2ONPs (F-J) before spiking in ADS. (A, F) The BF-TEM micrographs show the morphology of the SAED pattern of both commercial NPs (B, G). (C, H) The average size distribution of the TiO_2NPs and Ce_2ONPs was 25.1 ± 9.2 nm and 19.3 ± 10 nm, respectively, measured from (n = 200 particles) for several TEM micrographs by taking the average short and long dimensions of the structure (D, I) The XRD pattern of the NP powders indicates the Wurtzite hexagonal structure. (E, J) The EDS spectra for both BF-TEM images the CeO_2 NPs are phase pure.

5.3.1.2. The behaviour of anaerobic digestion within several ENPs

The parameters for the AD experiments were selected based on BMP assay guidelines, which had been tested by the collaborators at the University of Oxford. The ENPs were applied to their digester, which includes the same inoculum and substrate. The performance of the anaerobic digestion in the first batch was compared for the ENPs with the same concentration to show their impact under the same conditions. Variations in biogas production, pH, and VFA concentration were investigated. A higher concentration of ZnONPs was used to facilitate the imaging of these particles within the anaerobic sludge after incubation. The performance of ZnONPs at a concentration of 57 mg/l was compared to the 10 mg/l concentration of the rest of the ENPs, which are the AgNPs, Ag_2SNPs (25 nm), Ag_2SNPs (100 nm), TiO_2NPs (25 nm), and CeO_2NPs (20 nm).

Figure 5-3 shows the variation in pH for the inoculum incubated with the different ENPs during anaerobic digestion. In the first experiment, the pH was not adjusted, and the control was the pH of sludge after the samples were mixed with the medium for two hours incubation. The pH of all the ENPs and the control showed a steep decrease during the three days. The pH fluctuated between 7.58 and 7.9 within the control reactor, which illustrates that the ZnONPs had a minimum pH value after three days. The microorganisms in the anaerobic digestion function in different pH ranges. The methanogens process has been reported to be sensitive to a pH ranging between 6.5 and 7.5, with optimal pH values ranging between 7.0 and 7.2 [220]. The potential methane production has effectively operated in the range mentioned above of the optimal pH. However, the pH was reduced because of the formation of degradable mediates VFAs during digestion [221]. VFA is defined as a short-chain of carboxylic acids that contain one to five carbon atoms per molecule; it has a different formula depending on the number of carbon atoms [222].

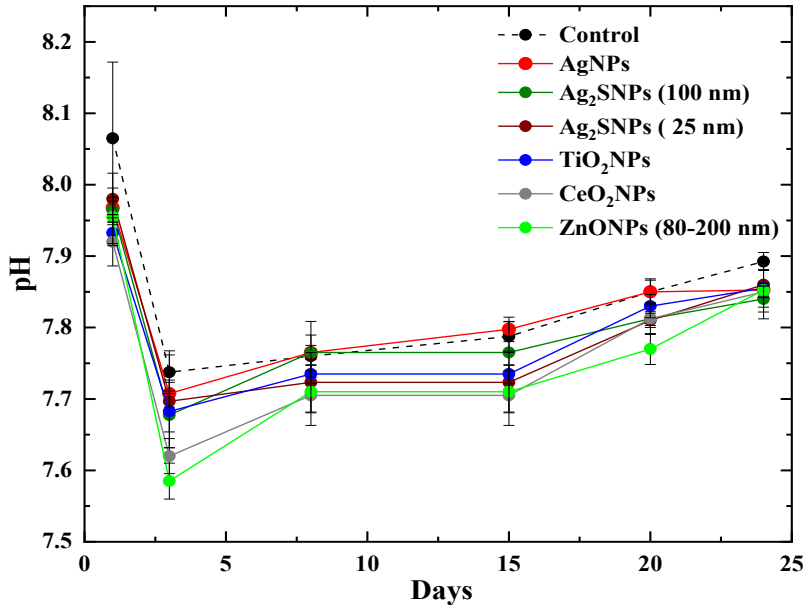

Figure 5-3: pH readings taken for AD inoculum sludge and artificial wastewater medium (control no ENMs) after incubation with AgNPs, Ag_2SNPs (100 nm), Ag_2SNPs (25 nm), TiO_2NPs, CeO_2NPs and ZnONPs (80-200 nm) at concentration of 10 mg/l except ZnONPs was at 57 mg/l after sampling time 3 hrs and 3,15, 20, 24 days.

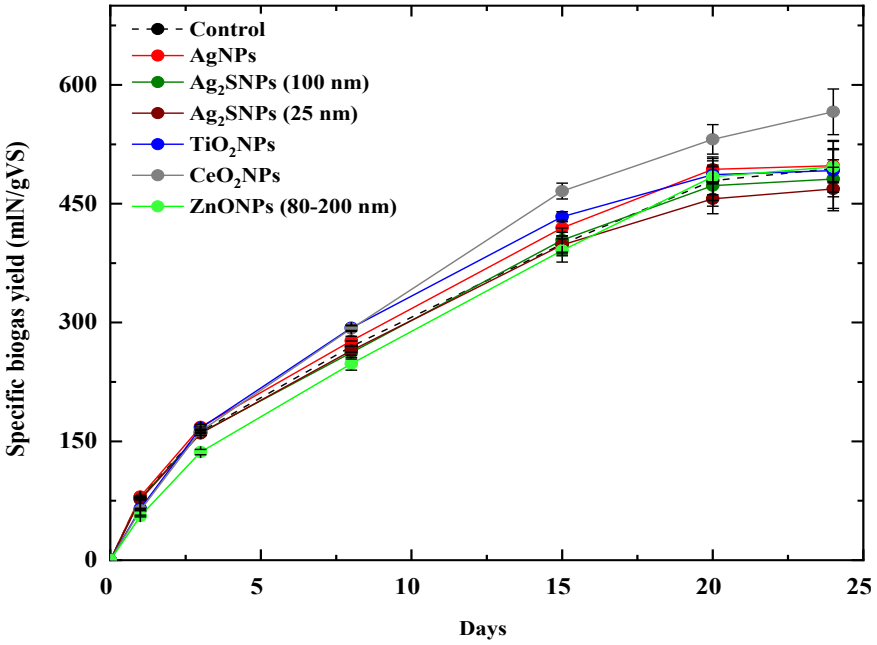

Figure 5-4: Specific biogas yield from AD inoculum sludge and artificial wastewater medium (control no ENMs) after incubation with AgNPs, Ag_2SNPs (100 nm), Ag_2SNPs (25 nm), TiO_2NPs, CeO_2NPs and ZnONPs (80-200 nm) at concentration of 10 mg/l except ZnONPs was at 57 mg/l over 3 hrs and 3,15, 20, 24 days for 24 days in total.

The effect of the ENMs on biogas production performance of the digested inoculum sludge within the substrate was measured. Figure 5-4 shows the specific yield of the biogas production for the control sample and all of the incubated ENP samples for 24 days, which was the last sampling time and the steady-state where no more biogas was produced. The specific biogas yield or the BMP assay is related to the volume of the biogases per the mass of the VS in the substrate, which is primarily organic matter. Almost all NPs enhanced the production of biogas in comparison to the control AD sludge with no NPs. Although the ZnONPs were added to the sludge in the highest concentration, the CeO_2NPs enhanced biogas production little more, but not very significant. D Nguyen et al. also studied the effect of CeO_2NPs and ZnONPs on biogas production at concentration of 10, 100, 500, 1000 mg/l mixed with AD inoculum sludge, deionised water and glucose as a sole source of carbon [223]. They showed that while both NPs had the same degree of inhibition towards biogas production, the reduction in biogas production was 65.3% for the ZnONPs with a concentration of 1000 mg/l and the production increased by 11% for the CeO_2NPs with a concentration of 10 mg/l [223]. The difference between this result and D Nguyen's work, the medium that they used deionised water with addition of glucose, while in this work artificial wastewater was used as medium. Here, comparison between ENMs with 10 mg/l and 57 mg/l of ZnONPs.

5.3.2. Part 2: Speciation of the ZnENMs during anaerobic digestion

5.3.2.1. Characterisation of the as-synthesised ZnONPs

Figure 5-5 shows the characterisation of different sizes of ZnONPs. The morphology of the small and large ZnONPs showed a uniform shape (Figure 5-5, A and F) and d-spacing indexed from the SAED to be the Wurtzite hexagonal structure. The hexagonal crystal structure of both sizes of ZnONPs was confirmed (Ref-00-005-0664) and (Ref -00-036-145), respectively. The average size of the diameters of the ZnONPs was 32.5 ± 10.1 nm and 164.38 ± 91.6 nm, respectively (Figure 5-5, C and H). The measurement of several NPs (n = 200) was obtained by taking the average length and width dimensions of each NP. The purity of the ZnONPs was checked by XRD and EDS to indicate the crystal structure and

elemental composition of the ZnONPs. TEM characterisation of the ZnSNPs shown in Figure 5-6 shows their irregular shape. SAED patterns confirmed they had a Wurtzite hexagonal structure, also characterised by EDS and XRD (Figure 5-6, B and D) (Ref-00-005-0492). The average size distribution histogram of ZnSNPs was 193.9 ± 74.4 nm (n=150 particles). EDS verified the composition of the NPs (Figure 5-6, C and E).

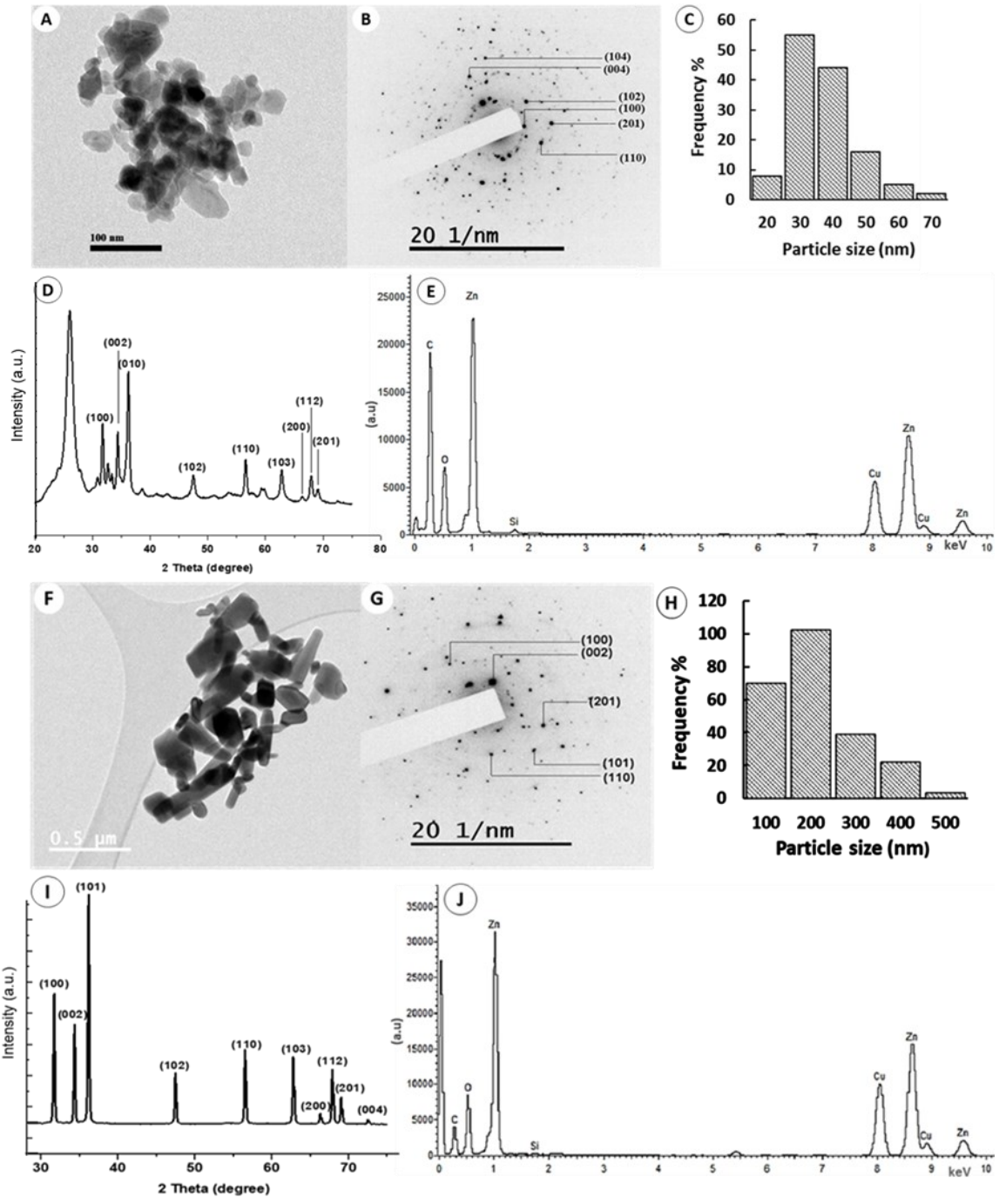

Figure 5-5:Physiochemical characterisation of pristine commercial ZnO NPs. Small ZnONPs (A-E) and large ZnONPs (F-J) before being spiked into the ADS. (A, F) The BF-TEM micrographs show the morphology of the ZnONPs. (B, G) The SAED pattern of the ZnO NPs. (C, H) The average size distribution of the ZnONPs is 32.5 ± 10.1 nm and 164.38 ± 91 nm, respectively (n = 200 particles). (D, I) The XRD pattern of both ZnONPs indicates that they have a Wurtzite hexagonal structure. (E, J) The EDS spectra for both BF-TEM images confirm that the NPs are phase pure.

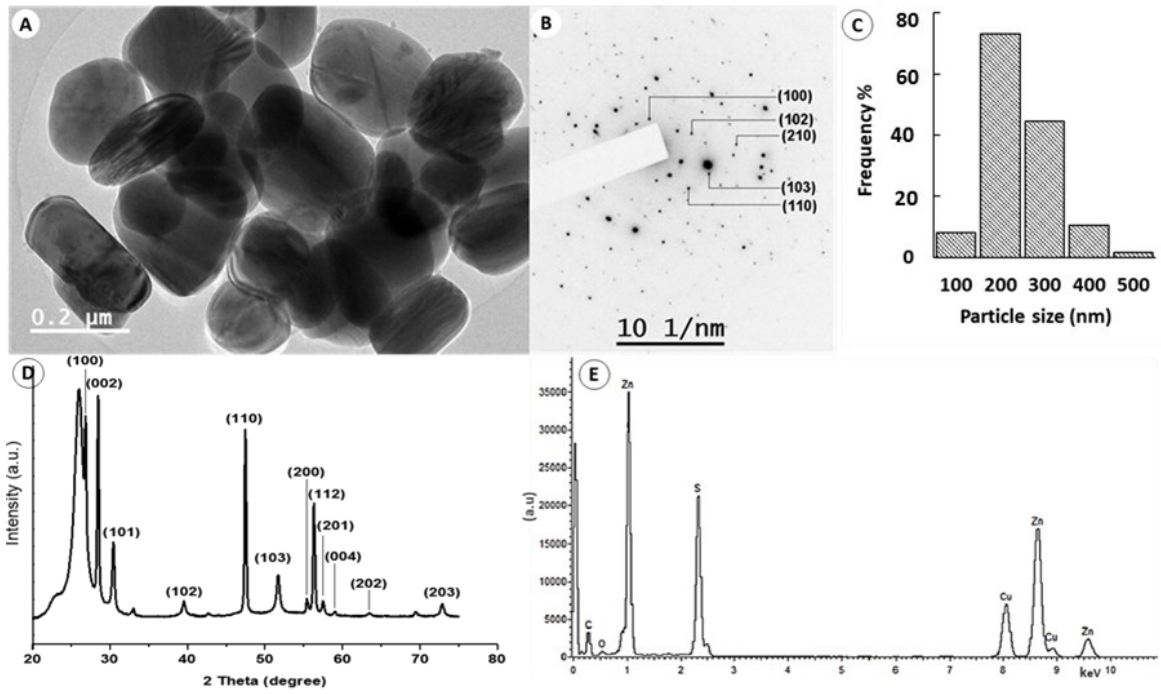

Figure 5-6: Characterisation of commercial ZnSNPs. (A) BF-TEM micrograph showing the morphology of the ZnSNPs. (B) The SAED pattern of the same area in (A) indicates their crystallinity and crystal structure. (C) The average size distribution was measured using ImageJ software. (D) The XRD of the powder pattern for the ZnSNPs which confirms the Wurtzite hexagonal structure. (E) The EDS spectra of the NPs.

5.3.2.2. The effect of Zn and Ag ENMs on the behaviour of the anaerobic digester

The pH readings of the digesters were measured following incubation of AD sludge with NPs at different concentrations during the digestion process. In this experiment, the pH was adjusted to 7.4 before digestion. Throughout the experiment, the pH was maintained between 6.8 and 8.25 under incubation in 37℃. Figure 5-7, A shows the pH of the digested

inoculum with ENMs and without the effect of the substrate. The pH ranged from 7.6 to 7.9 for the control sample and all of the ENMs, except for the ZnONPs at concentrations of 50 mg/l and 500 mg/l. The AD sludge showed different pH readings following incubation with both ZnONPs sizes in the first week before reaching stabilisation. The pH decreased in the 50 mg/l ZnONPs AD sludge in the digester, while the pH increased to 8.25 with the 500 mg/l ZnONPs. The behaviour of the control specimen with and without the substrate was compared to distinguish its influence on the biodegradation of organic matter. Figure 5-7, B shows that the control sample of (S+M) which digested inoculum sludge and medium has a pH of 7.9, while the control sample (S+M+Sub) which is digested inoculum sludge with medium and substrate has a pH of almost 7.6. The pH of most of the digested inoculum sludges incubated with ENMs ranged between 7.4 and 7.6. The same observation was shown for the changes in the pH of the AD sludge incubated with 50 mg/l and 500 mg/l of ZnONPs. For the digested inoculum sludge spiked with 50 mg/l ZnONPs, a decrease in the pH was confirmed after three hours, and then it increased on the third day. In contrast, the pH of the digested inoculum sludge spiked with 500 mg/l ZnONPs increased in comparison to the control (S+M+Sub) but decreased during the digestion process.

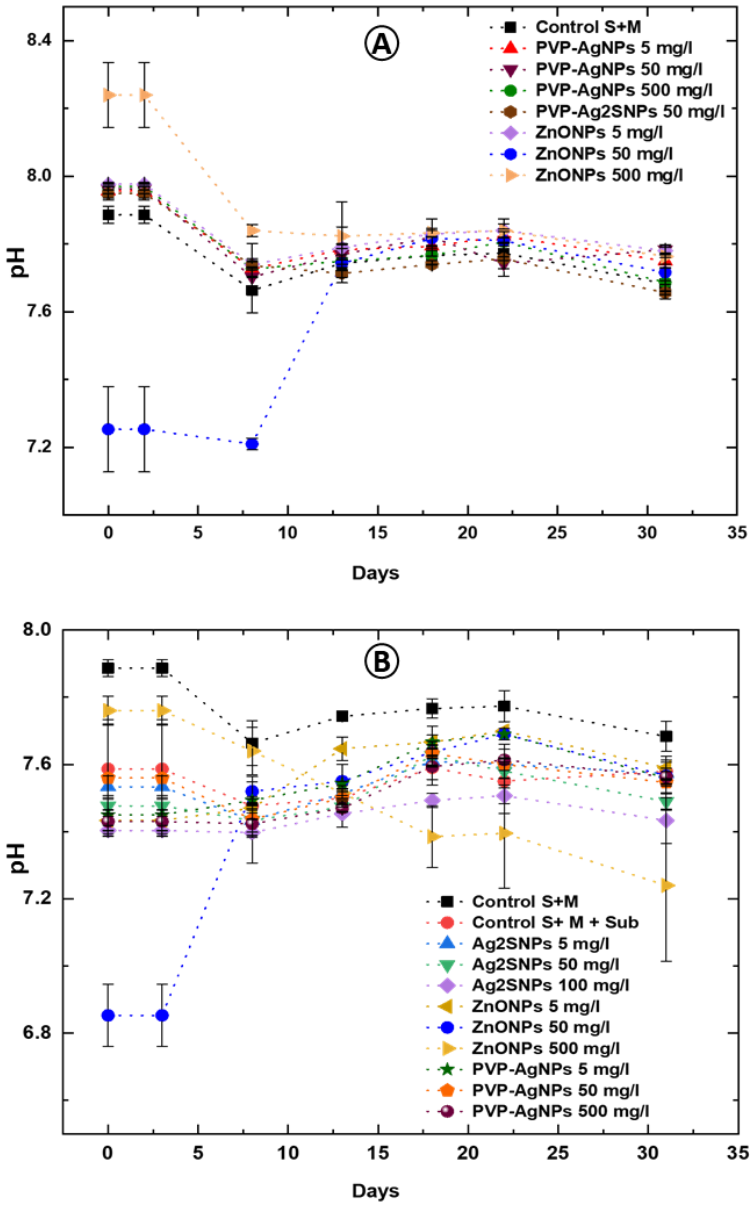

Figure 5-7: The pH of AD sludge incubated with ZnNMs and AgNMs. (A) the variation pH of AD sludge after incubation with different ENMs up 31 days without the addition of the substrate. (B) with the addition of the substrate.

Figure 5-8 shows the production of biogas in the anaerobic digestion system without the addition of the substrate. The comparison of different concentrations of ZnONPs (80–200 nm), PVP-AgNPs, and PVP-Ag_2SNPs demonstrates that the highest biogas production volume is for the 50 mg/l concentration of ZnONPs. The biogas increased by 90% during the two weeks before the system reached a steady state. Small percentages of biogas

production were shown for the 5 mg/l concentration of the ZnONPs. The PVP-AgNPs, PVP-Ag_2SNPs and the 500 mg/l concentration of ZnONPs were found to have almost the same trend as the control sample (S+M) digester in which no ENMs were added to inoculum sludge. The high concentration of ZnONPs could be more toxic to bacteria which affected the biogas production [223]. The system with no ENMs shows no biogas production enhancement during the entire period of anaerobic digestion, which is mainly inoculum and artificial wastewater medium. The same performance of no biogas is also observed for the high concentration of the ZnONPs and all concentrations of the Ag ENMs.

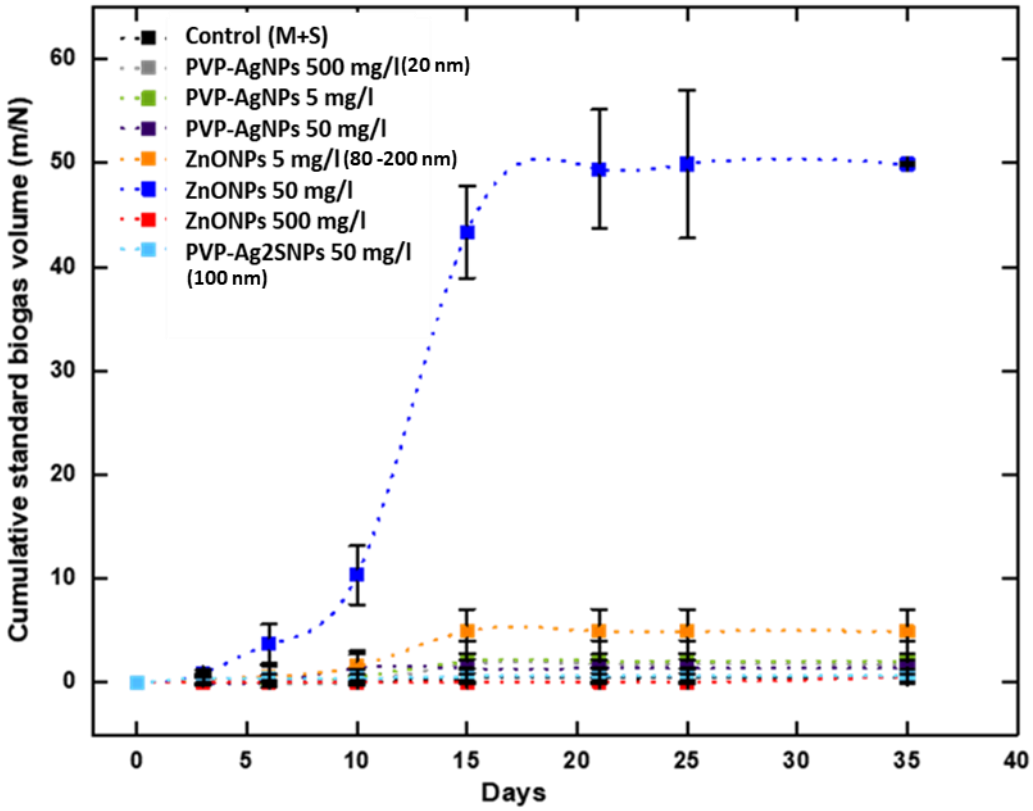

Figure 5-8*:* The total biogas volume measured in the incubated inoculum without the substrate and with different concentrations of ENMs in cases in which the entire digestion reactor was free from the substrate.

The performance of the digesters with the addition of the substrate was different from that of the digesters without the substrate. Figure 5-9 illustrates the total cumulative volume of biogas, which was compared between the different NPs with variations in their

concentrations. The resulting biogas production was confirmed based on the increase in the volume with the addition of the substrate. The greatest biogas production was obtained from the 50 mg/l ZnONPs samples. The middle region of the graph indicates a greater biogas volume after the addition of the ENMs with the presence of the substrate. This region contains inoculum sludge incubated with 5 mg/l of ZnONPs, 5, 50,100 mg/l of PVP-Ag_2SNPs and 5, 50, 500 mg/l of PVP-AgNPs. The PVP-AgNPs and PVP-Ag_2SNPs displayed almost the same range of biogas production, even with addition of substrate (which was used to enhance the biogas production). However, the inoculum sludge with substrate sample showed a decrease in biogas production after ten days and demonstrates a slight increase before the end of the experiment. The highest concentration of ZnONPs in each digester sample was the worst scenario; it stopped the biological degradation process performed by the anaerobic bacteria. During the organic matter biodegradation process, heavy metal compounds are unable to degrade; therefore, these compounds can accumulate and potentially be toxic to anaerobic compounds [224,225]. The impact of ZnONPs on AD system was reported to be dosage dependent and associated with release of Zn^{2+} which affected the methanogenesis and hydrolysis reactions in the AD process [226].

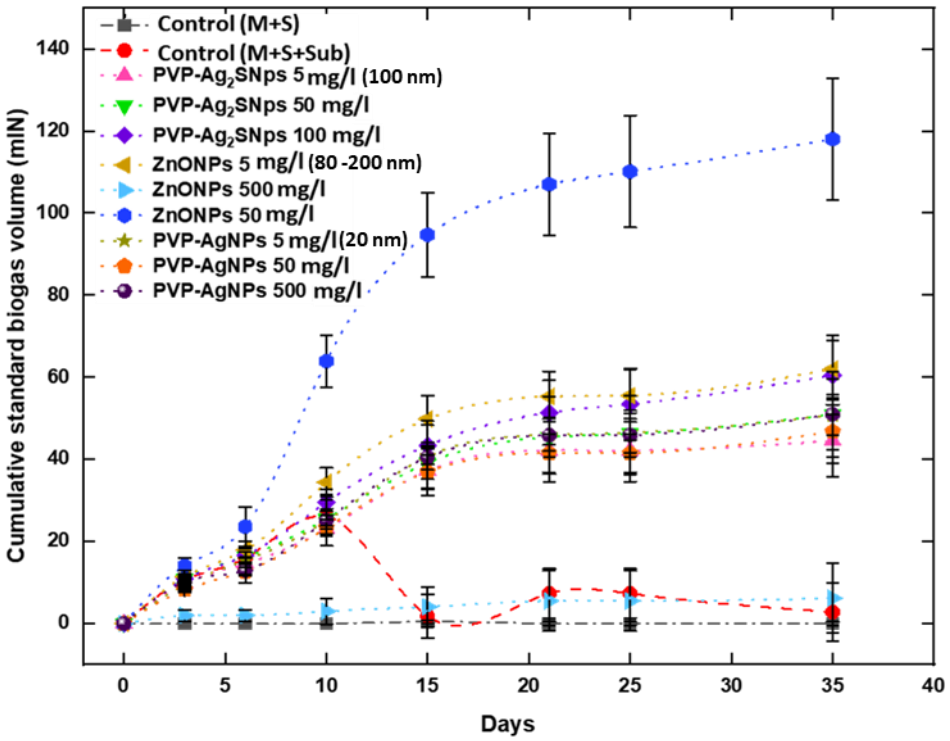

Figure 5-9: The total biogas volume measurement of the incubated inoculum with the substrate and different concentrations of ENMs, compared to the inoculum sludge control

sample without the substrate or the ENMs, described as the control with no ENMs and AD sludge with the substrate.

Since the ZnONPs had the greatest on biogas production in the AD system, their chemical speciation was studied by XANES to contribute to an understanding of how they degrade and transform chemically. This knowledge will help to predict their lifetime and changes to their bioreactivity during the AD process. To utilise the XANES technique, reference of Zn compounds were used to identify transformation products, these included ZnS, $Zn_3(PO_4)_2$ and Zn adsorbed onto Fe oxy-hydroxides (Zn-Fe (ox)).

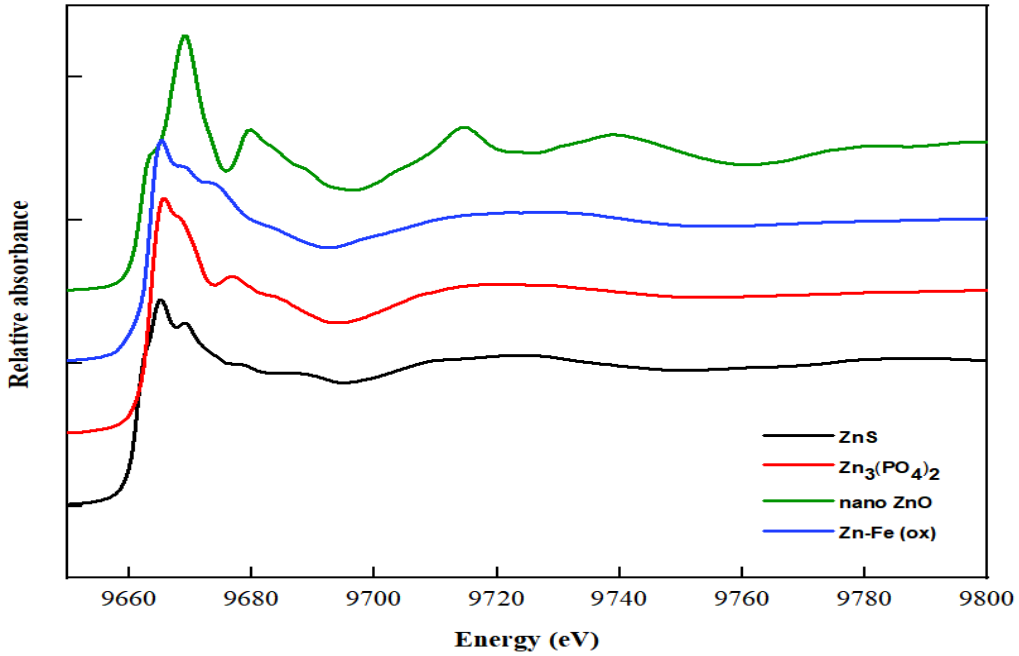

Figure 5-10: XANES spectra for ZnS, ZnONPs (nano size), $Zn_3(PO_4)_2$ and Zn adsorbed onto Fe oxy-hydroxides (Zn-Fe (ox)) standards to determine the speciation of Zn after digestion – selected using reference [185].

The reference material series of nano ZnO (80-200 nm, US-nano), bulk ZnO, ZnS, and $Zn_3(PO_4)_2$ and Zn adsorbed onto Fe oxy-hydroxides (Zn-Fe (ox)) were selected to determine the speciation of Zn after digestion. These references were measured in transmission, and have been previously described in the literature [7,227]. The XAS spectra of

these compounds are the reference materials shown in Figure 5-10. The resulting spectra of each Zn compound and incubation period in the digester were analysed by linear combination fitting (LCF).

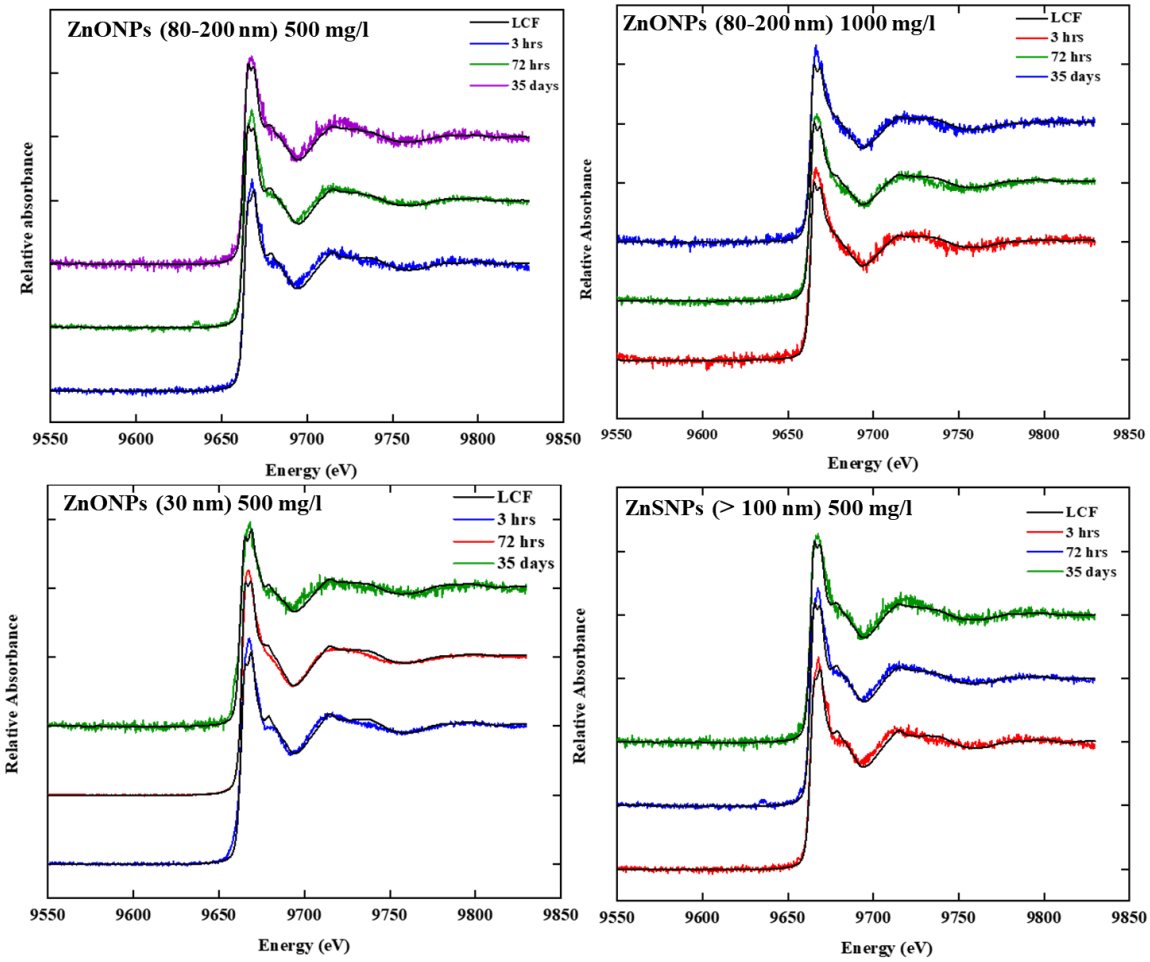

Figure 5-11: The XANES spectra of ZnONPs (80- 200 nm) for concentrations of 500 mg/l and 1000 mg/l) ZnONPs (30 nm of 500 mg/l) and ZnSNPs (> 100 nm, 500 mg/l). Their combinations were fitted and compared with the incubation time of anaerobic digestion.

The samples were fitted according to the expected Zn species and compared within the incubation time (Figure 5-11). As shown in this figure, the XAS spectra fit the combination of all the samples, and each sample is compared at each incubation time to evaluate the speciation of Zn as percentages. The resulting percentages of each sample are shown as pie charts in (Table 5-2).

The changes in the quantity of Zn speciation varied for the same ZnONPs (80–200 nm) at different concentrations of 1000 mg/l and 500 mg/l. For a concentration of 1000 mg/l of ZnONPs (80–200 nm), the highest quantity of Zn species was Zn-Fe (ox) during the digestion process for 35 days. Other Zn species, $Zn_3(PO_4)_2$, and ZnS were measured, and about 16 % of the ZnONPs had not transformed after 35 days. For the concentration of 500 mg/l of the ZnONPs (80–200 nm), after the incubation of 3 hours in the AD system, 19% of ZnONPs had not transformed, while 29 % were sulfided to become ZnS and the rest were $Zn_3(PO_4)_2$ and Zn-Fe (ox) sharing the same percentages. After 72 hours, more sulfided Zn was observed and there was a reduction in the contribution of Zn-Fe (ox). The AD process ended with the most of ZnONPs turning to Zn-Fe (ox) and ZnS, respectively.

For the ZnONPs (30 nm) at 3 hours in the AD sludge, there were similar transformations to the ZnONPs (80–200 nm) at concentration of 500 mg/l. At 72 hours, the contribution of $Zn_3(PO_4)_2$ had increased from 23 to 48% and the contribution of ZnS has disappeared, after 35 days the contribution of ZnS had increased again to 39% and all of the Zn phosphate had disappeared.

The transformation of ZnSNPs after 3 hours turned into 32 % of $Zn_3(PO_4)_2$, 32 % of Zn-Fe (ox) and 26 % of ZnONPs. After 72 hours, the Zn-Fe (ox) species had disappeared while 60 % $Zn_3(PO_4)_2$ and 23 % ZnS species were measured. At the end of digestion system, 11 % of Zn-Fe (ox) had appeared and the majority species was $Zn_3(PO_4)_2$ with slight changes of percentages between ZnS and ZnO species.

Table 5-2: Pie charts illustrating the percentages of Zn speciation for the ZnONPs with 80-200 and 30 nm diameters and ZnSNPs following anaerobic digestion without the substrate for 3, 72 hours and 35 days.

	ZnONPs (80-200 nm)- 1000 ppm	ZnONPs (80-200 nm)-500 ppm	ZnONPs (30 nm)-500 ppm	ZnSNPs (< 100 nm)-500 ppm
3 hrs	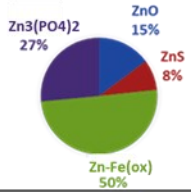	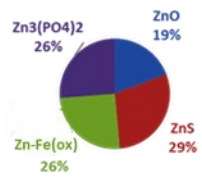	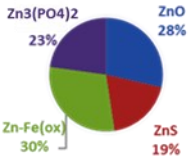	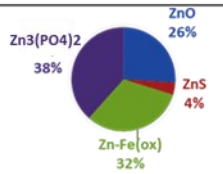
72 hrs	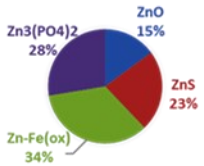	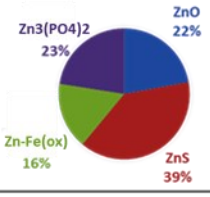	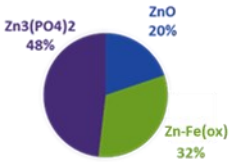	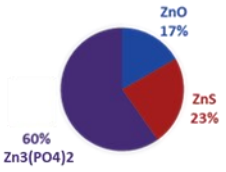
35 days	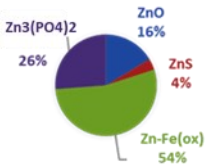	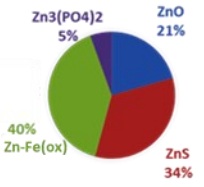	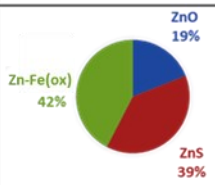	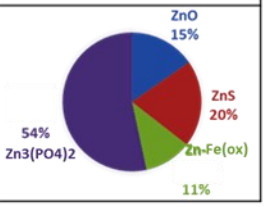

To sum up, larger 80-200 nm ZnO NPs transform to a greater extent to an intermediate ZnS phase than the smaller ZnO NPs that transform to an intermediate Zn phosphate phase instead, but the composition of the end products at 25 days are approximately the same. The ZnSNPs transformed very rapidly to Zn-Fe (ox) and Zn phosphate and surprisingly back to ZnS phase. The performance of AD within ZnONPs (80-200 nm) was investigated at concentration 50 mg/l which had increased the biogas production.

5.3.2.3. Ex situ microscopy

Dark-field TEM micrographs elucidated the morphology and chemistry of the ENMs after digestion. The ENMs studied by TEM were the ZnO NPs that that had transformed in the XAS study. The morphology of the ZnONPs and ZnSNPs that were incubated without substrate was imaged. Figure 5-12 shows dark-field TEM images of ZnONPs (80–200 nm) incubated in AD sludge at a concentration of 500 mg/l for three hours in the digester. In the HAADF-STEM image, bright nanosized particles were observed within the complex matrix of the sludge (Figure 5-12 B). These nanoparticles had different forms, some were diffuse, and others were more solid, and the different particles associated with different

structures within the sludge. The EDX spectral maps from the nanoparticle in the boxed region showed that a particle containing Zn and O which is more intense in the core than the P signal. The EDX spectrum in (Figure 5-12 F) show the total elements in the selected region which had some elements from background.

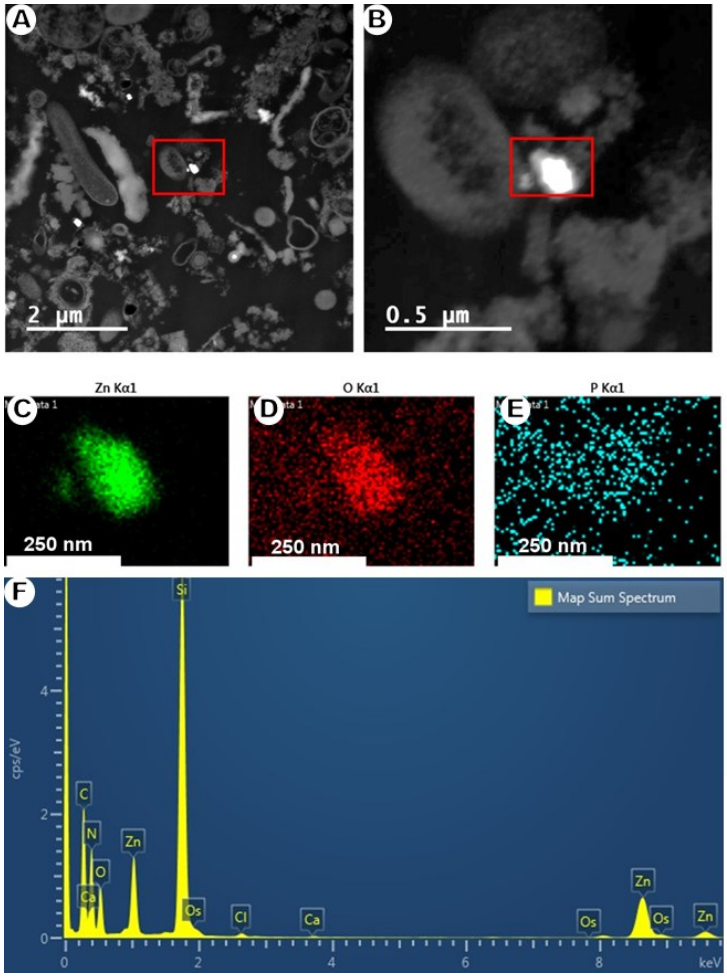

Figure 5-12: HAADF-STEM images (A) and (B) high magnification STEM image of the boxed region in a and STEM EDX maps (C-E) and EDX spectrum (F) of NPs in the boxed region in (B) for the ZnONPs (80–200 nm) incubated in AD sludge for 3 hours at a concentration of 500 mg/l.

HAADF-STEM images and EDX spectral maps of the ZnSNPs incubated in AD sludge for three hours are shown in (Figure 5-13); and incubation after 35 days is shown in (Figure 5-14). After 3 hours, nanoparticles that were predominantly Zn and S were imaged and mapped chemically. STEM-EDX maps also showed trace amounts of O, P and Fe co-

located to these nanoparticles after 35 days agglomerates of ZnS particles were observed associating with a less dense diffuse structure within the sludge. These nanoparticles had similar chemistry to the particles mapped at 3 hours, but after 35 days it shows more intense P and less Fe (Figure 5-14).

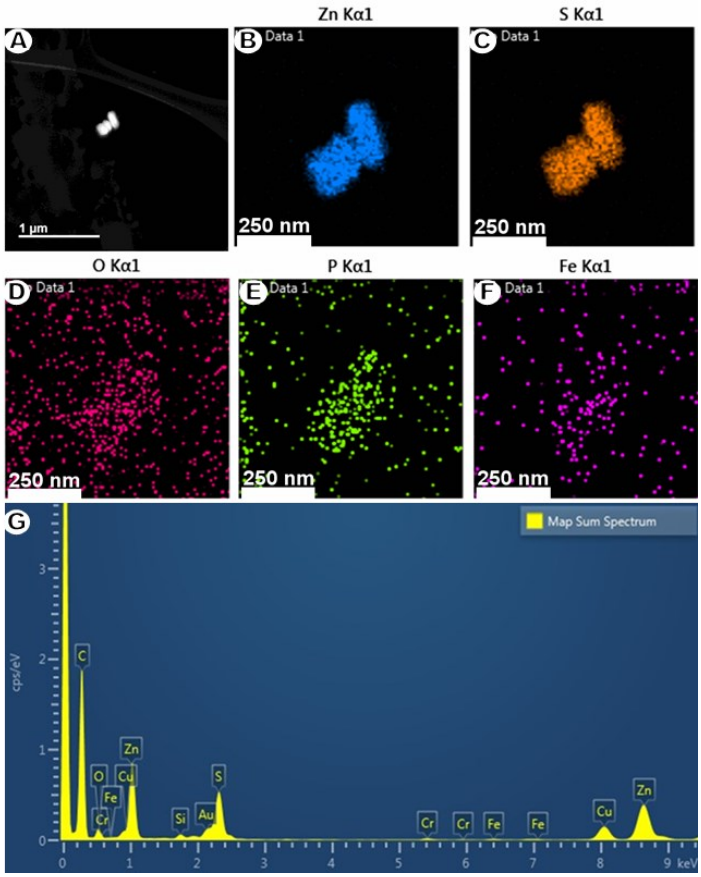

Figure 5-13: (A) HAADF-STEM image, (C-F) images corresponding STEM-EDX maps and (G) EDX spectrum showing ZnSNPs incubated for three hours in sludge under anaerobic digestion.

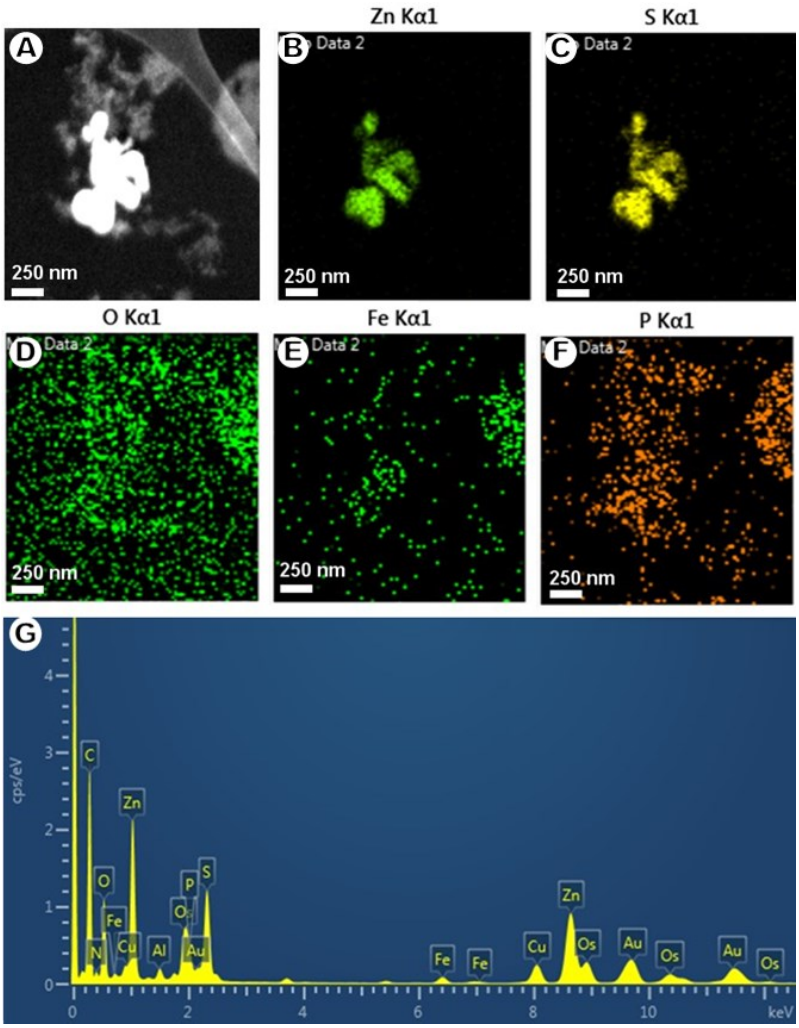

Figure 5-14: (A) HAADF STEM images showing an agglomerate of ZnONPs (30 nm) with a 500 mg/l concentration incubated for 35 days under anaerobic digestion. (B-F) STEM EDX chemical maps showing the composition of the nanoparticles in (A).

Figure 5-15 shows the morphology of the chemically transformed ZnONPs (30 nm) after 35 hours, at the end of the anaerobic digestion process and the distribution of elements within a ZnONPs structure. The HAADF-STEM images reveal the morphology of the core-shell structure of the selected area. The elemental analysis according to STEM-EDX maps show the presence of S, P and Fe associated with the ZnONPs. These elements are related to the phases of Zn-rich ENMs. The ZnONPs had partially transformed to ZnS with P and Fe on their surface. The size of transformed ZnONPs are larger than its pristine counterparts.

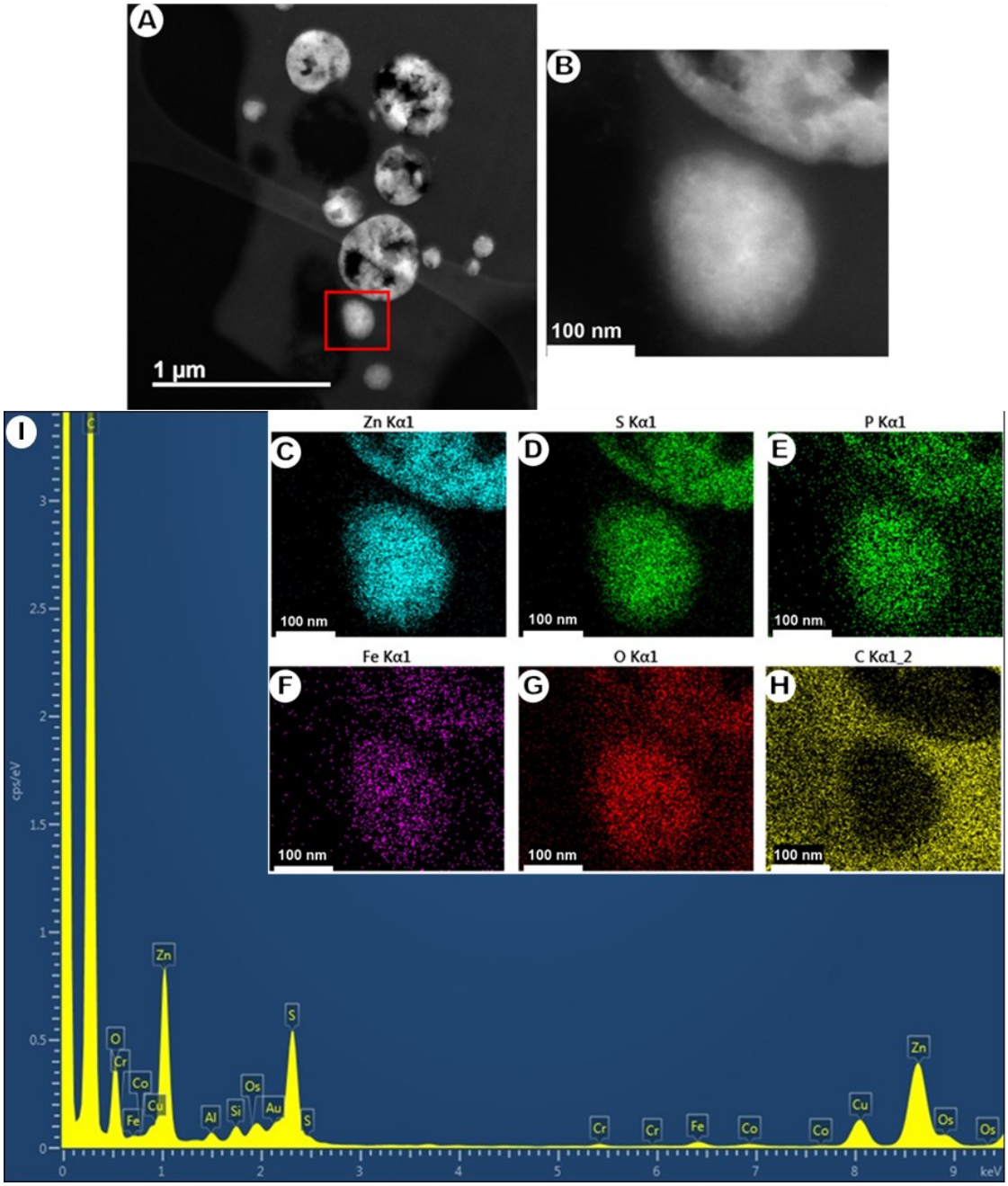

Figure 5-15: (A) HAADF STEM images showing ZnONPs (30 nm) with a 500 mg/l concentration incubated for 35 days under anaerobic digestion. (B) High magnification HAADF-STEM image of the boxed area in A. (C-H) STEM-EDX chemical maps showing the composition of the nanoparticles in (B). (I) EDX spectrum.

5.4. Discussion

This experiment used anaerobic digesters to investigate the performance of ENMs and focus on evaluating the performance, chemical transformation, and morphology of Zn ENMs. Comparison of the effect of different ENMs on biogas production performance showed that the ZnONPs (80–200 nm) with a 50 mg/l concentration had the most significant effect. The addition of ZnONPs to inhibit biogas production has been shown previously to be dependent on the dosage given to the AD sludge [226]. Using a higher concentration of 1000 mg/l of ZnONPs (80–200 nm) had no significant impact on biogas production, probably because the high load of Zn ions released deactivates the bacteria in the anaerobic digester. This is due to the production of reactive oxygen species (ROS) and the presence of the Zn^{2+}during digestion [226].

The low concentration of ZnONPs did not have a significant change on the biogas production, which has also been reported in literature [226]. The reason for this is that the sludges contain sulfate that had bio-converted to sulfide with Zn^{2+} under anaerobic digestion condition. Therefore, the toxicity of Zn^{2+} would reduced towards the bacteria [226].

In other work, the addition of ROS scavengers to the digestion system increased the biogas production of the ZnONPs digester [228]. The release of ROS can cause oxidative stress or peroxidation of the cell membrane, then imbalance in homeostasis of cell compartments leads to cell death. The higher dose of ZnONPs within the AD system can release higher $Zn^{2+,}$ which inhibited methane production [226].

In previous work, the effects of an additional substrate or organic waste on the digester were investigated: biogas production was higher with a substrate than, which could be attributed to the trace elements in the substrate that accumulate and induce degradation and phytotoxicity [148,229–231]. The organic substrate content can be converted into biogas because of their chemical composition and biodegradability, which are the main contributors to methane and biogas productions. The plant's substrates are rich in carbohydrates, commonly sugar, mostly used as food waste. These substrates can easily be decomposed by methanogenic communities, which responsible for volatile fatty acids [232]. The ENMs can be utilised as the substrate to enhance biogas production. Many parameters can affect the biogas production related to the microorganism community, such as the temperature, pH, chemical oxygen demand (COD), the carbon/nitrogen ratio (organic waste), and

nutrients. These factors support the growth and metabolism of the microorganisms. The greater biogas production better optimises the AD process [233].

The transformation of these particles was studied in triplication to check the particles' homogeneity by using a spatially resolved technique. The chemical transformation of ZnO nanorods in simulated wastewater over a short period (three hours) was reported in recent work [185]. The speciation of Zn has already been discussed; ZnO quickly dissolved as Zn^{2+}, then it was reprecipitated to cause the sulfidation of ZnONPs. This sulfidation generated a superficial ZnS nanoshell; however, the ZnS shell did not stop ZnO dissolution from releasing Zn^{2+}. In the present work, three hours' duration did not lead to the full transformation of the ZnONPs that had previously been shown for ZnO nanorods [185].

In general, the speciation of the small ZnONPs had slightly similar percentages to larger ZnONPs. However, after three days of incubation in AD sludge, significant differences in speciation were found between the small and large ZnONPs. The proportion of ZnS increased with the 500 mg/l concentration of ZnONPs (80–200 nm); this was less for the ZnONPs with a concentration of 1000 mg/l and disappeared with the ZnONPs (30 nm) with a concentration of 500 mg/l. A general observation was that the Zn phases were primarily transformed to either Zn absorbed to a Fe (ox) composite or $Zn_3(PO_4)_2$, which is an amorphous composite.

The Zn species were studied within liquid organic wastes, which are the separation liquid of post-treated AD plants. The majority of Zn species are nano-ZnS; however, that species is usually found in processed solid organic-rich waste [234]. While the speciation of ZnSNPs (>100 nm) within the same duration have been shown to rapidly be transformed into Zn absorbed to a Fe (ox) and $Zn_3(PO_4)_2$ phases with 4% of remaining nano-ZnS. This transformed species might continue to further transformation to other phases. It has been reported that ZnS particles have more of a tendency to aggregate, which induces sedimentation in the natural environment and WWTPs [235]. In a pilot WWTP for a biosolid formation study, it was found that most of the ZnS transformed to $Zn_3(PO_4)_2$ and Zn absorbed to a Fe (ox) after 60 days within an anaerobic digestion system [7].

AD sludge contains S, P and Fe. In recent work, daughter particles were observed for both $Zn_3(PO_4)_2$ and Zn-Fe (ox) within a short incubation period in the simulated primary sludge, which was confirmed using the traditional method of LCF of the Zn-reference spectra XRF

microscopy [185]. This is because ZnSNPs are not stable particles, so that further dissolution might occur during the preparation of the particles [236]. In the current investigation, the ZnSNPs were not coated, which might explain why ZnO was present during the short incubation period.

The anoxic environment lowered redox potential then decreased the dissolution of metallic nanoparticles by forming insoluble metallic sulfide on nanoparticles' surface, consequently reducing dissolution then less toxicity [237,238]. The redox condition has an impact on the toxicity and bioavailability of the nanoparticles [34]. The anoxic environment can affect the heterogeneous structure of ENMs, which changes the morphology and size of nanoparticles by aggregation. The size and morphology of both small and large ZnONPs also ZnSNPs within the sludge matrix had indicated uniform shape and larger size.

5.5 Summary

This chapter discussed the utilisation of different ENMs as digesters that were incubated under anaerobic conditions, and their effects on biogas performance were compared. The enhanced biogas production was observed in AD sludge incubated with 50 mg/l of ZnONPs. The chemical transformation of ZnNMs was identified by applying XAS to generate XANES spectra. The speciation of large and small ZnONPs (80-200 nm) had mostly transformed at the end to ZnS and Zn absorbed to a Fe (ox). The ZnSNPs mainly transferred to $Zn_3(PO_4)_2$ with Zn absorbed to Fe (ox) and ZnO phases. The morphology of the ZnNMs had investigated within the matrix of sludge. It shows that small ZnONPs had a core-shell structure.

Chapter 6: The Interaction of Silver Nanoparticles (AgNPs) with Green Freshwater Microalgae *Raphidocelis subcapitata* (*R. subcapitata*)

6. The Interaction of Silver Nanoparticles (AgNPs) with Green Freshwater Microalgae *Raphidocelis subcapitata (R. subcapitata)*

6.1. Introduction

Due to their inherent properties as antimicrobials, silver nanoparticles (AgNPs) have been used extensively in a range of consumer products. The increased product consumption has led to their discharge into wastewater, with the potential to enter environments such as freshwater aquatic ecosystems [239,240]. When these products are applied or discharged, they are passed with several conditions, such as exposure to natural light or transfer in the dark, which can alter their physicochemical properties and impact their environmental fate and lifecycle [241]. The ecotoxicity mechanisms of AgNPs will depend on environmental conditions, the type of microorganism that comes into contact with, and dissolution of toxic ions from the particle (e.g., release of Ag^+ ions). Several studies have investigated the toxicity of AgNPs with emphasis on whether Ag^+ release can trigger reactive oxygen species (ROS) generation and also on Ag+ bioaccumulation inside aquatic microorganisms, such as algae [242]. Plankton algae, which serves as a primary producer and the head of the food chain for other species in the system, is often the primary organism assayed.

Dissolution is a special mechanism for AgNPs and is considered one of the main processes that determine their toxicity in environmental systems. AgNPs could also agglomerate in natural waters, which will alter their surface, and bulk bioreactivity also influences sedimentation. Many factors influence their dissolution and aggregation behaviour that is related to various characteristics of nanoparticles, such as size, chemistry, and surface coatings (*i.e.,* functionalisation to confer specific charge or reactivity). Local environmental conditions will also have an effect, such as the ionic strength, pH, dissolved organic carbon (DOC), the oxygen content of the water, and daylight exposure [243]. The impacts of these factors on dissolution and agglomeration have been widely studied; however, few studies have considered the influence of light or UV-light exposure on nanoparticles during their interactions with microorganisms [244,245]. Light exposure to the AgNPs in the presence of oxidising species could lead to the photoinduced process that causes the release of Ag ions

then reprecipitation and transformation to Ag_2S [246,247]. The effect of light is known to increase the dissolution of AgNPs, releasing more ions and inducing the generation of a reactive oxygen species (ROS), which causes oxidative stress [243,244]. In river water, sunlight exposure and the presence of natural organic matter (NOM), ionic Ag, can be photoinduced and form AgNPs, resulting in Ag ions-(NOM) ligand reduction [248]. The same behaviour of Ag ion reduction in the presence of dissolved organic matter, such as fulvic and humic acid, is reduced to metallic Ag under UV-vis light, which either way leads to the absorption of OM on the surface of nanoparticles [249]. In the ambient dark condition, the silver ions were reduced to AgNPs in the presence of a low concentration of humic acid by bonding Ag ions with the carboxylic group to form Ag^+-HA ligands then reduced to metallic Ag [100]. In addition to the interaction of NOM with AgNPs, extracellular polymeric substances (EPS) are considered another type of NOM that can be produced by algae microorganisms, which could influence the stability of ENPs in an aquatic system [250].

EPS are high-molecular-weight polymers that are secreted from algae to provide an outer layer to shield cells. EPS are comprised mainly of proteins and polysaccharides as well as nucleic acids, fats, and inorganic substances [251]. EPS contains several polar functional groups; these proteins attach to aliphatic and aromatic monomers, and the polysaccharide has hydrophobic chains [248,249]. Therefore, the presence of EPS could alter how the AgNPs interact with the algae and induce changes in bioavailability and toxicity. Different capped AgNPs were studied based on their interaction with EPS with amino and aromatic carboxylic groups [252]. In this work, it was suggested that EPS could alleviate the algal toxicity of AgNPs by limiting their internalisation by restraining the Trojan-horse mechanism. This mechanism is described as the phagocytosis of AgNPs that are inflammatorily stimulated by ROS generation in the cells, causing cell membrane damage and apoptosis, resulting in a mechanism caused by the ionisation of AgNPs in the cells [253].

Different techniques have been used to investigate the interaction between AgNPs and *R. subcapitata*. These revealed that most AgNPs and dissolved Ag^+ products are localised on the algae cell walls [254]. Zhang *et al*. showed that the extracellular dissolution of AgNPs is caused by the oxidation of AgNPs at the cell wall. In brief, ROS generation is caused by the presence of oxidised AgNPs near the cell wall. AgNPs can then generate hydroxyl radicals, causing oxidative damage to the cells [255]. Using confocal laser scanning

microscopy (CLSM) and comparing Ag ions *vs.* AgNPs, dissolution of small AgNPs (20 nm) and the Ag ions ($AgNO_3$) subsequently diffuse into the cytoplasm cells. Therefore, the toxicity was caused by ion uptake, and smaller AgNPs were accounted for by algae[256]. The data show that AgNPs tend to be localised inside the cells with discrete pockets of Ag^+ ions. It is suggested here that AgNPs below a threshold diameter of 10 nm dissolve and the released ions diffuse into the cell. In another report, for $AgNO_3$ and AgNPs, the interaction between dissolved Ag and the cell wall surface was studied by Fourier transform infrared (FTIR), which showed that dissolved Ag reduces the aldehyde group to a carboxyl group regardless of the presence of EPS. This suggested that EPS did not affect the interaction between Ag ions released from AgNPs and $AgNO_3$ and algae cells. EPS had no impact on the influence of AgNPs and $AgNO_3$ on algae growth [257]. In the present work, *R. subcapitata*, an aquatic species commonly used in laboratory tests, was exposed to aged AgNPs coated with citrate and 20 nm in OECD media containing MOPS 3-(N-morpholino)propanesulfonic acid buffer under different light source exposures (light, 2% UV-light, and dark). The particle size was the same at the beginning of the experiment. The ageing conditions and medium were feeding and growth-inhibiting sources to mimic the natural sources. The interaction of AgNPs on the cell surface was carefully examined to understand the extra- and intra-cellular events leading to Ag ions release from the AgNPs. Electron energy-loss spectroscopy (EELS) combined with high-resolution transmission electron microscopy (HR-TEM) facilitated the mapping of the elemental composition to study whether the particles had entered, transformed, or dissolved inside the cells. EEL spectra were acquired to map Ag on the cell surface and the cell wall to characterise its chemical form and provide information regarding the interaction of silver with the cell surface.

6.2. Materials and Methods

6.2.1. Characterisation of AgNPs and the ageing experiment

A stock solution of citrate-capped AgNPs (BioPure) with a primary size of 20 nm that was sterile and endotoxin-free was obtained from nanoComposix (San Diego, USA). The silver colloidal solution was sonicated for 10 minutes before being diluted in an OECD-MOPS medium with a 3-Morpholine propanesulfonic acid buffer (MOPs), pH 7.3 ± 0.03 at 20 ± 2°C to produce a concentration of 1 mg/l of AgNPs. To investigate whether the AgNPs in

the OECD-MOPs medium under dark, light and UV conditions, the AgNPs were mixed with this medium by inversion and then characterised after being incubated at 0, 24, 48 and 72 hours under visible white light with and without 2% UV and separately placed at a distance that ensured the photosynthesis of 100 PPFD. These were 7.4 Klux and 5.4 Klux, respectively, for both light conditions, and in the dark sealed from light with aluminium foil. This experiment was carried out several times, and one of these samples was sent for algae incubation at Bristol University. For algae exposure, 75 ml of aged AgNPs media was decanted into 100 ml conical flasks and spiked with the algae at a concentration of 10 million cells per ml. Afterwards, the experiment was conducted in a continuous normal fluorescent light with no shaking for 24 hours. Dr Kelly Atkins carried out all algal exposures within the aged medium at Biological Sciences, Bristol University.

6.2.2. Algal culture assay

The algal stock culture of *R. subcapitata* (CCAP 278/4) is known as *Pseudokirchneriella subcapitata* and *Selenastrum capricornutum* and was collected in the UK. It was cultured according to the guidelines of the Organisation for Economic Co-operation and Development (OECD) 201 algal growth inhibition tests. A system for biological work was designed at Bristol University to grow the microorganisms during the photosynthesis process. The algal cells routinely maintained their growth in light/dark cycle with 14 hours in light and 10 hours in the dark. They were then spun down by centrifugation before transferring them into the OECD-MOPs medium. Dr Kelly Atkins carried out the cell culture at Biological Sciences, Bristol University.

6.2.3. EPS source preparation (Xanthan gum)

The effect of EPS on AgNPs was examined by adding 10 mg/l of Xanthan gum (XG, Sigma-Aldrich) to the same medium. XG is a high molecular weight exo-polysaccharide produced by the microorganism *Xanthomonas campestris* and is similar to the EPS produced by the algae studied here. It was employed to be modified as a polysaccharide source that contains polyanionic and polycationic, which contributes to adhesion and aggregation of cell [251]. Commercial XG is also used for various industrial and biomedical applications [258].

The purpose of using this gum is to study the impact of EPS on AgNPs, as it is considered the same source of EPS, which is released from the microorganisms. The XG was prepared

as described in the literature [259]. In brief, a stock solution of (0.1% m/v) was prepared by dissolving 0.1 g with deionised water by stirring at an ambient temperature and then heating it to 80 ºC for 30 minutes to ensure that the gum was completely solubilised. Once cooled, it was directly taken to be dialysed against deionised water for 72 hours using a dialysing tube (SnakeSkin Dialysis Tubing, 10K MWCO), which is designed to allow a molecular size of 10 kDa or less to pass through. The same methodology was applied to AgNPs incubated with a medium mixed with 10 mg/l of xanthan gum (XG). The gum was added to the same medium and mixed by stirring to ensure the homogeneity of the solution, which was then sealed and kept in a refrigerator. A TOC machine measured the total organic matter. When the XG had prepared, 1 ml had digested in a diluted HNO_3 to obtain a final solution with pH 2. The reason for digested the sample is to ensure all carbon content converted to $CO_{2;}$ then the machine can detect the concentration of TOC.

6.2.4. Physiochemical characterisation

AgNPs were characterised before and after exposure to the medium and light or no light sources, and the average hydrodynamic diameter was measured by DLS (Malvern Zetasizer Nano ZS, Malvern Instruments). The zeta potential was determined by the measurements of electrophoretic mobility with the same Malvern equipment (in parallel), and the pH of each suspension was measured using a pH meter (JENWAY 3510 pH meter), which was regularly calibrated with a VWR chemical standard buffer. The release of free Ag+ from 1 mg/l AgNPs was measured after ageing in the OECD-MOPs medium. Aliquots were collected at each time point for centrifugation at 4200g for one hour through 3 kDa (Amicon, Sigma Aldrich) filter tubes to remove AgNPs. The amount of ionic silver was measured by Inductively Coupled Plasma-Optical Emission Spectroscopy (ICP-OES, Thermo Scientific, UK).

6.2.5. Sample preparation for electron microscopy (EM), EDS and EELS characterisations

To evaluate the interaction of AgNPs with *R. subcapitata* algae by TEM, further preparation steps took place to observe their interaction under microscopy. Beginning with harvesting planktonic microalgae, a known volume of distributed algae in the aged medium was removed by centrifugation to obtain a pellet. The pellet samples were washed three times, with 0.9% sodium chloride. The primary fixation of algae was added to a solution containing a 0.001M hydroxyethyl piperazineethanesulfonic acid (HEPES) buffer, 0.2%

glutaraldehyde, and 0.2% formaldehyde and was then incubated overnight at 4°C in a refrigerator. The fixed sample was then washed three times with a 0.1M HEPES buffer and stored in a refrigerator at 4°C before the staining and embedding procedure. Dr Kelly Atkins carried out the call harvesting at Bristol University, and samples were received the next day for TEM preparation (the author carried out all other preparations).

Samples were washed and the supernatants removed, then the pellets were stained with a mixture of 0.2 M HEPES and 1% osmium tetroxide (OsO_4) for 48 hours. Washing with DIW was carried out to remove any residual OsO_4 buffer. Complete buffer removal was checked by assaying for unbound OsO_4 using 0.5% Thiocarbohydrazide (TCH), where a brown colour indicates further washing required. The samples were then fully immersed in 0.5% TCH for 30 minutes and then washed and immersed in 2% of OsO_4 in DIW for two hours in a refrigerator. Samples were incubated in 2% uranyl acetate for 24 hours before dehydration. Dehydration involved a series of dry ethanol (50, 70, 95, 100%) to remove any bound water from the cells, then washed with acetonitrile (Sigma Aldrich, UK). The samples were infiltrated within a resin based on a Quetol resin set, which was prepared by mixing 6 g Quetol, 7.75 g Nonenyl Succinic Anhydride (NSA), 3.3 g Methyl Acid Anhydride (MNA) and 0.3 g Benzyl Dimethylamine (BDMA) (Agar Scientific, UK). The infiltration of the sample began with 50, 70, and 100% acetonitrile, and the resin solution was freshly prepared each day. The pure resin of the embedded samples was incubated under a vacuum before being cured at 60°C for 48 hours. Using an ultramicrotome, resin blocks were sectioned to 100 nm thick sections using a diamond knife in a water bath and were collected onto 300 mesh lacey carbon copper grids.

The morphologies and chemistry of the AgNPs and organisms were characterised by transmission electron microscopy (TEM: JEM-2100F, Jeol, Tokyo, Japan, operated at 200 kV. Elemental analysis for the chemical composition of samples was identified using EDS, and high resolution scanning transmission electron microscopy (HR-STEM) combined with EELS tools were used by the JEOL Com, F200 (STEM camera length 40, 200 keV) to obtain detailed chemical and structural information for the sample (Dr Liam Spillane collected this subset of data, Gatan, Inc. USA, analysed by the author). For the data analysis of the pristine particles, EELS was applied with an energy dispersion of 0.5 eV/channel and the aperture size was 40 μm with the second condenser lens system, and the camera length

was 40 mm. The converging angle was 10 mrad, and the collection angle was 40 mrad. For the high loss (HL), EELS was collected with a time acquisition of 80 ms, while the low loss (LL) was 50 ms.

6.3. Results and Discussion

6.3.1. Characterisation of AgNPs

The morphology of the AgNPs revealed that they had a spherical morphology (Figure 6-1, A) and a crystal structure corresponding to cubic metallic silver (ref- 01-087-0597) by a selected area electron diffraction (SAED) (Figure 6-1, B). AgNPs had lattice fringes that were 0.236 nm, 0.204 nm, 0.145 nm, and 0.123 nm corresponding to the (111), (200), (220), and (311) planes, respectively. High-resolution TEM (HR-TEM) phase contrast imaging confirmed the interplanar distance of the (111) lattice planes (Figure 6-1, D). EDS was applied to confirm the purity of the nanoparticles before the experiment (Figure 6-1, C). The average distribution of the particle size was 19.6 ± 2.1 nm (Figure 6-1, E), which was measured based on several TEM images and calculated using ImageJ software. The average hydrodynamic diameter and zeta potentials were 25.12 ± 0.36 nm and -37.54 mV, respectively, in Milli-Q water at pH 7. In contrast, the average diameter measured in TEM was smaller than the hydrodynamic diameter measured by DLS. The large negative zeta potential values of AgNPs are consistent with citrate capping and with observations that they form a stable suspension.

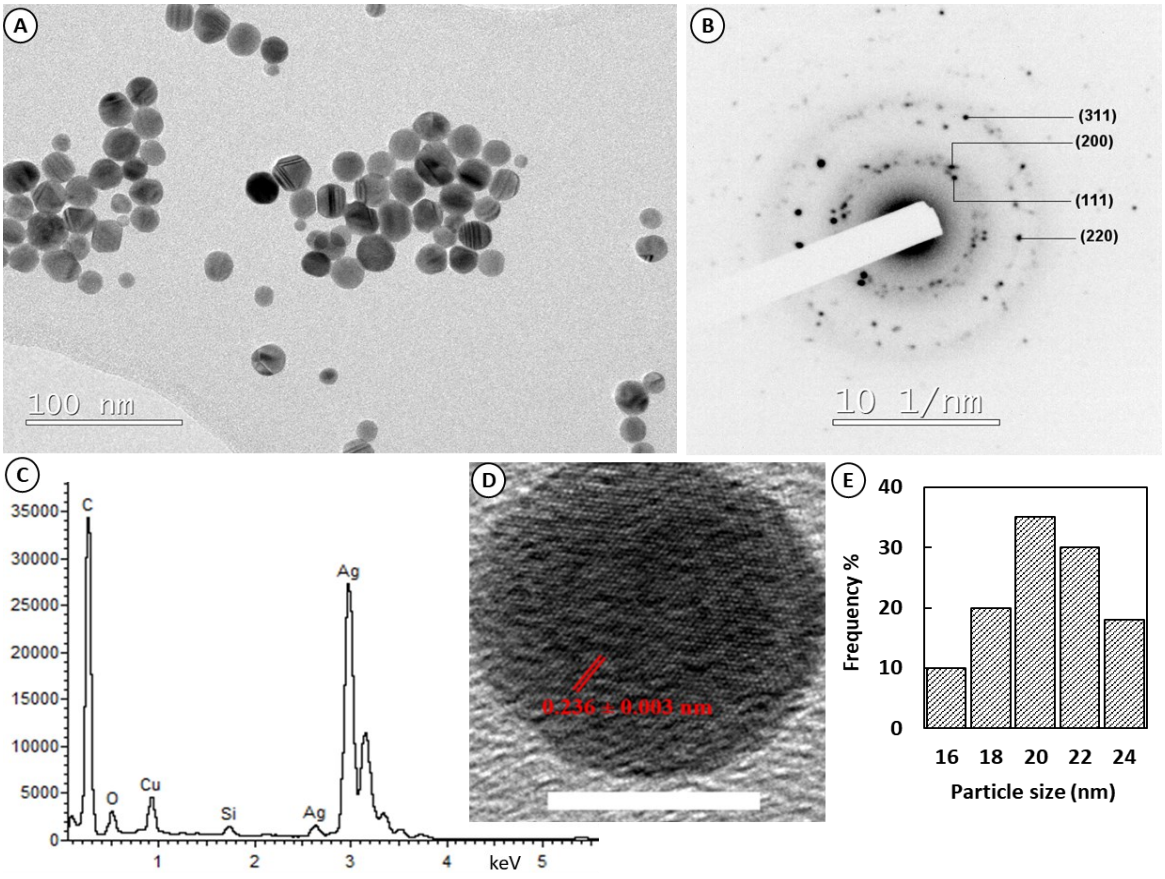

Figure 6-1: (A) Bright-field TEM micrograph of AgNPs, (B) SAED pattern of the AgNPs, (C) EDS spectrum collected from BF-TEM (y-axis of EDS spectrum is the intensity (au), (D) HRTEM image of the AgNPs showing the interplanar spacing between the (111) planes (scale bare = 10 nm), and (E) the size distribution of AgNPs measured by ImageJ software (n = 100).

The morphology and chemistry were tested by EEL spectroscopy to show the purity and density of the particles during imaging after incubation. Figure 6-2 shows the morphology of AgNPs in STEM by annular darkfield (ADF) and the spectra of the EELS map to help identify the EELS of AgNPs after incubation, as well as the chemistry by EDS maps that show no sulfidation. Also, this test was applied to determine the high loss and low loss of EELS spectra for the carbon, which represent the carbon film of the grid and indicate the EELS and EDS of M, L1, L2, and L3 shells for AgNPs.

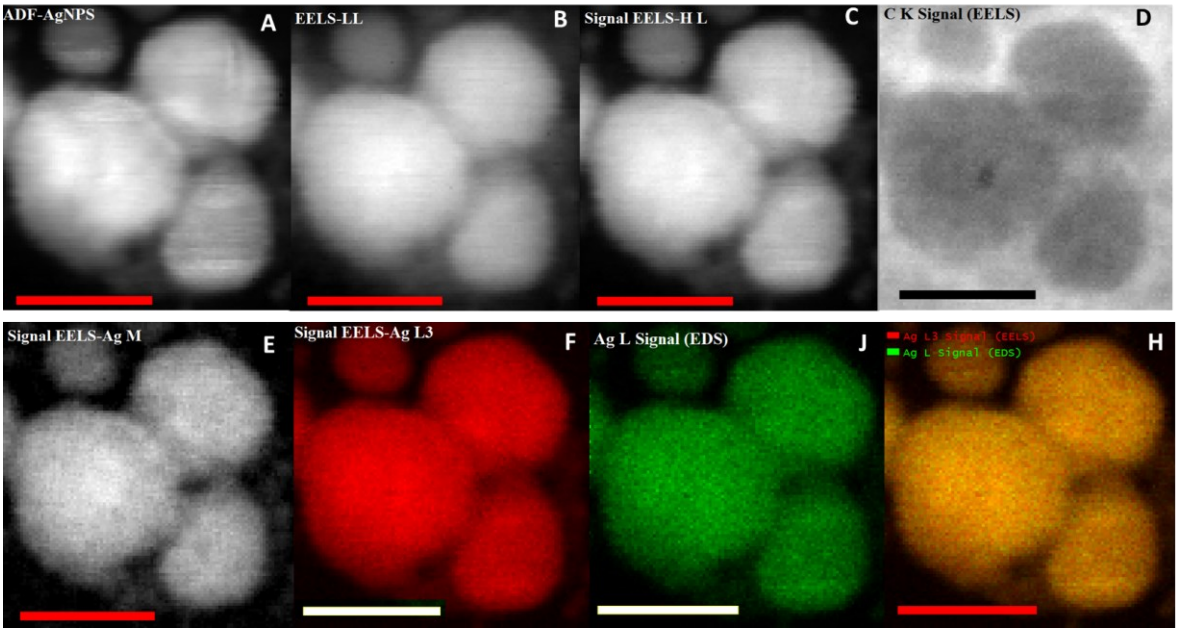

Figure 6-2: The characterisation of AgNPs pristine before incubation, (A) angular direct field (ADF) image, (B) EELS image of low loss, (C) for high loss (HL), (D) Carbon signal of EELS spectra as a background carbon, (E) Ag spectra of M shell, (F) EELS spectrum for AgL3 signal, J, hours are EDS maps for Ag L and the combined maps for EDS and EELS spectra of Ag L (scale bar = 10 nm).

6.3.2. Characterisation of aged AgNPs in OECD-MOPs under light, 2% UV light, and dark conditions

The physicochemical properties of AgNPs were investigated under various environmentally relevant conditions. These conditions included the presence and absence of visible light illumination in a cell culture medium, both with and without EPS. The AgNPs aggregated in the OECD-MOPs (as determined using DLS), and the agglomerate size of AgNPs in both incubation OECD-MOPs with and without EPS increased at similar rates, although under 2% UV light, the AgNPs had the largest agglomerated particles after 72 hours. In contrast, the size of the agglomerates of AgNPs incubated with EPS-containing medium at 48 hours was less variable under all lights and dark conditions, while the aged particles in OECD-MOPs under visible light had a smaller size (Figure 6-3, A and B). Surface zeta potential is linked to suspension stabilisation [20]. AgNPs without EPS medium aggregated over time due to change screening [260] or modification of the surface charge,

which was observed through the variation of zeta potential (Figure 6-3, C and D). The most significant factor affecting AgNPs aggregation was UV light, although this did not correlate entirely with the change in zeta potential.

The dissolution of AgNPs in the presence and absence of EPS was studied for its influence during the incubation of AgNPs in the cell culture medium. In general, the concentration of ions released was higher in the medium containing EPS than without (Figure 6-3, E and F). The concentration of released ions varied over the tested period, but it was noticeable that the amount released reduced under 2% UV light. The medium with EPS showed an increase in concentration within 48 h and then decreased. Introduction of the EPS to the medium probably resulted in protein adsorption onto the AgNPs, leading to a 'protein corona' around the AgNPs. This might prevent dissolution in some cases and increase aggregation; conversely, it may increase dissolution through chelation effects which binding the released ions directly associated with cell [114]. The effect of EPS on the aged AgNPs in the OECD-MOPs medium (Figure 6-3, E and F) was photoinduced. AgNPs during the incubation for 24 to 48 hours had oxidised and released ions then particles had formed by reduced to more stabilised particles [100].

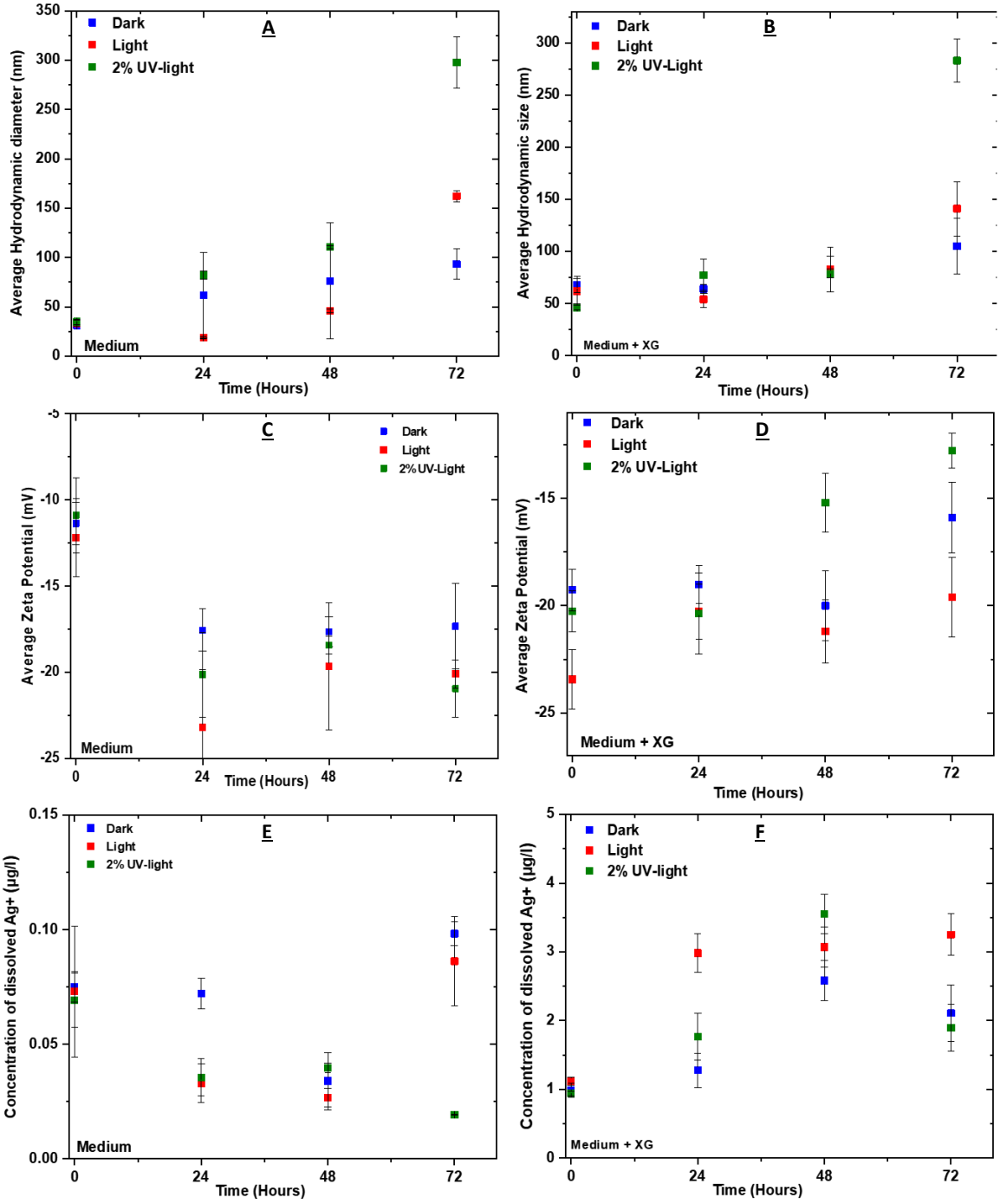

Figure 6-3: The size distribution of AgNPs measured by DLS after incubation in an OECD-MOPs medium (A) and in the same medium with 10 mg/l EPS (B), and the average surface charges of AgNPs in the same media are shown in (C) and (D), respectively. (E, F) The concentration of dissolved Ag ions after ageing in the OECD-MOPs medium with and without 10 mg/l of EPS, respectively.

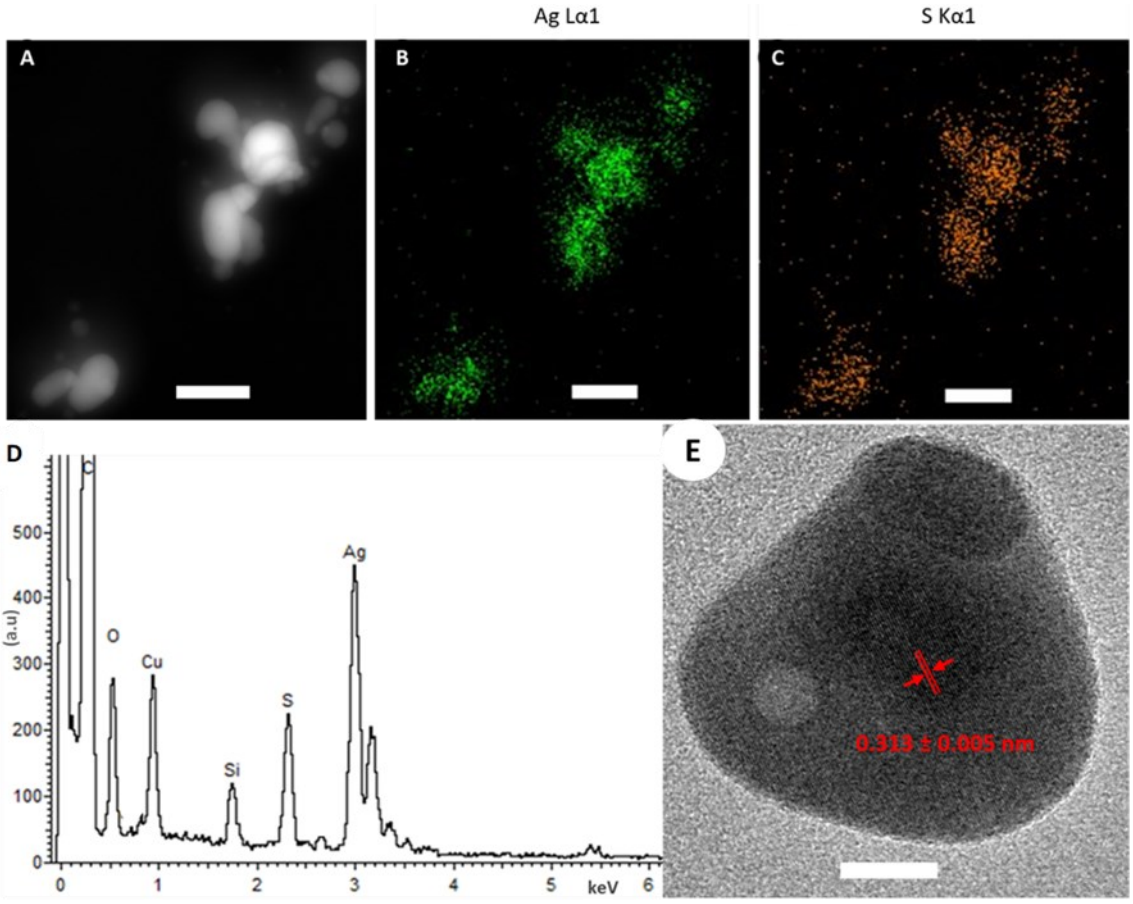

Figure 6-4: AgNPs incubated in OECD-MOPs aged under light for 24 h. (A) Dark-field-TEM micrograph (scale bar = 50 nm). (B, C) STEM-EDX maps for Ag (Lα) and S (Kα) peaks. (D) Confirms the transformation of AgNPs to Ag_2S by EDX spectroscopy, (E) HR-TEM of a single nanoparticle showing its structure with an interplanar distance corresponding to the Ag_2S monoclinic structure and showing a bright spot at the surface (scale bar = 10 nm).

The morphology of AgNPs after incubation in OECD-MOPs medium was measured to elucidate their transformation under both light and dark conditions. The OECD-MOPs medium AgNPs induce aggregation and also caused a structural transformation (Figure 6-4). The formation of hollow Ag_2S-NPs was observed in the bright-field and dark-field TEM. The morphology of transformed AgNPs was near-spherical in shape (Figure 6-4, A). STEM-EDX mapping of the NPs showed that sulfur and silver were concentrated together, which confirms the transformation to Ag_2S nanoparticles (Figure 6-4, B-D). The STEM-

EDX elemental analysis confirmed the presence of a sulfur (Kα) peak at 2.31 keV (Figure 6-4, E). HR-TEM identified a lattice spacing of 0.313 ± 0.005 nm, corresponding to the (021) plane of the Ag_2S monoclinic structure (Ref- 01-075-1051). A bright hollow was also observed within the NP (Figure 6-4, F).

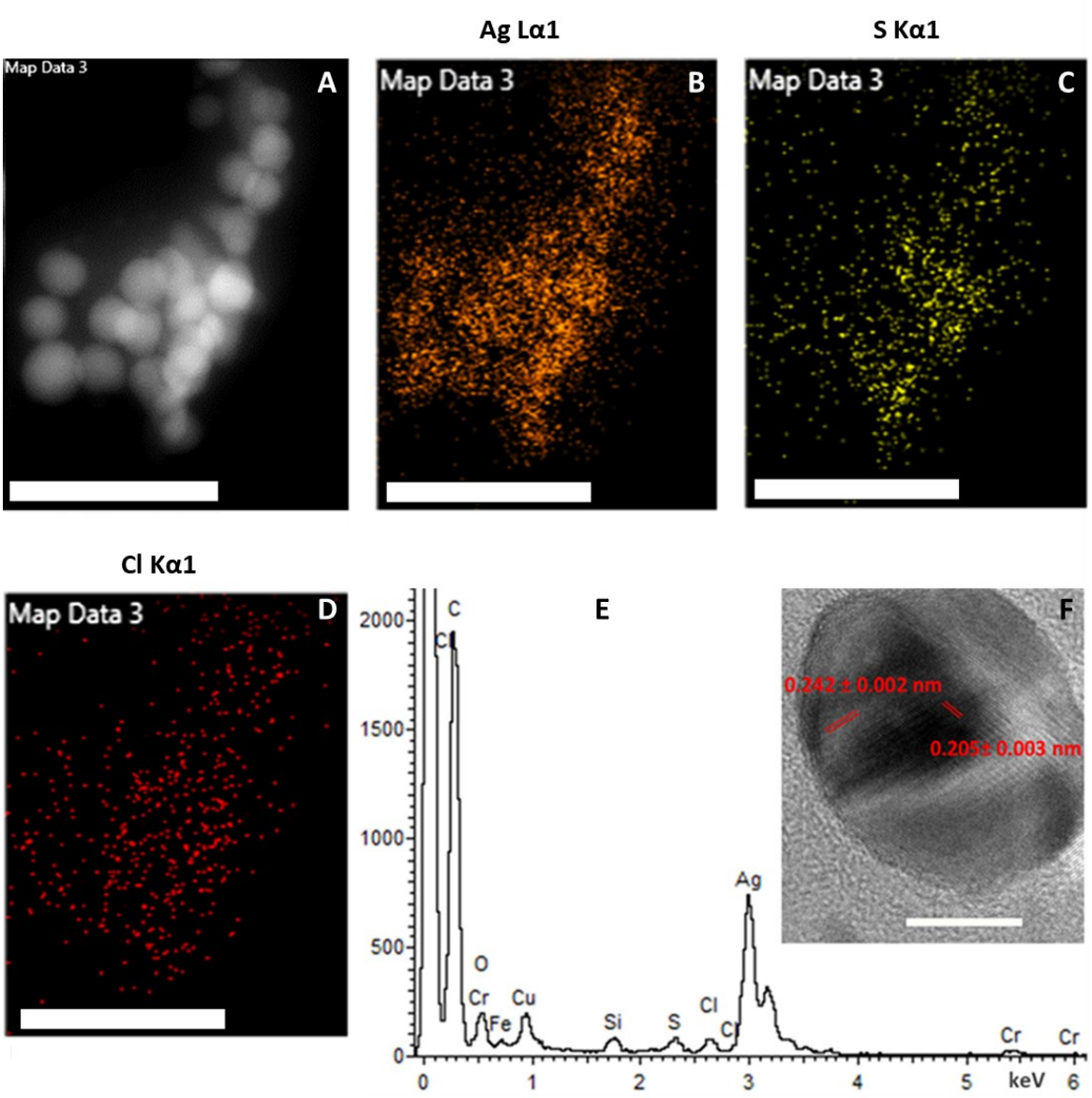

Figure 6-5: (A) AgNPs incubated in OCED-MOPs + EPS exposed to light for 24 h, (A) Dark-field TEM micrograph incubated nanoparticles (scale bar = 100 nm). (B-D) STEM-EDX elemental maps for Ag, S, and Cl, (E) confirms the presence of these elements in STEM-EDX spectrum of the transformed AgNPs, and (F) HR-TEM structure of a single transformed nanoparticle showing its structure with an interplanar corresponding to the Ag_2S monoclinic structure (scale bar = 10 nm).

The same analysis was applied for spherical AgNPs in the medium containing 10 mg/l of EPS to show the alteration in the morphology of the aged AgNPs for 24 h (under light and UV-light). Figure 6-5 shows the morphology of several particles after 24 hours in OCED-MOPs + EPS (Figure 6-5, A). STEM-EDX mapping of the particles showed the presence of silver, sulfur, and chlorine (Figure 6-5, A-E). Indexing of lattice fringes in an HR-TEM micrograph of the NPs showed that the interplanar distances were 0.242 ± 0.002 nm and 0.205 ± 0.003 nm, corresponding to the (121) and (200) planes, respectively (Figure 6-5, F), which confirmed the Ag_2S monoclinic structure (Ref- 00-014-0072). Figure 6-6 shows AgNPs incubated for the same time and within the same medium containing EPS under UV light. A darkfield STEM micrograph shows the morphology of aged AgNPs, and EDS confirmed the presence of Ag, S, and Cl (Figure 6-6, A-E). The aged particles exposed to UV light transformed to Ag_2SPs (average size 70 nm)with a larger diameter than Ag_2S NPs (average size about 50 nm) aged in light .

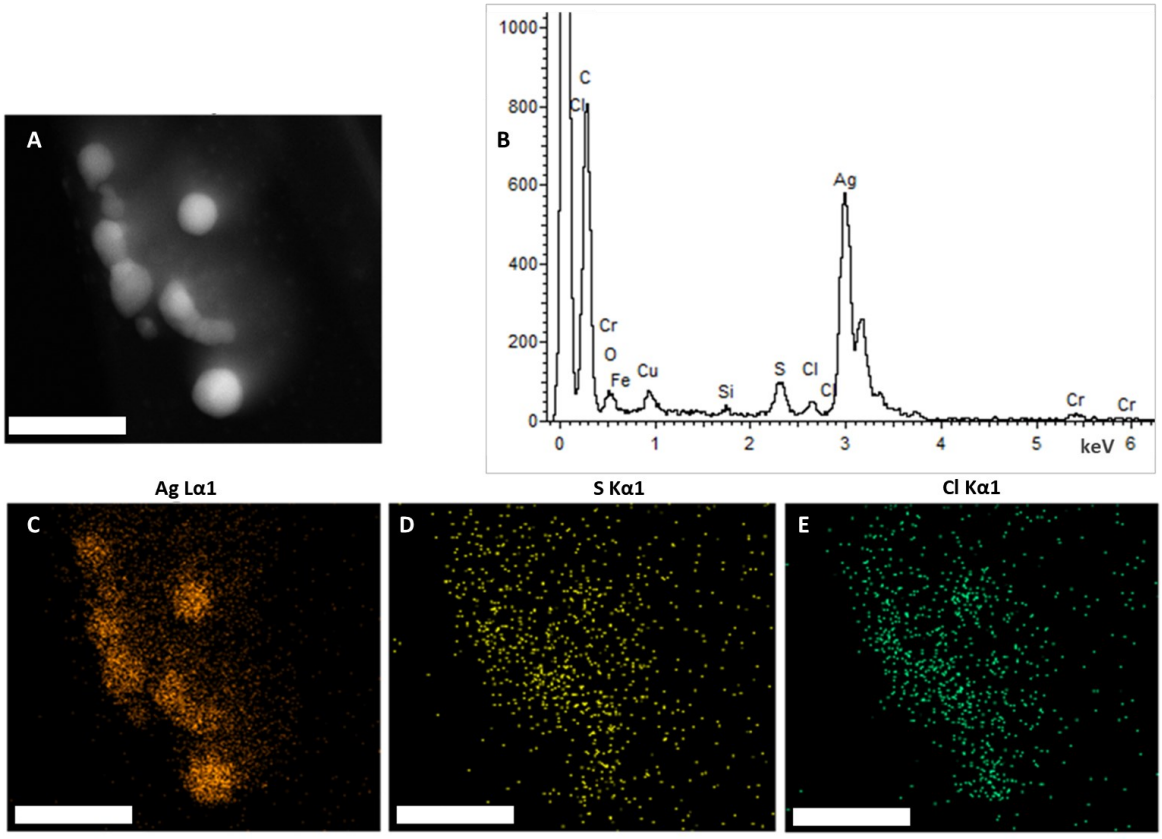

Figure 6-6: (A) AgNPs incubated in OCED-MOPs + EPS and exposed to 2% UV light for 24 h. (A) Darkfield STEM image of the aged AgNPs after 24 hours incubated in the

medium with EPS, (B) the EDS spectrum was acquired for the cluster in (A), (C-E) illustrated the elemental mapping for Ag, S, and Cl (Scale bar =100 nm).

In summary, the morphology of AgNPs aged in OECD-MOPs medium was similar to pure AgNPs with spherical shape. EDX spectra taken from cluster and maps confirmed the presence of S and Cl rich species, possibly Ag sulfide and chloride. Using HRTEM imaging, the interplanar distance confirmed the transformation of these particles to Ag_2SNPs.

6.3.3. Cell morphology and ultrastructure

6.3.3.1. Incubation with OECD-MOPs medium with aged AgNPs for 24 hours under visible light

The freshwater green microalgae *R. subcapitata* is sickle-shaped and exists in unicellular form[261]. Electron microscopy can provide valuable information about the interaction between nanoparticles and algal cells. Morphology and cell structure were investigated after 24 h of incubation with aged AgNPs. Two conditions of aged AgNPs were studied under visible light for 24 hours and 2% UV light for 24, 48, and 72 hours. Most control cells had not been treated with aged nanoparticles. The control cells had a thin wavy cell wall and showed normal and healthy granules, such as the nucleus, chloroplast, phosphate bodies, mitochondria, pyrenoid, and starch grains (Figure 6-7, A and B). In the bright-field TEM micrograph, the cell wall could be discriminated between the outer and inner wall layers as being electron-opaque, dense, and less electron-dense.

Algae were exposed to AgNPs (1mg/l) that had been aged for 24 hours under visible light. Many perturbations of cell ultrastructure organelles were observed, ranging from a diffuse cell membrane appearance to ruptured cell walls. Also, a slight detachment of the cell wall between the inner layer and outer layer membranes, creating a gap, was observed. This detachment between the cell layers was particularly noticeable when the algae were in direct contact with aggregated NPs (Figure 6-7, C). There were also indications of a fine hair-like structure on the cell wall that trapped the aggregated particles together, creating a network, but this was difficult to observe using dark-field TEM.

Shrinkage of the nucleus, chloroplasts, lipid body, and vacuoles was observed in Figure 6-7, C where disorganised, thicker, and less dense cell walls could be distinguished (Figure 6-7, C, emphasis on arrows). Figure 6-7, D shows an alga containing a large number of starch grains (the dark oval-shaped structures), vacuoles, and lipid bodies (LB). The magnified area shows detachment between the outer and inner layers of the wall (Figure 6-7, E) and STEM-EDX maps of the aggregated particles trapped near the cell wall confirmed the presence of Ag and S. The EDS analysis shows no evidence of internalised NPs in these specific cells; instead, it shows a diffuse background of Ag inside the cell. The cell wall had detached slightly from the cytoplasm and showed slight shrinkage of the cell wall (Figure 6-7, C). A similar effect has been reported in algae exposed to ceria nanoparticles [262].

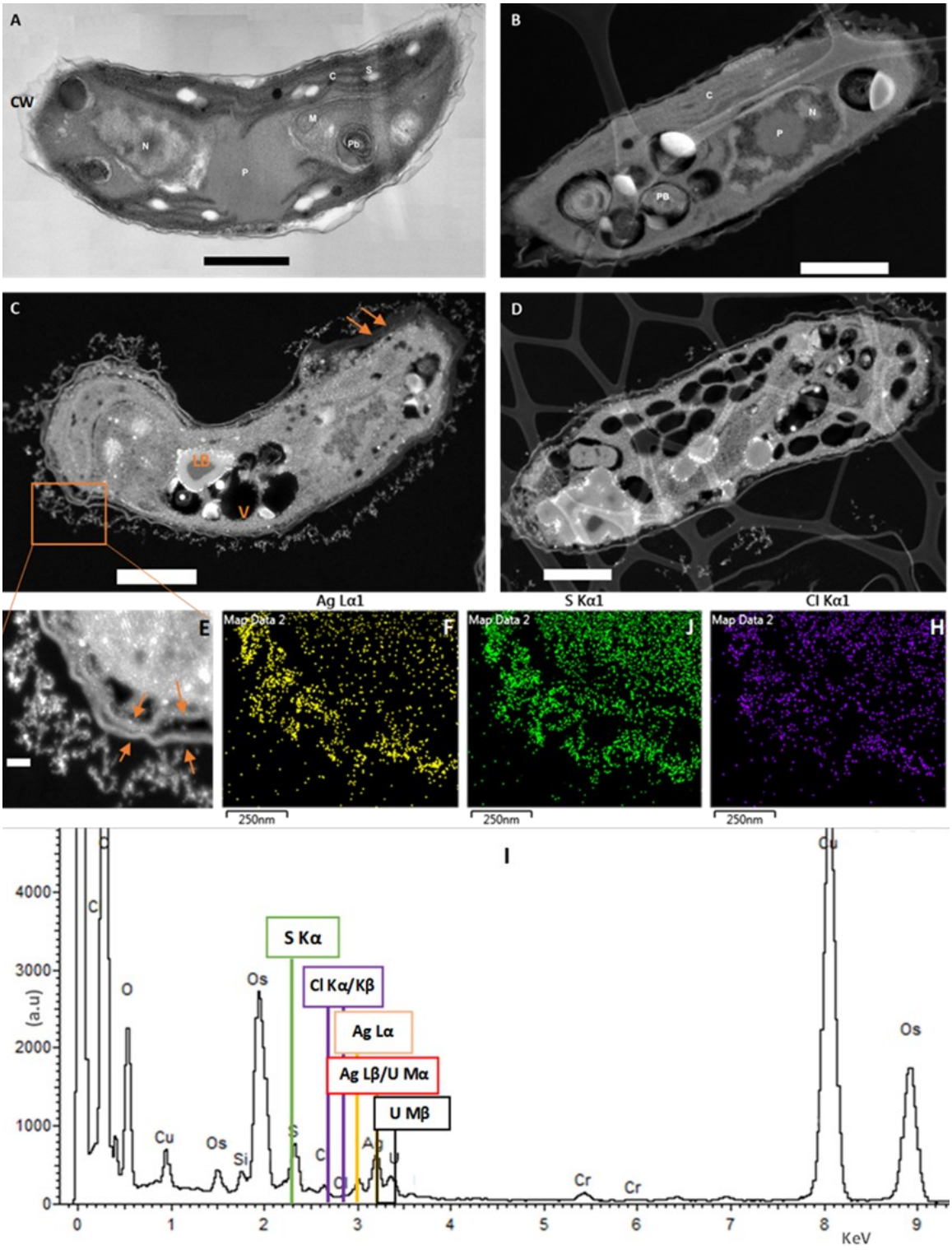

Figure 6-7: Algal cells incubated for 24 hours with OECD-MOPs medium had aged 1 mg/l of AgNPs for 24 hours under light exposure. (A) Bright-field TEM and (B) dark-field STEM micrographs of non-exposed *R. subcapitata* cells. The labels of the organelles of the cell are as follows: (CW) cell wall, (N) nucleus, (C) chloroplast, (M) mitochondrion, (P)

pyrenoid, (Pb) phosphate bodies, and (S) starch. (C, D) Darkfield STEM images for treated cells by aged AgNPs, (LB) Lipid body, (V) vacuoles; (A–D scale bar = 1μm). (E) Magnified area of the boxed region of the cell wall in C (scale bar = 200 nm). (F–H) STEM-EDX mapping of the cell wall confirming the distribution of Ag and S within the aggregated particles, (I) EDS spectrum for the area in (E), which shows the Ag Lα= 2.98 KeV does not overlap, but Ag Lβ =3.15 keV overlaps with U Mα = 3.17keV.

Figure 6-8, A and B show cells incubated for 24 hours in OECD-MOPs medium within aged particles under light. Several observations where the outer layer of the cell wall appears to have a "hair-like" shape (H.S.). The left arrow in (Figure 6-8), A shows that the cell wall has ruptured and possibly leaked intracellular content. Small particles have breached the cell wall and are found in the cytoplasm and periplasmic space. The indexing of the HRTEM micrograph in (Figure 6-8, C) shows that one particle had a lattice spacing of 0.206 ± 0.001 nm, which corresponds to the (200) lattice planes of Ag_2SNPs (Ref-00-014-0072). Several other responses of the algae to aged AgNPs exposure were also monitored, including a dramatically detached or disrupted outer layer to hair-like fibres, deformation, and cell swelling (Figure 6-8, D, E, emphasis on arrows). The extracellular filamentous structure observed in (Figure 6-8, D) could have been formed if the algal cell released an extracellular polymeric substance (EPS) in response to UV light and AgNPs. This behaviour is considered to be a defence mechanism that algae have against toxic agents and depends on the composition of the cell wall [263]. The hair-like structure of the outer layer cell wall has been observed in some types of algae. For example, chlorella uses the same mechanism against the PBCV-1 virus [264]. *C.vulagris* has a cell wall composition and can form this structure of the outer layer [265]. Also, the *N.oleoabundans* cell has this wall type of hairy structure and accumulated cell wall by a high concentration of proteins in a growth medium [266]. Therefore, the main factor inducing this structure can be related to similarities in the cell wall composition [267].

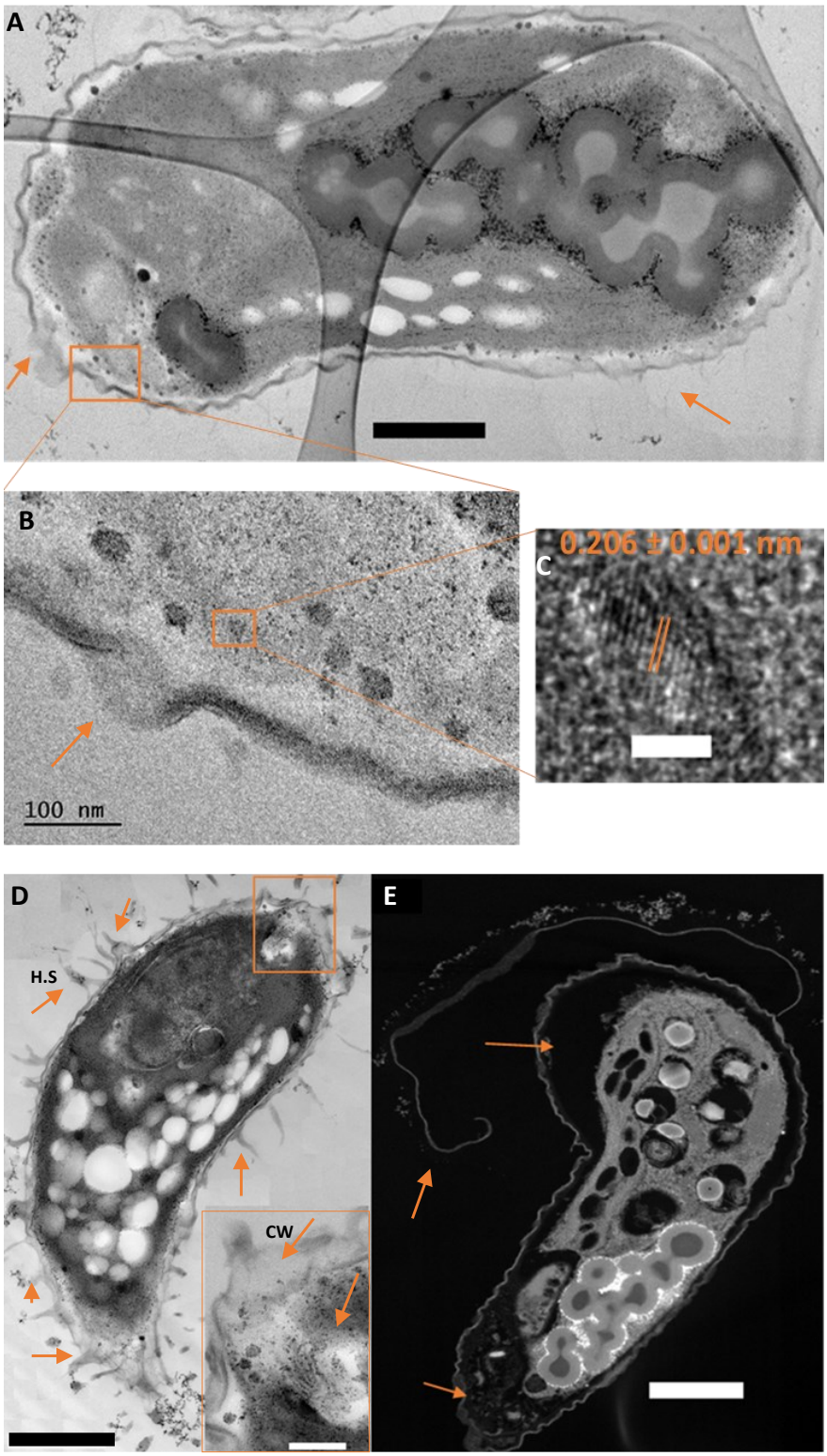

Figure 6-8: (A, B) BF-TEM for algal cells exposed to 1 mg/l of aged AgNPs for 24 hours under visible light, (A scale bar = 0.5 µm) (C) HRTEM of the AgNPs in the boxed region in B showing an interplanar distance corresponding to crystalline Ag_2S (scale bar = 2 nm),

(D) BF-TEM micrograph where the boxed region indicates rupture of the cell wall (scale bar = 200 nm). (E) DF-STEM for the same condition of exposed algal cells that shows the detachment of the cell wall (D, E scale bar = 1µm)

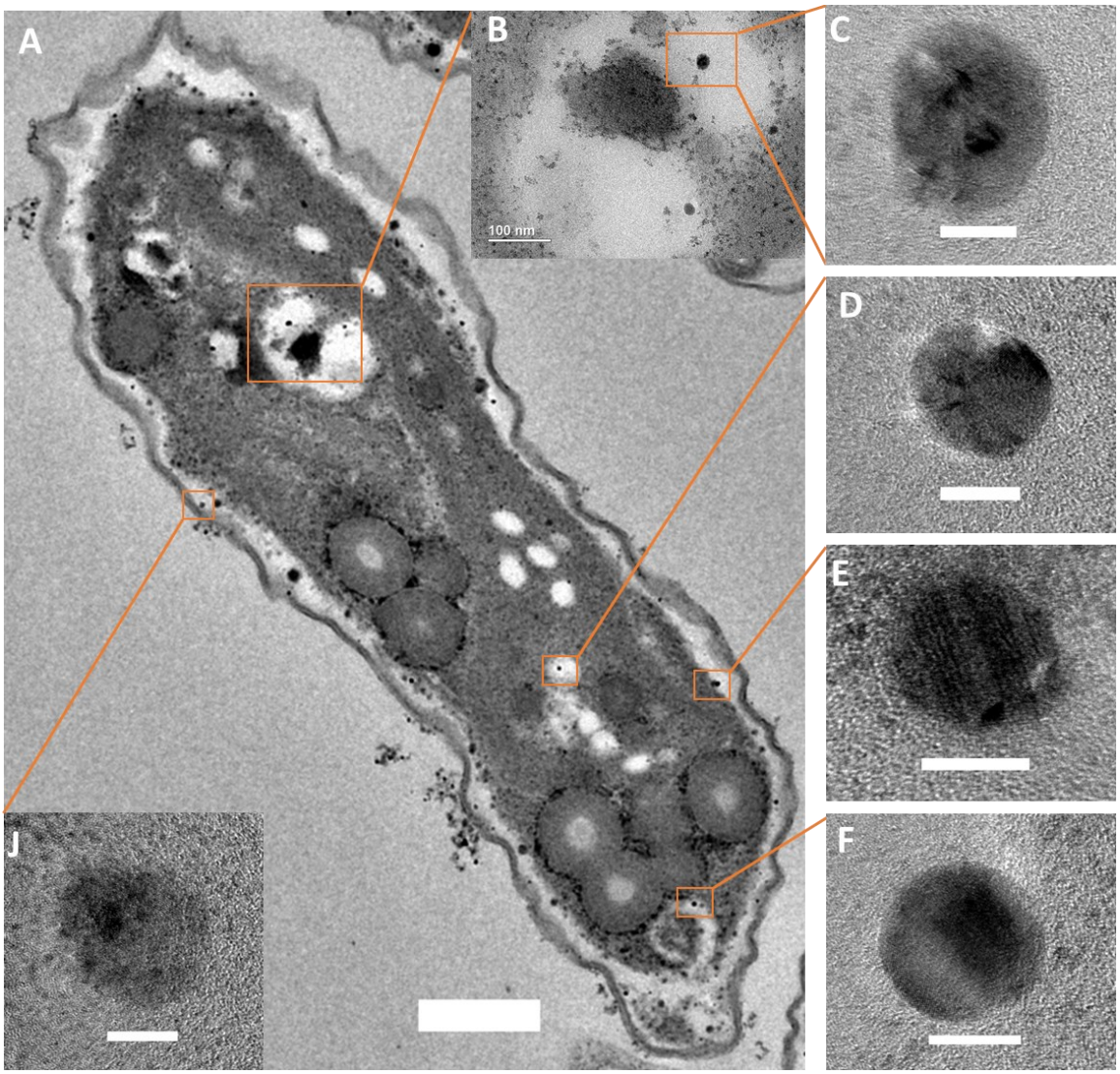

Figure 6-9: (A) Algae cells were incubated with OECD-MOPs medium-aged with 1 mg/l of AgNPs for 24 h and exposed to visible light. (B) A magnified area of vacuoles contained some nanoparticles. One is shown in (C), (D) another nanoparticle found in the starch granule; (E) a nanoparticle near to the cytoplasm and plasma membrane; (F) a nanoparticle in the extracellular space; (J) a nanoparticle near to cell wall (in the periplasmic space). Scale bars C-J = 10 nm; scale bar A = 500 nm.

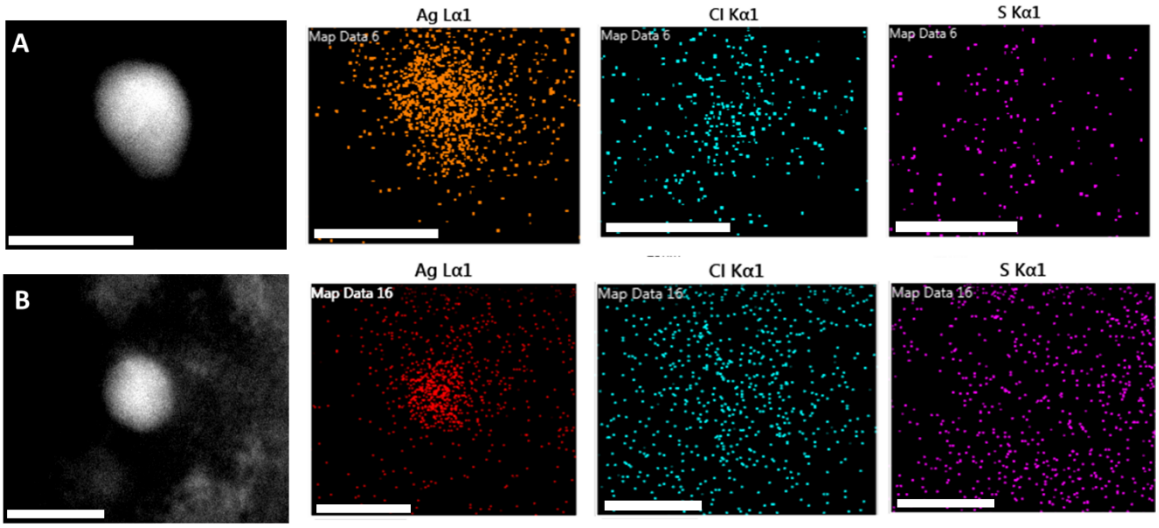

Figure 6-10: (A) Aged AgNPs under visible light for 24 hrs from Figure 6-9, C shows the STEM and elemental analysis maps and the same of (B) Aged AgNPs of the same condition from Figure 6-9, F (scale bar= 25 nm).

Figure 6-9 shows a variation in the distribution of spherical particles located in different compartments in the algae cell which incubated for 24 hrs with 1 mg/l AgNPs which had been aged for 24 hrs under visible light. Figure 6-9, A-C shows AgNPs located between the periplasmic space and the inner layer under the cell wall, with an average diameter of 14.3 ± 0.5 nm, which suggests that the smaller AgNPs were internalised through the cell wall. Previous work has proposed that the toxicity of AgNPs to algae is associated directly with the ability for internalisation. The aged particles were released and then interlaced and precipitated AgCl or Ag_2SNPs [268].

Figure 6-10 shows some maps of Aged AgNPs within 24 hrs under light which had imaged in (Figure 6-9, C and F). The average size of several particles within the cell was measured by TEM and was 15 ± 2 nm (Figure 6-10), which is smaller than the pristine particles (Figure 6-1) and transformed NPs (Figure 6-5), suggesting that there may be a maximum threshold size able to translocate inside the Algae. EDS data is challenging to collect and interpret here due to the Ag energy peak (3.15 keV) overlap with uranyl acetate (3.17 keV) (used in the staining process) and to isolate the background signal (Figure 6-7). STEM-EELS can be used to discriminate the Ag and O to identify the localisation and speciation

(such as oxidization), of aged AgNPs within the algal cell. Therefore, a further investigation using STEM was combined with EELS to map the chemistry of the AgNPs within and outside the algae.

6.3.3.2. Incubation with OECD-MOPs medium with aged AgNPs for 24, 48, and 72 hours under 2% ultraviolet light

The cellular structure of this algae was investigated under conditions where the algae were incubated for 24 hours in a medium that contained the AgNPs (1 mg/l) that had been aged for different times (24, 48, 72 h) under UV light. Figure 6–11 shows the different algal cells treated with aged AgNPs in OECD-MOPs medium with UV-light exposure. Figure 6-11, A shows the control sample no treatment with particles and incubated in OECD-MOPS medium for 24 h; in many samples the algae shrunk, and EPS formed around the outer cell wall. Algae that had been incubated with AgNPs and aged for 24 and 48 hours under UV light (Figure 6-11, B and C) show a detachment of the cell wall, and more EPS had been produced compared to cells incubated in an aged medium of 72 hours (Figure 6-11, D). As a general observation, they showed features indicating the same degree of cellular destruction and had become smaller than the cells treated with light. In the dissolution test of OECD-MOPs (Figure 6-3, F) incubated with EPS or XG, and the AgNPs, the concentration of Ag ions increased over 24 and 48 hours (Figure 6-3, B and C). Release of ions might explain the observation that the cells were less damaged at 72 hours compared to the AgNPs aged for 24 and 48 hours. The 72 hours aged particles were hard to discern, the algae had the hairy shape, but a less detached of cell wall compared to the non-treated cells.

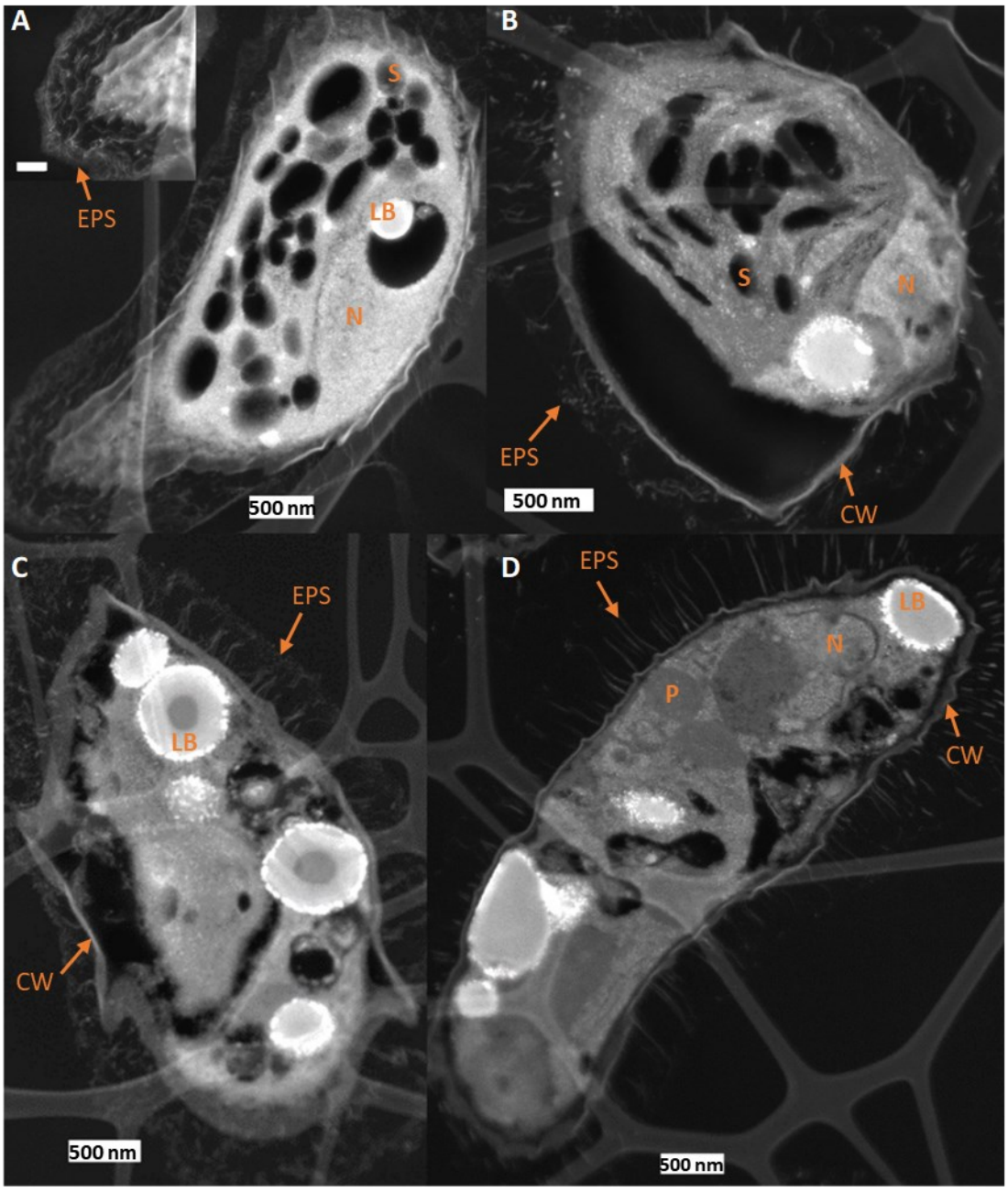

Figure 6-11: HAADF-STEM micrograph of algae incubation within OECD-MOPs medium without and with aged 1 mg/l of AgNPs under UV light for 24 hrs. (A) Control sample with no AgNPs added. The magnified image (inset on the upper left) shows the EPS released from the cells after incubation with OECD-MOPs medium under UV light (scale bar = 200 nm), (B) Algal cells had incubated for 24 hrs with 1 mg/l of aged AgNPs under the same UV light for 24 h, (C) 48 h, and (D) 72 h .The labels of the organelles of the cell are as follows: (CW) cell wall, (N) nucleus, (EPS) Extracellular polymer, (P) pyrenoid, (LB) Lipid body, and (S) starch.

6.3.3.3. EELS spectrum imaging demonstrates the speciation of aged AgNPs for 24 h under light.

Figure 6-12, A shows AgNPs attached to the cell wall membrane (yellow square). A magnified profile annular darkfield (ADF) image illustrates well-defined spherical AgNPs with a size of 15 nm (Figure 6-12, B) and an EEL mapping image highlighted with a red square to provide the EELS spectrum image (SI) in (Figure 6-12, C). The aged AgNPs in the medium had reached the cell membrane and localised at periplasmatic space; therefore, the EEL spectra for high core loss (HL) and low core loss (LL) had acquired to identified Ag M-edge, oxygen O K-edge and Ag L-edge (Figure 6-12, D and E). In the spectrum of EEL (LL), the Ag M-edge at 395 eV can be identified in (Figure 6-12, D), but there was no trace of the oxygen signals in the spectrum located at 538 eV, which indicates that the AgNPs have not oxidised. Figure 6-12, E, indicates the EEL (HL) spectrum and provides the Ag L-edge in the spectrum acquired to apply further fitting for the edge by using multilinear least-squares (MLLS). This technique facilitates the fitting of this data to the data of pristine AgNPs EELS L_3 for standard. This approach allows the individual EEL spectrum of different AgNPs to be compared regarding their location in the algal cell. The resulting spectrum of the signal after applying the MLLS matched the energy loss near edge structure (ELNES) and showed no strong residual. That had suggested silver could be in the Ag(O) valence or the oxidised Ag was below the detection limit in the dataset. Figure 6-13, A, illustrates the signal of the spectrum image (SI) after selecting the EELS edge and subtracting the background signals. Then ELNES fingerprinting as a reference was applied to determine the chemical states of the selected edge, which show the MLLS fitting in (Figure 6-13, B).

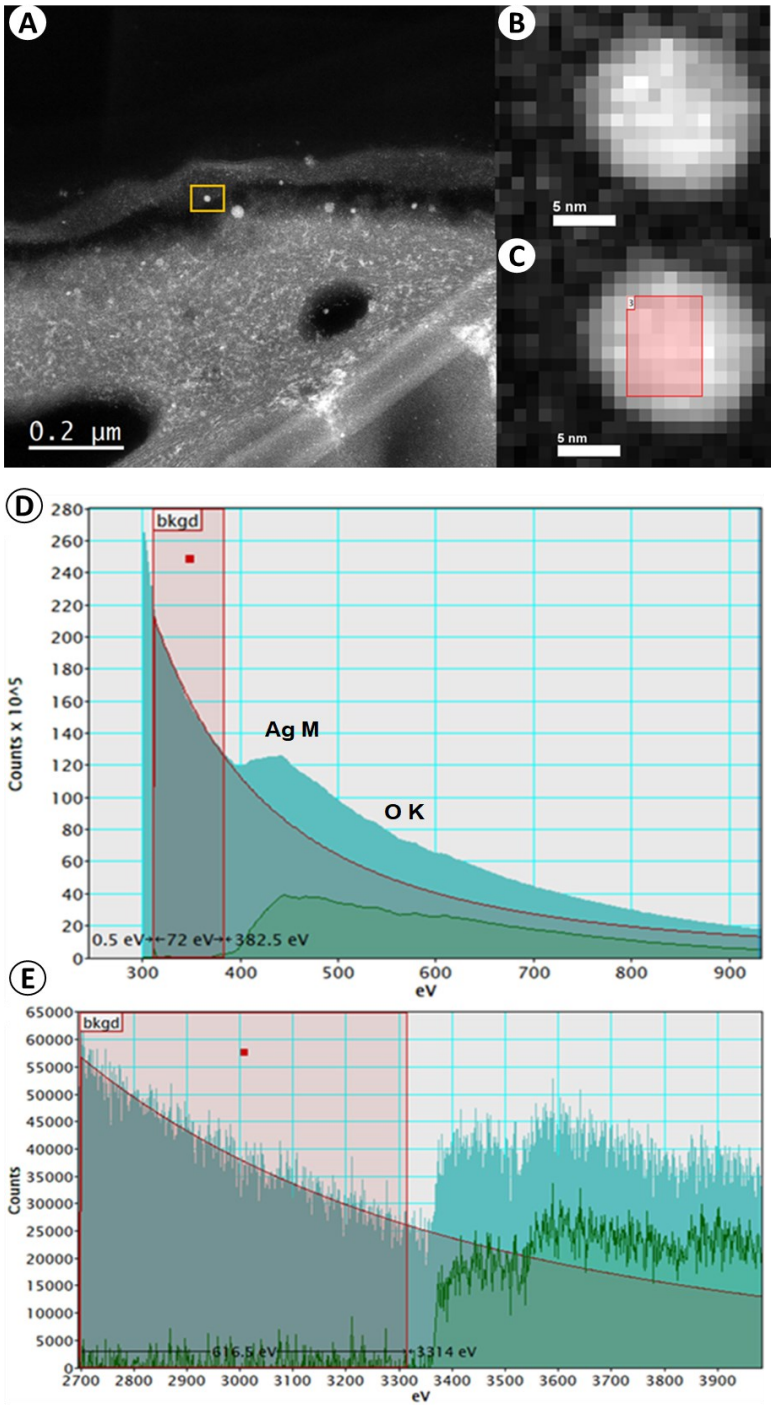

Figure 6-12: (A) A large view of cell wall algae with AgNPs shown in the yellow square. The algae were incubated for 24 h under light conditions. (B) A magnified annular darkfield (ADF) image was acquired, (C) EEL spectrum image from the selected area in c (red square) indicating the elemental composition of the particle, (D) EELS spectrum of low core loss, and (E) EELS of high core-loss spectra were constructed from the EELS spectrum image in (C).

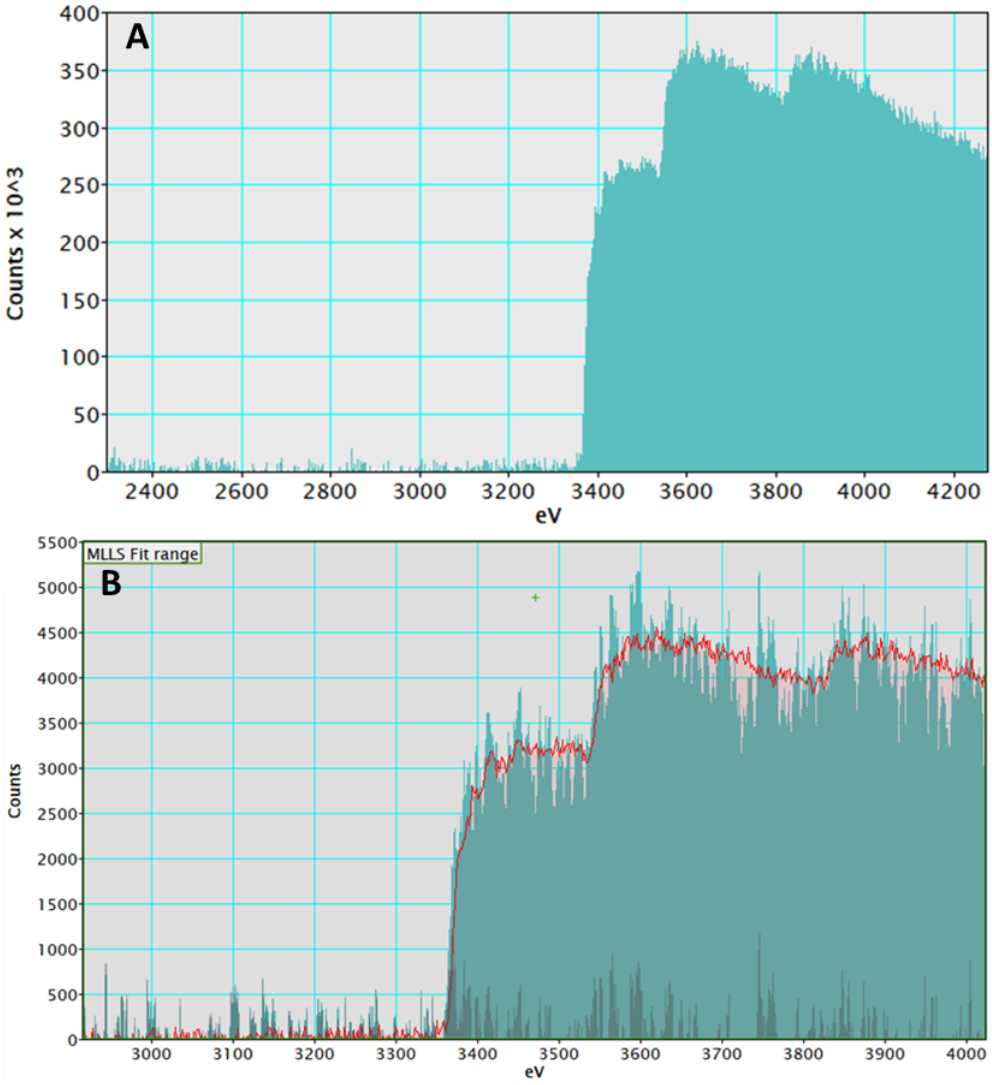

Figure 6-13: The EEL (HL) spectrum from figure 6-12 ,E for AgNPs incubated for 24 hrs under light. (A) The signal of EEL (HL) spectrum after removing the background signals and selecting the Ag L-edge; (B) the MLLS fitting in the selected range of the Ag L-edge.

The study of the chemical state of AgNPs according to the position in the algal cell was achieved by applying the MLLS maps to the selected region (Figure 6-14, A). The analysis was acquired by finding the spectrum image for the high core loss of EELS, which had identified for the whole edge of the following elements: C, N, Ag, Ca, and U. MLLS fitting maps were then compared with the Ag map identified from the pristine Ag. Due to the complexity of the targeted area, the quantification of EELS could have contributions from plural scattering during the analysis that had occurred and impacted the quantification.

Plural scattering can be neglected if the sample thickness is too low. In this case, it should be removed by Fourier deconvolution, which would help to produce a signal scattering distribution that would assist in the interpretation of ELNES. Figure 6-14, A micrograph of algal cells was selected with an area in the yellow box to show the distribution of some AgNPs in a magnified micrograph presented in (Figure 6-14, B). The same micrograph was demonstrated by different colours to show the EELS of the selected edges (Figure 6-14, C). Some selected AgNPs in the algal cell were specified by acquiring their ELNES and compared in the same graph in (Figure 6-14, D). The ELNES of selected AgNPs were compared and shown there were delays in the Ag M-edge with maximum approximation at 430 to 440 eV for AgNPs 1, 2, and 3. The ELNES of AgNPs 4 shows a sharp sawtooth at the 400 eV edge, which characterises the N K-edge. Sharp peaks were observed on the O K-edge at 530 eV for AgNPs 2, 3, and 4, but were not for AgNPs in 1. According to the location of AgNPs within the cell compartment, the speciation of oxidised AgNPs was near the vacuoles. In the location of AgNPs 4 had shown both N K-edge and O K-edge.

The chemical composition of the AgNPs trapped by EPS is shown in (Figure *6-15*). A transparent film appeared around the outer cell wall, which had detached from the cytoplasm. This transparent film is the EPS, which is trapped with some aggregated aged AgNPs in yellow square in (Figure 6-15), A and shown a magnified micrograph in (Figure 6-15, B). The chemical composition was identified by constructing the EEL low core loss spectrum from the mapping image (red square) in (Figure 6-15, C). The EEL spectrum is indicated with Ag-M-edge and O K-edge positions where the Ag appears while O is absent. Therefore, the presence of aged AgNPs confirmed their entrapment within EPS. An EDS spectrum was acquired to identify the chemical compositions of the same aggregated particles in outer cell wall of algae (Figure 6-16) which EDS identified for the selected area (red square). The spectrum taken from the aggregated AgNP indicated the presence of O and Ag suggesting that Ag aggregated after becoming oxidised and sulfided within the EPS. Also, some elements observed in the EDS spectrum are from the background and the embedding and staining chemicals. The aged AgNPs were probably oxidised and then precipitated as sulfided AgNPs.

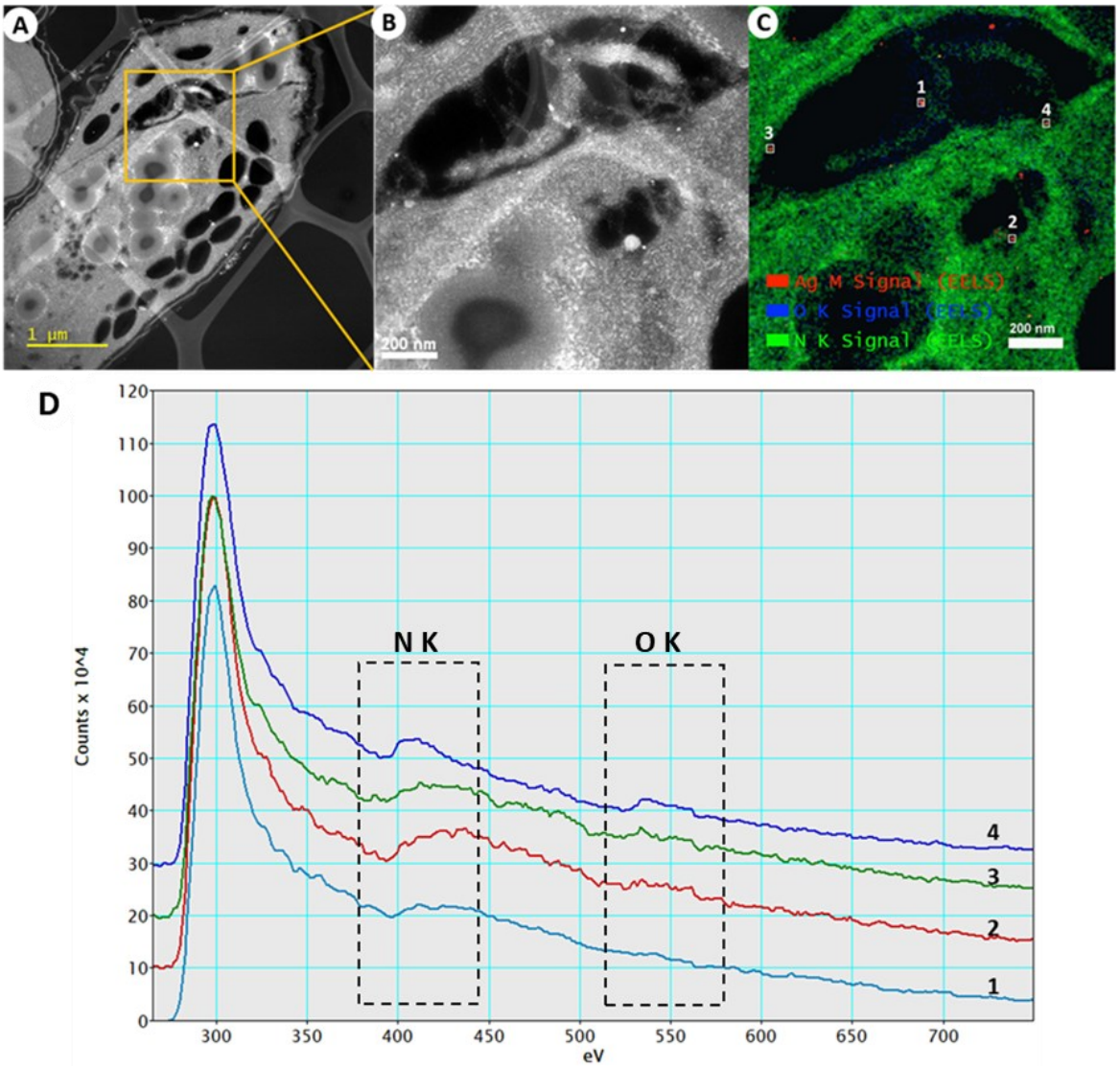

Figure 6-14: (A) Annular darkfield (ADF) imaging taken at a low magnification to illustrate the morphology of algal cells which exposed to AgNPs incubated for 24 hrs under light and selected a yellow box to show (B) a magnified (ADF) image. (C) An EEL spectrum image was collected from the selected area in A. The different colours are spectral chemical maps of the Ag M-edge (red), O K-edge (blue), and N K-edge (green). D shows the EELS spectra taken across the Ag, N and C edges taken at different locations 1-4 (D).

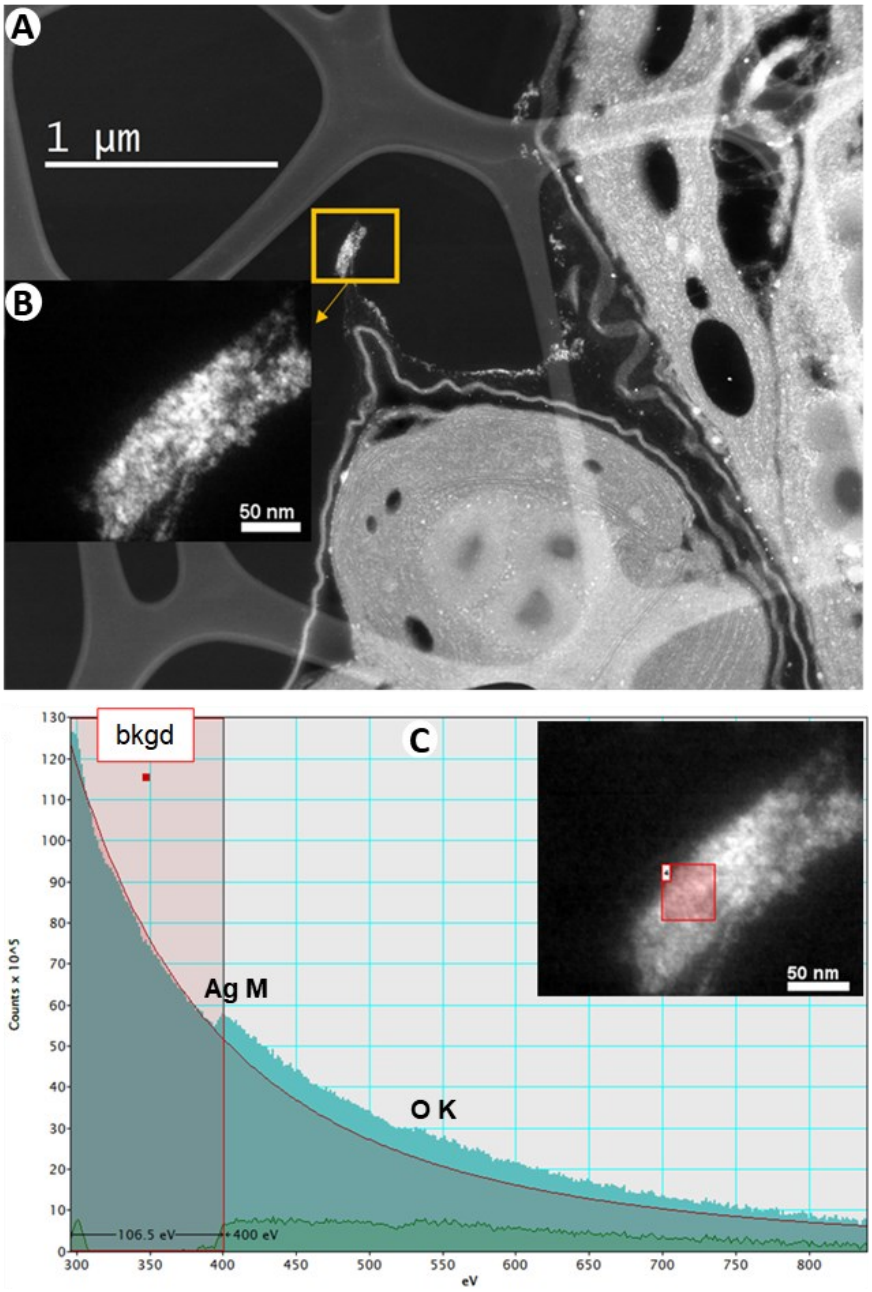

Figure 6-15: (A) an annular dark field image of a montage of images showing the outer cell wall of algae exposed to AgNPs (1mg/l) under light for 24 h. (B) The magnified area in the yellow square showing the EPS released from the outer cell wall which had trapped AgNPs. (C) EEL spectrum from the selected area within the red square in the inset (taken from the yellow square in image A). The EEL spectrum shows both the Ag M-edge and the O K-edge and indicates presence of an Ag peak but an absence of the O peak.

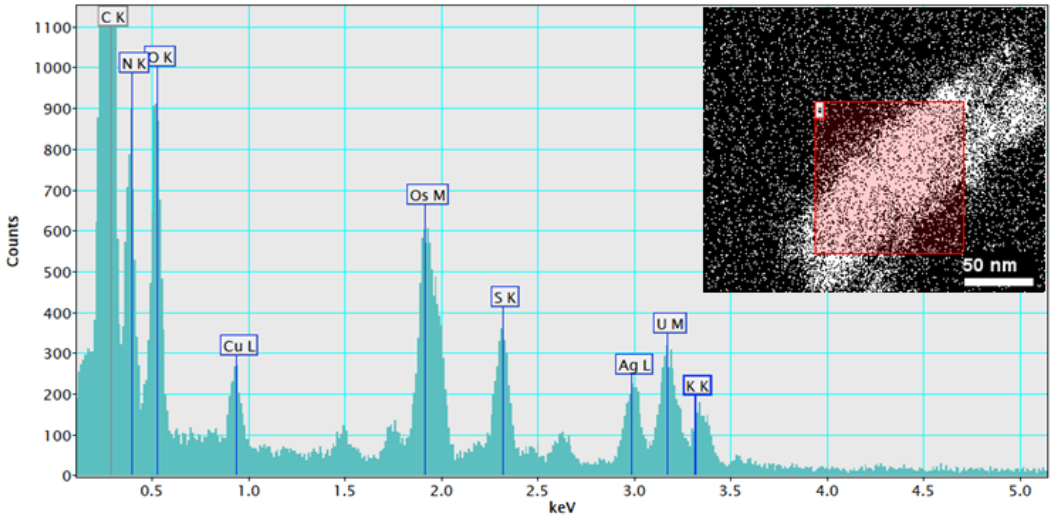

Figure 6-16: EDS has identified the elemental composition of the aggregated Ag with EPS located on the outer cell wall of algae exposed to AgNPs (1mg/l) under light for 24 h. The EDS had taken from the area in the red square image in the right.

To sum up, this work had shown the chemistry of AgNPs in OECD-MOPs medium under different light conditions before and after incubated within *R. subcapitata* algae. The dissolution of AgNPs in OECD-MOPS in presence and absence of EPS were studied to illustrate the effect of EPS which lead a protein corona around AgNPs. In contrast, ageing AgNPs without EPS had oxidised and ions releases then particles formed to more stabilised particles. The impact of aged AgNPs on the intercellular structure shows deformation and EPS release from the outer cell wall. Even though EPS were released around the outer cell wall as a protection mechanism, that could not protect the algae from AgNPs which breached the cell wall and found in the cytoplasm and periplasmic spaces, creating a filamentous structure. The observations of the cellular structure under light and UV-light have the same effect, but under UV-light, the hairy shape of EPS formed on both the non-treated and treated algae following incubation with the aged AgNPs.

Using EELS and finding ELNES techniques in a complex environment such as the cell compartment is unique, which first time applied in this work. These approved that chemistry of the aged AgNPs under light for 24 hr incubation which have reached different cell compartments. The speciation of aged AgNPs within the cell compartments showed a signal at the O K-edge confirming that the oxidised AgNPs are located near vacuoles. While

the presence of N K-edge and O K-edge for AgNPs showed they are located within subcellular organelles and bind to proteins within these structures. The chemical speciation of PVP-AgNPs in *Chlamydomonas reinhardtii* after cellular internalised has previously been investigated by synchrotron X-ray absorption spectroscopy. In that report, PVP-AgNPs located inside the cytoplasm in crystalline and amorphous forms that were identified them as β-Ag_2S and silver thiolates [269]. In different report, the speciation of Ag within treated bacteria was studied by XANES and showed that the Ag had mainly bound to sulfur, nitrogen and oxygen. This can be explained by the fact that silver strongly binds to enzymes which have S-containing side chains, while the Ag-N and Ag-O bonds bind to nucleic acids in DNA [270].

In contrast, the speciation of aged AgNPs trapped by EPS had showed no O K-edge, which confirmed no oxidation of AgNPs. However, the EDS showed oxygen and sulfur peaks, indicating that AgNPs had oxidised before aggregating and sulfided within the EPS which contains sulfur. The interaction between EPS and AgNPs can be involved by amino and aromatic carboxylic groups in the EPS [271]. Both AgNPs and $AgNO_3$ were oxidised the aldehyde groups on the cell surface to carboxyl groups by Ag+ in the presence of EPS in algal cells [257].

Regarding the impact of medium speciation, calculations applied by VISUAL MINTEQ software found that the majority of speciation caused by concentration of Cl , followed by thiosulfate; this was reported at low concentration of Ag, when chloride is a vital component in a medium [267]. Even though 1 mg/l AgNPs is considered a high concentration for cell incubation, the chloride speciation effects remarkably complied with this concentration. Presumably, the dissolution rate might have increased during the ageing time and photoinduced process. As a result, more Ag ions were released and suspended in the medium or underwent aggregation and complexation by the formation of AgCl and AgS_2O_3 speciation. However, calculations could not predict the speciation in the medium when considering EPS composition and the photo-transformation impact in the calculations.

6.3.3.4. The effect of dose-dependency of ENPs on algal cells

The toxicity of nanoparticles is significantly dependent on the dose of the nanoparticles applied to the microorganisms. The most important factor is the dose of nanoparticles,

which indicates the minimum dose that causes toxicity to microorganisms. The cell viability depends on the dose and exposure conditions. For example, *C. vulgaris* treated with ZnO NPs showed a significant reduction in cell viability concentrations of 50, 100, 200, and 300 mg/l [140]. The viability of *S. aureus* (*Staphylococcus aureus*) and *K. pneumoniae* (*Klebsiella pneumoniae*) after treatment with AgClNPs also responded *via* a dose-dependent effect. According to the calculated concentration, which decreased the viability by 50% (IC_{50}), the treated *S. aureus* and *K. pneumoniae* with AgCl-NPs (silver chloride nanoparticles) had IC_{50} values of 156.8 µg/mL and 247.2 µg/mL, respectively [272].

A dose-dependent effect of AgNPs on algal cells has been studied to show its influence their growth [255,273]. In one study, the value of 50% growth inhibition, indicated as (EC_{50}), was calculated following a 72 hrs dose-response of *Euglena gracilis* algae to AgNPs and Ag+ in cell culture medium. The result indicated that the EC_{50} of Cit-AgNPs 20 nm and Cit-AgNPs 60 nm were respectively 2741 ± 410 µg/L and 5030 ± 416 µg/L while for Ag^{+} ions it was 162 ± 13 µg/L. This means that silver ions demonstrated more toxicity than Cit-AgNPs [256]. The growth inhibition values of the same tested algae exposed to AgNPs showed variability in some studies. For example, *R. subcapitata* were treated with AgNPs for 72 h, and the value of EC_{50} was 1.63 mg/l [240] while in other reports the IC_{50} was 0.19 mg/l [274]. In this thesis, the concentration of the aged AgNPs (1 mg/l) was selected to illustrate the impact of aged particles, which caused cell death and changed the cell morphology compared to the control one. In literature several methods are used to measure how the toxicological behaviour of ENPs are linked to different effects that contribute to the set of environmental guidelines.

6.3.3.5. The particle size effect on the internalisation processes

The mechanism of the internalisation of nanoparticles is explained as the accumulation of the particles inside the cell compartments. This mechanism strongly depends on the size of nanoparticles and their ability to exhibit a further release of ions and cause toxicity to algal cells. In this thesis, the internalisation of AgNPs has confirmed within the cell compartment with an average size of 14.3 ± 0.5 nm. The release of EPS contributed to binding of the AgNPs and Ag ions which can inhibit the cell internalisation and nanotoxicity [252]. Jiang et al. found that internalisation relies on the size of Herceptin-coated gold and Herceptin-coated silver nanoparticles, which strongly regulate the binding and activation of

membrane receptors and subsequent protein expression [275]. The penetration of the nanoparticles into bacterial cells was observed within a size of less than 10 nm [276]. The same mechanism was noticed for Ag^+ ions released from AgNPs and found in the cytoplasm as a form of Ag_2S [277]. The internalisation of AgNPs coated with branched polyethyleneimine had confirmed within *R. subcapitata* algae surface [254].

The treatment of $AgNO_3$ had observed more internalisation than the AgNPs (size between 10 and 60 nm), which showed more accumulation on the surface of *C. vulgaris* cells irrespective of EPS [257]. The presence and absence of EPS have indicated a different behaviour towards AgNPs and Ag^+ ions, which had bound causing reduction in the toxicity and internalisation [252]. In contrast, Zhang et al. reported no internalisation of AgNPs with different sizes (20 and 60 nm) toward *E.gracilis* algae [256]. The volume of *E.gracilis* was doubled after exposure to AgNPs (20 nm) with no noticeable internalisation, but an interaction of Ag ions released from AgNPs, with thiol groups of glycoproteins [278]. AgNPs (38–73 nm) were adsorbed on the algal cell by binding with extracellular and intracellular proteins [279].

6.4. Summary and conclusions

Different sizes of AgNPs could show a variation in cell reaction. The pore size on the cell wall and the size of nanoparticles can affect the pathway of the interaction between cells and nanoparticles; and also their aggregation state [267]. It has been suggested that AgNPs with a 20 nm size are more soluble and induce more releases of Ag ions, which allows for a higher degree of intracellular Ag ion uptake and therefore has high toxicity [256]. Another characteristic of smaller sizes is that they have larger surface areas, which facilitates direct contact between particles and increases the possibility of being absorbed by an organism [280]. Also, the capping agent is the stabilised coating layer on the surface of AgNPs, which may have a substantial influence on potential toxicity. It has been reported that Cit-AgNPs were more toxic than PVP-AgNPs regardless of their size and dissolution rate [281]. However, as there was no measurement of the concentration of Ag ions after incubation in the medium in the study, other factors that might have direct or indirect effects on the toxicological outcomes should not be neglected.

The toxicity mechanism depends on the physicochemical properties of nanoparticles, which

will be of greater concern when the main properties have an antibiotic effect. In principle, the dissolution of AgNPs is the foremost mechanism that induces toxicity for several reasons. This concentration (1 mg/l) was not the only reason for cell death, even though this is still considered the worst-case scenario for *R. subcapitata* algae caused by aged AgNPs. The observations of this investigation were that the AgNPs had shown an oxidation state when they reached the comportment of algae according to ELNES analysis. Also, some of these oxidised AgNPs were localised in the cytoplasm. Some of the aged AgNPs showed no oxidisation, but an N K-edge appeared in the ELNES analysis, which might confirm another speciation of Ag. Some AgNPs were found in an ionic state, which was confirmed by ICP-MS that some Ag^+ ions had released during the incubation. Regardless of the location of Ag found within the algal cell, the average size was 13±5 nm.

In summary, aged AgNPs can degrade intracellularly and taken up as Ag or AgO and trapped outside the cell as AgCl or Ag_2S. The aged AgNPs may dissolve in an acidic pH in the lysosomes that can lead to the release of Ag^+ ions and aggregated AgNPs then precipitated. The ageing process of AgNPs might not halt, therefore, and the transformation could be a source of cytotoxicity to the microorganism.

.

Chapter 7: Conclusion and future work

7. Conclusions and future work

In this thesis, the bioavailability of engineered nanoparticles is analysed to identify their transformation and potential impact on environmental microorganisms. AgNPs and other ENPs had utilized in many personal products. Therefore, this thesis tracked the possible pathways through which these ENPs could be passed through several environmental mediums and conditions. The first chapter focused on sulfidation by H_2S gas with and without organic matter, such as humic acid. In the second chapter, when the ENPs reached the WWTP, most of them would be incubated within sludge that had been anaerobically digested. The sewage sludge after the digestion process could mostly apply to the agricultural industry, which might allow ENPs to reach the environmental species.

The transformation of Cit-AgNPs has been investigated by mimicking environmental conditions. The Cit-AgNPs were sulfided under *in situ* conditions, which were based on generating H_2S gas and infused into colloidal solutions of Cit-AgNPs and HA-AgNPs. This investigation has been observed the physicochemical properties involved in size, crystallinity, and morphology. The sulfidation of AgNPs is a kinetic process that might be controlled by various environmental parameters. The direct sulfidation of the Cit-AgNPs within and without humic acid has shown a redox reaction could change the structure of Ag_2SNPs. The stable structure of Ag_2SNPs within humic acid represents their transformation in the environment. As the sulfidation process is a more favourable environmental interaction, therefore synthesising Ag_2SNPs with different coating agents have achieved to study their transformation and performance on the anaerobic digestion process.

In the present work, different ENMs were tested to compare their performance during anaerobic digestion with a focus on ZnENMs. The behaviour of selected ENMs (ZnONPs (80-200 nm), CeO_2, TiO_2, Cit-AgNPs, PVP-Ag_2SNPs (100 nm), and Cit-Ag_2SNPs) have been evaluated through studying their influence on changing pH and biogas production. These ENMs were set and measured to be the same concentration (10 mg/l) except the ZnONPs which had a concentration of 57 mg/l. In the literature, 1000 mg/l of ZnONPs inhibited the generation of biogas [223]; additionally, 57.4 mg/l of nano ZnONPs was estimated to inhibit methane production [224]. Therefore, in the first part, most ENMs had

shown the same trends of biogas production, except CeO_2, which had the highest biogas production.

In the second part, the performance of anaerobic digestion was analysed to demonstrate the effect of the ZnENMs and AgNMs on the biogas and pH of the digesters. This experiment was the first to study the chemical speciation of ZnONPs of two sizes and ZnSNPs. XAS helped to identify the speciation of ZnONPs, which has shown the majority of Zn adsorbed as Zn-Fe (ox) and the presence of ZnO at the end of the digestion. However, ZnSNPs had mostly transformed into $Zn_3(PO_4)_2$ at the end of the experiment. Moreover, ZnONPs with size of 80-200 nm and concentration of 50 mg/l had significant effects on the biogas production while the same ZnONPs with concentration of 500 mg/l had no effect that had the same for ZnSNPs at concentration of 500 mg/l.

At a fundamental level, the physiochemical properties of AgNPs can substantially alter their bioavailability in the environment. Depending on the conditions and parameters, the transformation of AgNPs can also be examined to recognize and monitor their changes towards several environmental species. The green freshwater microalgae *R. subcapitata* is a species that is noticeably sensitive to toxins and has a fast growth rate; accordingly, these are considered factors for a toxicity test [144,282]. Performing a biological assay investigating this alga was carefully planned by using a cultural medium with known composition, involving parameters to mimic real environments by utilizing light and dark exposure, ageing time, and EPS composition. In this experiment, the same methodology and parameters were applied for different types of AgNPs.

Interestingly, AgNPs showed diverse outcomes. In this investigation, the transformed nanoparticles impacted the cell structure. The cell wall changed to a hair-like structure by releasing EPS for protection. This algal cell can change its shape and size to avoid toxins reaching the intracellular organelles. The EPS in this investigation was represented by xanthan gum, which shows an impact on the AgNPs by releasing more ionic Ag. Therefore, released EPS did not protect the algal cell from the transformed AgNPs and the ionic form, which had reached the algae compartments and cytoplasm. The aged AgNPs were smaller and different chemistries according to the result of TEM micrographs and EELS spectra. Thus, the aged AgNPs had caused cell death to algae which have to be considered for environmental risks.

The toxic response of a microorganism has a direct relationship to cell density, growth inhibition, and reactive oxygen species (ROS). The impact of NPs on the cells is seen in different reactions that depend on the cell's density. This feature is also an important factor for growth, biochemical and physiological response, and ROS generation [283]. For example, according to the age of the cell when the cell undergoes division, daughters have no coat or a coat that is smaller than the mothers. Due to the EPS matrix arrangement, cells densities within biofilms are remarkably higher than for planktonic cells [284].

The toxicity of AgNPs has been studied together with growth inhibition. It was reported that AgNPs are considered very toxic, even in low concentrations, and inhibit growth. According to published work [240], 1.63 mg/l of AgNPs reduced the growth rate of *R. subcapitata* cells by 50%. The growth inhibition proved to be positively related to toxicity. However, a recent study showed a reduction in growth inhibition of *R. subcapitata* algae, when exposed to AgNPs, was due to medium characterisation influencing the changes in speciation, time, and algae concentration [273]. Moreover, for the same algal cells were found the impact of both AgNPs and Ag ions (100 µg/l and 124 µg/l, respectively) had increased the growth inhibition by more than 100% depending on dose-response of until 50 µg/l [285].

Likewise, it was observed that several variations and inversions between AgNPs and $AgNO_3$ toxicity responses, which equally affected growth inhibition, were likely to be dose-response relationships. Therefore, the dissolution of Ag ions was related to the dynamic system of a cell culture medium that contained chloride [285]. The dissolution kinetics of AgNPs is strongly dependent on the ratio of Ag/Cl, which can be expected [286]. Thus, chloride in the medium would cause a reduction in the toxicity of $AgNO_3$ towards this alga because of its low solubility [287]. Increasing the concentration of Ag thiosulphate complexes with low Ag ions in the medium was observed to heighten the ability of *R. subcapitata* algae to accumulate Ag [288]. Furthermore, a combination of physical and chemical properties are attributed to cell–nanoparticle interaction and toxicity, such as the aggregation rate, the size of the nanoparticles, and the capping agent. The high aggregation rate of high-density nanoparticles in a medium could impair cell division and therefore reduce growth rate, causing what has been called shading effects and photosynthesis inhibition [144].

For future work, to fully confirm the hollow sphere structure, 3D tomography would be advantageous. A proposal has been granted time Diamond Light Source to carry out these experiments in the near future. Central facility access is required since the system is optimised for 80 keV imaging, and the sample holder can access a wide-angle for full tomographic analysis (70° to -70°). Attempts were made at Imperial with 200 keV, but the sample was not stable because of the hydrocarbon content. Some preliminary result for tomography were taken in Imperial College (Figure 7-1, A and C), and the rest were taken in Diamond facility with Dr Emanuel Liberati (Figure 7-1, D-I).

Further investigation to understand the impact of these transformation on next stages of WWTP on soils such as incubation of transformed ENMs on biomass amended to soil. Also, more study can be applied to show the effects in the freshwater algae within in vitro study and link that to real word scenario. This study will extend more understanding the impact of aged AgNPs on algal health and their behaviour in much more depth.

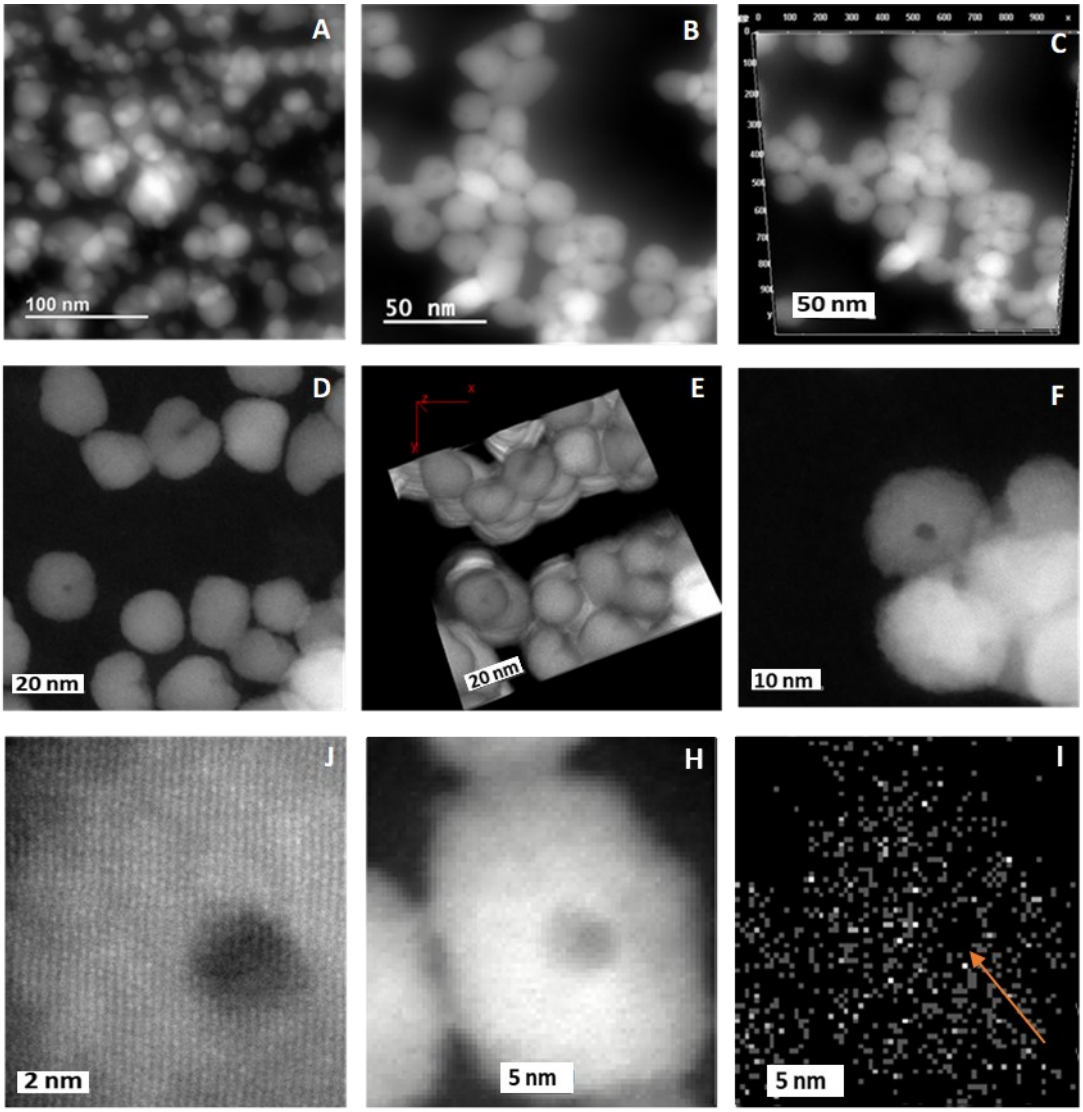

Figure 7-1: (A) HA-Ag_2SNPs were imaging directly without washing; (B) after washing the particles, more stability was observed (200 keV); (C) several of combined images were reconstructed (Tilt angle = 0-22 degrees and to -28 degrees); (D) in diamond facility DF-TEM have tested their stability by taking images or the same area until contamination was noticed; (E) 3D reconstruction for some images by ImageJ showing the hollow within a group of particles, (F) HR-HAADF of a particle with hollow structure, (J) Magnified image for the same particle (20Mx), (H) Annular darkfield image (ADF) 1.2M magnification, (I) EDS mapping for ADF image shows a cavity in the particle.

8. References

1. Lovestam, G. *et al. Considerations on a definition of nanomaterial for regulatory purposes*. *JRC Reference Reports* **24403**, (2010).

2. Tejamaya, M., Römer, I., Merrifield, R. C. & Lead, J. R. Stability of citrate, PVP, and PEG coated silver nanoparticles in ecotoxicology media. *Environ. Sci. Technol.* **46**, 7011–7017 (2012).

3. Nowack, B. & Bucheli, T. D. Occurrence, behavior and effects of nanoparticles in the environment. *Environ. Pollut.* **150**, 5–22 (2007).

4. Ansari, A. A., Alhoshan, M., Alsalhi, M. S. & Aldwayyan, A. S. Prospects of nanotechnology in clinical immunodiagnostics. *Sensors* **10**, 6535–6581 (2010).

5. Piccinno, F., Gottschalk, F., Seeger, S. & Nowack, B. Industrial production quantities and uses of ten engineered nanomaterials in Europe and the world. *J. Nanoparticle Res.* **14**, (2012).

6. Kim, B., Park, C. S., Murayama, M. & Hochella, M. F. Discovery and characterization of silver sulfide nanoparticles in final sewage sludge products. *Environ. Sci. Technol.* **44**, 7509–7514 (2010).

7. Ma, R. *et al.* Fate of zinc oxide and silver nanoparticles in a pilot wastewater treatment plant and in processed biosolids. *Environ. Sci. Technol.* **48**, 104–112 (2014).

8. Barton, B. Mineral. Soc. Amer. Spec. Pap. 3, 187-198 (1970). **198**, 187–198 (1970).

9. Environment Agency The determination of easily liberated sulphide in soils and similar matrices (2010). (2010).

10. Edwards, P. Sulfur cycling, retention, and mobility in soils: a review. *Gen. Tech. Rep.* **NE-250**, 1–18 (1998).

11. Lombi, E. *et al.* Fate of zinc oxide nanoparticles during anaerobic digestion of wastewater and post-treatment processing of sewage sludge. *Environ. Sci. Technol.* **46**, 9089–9096 (2012).

12. Wang, Y., Westerhoff, P. & Hristovski, K. D. Fate and biological effects of silver, titanium dioxide, and C 60 (fullerene) nanomaterials during simulated wastewater treatment processes. *J. Hazard. Mater.* **201**–**202**, 16–22 (2012).

13. Gottschalk, F., Sonderer, T., Scholz, R. W. & Nowack, B. Modeled Environmental Concentrations of Engineered Fullerenes) for Different Regions. *Environ. Sci. Technol.* **43**, 9216–9222 (2009).

14. Durenkamp, M. *et al.* Nanoparticles within WWTP sludges have minimal impact on leachate quality and soil microbial community structure and function. *Environ. Pollut.* **211**, 399–405 (2016).

15. THURMAN, E. M. *ORGANIC GEOCHEMISTRY OF NATURAL WATERS*. *Martinus NijhofflDr W. Junk Publishers,* (1985). doi:110.1007/978-94-009-5095-5

16. Świetlik, J., Dąbrowska, A., Raczyk-Stanisławiak, U. & Nawrocki, J. Reactivity of natural organic matter fractions with chlorine dioxide and ozone. *Water Res.* **38**, 547–558 (2004).

17. Sillanpää, M., Matilainen, A. & Lahtinen, T. *Characterization of NOM*. *Natural Organic Matter in Water: Characterization and Treatment Methods* (Elsevier Inc., 2015). doi:10.1016/B978-0-12-801503-2.00002-1

18. Collin, B., Tsyusko, O. V., Starnes, D. L. & Unrine, J. M. Effect of natural organic matter on dissolution and toxicity of sulfidized silver nanoparticles to: Caenorhabditis elegans. *Environ. Sci. Nano* **3**, 728–736 (2016).

19. Jiang, C., Aiken, G. R. & Hsu-Kim, H. Effects of Natural Organic Matter Properties on the Dissolution Kinetics of Zinc Oxide Nanoparticles. *Environ. Sci. Technol.* **49**, 11476–11484 (2015).

20. Huang, T., Sui, M., Yan, X., Zhang, X. & Yuan, Z. Anti-algae efficacy of silver

nanoparticles to Microcystis aeruginosa: Influence of NOM, divalent cations, and pH. *Colloids Surfaces A Physicochem. Eng. Asp.* **509**, 492–503 (2016).

21. Gottschalk, F., Sun, T. & Nowack, B. Environmental concentrations of engineered nanomaterials: Review of modeling and analytical studies. *Environ. Pollut.* **181**, 287–300 (2013).

22. Cervantes-avilés, P., Ida, J., Toda, T. & Cuevas-rodríguez, G. E ff ects and fate of TiO 2 nanoparticles in the anaerobic treatment of wastewater and waste sludge. **222**, 227–233 (2018).

23. Li, H., Cui, F., Liu, Z. & Li, D. Transport, fate, and long-term impacts of metal oxide nanoparticles on the stability of an anaerobic methanogenic system with anaerobic granular sludge. *Bioresour. Technol.* **234**, 448–455 (2017).

24. Mousavi, M. P. S. *et al.* Dynamic silver speciation as studied with fluorous-phase ion-selective electrodes: Effect of natural organic matter on the toxicity and speciation of silver. *Sci. Total Environ.* **537**, 453–461 (2015).

25. Von Moos, N., Bowen, P. & Slaveykova, V. I. Bioavailability of inorganic nanoparticles to planktonic bacteria and aquatic microalgae in freshwater. *Environmental Science: Nano* **1**, 214–232 (2014).

26. Klaine, S. J. *et al.* Nanomaterials in the environment: Behavior, fate, bioavailability, and effects. *Environmental Toxicology and Chemistry* **27**, 1825–1851 (2008).

27. Elsaesser, A. & Howard, C. V. Toxicology of nanoparticles. *Advanced Drug Delivery Reviews* **64**, 129–137 (2012).

28. Sonström, P. & Bäumer, M. Supported colloidal nanoparticles in heterogeneous gas phase catalysis: On the way to tailored catalysts. *Physical Chemistry Chemical Physics* **13**, 19270–19284 (2011).

29. Mafuné, F., Kohno, J. Y., Takeda, Y., Kondow, T. & Sawabe, H. Structure and stability of silver nanoparticles in aqueous solution produced by laser ablation. *J. Phys. Chem. B* **104**, 8336–8337 (2000).

30. Bhatt, I. & Tripathi, B. N. Interaction of engineered nanoparticles with various components of the environment and possible strategies for their risk assessment. *Chemosphere* **82**, 308–317 (2011).

31. Hunter, R. J. Zeta Potential in Colioid Science, Pbincipies and Applicution. *colloids Surf.* (1982).

32. Bond, A. M. *et al. Electroanalytical Methods Guide to Experiments and Applications 2nd, revised and extended edition*. (2009).

33. Ai, Y., Zhang, M., Joo, S. W., Cheney, M. A. & Qian, S. Effects of electroosmotic flow on ionic current rectification in conical nanopores. *J. Phys. Chem. C* **114**, 3883–3890 (2010).

34. Kobayashi, M., Juillerat, F., Galletto, P., Bowen, P. & Borkovec, M. Aggregation and charging of colloidal silica particles: Effect of particle size. *Langmuir* **21**, 5761–5769 (2005).

35. Behrens, S. H., Christl, D. I., Emmerzael, R., Schurtenberger, P. & Borkovec, M. Charging and aggregation properties of carboxyl latex particles: Experiments versus DLVO theory. *Langmuir* **16**, 2566–2575 (2000).

36. Li, X., Lenhart, J. J. & Walker, H. W. Aggregation kinetics and dissolution of coated silver nanoparticles. *Langmuir* **28**, 1095–1104 (2012).

37. Navarro, E. *et al.* Environmental behavior and ecotoxicity of engineered nanoparticles to algae, plants, and fungi. *Ecotoxicology* **17**, 372–386 (2008).

38. Lau, E. Preformulation studies. *Sep. Sci. Technol.* **3**, 173–233 (2001).

39. Mihranyan, A. & Strømme, M. Solubility of fractal nanoparticles. *Surf. Sci.* **601**, 315–319 (2007).

40. Ju-Nam, Y. & Lead, J. R. Manufactured nanoparticles: An overview of their chemistry, interactions and potential environmental implications. *Sci. Total Environ.* **400**, 396–414 (2008).

41. Daniel, M. C. & Astruc, D. Gold Nanoparticles: Assembly, Supramolecular Chemistry, Quantum-Size-Related Properties, and Applications Toward Biology, Catalysis, and Nanotechnology. *Chem. Rev.* **104**, 293–346 (2004).

42. Rotello, V. *Nanoparticles Building Blocks for Nanotechnology N anostructure Science and Technology*. *Nanostructure Science and Technology* (New York, Springer, 2003).

43. Roche, I. R. The ecotoxicological and environmental behaviour and transformations of silver nanoparticles By. (2012).

44. Turkevich, J., Stevenson, P. C. & Hillier, J. A study of the nucleation and growth processes in the synthesis of colloidal gold. *Discuss. Faraday Soc.* **11**, 55 (1951).

45. Li, C., Li, D., Wan, G., Xu, J. & Hou, W. Facile synthesis of concentrated gold nanoparticles with low size-distribution in water: temperature and pH controls. *Nanoscale Res. Lett.* **6**, 440 (2011).

46. Solomon, S. D. *et al.* Synthesis and study of silver nanoparticles. *J. Chem. Educ.* **84**, 322–325 (2007).

47. Glavee, G. N., Klabunde, K. J., Sorensen, C. M. & Hadjapanayis, G. C. Borohydride reductions of metal ions. A new understanding of the chemistry leading to nanoscale particles of metals, borides, and metal borates. *Langmuir* **8**, 771–773 (1992).

48. Silvert, P.-Y., Herrera-Urbina, R. & Tekaia-Elhsissen, K. Preparation of colloidal silver dispersions by the polyol process. *J. Mater. Chem.* **7**, 293–299 (1997).

49. Pillai, Z. S. & Kamat, P. V. What Factors Control the Size and Shape of Silver Nanoparticles in the Citrate Ion Reduction Method? *J. Phys. Chem. B* **108**, 945–951 (2004).

50. Belloni, J., Mostafavi, M., Remita, H., Marignier, J.-L. & Delcourt, and M.-O. Radiation-induced synthesis of mono- and multi-metallic clusters and nanocolloids. *New J. Chem.* **22**, 1239–1255 (1998).

51. Roh, J. *et al.* Dispersion stability of citrate- and PVP-AgNPs in biological media for

cytotoxicity test. *Korean J. Chem. Eng.* **30**, 671–674 (2013).

52. ENV/CHEM/NANO. OECD WPMN, Dossier develoment plan: Silver nanoparticles,. (2009).

53. Graf, C., Dembski, S., Hofmann, A. & Rühl, E. A general method for the controlled embedding of nanoparticles in silica colloids. *Langmuir* **22**, 5604–5610 (2006).

54. Al-Saidi, W. A., Feng, H. & Fichthorn, K. A. Adsorption of polyvinylpyrrolidone on Ag surfaces: Insight into a structure-directing agent. *Nano Lett.* **12**, 997–1001 (2012).

55. Xiong, Y. *et al.* Synthesis and mechanistic study of palladium nanobars and nanorods. *J. Am. Chem. Soc.* **129**, 3665–3675 (2007).

56. Kedia, A. & Kumar, P. S. Solvent-adaptable poly(vinylpyrrolidone) binding induced anisotropic shape control of gold nanostructures. *J. Phys. Chem. C* **116**, 23721–23728 (2012).

57. Kwon, S. & Messing, G. L. The effect of particle solubility on the strength of nanocrystalline agglomerates: Boehmite. *Nanostructured Mater.* **8**, 399–418 (1997).

58. Baalousha, M., Nur, Y., Römer, I., Tejamaya, M. & Lead, J. R. Effect of monovalent and divalent cations, anions and fulvic acid on aggregation of citrate-coated silver nanoparticles. *Sci. Total Environ.* **454**–**455**, 119–131 (2013).

59. BUTLER, J. A. V. Theory of the Stability of Lyophobic Colloids. *Nature* **162**, 315–316 (1948).

60. Piacenza, E. *et al.* stabilization theory of chemical nanostructures Stability of biogenic metal (loid) nanomaterials related to the colloidal stabilization theory of chemical nanostructures. *Crit. Rev. Biotechnol.* **0**, 1–20 (2018).

61. Milani, N. & McLaughlin, M. J. Zinc oxide nanoparticles in the soil environment: dissolution, speciation, retention and bioavailability. *Soil Sci. Group, Sch. Agric. Food Wine* **Doctor of**, 164 (2011).

62. Hotze, E. M., Phenrat, T. & Lowry, G. V. Nanoparticle Aggregation: Challenges to Understanding Transport and Reactivity in the Environment. *J. Environ. Qual.* **39**, 1909 (2010).

63. He, Y. T., Wan, J. & Tokunaga, T. Kinetic stability of hematite nanoparticles: The effect of particle sizes. *J. Nanoparticle Res.* **10**, 321–332 (2008).

64. Mitrano, D. M., Motellier, S., Clavaguera, S. & Nowack, B. Review of nanomaterial aging and transformations through the life cycle of nano-enhanced products. *Environ. Int.* **77**, 132–147 (2015).

65. Klaine, S. J. *et al.* Paradigms to assess the environmental impact of manufactured nanomaterials. *Environ. Toxicol. Chem.* **31**, 3–14 (2012).

66. Office, U. P. Extract of Patent List of AgNP applications. *US Pat. 2,996,236* (1961).

67. European Environment Agency. Waste Sewage sludge -a future waste problem? 7 (2001).

68. Gorka, D. E. *et al.* Reducing Environmental Toxicity of Silver Nanoparticles through Shape Control. *Environ. Sci. Technol.* **49**, 10093–10098 (2015).

69. Kaegi, R. *et al.* Behavior of metallic silver nanoparticles in a pilot wastewater treatment plant. *Environ. Sci. Technol.* **45**, 3902–3908 (2011).

70. Kaegi, R. *et al.* Fate and transformation of silver nanoparticles in urban wastewater systems. *Water Res.* **47**, 3866–3877 (2013).

71. Barron, M. F. E. The Effects of Early Reflections on Subjective Acoustical Quality in Concert Halls. *Philosophy* **93**, 241 (1974).

72. Donner, E. *et al.* Non-labile silver species in biosolids remain stable throughout 50 years of weathering and ageing. *Environ. Pollut.* **205**, 78–86 (2015).

73. Levard, C. *et al.* Sulfidation of silver nanoparticles: Natural antidote to their toxicity. *Environ. Sci. Technol.* **47**, 13440–13448 (2013).

74. Levard, C., Hotze, E. M., Lowry, G. V. & Brown, G. E. Environmental

transformations of silver nanoparticles: Impact on stability and toxicity. *Environmental Science and Technology* **46**, 6900–6914 (2012).

75. Liu, J. & Jiang, G. Silver nanoparticles in the environment. *Silver Nanoparticles Environ.* 1–152 (2015). doi:10.1007/978-3-662-46070-2

76. Liu, J., Pennell, K. G. & Hurt, R. H. Kinetics and mechanisms of nanosilver oxysulfidation. *Environ. Sci. Technol.* **45**, 7345–7353 (2011).

77. Peretyazhko, T. S., Zhang, Q. & Colvin, V. L. Size-controlled dissolution of silver nanoparticles at neutral and acidic pH conditions: Kinetics and size changes. *Environ. Sci. Technol.* **48**, 11954–11961 (2014).

78. Zhang, W., Yao, Y., Sullivan, N. & Chen, Y. Modeling the primary size effects of citrate-coated silver nanoparticles on their ion release kinetics. *Environ. Sci. Technol.* **45**, 4422–4428 (2011).

79. Stabryla, L. M., Johnston, K. A., Millstone, J. E. & Gilbertson, L. M. Emerging investigator series: It's not all about the ion: Support for particle-specific contributions to silver nanoparticle antimicrobial activity. *Environ. Sci. Nano* **5**, 2047–2068 (2018).

80. Liu, J. & Hurt, R. H. Ion release kinetics and particle persistence in aqueous nano-silver colloids. *Environ. Sci. Technol.* **44**, 2169–2175 (2010).

81. Molleman, B. & Hiemstra, T. Surface Structure of Silver Nanoparticles as a Model for Understanding the Oxidative Dissolution of Silver Ions. *Langmuir* **31**, 13361–13372 (2015).

82. Reinsch, B. C. *et al.* Sulfidation of Silver Nanoparticles Decreases Escherichia coli Growth Inhibition. (2012). doi:10.1021/es203732x

83. He, D. *et al.* Silver sulfide nanoparticles in aqueous environments: Formation, transformation and toxicity. *Environ. Sci. Nano* **6**, 1674–1687 (2019).

84. Li, L., Xu, Z., Wimmer, A., Tian, Q. & Wang, X. New Insights into the Stability of Silver Sul fi de Nanoparticles in Surface Water: Dissolution through Hypochlorite

Oxidation. (2017). doi:10.1021/acs.est.7b01738

85. Nichols, G. *et al.* A review of the terms agglomerate and aggregate with a recommendation for nomenclature used in powder and particle characterization. *J. Pharm. Sci.* **91**, 2103–2109 (2002).

86. He, D. *et al.* Silver Sulfide Nanoparticles in Aqueous Environments : Formation , Transformation and Toxicity. (2019).

87. Manoharan, V., Ravindran, A. & Anjali, C. H. Mechanistic Insights into Interaction of Humic Acid with Silver Nanoparticles. *Cell Biochem. Biophys.* **68**, 127–131 (2014).

88. F. J. Stevenson. Humus chemistry: Genesis, composition, reactions. *Wiley* **2**, 223 (1994).

89. De Melo, B. A. G., Motta, F. L. & Santana, M. H. A. Humic acids: Structural properties and multiple functionalities for novel technological developments. *Mater. Sci. Eng. C* **62**, 967–974 (2016).

90. Mirza, M. A. *et al.* Role of humic acid on oral drug delivery of an antiepileptic drug. *Drug Dev. Ind. Pharm.* **37**, 310–319 (2011).

91. Zhu, T., Lawler, D. F., Chen, Y. & Lau, B. L. T. Effects of natural organic matter and sulfidation on the flocculation and filtration of silver nanoparticles. *Environ. Sci. Nano* **3**, 1436–1446 (2016).

92. Leyton, P. *et al. Humic acids as molecular assemblers in the surface-enhanced Raman scattering detection of polycyclic aromatic hydrocarbons*.

93. Scott, D. T., Mcknight, D. M., Blunt-Harris, E. L., Kolesar, S. E. & Lovley, D. R. Quinone moieties act as electron acceptors in the reduction of humic substances by humics-reducing microorganisms. *Environ. Sci. Technol.* **32**, 2984–2989 (1998).

94. Kappler, A., Benz, M., Schink, B. & Brune, A. Electron shuttling via humic acids in microbial iron(III) reduction in a freshwater sediment. *FEMS Microbiol. Ecol.* **47**, 85–92 (2004).

95. Lovley, D. R., Coatest, J. D., Blunt-harris, E. L., Phillipst, E. J. P. & Woodward, J. C. Humic substances as electron acceptors for microbial respiration. *Nature* **382**, 445–448 (1996).

96. Heitmann, T. & Blodau, C. Oxidation and incorporation of hydrogen sulfide by dissolved organic matter. *Chem. Geol.* **235**, 12–20 (2006).

97. Yu, Z. G., Peiffer, S., G??ttlicher, J. & Knorr, K. H. Electron transfer budgets and kinetics of abiotic oxidation and incorporation of aqueous sulfide by dissolved organic matter. *Environ. Sci. Technol.* **49**, 5441–5449 (2015).

98. Yu, Z. G., Orsetti, S., Haderlein, S. B. & Knorr, K. H. Electron Transfer Between Sulfide and Humic Acid: Electrochemical Evaluation of the Reactivity of Sigma-Aldrich Humic Acid Toward Sulfide. *Aquat. Geochemistry* **22**, 117–130 (2016).

99. Sánchez-Cortés, S., Francioso, O., Ciavatta, C., García-Ramos, J. V. & Gessa, C. pH-Dependent adsorption of fractionated peat humic substances on different silver colloids studied by surface-enhanced Raman spectroscopy. *J. Colloid Interface Sci.* **198**, 308–318 (1998).

100. Dong, B., Liu, G., Zhou, J., Wang, J. & Jin, R. Transformation of silver ions to silver nanoparticles mediated by humic acid in darkness at ambient temperature. *J. Hazard. Mater.* **383**, 121190 (2019).

101. Wang, L. *et al.* Use of Synchrotron Radiation-Analytical Techniques to Reveal Chemical Origin of Silver-Nanoparticle Cytotoxicity. *ACS Nano* **9**, 6532–6547 (2015).

102. Kent, R. D., Oser, J. G. & Vikesland, P. J. Controlled evaluation of silver nanoparticle sulfidation in a full-scale wastewater treatment plant. *Environ. Sci. Technol.* **48**, 8564–8572 (2014).

103. Baalousha, M., Arkill, K. P., Romer, I., Palmer, R. E. & Lead, J. R. Transformations of citrate and Tween coated silver nanoparticles reacted with Na2S. *Sci. Total Environ.* **502**, 344–353 (2015).

104. Thalmann, B., Voegelin, A., Morgenroth, E. & Kaegi, R. *Effect of Humic Acid on the Kinetics of Silver Nanoparticle Sulfidation*. (2015).

105. Levard, C. *et al.* Sulfidation processes of PVP-coated silver nanoparticles in aqueous solution: Impact on dissolution rate. *Environ. Sci. Technol.* **45**, 5260–5266 (2011).

106. Li, L., Wang, Y., Liu, Q. & Jiang, G. Rethinking Stability of Silver Sulfide Nanoparticles (Ag2S-NPs) in the Aquatic Environment: Photoinduced Transformation of Ag2S-NPs in the Presence of Fe(III). *Environ. Sci. Technol.* **50**, 188–196 (2016).

107. Li, M., Lin, D. & Zhu, L. Effects of water chemistry on the dissolution of ZnO nanoparticles and their toxicity to Escherichia coli. *Environ. Pollut.* **173**, 97–102 (2013).

108. Taglietti, A. *et al.* Antibacterial activity of glutathione-coated silver nanoparticles against gram positive and gram negative bacteria. *Langmuir* **28**, 8140–8148 (2012).

109. Kim, J. S. *et al.* Antimicrobial effects of silver nanoparticles. *Nanomedicine Nanotechnology, Biol. Med.* **3**, 95–101 (2007).

110. J. Ruben Morones-Ramirez, Jonathan A. Winkler Catherine S. Spina, and J. J. C. Silver Enhances Antibiotic Activity Against Gram-negative Bacteria. *Sci Transl Med* **5**, (2013).

111. Yu, S. *et al.* Silver nanoparticles in the environment. *Environ. Sci. Process. Impacts* **15**, 78–92 (2013).

112. Bondarenko, O., Ivask, A., Käkinen, A., Kurvet, I. & Kahru, A. Particle-Cell Contact Enhances Antibacterial Activity of Silver Nanoparticles. *PLoS One* **8**, (2013).

113. Le Ouay, B. & Stellacci, F. Antibacterial activity of silver nanoparticles: A surface science insight. *Nano Today* **10**, 339–354 (2015).

114. Xiu, Z. M., Zhang, Q. B., Puppala, H. L., Colvin, V. L. & Alvarez, P. J. J. Negligible particle-specific antibacterial activity of silver nanoparticles. *Nano Lett.* **12**, 4271–4275 (2012).

115. Fabrega, J., Fawcett, S. R., Renshaw, J. C. & Lead, J. R. Silver nanoparticle impact on bacterial growth: Effect of pH, concentration, and organic matter. *Environ. Sci. Technol.* **43**, 7285–7290 (2009).

116. Das, P., Xenopoulos, M. A., Williams, C. J., Hoque, M. E. & Metcalfe, C. D. Effects of silver nanoparticles on bacterial activity in natural waters. *Environ. Toxicol. Chem.* **31**, 122–130 (2012).

117. Wang, J. *et al.* Phytostimulation of poplars and Arabidopsis exposed to silver nanoparticles and Ag+ at sublethal concentrations. *Environ. Sci. Technol.* **47**, 5442–5449 (2013).

118. Dimkpa, C. O. *et al.* Silver nanoparticles disrupt wheat (Triticum aestivum L.) growth in a sand matrix. *Environ. Sci. Technol.* **47**, 1082–1090 (2013).

119. Kaveh, R. *et al.* Changes in *Arabidopsis thaliana* Gene Expression in Response to Silver Nanoparticles and Silver Ions. *Environ. Sci. Technol.* **47**, 130909124000000 (2013).

120. Kwok, K. W. H. *et al.* Uptake of silver nanoparticles and toxicity to early life stages of Japanese medaka (Oryzias latipes): Effect of coating materials. *Aquat. Toxicol.* **120**–**121**, 59–66 (2012).

121. Bar-Ilan, O., Albrecht, R. M., Fako, V. E. & Furgeson, D. Y. Toxicity assessments of multisized gold and silver nanoparticles in zebrafish embryos. *Small* **5**, 1897–1910 (2009).

122. Gallo, L. C. *et al.* The Hispanic Community Health Study/Study of Latinos Sociocultural Ancillary Study: Sample, design, and procedures. *Ethn. Dis.* **24**, 77–83 (2014).

123. Warden, S. J. & Mantila Roosa, S. M. Physical activity completed when young has residual bone benefits at 94 years of age: A within-subject controlled case study. *J. Musculoskelet. Neuronal Interact.* **14**, 239–243 (2014).

124. Doolette, C. L. *et al.* Transformation of PVP coated silver nanoparticles in a

simulated wastewater treatment process and the effect on microbial communities. *Chem. Cent. J.* **7**, 1–19 (2013).

125. Meier, C. *et al.* Transformation of Silver Nanoparticles in Sewage Sludge during Incineration. *Environ. Sci. Technol.* **50**, 3503–3510 (2016).

126. Ma, R. *et al.* Fate of zinc oxide and silver nanoparticles in a pilot waste water treatment plant and in processed biosolids Fate of zinc oxide and silver nanoparticles in a pilot waste water treatment plant and in processed biosolids. *Environ. Sci. Technol* **48**, 104–112 (2014).

127. Rick VandeVoort, A., Tappero, R. & Arai, Y. Residence time effects on phase transformation of nanosilver in reduced soils. *Environ. Sci. Pollut. Res.* **21**, 7828–7837 (2014).

128. Lowry, G. V. *et al.* Long-term transformation and fate of manufactured Ag nanoparticles in a simulated large scale freshwater emergent wetland. *Environ. Sci. Technol.* **46**, 7027–7036 (2012).

129. Chester, R. *et al. Pollution*. (The Royal Society of Chemistry, 2001). doi:10.1039/9781847551719

130. Garg, N. K. Multicriteria Assessment of Alternative Sludge Disposal Methods Neeraj Kumar Garg. *Environment* 1–81 (2009).

131. Sirelkhatim, A. *et al.* Review on zinc oxide nanoparticles: Antibacterial activity and toxicity mechanism. *Nano-Micro Lett.* **7**, 219–242 (2015).

132. Safa Kasap, P. C. (Eds. . *Springer Handbook of Electronic and Photonic Materials:Doping Aspects of Zn-Based Wide-Band-Gap Semiconductors*. (2006).

133. Fan, Z. & Lu, J. G. Zinc oxide nanostructures: Synthesis and properties. *J. Nanosci. Nanotechnol.* **5**, 1561–1573 (2005).

134. Wang, Z. L. & Song, J. *Piezoelectric Nanogenerators Based on Zinc Oxide Nanowire Arrays*.

135. Janotti, A. & Van De Walle, C. G. Fundamentals of zinc oxide as a semiconductor. *Reports Prog. Phys.* **72**, (2009).

136. Zhang, Y., Ram, M. K., Stefanakos, E. K. & Goswami, D. Y. Synthesis, characterization, and applications of ZnO nanowires. *J. Nanomater.* **2012**, (2012).

137. Schmidt-Mende, L. & MacManus-Driscoll, J. L. ZnO - nanostructures, defects, and devices. *Mater. Today* **10**, 40–48 (2007).

138. Wellings, J. S., Chaure, N. B., Heavens, S. N. & Dharmadasa, I. M. Growth and characterisation of electrodeposited ZnO thin films. *Thin Solid Films* **516**, 3893–3898 (2008).

139. Song, Z. *et al.* Characterization of optical properties of ZnO nanoparticles for quantitative imaging of transdermal transport. *Biomed. Opt. Express* **2**, 3321 (2011).

140. Suman, T. Y., Radhika Rajasree, S. R. & Kirubagaran, R. Evaluation of zinc oxide nanoparticles toxicity on marine algae chlorella vulgaris through flow cytometric, cytotoxicity and oxidative stress analysis. *Ecotoxicol. Environ. Saf.* **113**, 23–30 (2015).

141. Yung, M. M. N., Mouneyrac, C. & Leung, K. M. Y. Ecotoxicity of Zinc Oxide Nanoparticles in the Marine Environment. in *Encyclopedia of Nanotechnology* 1–17 (Springer Netherlands, 2014). doi:10.1007/978-94-007-6178-0_100970-1

142. Lee, W. M. & An, Y. J. Effects of zinc oxide and titanium dioxide nanoparticles on green algae under visible, UVA, and UVB irradiations: No evidence of enhanced algal toxicity under UV pre-irradiation. *Chemosphere* **91**, 536–544 (2013).

143. Samei, M., Sarrafzadeh, M. H. & Faramarzi, M. A. The impact of morphology and size of zinc oxide nanoparticles on its toxicity to the freshwater microalga, Raphidocelis subcapitata. *Environ. Sci. Pollut. Res.* **26**, 2409–2420 (2019).

144. Aruoja, V., Dubourguier, H., Kasemets, K. & Kahru, A. Toxicity of nanoparticles of CuO , ZnO and TiO 2 to microalgae Pseudokirchneriella subcapitata. *Sci. Total Environ.* **407**, 1461–1468 (2008).

145. Yung, M. M. N. *et al.* Physicochemical characteristics and toxicity of surface-modified zinc oxide nanoparticles to freshwater and marine microalgae. *Sci. Rep.* **7**, (2017).

146. Manzo, S., Miglietta, M. L., Rametta, G., Buono, S. & Di Francia, G. Toxic effects of ZnO nanoparticles towards marine algae Dunaliella tertiolecta. *Sci. Total Environ.* **445**–**446**, 371–376 (2013).

147. Ji, J., Long, Z. & Lin, D. Toxicity of oxide nanoparticles to the green algae Chlorella sp. *Chem. Eng. J.* **170**, 525–530 (2011).

148. Legros, S., Levard, C., Marcato-Romain, C. E., Guiresse, M. & Doelsch, E. Anaerobic Digestion Alters Copper and Zinc Speciation. *Environ. Sci. Technol.* **51**, 10326–10334 (2017).

149. GRAEME E. BATLEY, JASON K. KIRBY, A. M. J. M. Fate and Risks of Nanomaterials in Aquatic and Terrestrial Environments GRAEME. *Acc. Chem. Res.* **46**, 854–862 (2013).

150. Del Real, A. E. P. *et al.* Fate of Ag-NPs in Sewage Sludge after Application on Agricultural Soils. *Environ. Sci. Technol.* **50**, 1759–1768 (2016).

151. Tourinho, P. S. *et al.* Metal-based nanoparticles in soil: Fate, behavior, and effects on soil invertebrates. *Environ. Toxicol. Chem.* **31**, 1679–1692 (2012).

152. El Badawy, A. M. *et al.* Impact of environmental conditions (pH, ionic strength, and electrolyte type) on the surface charge and aggregation of silver nanoparticles suspensions. *Environ. Sci. Technol.* **44**, 1260–1266 (2010).

153. Cornelis, G. *et al.* Solubility and batch retention of CeO2 nanoparticles in soils. *Environ. Sci. Technol.* **45**, 2777–2782 (2011).

154. Lead, J. R. & Wilkinson, K. J. Aquatic colloids and nanoparticles: Current knowledge and future trends. *Environ. Chem.* **3**, 159–171 (2006).

155. Arnaout, C. L. *Assessing the Impacts of Silver Nanoparticles on the Growth, Diversity, and Function of Wastewater Bacteria*. (2012).

156. Schrick, B., Hydutsky, B. W., Blough, J. L. & Mallouk, T. E. Delivery vehicles for zerovalent metal nanoparticles in soil and groundwater. *Chem. Mater.* **16**, 2187–2193 (2004).

157. Allison, D. G. The Biofilm Matrix. *Biofouling* **19**, 139–150 (2003).

158. Xiao, Y. & Wiesner, M. R. Transport and retention of selected engineered nanoparticles by porous media in the presence of a biofilm. *Environ. Sci. Technol.* **47**, 2246–2253 (2013).

159. Mitzel, M. R. & Tufenkji, N. Transport of industrial PVP-stabilized silver nanoparticles in saturated quartz sand coated with Pseudomonas aeruginosa PAO1 biofilm of variable age. *Environ. Sci. Technol.* **48**, 2715–2723 (2014).

160. Ogendal, L. Light Scattering Demystified Theory and Practice. *Light Scatt. Demystified Theory Pract.* 129 (2019).

161. Araujo, J. V., Davidenko, N., Danner, M., Cameron, R. E. & Best, S. M. Novel porous scaffolds of pH responsive chitosan/carrageenan-based polyelectrolyte complexes for tissue engineering. *J. Biomed. Mater. Res. - Part A* **102**, 4415–4426 (2014).

162. Darlington, T. K., Neigh, A. M., Spencer, M. T., Nguyen, O. T. & Oldenburg, S. J. Nanoparticle characteristics affecting environmental fate and transport through soil. *Environ. Toxicol. Chem.* **28**, 1191–1199 (2009).

163. Li, X., Lenhart, J. J. & Walker, H. W. Dissolution-accompanied aggregation kinetics of silver nanoparticles. *Langmuir* **26**, 16690–16698 (2010).

164. Pillai, Z. S. & Kamat, P. V. What factors control the size and shape of silver nanoparticles in the citrate ion reduction method? *J. Phys. Chem. B* **108**, 945–951 (2004).

165. Ammari, H., Deng, Y. & Millien, P. Surface Plasmon Resonance of Nanoparticles and Applications in Imaging. *Arch. Ration. Mech. Anal.* **220**, 109–153 (2016).

166. Lakowicz, J. R. *Principles of fluorescence spectroscopy*. *Principles of Fluorescence*

Spectroscopy (2006). doi:10.1007/978-0-387-46312-4

167. Life, P. & Sciences, A. Concepts, Instrumentation and techniques in ICP-OES (nice book). *PerkinElmer* (2004).

168. Fatama Khan, K. Application, principle and operation of ICP-OES in pharmaceutical analysis. *~ 281 ~ Pharma Innov. J.* **8**, 281–282 (2019).

169. Williams, D. B. & Carter, C. B. *Transmission Electron Microscopy*. (Springer US, 1996). doi:10.1007/978-1-4757-2519-3

170. MA., H. *Principles and techniques of electron microscopy: biological applications. Cambridge University Press* (Cambridge University Press, 2000).

171. David C. Bell; Natasha Erdman & Bell, David C. ; Erdman, N. Introduction to the Theory and Advantages of Low Voltage Electron Microscopy. *Low Volt. Electron Microsc. Princ. Appl.* 1–218 (2013).

172. Chaffey, N. Hayat MA. 2000. Principles and techniques of electron microscopy: biological applications. 4th edn . 543pp. Cambridge: Cambridge University Press. £65 (hardback). . *Ann. Bot.* **87**, 546–548 (2001).

173. Fultz, B. & Howe, J. M. *Transmission Electron Microscopy and Diffractometry of Materials (Third Edition) Diffraction and the X-Ray Powder Diffractometer*. *Springer Science & Business Media* (2007). doi:10.1007/978-3-642-29761-8

174. Williams David B. (David Bernard), 1949-. *Transmission electron microscopy : a textbook for materials science. Part 1: Basics*. (Springer, 2009).

175. Luo, Z. *A Practical Guide to Transmission Electron Microscopy, Volume II*. **II**, (Momentum Press).

176. Carter, D. B. W. & C. B. *Transmission Electron Microscopy*. *Springer* (2018).

177. Browning, N. D. & Pennycook, S. J. Characterization of High Tc Materials and Devices by Electron Microscopy. *Charact. High Tc Mater. Devices by Electron Microsc.* (2000). doi:10.1017/cbo9780511534829

178. *Nanocharacterisation*. (The Royal Society of Chemistry, 2007). doi:10.1039/9781847557926

179. Williams, D. B. & Carter, C. B. *Transmission Electron Microscopes A Textbook for Materials Science*. (Springer, 2009).

180. Koningsberger, D. C. & Prins, R. *X-ray absorption : principles, applications, techniques of EXAFS, SEXAFS, and XANES*. (New York : Wiley, 1988).

181. Penner-Hahn, J. E. X-ray Absorption Spectroscopy. *Compr. Coord. Chem. II* **2**, 159–186 (2003).

182. Heald, S. *XAFS SPECTROSCOPY*.

183. Leo, B. F. *et al.* The stability of silver nanoparticles in a model of pulmonary surfactant. *Environ. Sci. Technol.* **47**, 11232–11240 (2013).

184. Sk, M. H. *et al.* Effect of Trace H 2 S on the Scale Formation Behavior in a Predominant CO 2 Environment under Hydrodynamic Control: Role of Cr/Mo Micro-Alloying in Plain Carbon Steel . *J. Electrochem. Soc.* **166**, C3233–C3240 (2019).

185. Gomez-Gonzalez, M. A. *et al.* Spatially Resolved Dissolution and Speciation Changes of ZnO Nanorods during Short-Term in Situ Incubation in a Simulated Wastewater Environment. *ACS Nano* **13**, 11049–11061 (2019).

186. Gusev, A. I. & Sadovnikov, S. I. Acanthite–argentite transformation in nanocrystalline silver sulfide and the Ag2S/Ag nanoheterostructure. *Semiconductors* **50**, 682–687 (2016).

187. Wang, P. *et al.* Silver sulfide nanoparticles (Ag2S-NPs) are taken up by plants and are phytotoxic. *Nanotoxicology* **9**, 1041–1049 (2015).

188. Sadovnikov, S. I., Kuznetsova, Y. V. & Rempel, A. A. Ag2S silver sulfide nanoparticles and colloidal solutions: Synthesis and properties. *Nano-Structures and Nano-Objects* **7**, 81–91 (2016).

189. Zhang, Y., Xia, J., Liu, Y., Qiang, L. & Zhu, L. Impacts of Morphology, Natural Organic Matter, Cations, and Ionic Strength on Sulfidation of Silver Nanowires. *Environ. Sci. Technol.* **50**, 13283–13290 (2016).

190. Chen, S. *et al.* High-resolution analytical electron microscopy reveals cell culture media-induced changes to the chemistry of silver nanowires. *Environ. Sci. Technol.* **47**, 13813–13821 (2013).

191. Akaighe, N. *et al.* Humic acid-induced silver nanoparticle formation under environmentally relevant conditions. *Environ. Sci. Technol.* **45**, 3895–3901 (2011).

192. Zou, X., Shi, J. & Zhang, H. Morphological evolution and reconstruction of silver nanoparticles in aquatic environments: The roles of natural organic matter and light irradiation. *J. Hazard. Mater.* **292**, 61–69 (2015).

193. Elechiguerra, J. L. *et al.* Corrosion at the nanoscale: The case of silver nanowires and nanoparticles. *Chem. Mater.* **17**, 6042–6052 (2005).

194. Jovanović, Ž. *et al.* Structural and optical characteristics of silver/poly(N-vinyl-2-pyrrolidone) nanosystems synthesized by γ-irradiation. *Radiat. Phys. Chem.* **81**, 1720–1728 (2012).

195. Li, L., Zhou, Q., Geng, F., Wang, Y. & Jiang, G. Formation of nanosilver from silver sulfide nanoparticles in natural waters by photoinduced Fe(II, III) redox cycling. *Environ. Sci. Technol.* **50**, 13342–13350 (2016).

196. Liu, D. *et al.* Perfluorooctanoic acid degradation in the presence of Fe(III) under natural sunlight. *J. Hazard. Mater.* **262**, 456–463 (2013).

197. Liu, X., Wu, F. & Deng, N. Photoproduction of Hydroxyl Radicals in Aqueous Solution with Algae under High-Pressure Mercury Lamp. *Environ. Sci. Technol.* **38**, 296–299 (2004).

198. Tokumura, M., Morito, R., Hatayama, R. & Kawase, Y. Iron redox cycling in hydroxyl radical generation during the photo-Fenton oxidative degradation: Dynamic change of hydroxyl radical concentration. *Appl. Catal. B Environ.* **106**,

565–576 (2011).

199. Burns, J. M., Craig, P. S., Shaw, T. J. & Ferry, J. L. Multivariate examination of Fe(II)/Fe(III) cycling and consequent hydroxyl radical generation. *Environ. Sci. Technol.* **44**, 7226–7231 (2010).

200. Sand, W., Gehrke, T., Jozsa, P. G. & Schippers, A. (Bio)chemistry of bacterial leaching - direct vs. indirect bioleaching. *Hydrometallurgy* **59**, 159–175 (2001).

201. Schippers, A. & Sand, W. Bacterial leaching of metal sulfides proceeds by two indirect mechanisms via thiosulfate or via polysulfides and sulfur. *Appl. Environ. Microbiol.* **65**, 319–321 (1999).

202. Huang, K. *et al.* Room Temperature Cation Exchange Reaction in Nanocrystals for Ultrasensitive Speciation Analysis of Silver Ions and Silver Nanoparticles. *Anal. Chem.* **87**, 6584–6591 (2015).

203. Liu, J., Sonshine, D. A., Shervani, S. & Hurt, R. H. Controlled release of biologically active silver from nanosilver surfaces. *ACS Nano* **4**, 6903–6913 (2010).

204. Moskovits, M. & Vlčková, B. Adsorbate-induced silver nanoparticle aggregation kinetics. *J. Phys. Chem. B* **109**, 14755–14758 (2005).

205. Tolaymat, T. M. *et al.* An evidence-based environmental perspective of manufactured silver nanoparticle in syntheses and applications: A systematic review and critical appraisal of peer-reviewed scientific papers. *Sci. Total Environ.* **408**, 999–1006 (2010).

206. Croteau, M. N., Misra, S. K., Luoma, S. N. & Valsami-Jones, E. Silver bioaccumulation dynamics in a freshwater invertebrate after aqueous and dietary exposures to nanosized and ionic Ag. *Environ. Sci. Technol.* **45**, 6600–6607 (2011).

207. Gutierrez, L., Aubry, C., Cornejo, M. & Croue, J. P. Citrate-Coated Silver Nanoparticles Interactions with Effluent Organic Matter: Influence of Capping Agent and Solution Conditions. *Langmuir* **31**, 8865–8872 (2015).

208. Gunsolus, I. L., Mousavi, M. P. S., Hussein, K., Bühlmann, P. & Haynes, C. L.

Effects of Humic and Fulvic Acids on Silver Nanoparticle Stability, Dissolution, and Toxicity. *Environ. Sci. Technol.* **49**, 8078–8086 (2015).

209. Zhu, G. & Yin, J. Fluorescence Quenching of Humic Acid by Coated Metallic Silver Particles. *J. Fluoresc.* **27**, 1233–1243 (2017).

210. Sadovnikov, S. I. & Gusev, A. I. Recent progress in nanostructured silver sulfide: From synthesis and nonstoichiometry to properties. *J. Mater. Chem. A* **5**, 17676–17704 (2017).

211. Milieu Environmental Law and Policy. Final Report Environmental Exposure to Nanomaterials – Data Scoping Study November. 227 (2012).

212. Sotiriou, G. A. & Pratsinis, S. E. Antibacterial activity of nanosilver ions and particles. *Environ. Sci. Technol.* **44**, 5649–5654 (2010).

213. McLaughlin, J. & Bonzongo, J. C. J. Effects of natural water chemistry on nanosilver behavior and toxicity to Ceriodaphnia dubia and Pseudokirchneriella subcapitata. *Environ. Toxicol. Chem.* **31**, 168–175 (2012).

214. González, J., Sánchez, M. & Gómez, X. Enhancing Anaerobic Digestion: The Effect of Carbon Conductive Materials. *C* **4**, 59 (2018).

215. Anukam, A., Mohammadi, A., Naqvi, M. & Granström, K. A review of the chemistry of anaerobic digestion: Methods of accelerating and optimizing process efficiency. *Processes* **7**, 1–19 (2019).

216. Sato, M. Persistency-field Eh-pH diagrams for sulfides and their application to supergene oxidation and enrichment of sulfide ore bodies. *Geochim. Cosmochim. Acta* **56**, 3133–3156 (1992).

217. Donner, E. *et al.* X-ray absorption and micro X-ray fluorescence spectroscopy investigation of copper and zinc speciation in biosolids. *Environ. Sci. Technol.* **45**, 7249–7257 (2011).

218. Luis, R. *et al.* Bioresource Technology Enrichment and acclimation of an anaerobic mesophilic microorganism ' s inoculum for standardization of BMP assays.

Bioresour. Technol. **219**, 21–28 (2016).

219. Kanematsu, M., Perdrial, N., Um, W., Chorover, J. & O'Day, P. A. Influence of phosphate and silica on U(VI) precipitation from acidic and neutralized wastewaters. *Environ. Sci. Technol.* **48**, 6097–6106 (2014).

220. Taber, W. A. *Wastewater microbiology. Annual review of microbiology* **30**, (1976).

221. Musa, M. A., Idrus, S., Hasfalina, C. M. & Daud, N. N. N. Effect of organic loading rate on anaerobic digestion performance of mesophilic (UASB) reactor using cattle slaughterhouse wastewater as substrate. *Int. J. Environ. Res. Public Health* **15**, (2018).

222. Farquhar, G. B. A Review and Update of the Role of Volatile Fatty Acids (VFA's) in Seawater Injection Systems. *CORROSION 98* 11 (1998).

223. Nguyen, D., Visvanathan, C., Jacob, P. & Jegatheesan, V. International Biodeterioration & Biodegradation Effects of nano cerium (IV) oxide and zinc oxide particles on biogas production. *Int. Biodeterior. Biodegradation* **102**, 165–171 (2015).

224. Luna-delRisco, M., Orupõld, K. & Dubourguier, H. C. Particle-size effect of CuO and ZnO on biogas and methane production during anaerobic digestion. *J. Hazard. Mater.* **189**, 603–608 (2011).

225. Chen, Y., Cheng, J. J. & Creamer, K. S. Inhibition of anaerobic digestion process: A review. *Bioresour. Technol.* **99**, 4044–4064 (2008).

226. Mu, H. & Chen, Y. Long-term effect of ZnO nanoparticles on waste activated sludge anaerobic digestion. *Water Res.* **45**, 5612–5620 (2011).

227. Cismasu, A. C., Levard, C., Michel, F. M. & Brown, G. E. Properties of impurity-bearing ferrihydrite II: Insights into the surface structure and composition of pure, Al- and Si-bearing ferrihydrite from Zn(II) sorption experiments and Zn K-edge X-ray absorption spectroscopy. *Geochim. Cosmochim. Acta* **119**, 46–60 (2013).

228. Zheng, L. *et al.* Mechanistic investigation of toxicological change in ZnO and TiO

2 multi-nanomaterial systems during anaerobic digestion and the microorganism response. *Biochem. Eng. J.* **147**, 62–71 (2019).

229. Dœlsch, E., Deroche, B. & Van de Kerchove, V. Impact of sewage sludge spreading on heavy metal speciation in tropical soils (Réunion, Indian Ocean). *Chemosphere* **65**, 286–293 (2006).

230. Legros, S. *et al.* Combining Size Fractionation, Scanning Electron Microscopy, and X-ray Absorption Spectroscopy to Probe Zinc Speciation in Pig Slurry. *J. Environ. Qual.* **39**, 531–540 (2010).

231. Tella, M. *et al.* Increased zinc and copper availability in organic waste amended soil potentially involving distinct release mechanisms. *Environ. Pollut.* **212**, 299–306 (2016).

232. Hagos, K., Zong, J., Li, D., Liu, C. & Lu, X. Anaerobic co-digestion process for biogas production: Progress, challenges and perspectives. *Renew. Sustain. Energy Rev.* **76**, 1485–1496 (2017).

233. Goswami, R., Chattopadhyay, P. & Shome, A. An overview of physico-chemical mechanisms of biogas production by microbial communities : a step towards sustainable waste management. *3 Biotech* **6**, 1–12 (2016).

234. Le Bars, M. *et al.* Drastic Change in Zinc Speciation during Anaerobic Digestion and Composting: Instability of Nanosized Zinc Sulfide. *Environ. Sci. Technol.* **52**, 12987–12996 (2018).

235. Ma, R., Levard, C., Michel, F. M., Brown, G. E. & Lowry, G. V. *Sulfidation Mechanism for Zinc Oxide Nanoparticles and the Effect of Sulfidation on Their Solubility*.

236. Chen, S. & Liu, W. Preparation and characterization of surface-coated ZnS nanoparticles. *Langmuir* **15**, 8100–8104 (1999).

237. Sharma, V. K., Filip, J., Zboril, R. & Varma, R. S. Natural inorganic nanoparticles – formation, fate, and toxicity in the environment. *Chem. Soc. Rev.* **44**, 8410–8423

(2015).

238. Zhang, W., Yao, Y., Li, K., Huang, Y. & Chen, Y. Influence of dissolved oxygen on aggregation kinetics of citrate-coated silver nanoparticles. *Environ. Pollut.* **159**, 3757–3762 (2011).

239. Wang, Z., Chen, J., Li, X., Shao, J. & Peijnenburg, W. J. G. M. Aquatic toxicity of nanosilver colloids to different trophic organisms: Contributions of particles and free silver ion. *Environ. Toxicol. Chem.* **31**, 2408–2413 (2012).

240. Małgorzata Ksiazyk, Monika Asztemborska, Romuald Steborowski, G. B.-P. Toxic effect of silver and platinum nanoparticles toward the freshwater microalga Pseudokirchneriella subcapitata. *Bull. Environ. Contam. Toxicol.* (2015). doi:10.1007/s00128-015-1505-9

241. Sun, T. Y., Bornhöft, N. A., Hungerbühler, K. & Nowack, B. Dynamic Probabilistic Modeling of Environmental Emissions of Engineered Nanomaterials. *Environ. Sci. Technol.* **50**, 4701–4711 (2016).

242. Leclerc, S. & Wilkinson, K. J. Bioaccumulation of nanosilver by Chlamydomonas reinhardtii - Nanoparticle or the free ion? *Environ. Sci. Technol.* **48**, 358–364 (2014).

243. González, A. G. *et al.* Silver nanoparticles impact phototrophic biofilm communities to a considerably higher degree than ionic silver. *Environ. Sci. Pollut. Res. Int.* (2015). doi:10.1007/s11356-014-3978-1

244. Elzey, S. & Grassian, V. H. Agglomeration, isolation and dissolution of commercially manufactured silver nanoparticles in aqueous environments. *J. Nanoparticle Res.* **12**, 1945–1958 (2010).

245. Zook, J. M., Long, S. E., Cleveland, D., Geronimo, C. L. A. & MacCuspie, R. I. Measuring silver nanoparticle dissolution in complex biological and environmental matrices using UV-visible absorbance. *Anal. Bioanal. Chem.* **401**, 1993–2002 (2011).

246. Jin, R. *et al.* Photoinduced conversion of silver nanospheres to nanoprisms. *Science*

(80-.). **294**, 1901–1903 (2001).

247. Keast, V. J., Myles, T. A., Shahcheraghi, N. & Cortie, M. B. Corrosion processes of triangular silver nanoparticles compared to bulk silver. *J. Nanoparticle Res.* **18**, 1–11 (2016).

248. Hou, W. C., Stuart, B., Howes, R. & Zepp, R. G. Sunlight-driven reduction of silver ions by natural organic matter: Formation and transformation of silver nanoparticles. *Environ. Sci. Technol.* **47**, 7713–7721 (2013).

249. Gatselou, V. A., Giokas, D. L. & Vlessidis, A. G. Determination of dissolved organic matter based on UV-light induced reduction of ionic silver to metallic nanoparticles by humic and fulvic acids. *Anal. Chim. Acta* **812**, 121–128 (2014).

250. Adeleye, A. S. & Keller, A. A. Interactions between Algal Extracellular Polymeric Substances and Commercial TiO_2 Nanoparticles in Aqueous Media. *Environ. Sci. Technol.* **50**, 12258–12265 (2016).

251. Sheng, G., Yu, H. & Li, X. Extracellular polymeric substances (EPS) of microbial aggregates in biological wastewater treatment systems : A review. *Biotechnol. Adv.* **28**, 882–894 (2010).

252. Zhou, K., Hu, Y., Zhang, L., Yang, K. & Lin, D. The role of exopolymeric substances in the bioaccumulation and toxicity of Ag nanoparticles to algae. *Sci. Rep.* **6**, 1–11 (2016).

253. Park, E. J., Yi, J., Kim, Y., Choi, K. & Park, K. Silver nanoparticles induce cytotoxicity by a Trojan-horse type mechanism. *Toxicol. Vitr.* **24**, 872–878 (2010).

254. Sekine, R. *et al.* Complementary Imaging of Silver Nanoparticle Interactions with Green Algae: Dark-Field Microscopy, Electron Microscopy, and Nanoscale Secondary Ion Mass Spectrometry. *ACS Nano* **11**, 10894–10902 (2017).

255. Zhang, L., Wu, L., Si, Y. & Shu, K. Size-dependent cytotoxicity of silver nanoparticles to Azotobacter vinelandii: Growth inhibition, cell injury, oxidative stress and internalization. *PLoS One* **13**, 1–18 (2018).

256. Zhang, L. & Wang, W. X. Dominant Role of Silver Ions in Silver Nanoparticle Toxicity to a Unicellular Alga: Evidence from Luminogen Imaging. *Environ. Sci. Technol.* **53**, 494–502 (2019).

257. Zheng, S. *et al.* Role of extracellular polymeric substances on the behavior and toxicity of silver nanoparticles and ions to green algae Chlorella vulgaris. *Sci. Total Environ.* **660**, 1182–1190 (2019).

258. Czaczyk, K. & Myszka, K. Biosynthesis of extracellular polymeric substances (EPS) and its role in microbial biofilm formation. *Polish J. Environ. Stud.* **16**, 799–806 (2007).

259. More, T. T., Yadav, J. S. S., Yan, S., Tyagi, R. D. & Surampalli, R. Y. Extracellular polymeric substances of bacteria and their potential environmental applications. *J. Environ. Manage.* **144**, 1–25 (2014).

260. Römer, I. *et al.* Aggregation and dispersion of silver nanoparticles in exposure media for aquatic toxicity tests. *J. Chromatogr. A* **1218**, 4226–4233 (2011).

261. Krienitz, L., Bock, C., Nozaki, H. & Wolf, M. Ssu rRNA gene phylogeny of morphospecies affiliated to the bioassay alga 'selenastrum capricornutum' recovered the polyphyletic origin of crescent-shaped chlorophyta. *J. Phycol.* **47**, 880–893 (2011).

262. Pulido-reyes, G., Rodea-palomares, I., Das, S. & Sakthivel, T. S. Untangling the biological effects of cerium oxide nanoparticles : the role of surface valence states. *Nat. Publ. Gr.* 1–14 doi:10.1038/srep15613

263. Wang, Q., Kang, F., Gao, Y., Mao, X. & Hu, X. Sequestration of nanoparticles by an EPS matrix reduces the particle- specific bactericidal activity. *Nat. Publ. Gr.* 1–10 (2016). doi:10.1038/srep21379

264. Buchmann, J. P. & Holmes, E. C. Cell Walls and the Convergent Evolution of the Viral Envelope. **79**, 403–418 (2015).

265. Gerken, H. G., Donohoe, B. & Knoshaug, E. P. Enzymatic cell wall degradation of

Chlorella vulgaris and other microalgae for biofuels production. 239–253 (2013). doi:10.1007/s00425-012-1765-0

266. Rashidi, B. & Trindade, L. M. Detailed biochemical and morphologic characteristics of the green microalga Neochloris oleoabundans cell wall. *Algal Res.* **35**, 152–159 (2018).

267. Ribeiro, F. *et al.* Uptake and elimination kinetics of silver nanoparticles and silver nitrate by Raphidocelis subcapitata: The influence of silver behaviour in solution. *Nanotoxicology* **9**, 686–695 (2015).

268. Theodorou, I. G. *et al.* Silver Nanowire Particle Reactivity with Human Monocyte-Derived Macrophage Cells: Intracellular Availability of Silver Governs Their Cytotoxicity. (2017). doi:10.1021/acsbiomaterials.7b00479

269. Wang, S., Lv, J., Ma, J. & Zhang, S. Cellular internalization and intracellular biotransformation of silver nanoparticles in Chlamydomonas reinhardtii. *Nanotoxicology* **10**, 1129–1135 (2016).

270. Bovenkamp, G. L., Zanzen, U., Krishna, K. S., Hormes, J. & Prange, A. X-Ray absorption near-edge structure (XANES) spectroscopy study of the interaction of silver ions with Staphylococcus aureus, Listeria monocytogenes, and Escherichia coli. *Appl. Environ. Microbiol.* **79**, 6385–6390 (2013).

271. Zhou, K., Hu, Y., Zhang, L., Yang, K. & Lin, D. The role of exopolymeric substances in the bioaccumulation and toxicity of Ag nanoparticles to algae. *Sci. Rep.* **6**, (2016).

272. da Silva Ferreira, V. *et al.* Green production of microalgae-based silver chloride nanoparticles with antimicrobial activity against pathogenic bacteria. *Enzyme Microb. Technol.* **97**, 114–121 (2017).

273. Kleiven, M., Macken, A. & Oughton, D. H. Growth inhibition in Raphidocelis subcapita – Evidence of nanospecific toxicity of silver nanoparticles. *Chemosphere* **221**, 785–792 (2019).

274. Becaro, A. A. *et al.* Toxicity of PVA-stabilized silver nanoparticles to algae and microcrustaceans. *Environ. Nanotechnology, Monit. Manag.* **3**, 22–29 (2015).

275. Jiang, W., Kim, B. Y. S., Rutka, J. T. & Chan, W. C. W. Nanoparticle-mediated cellular response is size-dependent. *Nat. Nanotechnol.* **3**, 145–150 (2008).

276. Morones, J. R. *et al.* The bactericidal effect of silver nanoparticles. *Nanotechnology* **16**, 2346–2353 (2005).

277. Chen, S. *et al.* Sulfidation of silver nanowires inside human alveolar epithelial cells: A potential detoxification mechanism. *Nanoscale* **5**, 9839–9847 (2013).

278. Li, X. *et al.* Silver nanoparticle toxicity and association with the alga Euglena gracilis. *Environ. Sci. Nano* **2**, 594–602 (2015).

279. Yue, Y. *et al.* Interaction of silver nanoparticles with algae and fish cells: A side by side comparison. *J. Nanobiotechnology* **15**, 1–12 (2017).

280. Ma, S. & Lin, D. The biophysicochemical interactions at the interfaces between nanoparticles and aquatic organisms: adsorption and internalization. *Environ. Sci. Process. Impacts* **15**, 145–160 (2013).

281. Moreno-Garrido, I., Pérez, S. & Blasco, J. Toxicity of silver and gold nanoparticles on marine microalgae. *Mar. Environ. Res.* **111**, 60–73 (2015).

282. Blinova, I. Use of Freshwater Algae and Duckweeds for Phytotoxicity Testing. 425–428 (2004). doi:10.1002/tox.20042

283. Hong, Y., Hu, H. Y. & Li, F. M. Growth and physiological responses of freshwater green alga Selenastrum capricornutum to allelochemical ethyl 2-methyl acetoacetate (EMA) under different initial algal densities. *Pestic. Biochem. Physiol.* **90**, 203–212 (2008).

284. Flemming, H.-C. EPS—Then and Now. *Microorganisms* **4**, 41 (2016).

285. Ribeiro, F. *et al.* Silver nanoparticles and silver nitrate induce high toxicity to Pseudokirchneriella subcapitata, Daphnia magna and Danio rerio. *Sci. Total*

Environ. **466**–**467**, 232–241 (2014).

286. Levard, C. *et al.* Effect of chloride on the dissolution rate of silver nanoparticles and toxicity to E. coli. *Environ. Sci. Technol.* **47**, 5738–5745 (2013).

287. Lee, D. Y., Fortin, C. & Campbell, P. G. C. Contrasting effects of chloride on the toxicity of silver to two green algae, Pseudokirchneriella subcapitata and Chlamydomonas reinhardtii. *Aquat. Toxicol.* **75**, 127–135 (2005).

288. Hiriart-Baer, V. P., Fortin, C., Lee, D. Y. & Campbell, P. G. C. Toxicity of silver to two freshwater algae, Chlamydomonas reinhardtii and Pseudokirchneriella subcapitata, grown under continuous culture conditions: Influence of thiosulphate. *Aquat. Toxicol.* **78**, 136–148 (2006).

Appendix A

Appendix A-1: chapter 5 (XAS)

Table A1: XAS spectra for ZnENMs after anaerobic digestion in different time and table of each speciation ration where the total =1 with R- factor which indicated the accuracy the fitting data set.

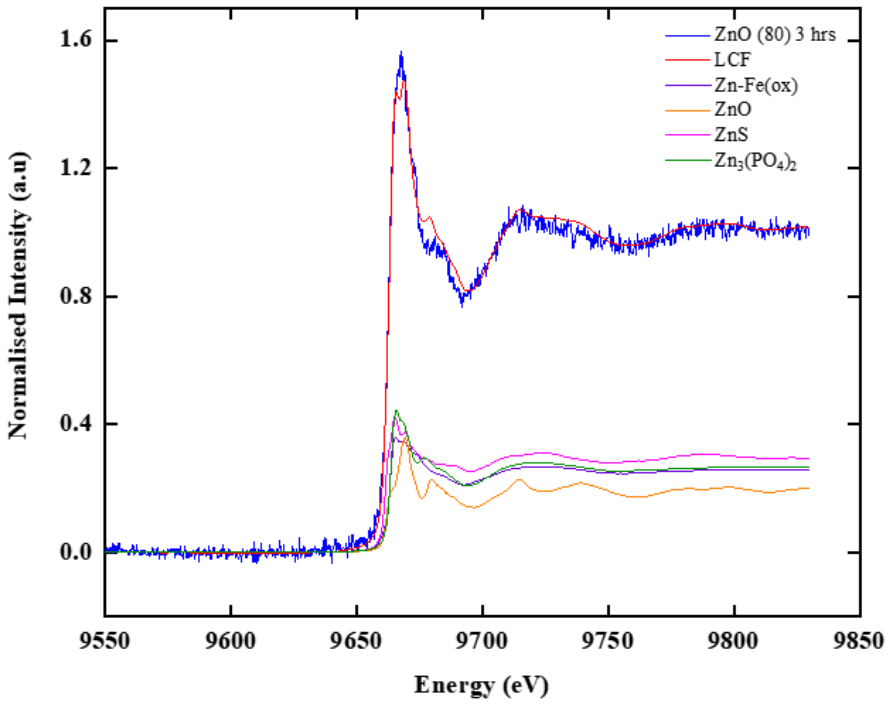	ZnONPs (80-200 nm) 500 ppm in ADS 3 hrs
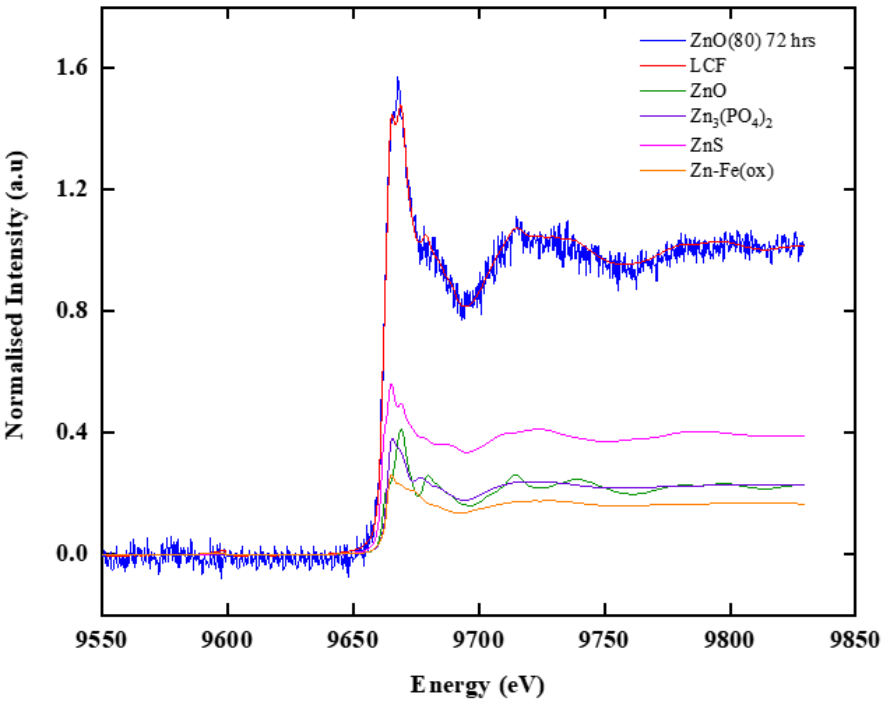	ZnONPs (80-200 nm) 500 ppm in ADS 72 hrs

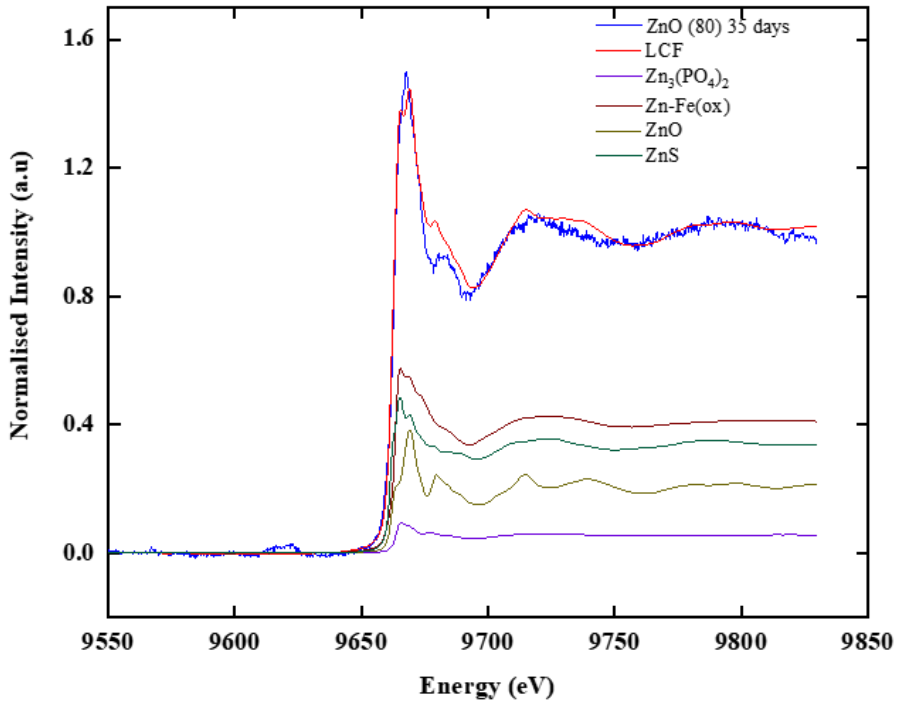

ZnONPs (80-200 nm) 500 ppm in ADS

35 days

Incubation Time (hrs)	ZnONPs (80-200 nm) 500 ppm in ADS				
	ZnO	ZnS	Zn-Fe(ox)	Zn3(PO4)2	R-Factor
3	0.192	0.293	0.253	0.262	0.0072
72	0.221	0.389	0.165	0.225	0.0052
840 (35 days)	0.206	0.336	0.403	0.055	0.0098

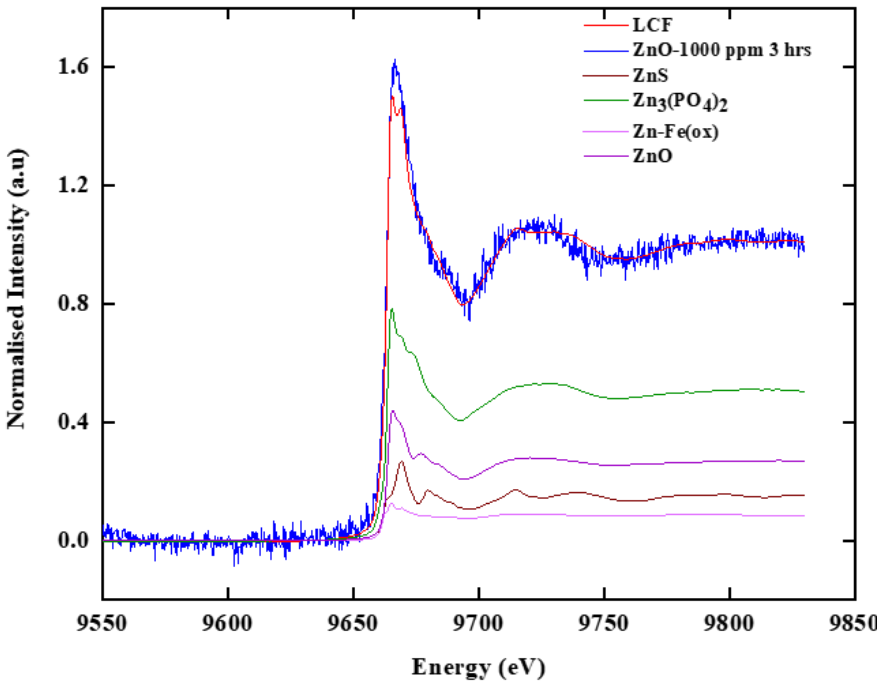	ZnONPs (80-200 nm) 1000 ppm in ADS 3 hrs
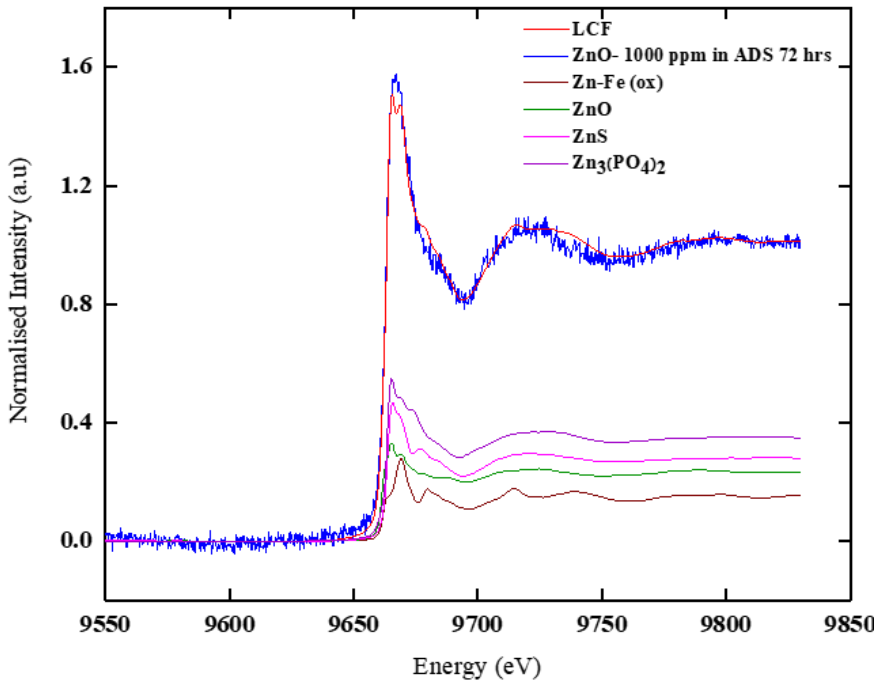	ZnONPs (80-200 nm) 1000 ppm in ADS 72 hrs

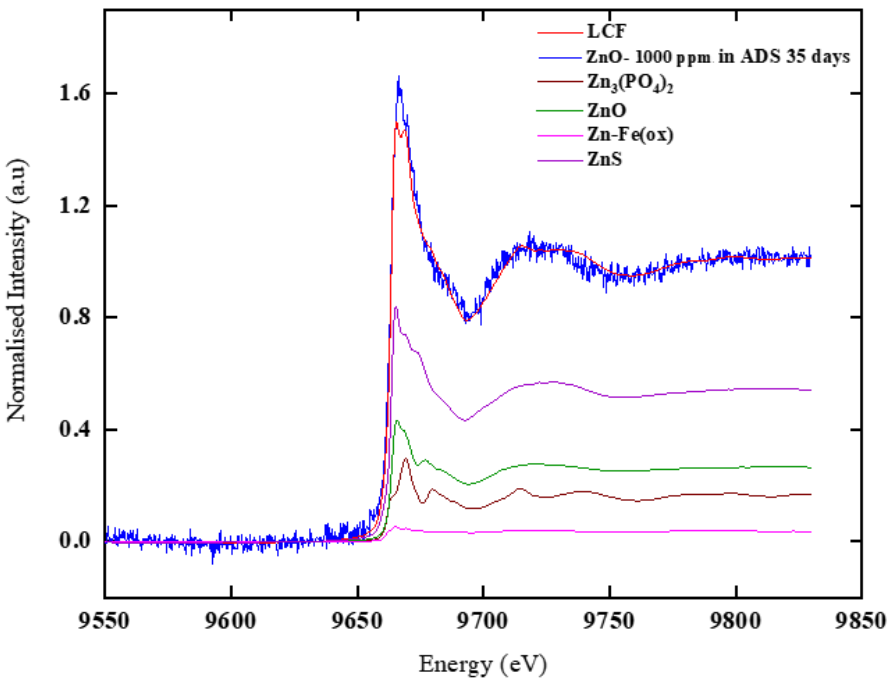

ZnONPs (80-200 nm) 1000 ppm in ADS

35 days

Incubation Time	ZnONPs (80-200 nm) 1000 ppm in ADS				
	ZnO	ZnS	Zn-Fe(ox)	Zn3(PO4)2	R-Factor
3 hrs	0.148	0.085	0.502	0.265	0.0093
72 hrs	0.149	0.23	0.345	0.276	0.0064
840 (35 days)	0.164	0.036	0.538	0.262	0.0086

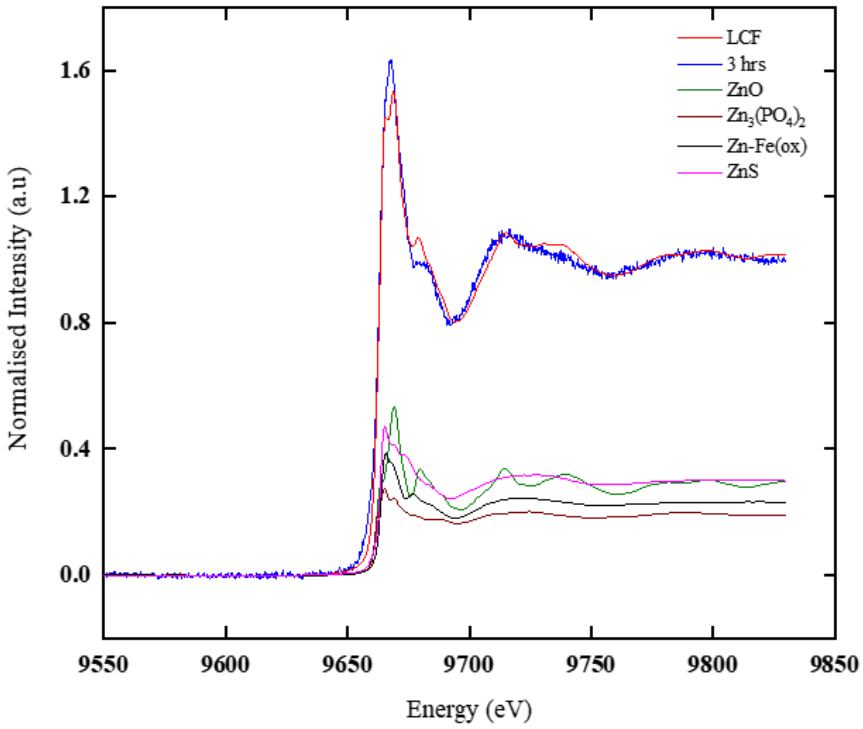	ZnONPs (30 nm) 500 ppm in ADS 3 hrs
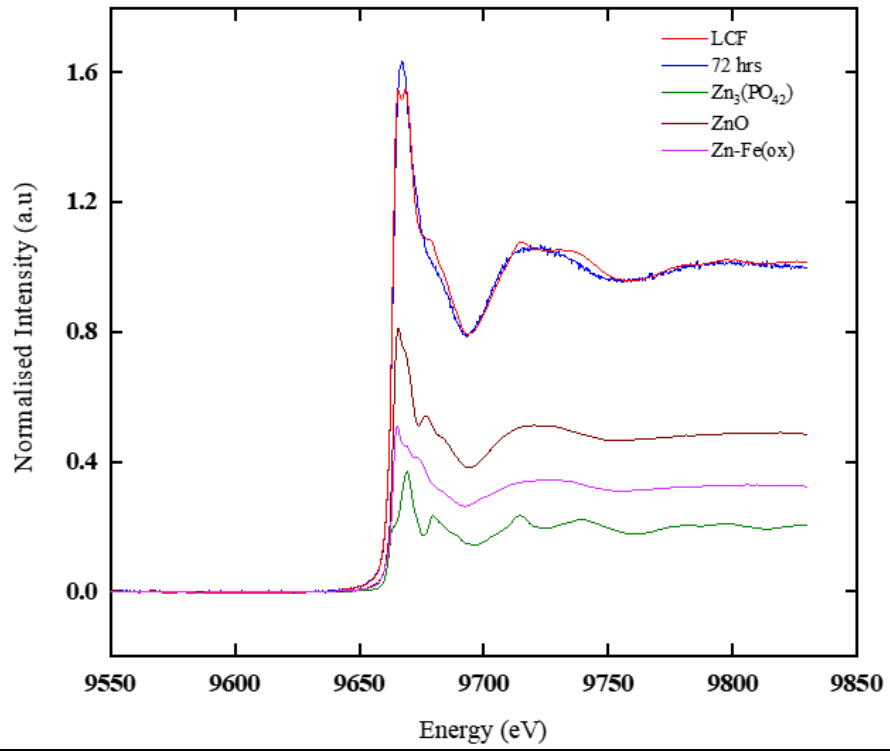	ZnONPs (30 nm) 500 ppm in ADS 72 hrs

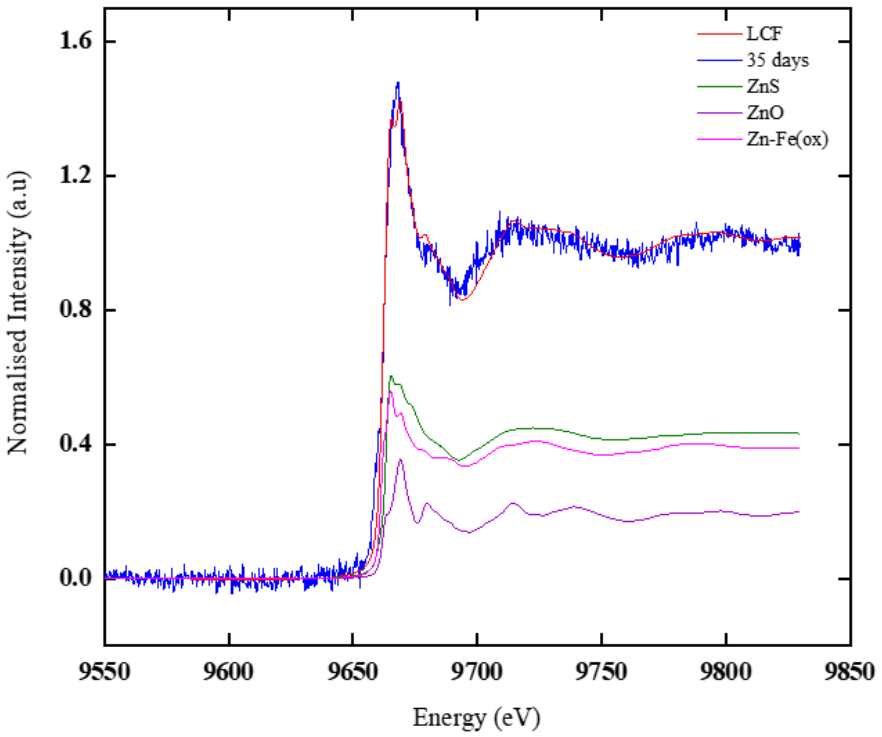

ZnONPs (30 nm) 500 ppm in ADS

35 days

Incubation Time	ZnONPs (30 nm) 500 ppm in ADS				
	ZnO	ZnS	Zn-Fe(ox)	Zn3(PO4)2	R-Factor
3 hrs	0.286	0.19	0.296	0.228	0.009
72 hrs	0.198	…….	0.321	0.481	0.003
840 (35 days)	0.19	0.386	0.424	…….	0.01

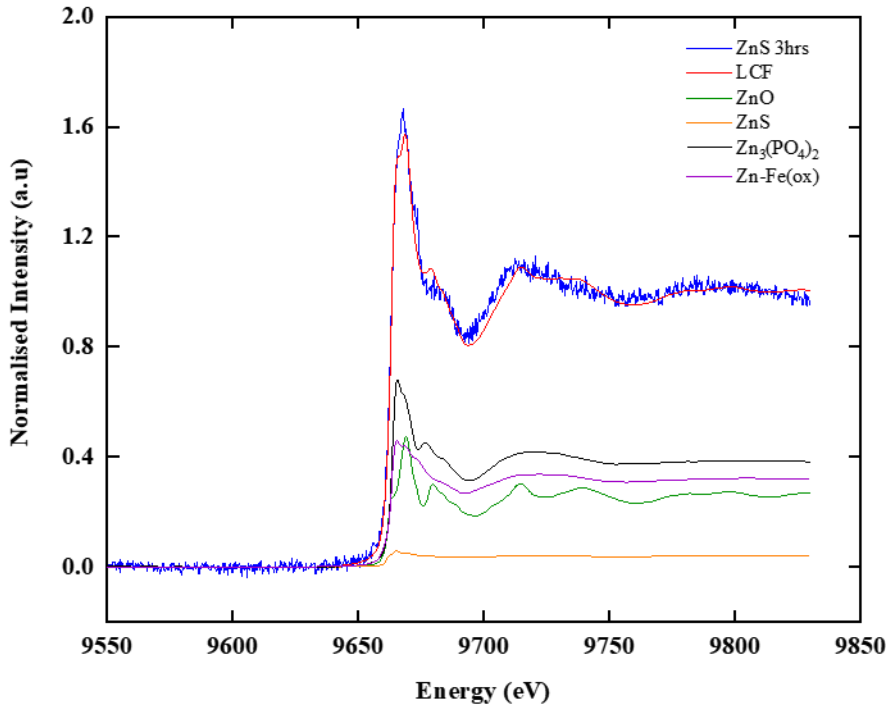	ZnSNPs (200 nm) 500 ppm in ADS 3 hrs
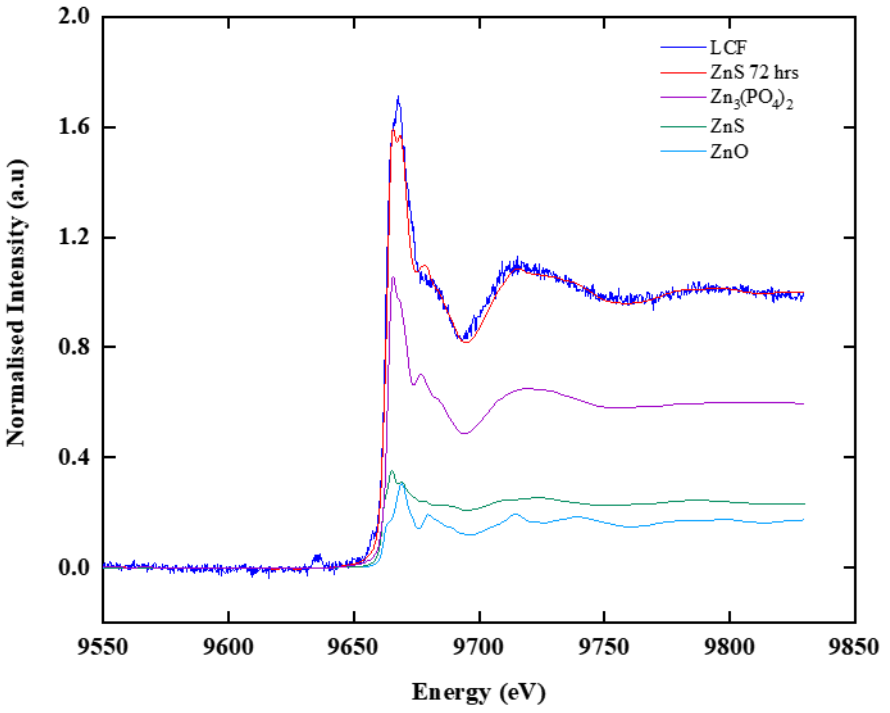	ZnSNPs (200 nm) 500 ppm in ADS 72 hrs

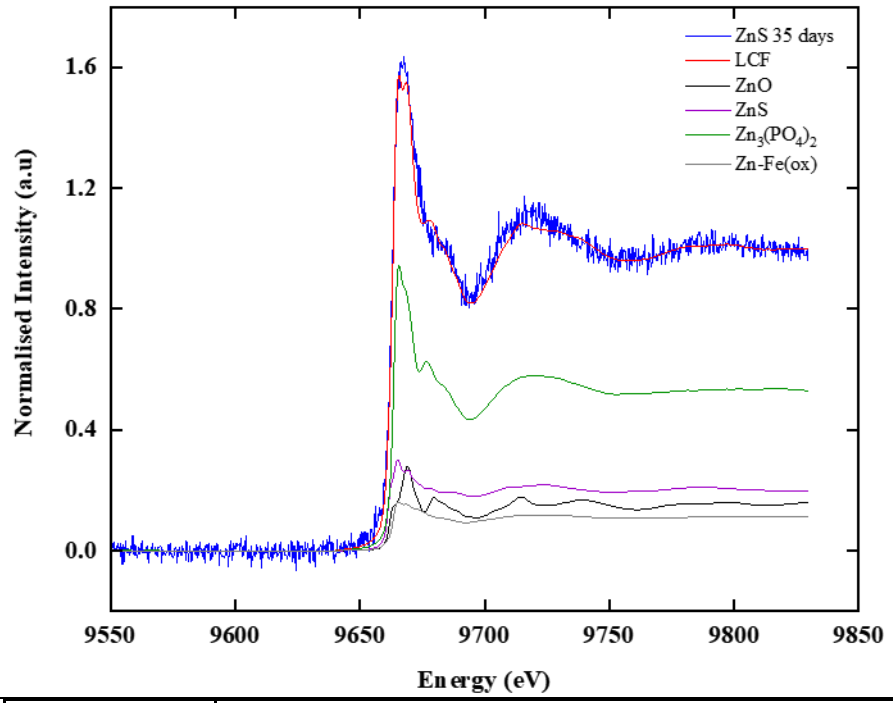

ZnSNPs (200 nm) 500 ppm in ADS

35 days

Incubation Time	ZnSNPs (200 nm) 500 ppm in ADS				
	ZnO	ZnS	Zn-Fe(ox)	Zn3(PO4)2	R-Factor
3 hrs	0.26	0.038	0.318	0.384	0.0053
72 hrs	0.167	0.235	…….	0.597	0.0082
840 (35 days)	0.153	0.202	0.111	0.533	0.0069

Appendix A-1: chapter 5

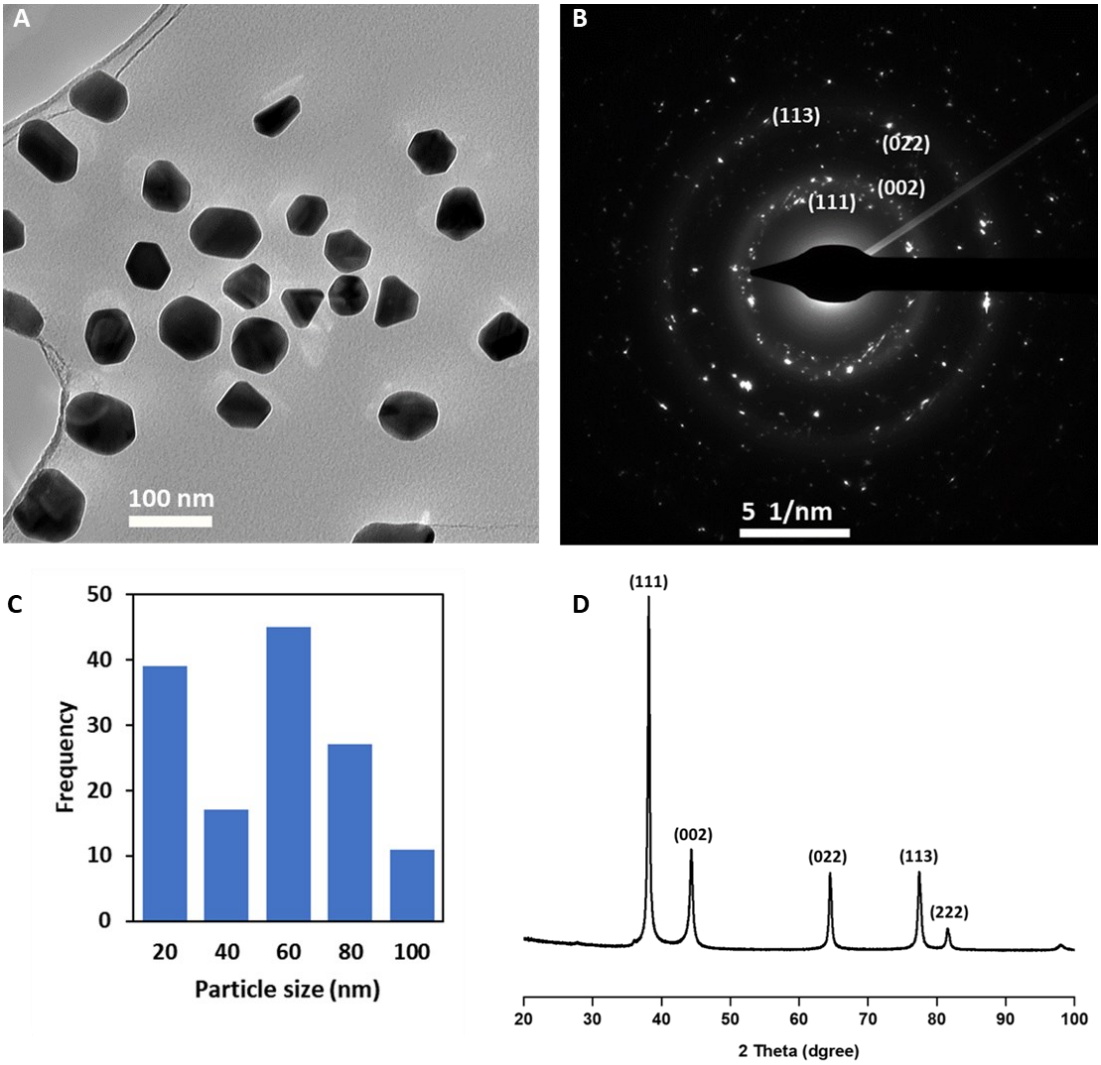

Figure A1: The characterisation of commercial PVP-AgNPs pristine (A) Bright-field TEM micrograph for AgNPs (B) Selected electron diffraction pattern (SADP) revealed the corresponding planes (111), (002), (022) and (113) to the interplanar distance 0.241 ± 0.01 nm, 0.209 ± 0.005 nm, 0.145 ± 0.001 nm, and 0.125 ± 0.002 nm, respectively (camera length 30 cm) (C) The size distribution of AgNPs calculated for n = 140 particles using ImageJ software (43.91 ± 23.83 nm) (D) X-ray diffraction pattern for PVP-AgNPs has the pattern of the (SADP).